Fakultät für Physik
Technische Universität München

Top-Quark Mass Determinations in the $e\mu$ Dilepton Channel

and

Top-Quark Mass Effects in Higgs Boson Pair Production

Ludovic M. Scyboz

Vollständiger Abdruck der von der Fakultät für Physik der Technischen Universität München zur Erlangung des akademischen Grades eines

Doktors der Naturwissenschaften (Dr. rer. nat.)

genehmigten Dissertation.

Vorsitzender:
Prof. Dr. Andreas Weiler

Prüfende der Dissertation:
1. Priv.-Doz. Dr. Stefan Kluth
2. Prof. Dr. Martin Beneke

Die Dissertation wurde am 31.05.2019 bei der Technischen Universität München eingereicht und durch die Fakultät für Physik am 15.07.2019 angenommen.

Abstract

The top quark is a centerpiece of the Standard Model (SM) of Particle Physics. It interacts across all sectors and with all gauge fields, and has been successfully used as a portal to precision measurements of the SM parameters. Top quarks are also indirectly related to other SM sectors, for example to Higgs boson production processes which are induced predominantly by top-quark loops at the Large Hadron Collider (LHC). During Runs I and II of the LHC, a large number of top-quark pair ($t\bar{t}$) and single-top events were recorded. They allow to reduce the experimental uncertainty on top-quark properties, like the top-quark mass, spin correlations and W-boson polarization in $t\bar{t}$ events, the Wtb coupling, or flavor-changing neutral currents. In the case of the top-quark mass, the experimental uncertainties of the latest ATLAS and CMS combinations are now competing with theoretical uncertainties: approximations that were previously thought to be appropriate must be reevaluated.

In particular, the narrow-width approximation (NWA) for top-quark pair processes assumes the production of an on-shell top and anti-top quark, and is used in Monte-Carlo (MC) predictions for most experimental measurements. Since the actual final-state is composed of the top-quark pair decay products, a more accurate description of the signal should consider $W^+W^-b\bar{b}$ final-states instead. The full final-state includes contributions that cannot be factorized in both top-quark decay legs, or that do not contain a top-quark pair to begin with. These diagrams are called non-factorizing, respectively non-doubly resonant. In cases where measurements rely on phase-space regions sensitive to these contributions, the extracted top-quark mass will be biased.

In this work, the ATLAS top-quark mass analysis in the $e\mu$ dilepton channel is taken as an example. The analysis uses simulated template distributions to extract the MC top-quark mass via an unbinned likelihood fit. In a setup similar to the experimental analysis, the extracted top-quark mass is compared at parton level in different theoretical descriptions of the $t\bar{t}$ final-state at next-to-leading order (NLO) in production. MC events are produced for different descriptions of the top-quark decay in the NWA, as well as for the full $W^+W^-b\bar{b}$ process at NLO QCD in production. The top-quark mass m_t^{MC} extracted by the template fit method is compared for each of these theoretical descriptions, and important offsets of up to $\Delta m_t^{\mathrm{MC}} \sim 1\,\mathrm{GeV}$ are underlined. A more realistic assessment is presented, where these predictions are folded to detector level.

As mentioned, the top-quark mass also plays an important role in other sectors of the SM. In di-Higgs production with non-SM values of the Higgs couplings, it is shown that the m_t-dependence of QCD NLO corrections introduces sizable differences with respect to predictions where the top-quark degrees of freedom are integrated out. A full-fledged MC event generator is introduced with the possibility of varying the Higgs self-coupling and the top-Higgs Yukawa coupling.

Zusammenfassung

Im Standard-Modell (SM) der Teilchenphysik spielt das Top-Quark eine zentrale Rolle. Es wechselwirkt mit Teilchen aller Sektoren sowie mit allen quantentheoretischen Eichfeldern, und wurde in verschiedenen Zusammenhängen als Grundpfeiler für Präzisionsmessungen des SM verwendet. Top-Quarks sind auch indirekt mit anderen Sektoren des SM eng verbunden: Higgs-Bosonen zum Beispiel werden am Large Hadron Collider (LHC) überwiegend durch Top-Quark-Schleifen erzeugt. Während Run I und II des LHC wurde eine große Anzahl an Top-Quark-Paaren ($t\bar{t}$) und Einzel-Top-Events ermittelt. Diese ermöglichen es, Messungen von Top-Quark-Eigenschaften bedeutend zu verbessern, beispielsweise die der Top-Quark-Masse. In diesem Fall sind die von ATLAS und CMS angegebenen experimentellen Unsicherheiten zu dem Punkt gekommen, wo sie mit den aktuellen theoretischen Unsicherheiten konkurrieren: das heisst insbesondere, dass früher verwendete Näherungen neu evaluiert werden müssen.

Die sogenannte Schmal-Breite-Näherung (NWA), bei der ein Top-Quark-Paar on-shell produziert wird, wird üblicherweise in den meisten Monte-Carlo (MC) Generatoren verwendet. Weil der gemessene $t\bar{t}$-Endzustand aber von den Top-Zerfallsprodukten gebildet wird, sollte eine konsistente Beschreibung des Signals eher auf dem intermediären $W^+W^-b\bar{b}$ Zustand beruhen. Letzerer beinhaltet Feynman-Diagramme, die entweder nicht in zwei Top-Zerfall-Kanäle faktorisieren, oder überhaupt keine zwei Top-Propagatoren aufweisen. Diese Diagramme heissen nicht-faktorisierend, bzw. nicht-doppelt-resonant. Wenn Messungen durchgeführt werden, welche sensitiv auf solche Beiträge sind, kann es zu einer Verzerrung der extrahierten Top-Quark-Masse kommen.

Die ATLAS Top-Quark-Massenanalyse im $e\mu$-Dileptonkanal, welche simulierte Templates zur Bestimmung der Top-Quark-Masse verwendet, wird als Beispiel genommen. In einem ähnlichen Setup wird die extrahierte Top-Masse verglichen, wo unterschiedliche $t\bar{t}$- Endzustandsbeschreibungen in nächstführender Ordnung der Störungstheorie (NLO) in der Produktion verwendet werden. Genauer werden für drei verschiedene Beschreibungen des Top-Quark-Zerfalls, sowie für die volle NLO $W^+W^-b\bar{b}$-Rechnung, Verteilungen erzeugt. Die mithilfe der Template-Fit-Methode extrahierte Top-Quark-Masse m_t^{MC} zeigt erhebliche Unterschiede bis zu $\Delta m_t^{\mathrm{MC}} \sim 1$ GeV. Eine realistischere Studie wird eingeführt, in welcher Particle-Level-Vorhersagen auf Detektor-Level gefaltet werden.

Außerdem wirken Top-Quark-Effekte auch im Higgs-Sektor. Anhand des Beispiels von Higgs-Paar-Produktion (hh) beim LHC wird gezeigt, dass die m_t-Abhängigkeit von hh-Produktion auf NLO QCD zu Unterschieden in differentiellen Verteilungen führt im Vergleich zu Vorhersagen, wo die Top-Quark-Freiheitsgrade ausintegriert werden. Ein vollständiges MC-Programm zur Erzeugung von Higgs-Paar-Events, wo die trilineare Higgs-Selbstkopplung sowie die Higgs-Top-Yukawakopplung variiert werden können, wird präsentiert.

Contents

1 Introduction

The Standard Model (SM) of Particle Physics is one of the most successful physical theories to date. While it still raises some unanswered questions that are outlined in Chapter 2, the precision to which its predictions were tested by high-energy colliders, but also in low-energy experiments or larger-scale universe phenomena, is extremely convincing. In particular, the SM bases on mathematical concepts that allow for a significant predictive power. Considering that physicists tend to prefer a theory with the least amount of free parameters and a maximal predictive power, the SM fares rather well: it contains only 19 parameters, namely the angles of the Cabibbo-Kobayashi-Maskawa mixing matrix and its CP-violating phase (3 + 1), the gauge couplings corresponding to the model's underlying symmetries (3), the lepton and quark masses (9), the QCD vacuum angle (1), and the Higgs mass and vacuum expectation value (2). Since most of these parameters have been measured to an excellent precision, efforts have largely concentrated on the more elusive parameters, one of these being the top-quark mass.

Because the top quark is the heaviest known elementary particle, with a mass from the world combination measured at $m_t = 173.0 \pm 0.4\,\text{GeV}$ [1], physicists had to wait until 1995 for its observation by the CDF [2] and DØ [3] experiments at Fermilab, 23 years after it was predicted. Only then did the last missing piece of the three quark generations fall into place. Nowadays, abundant production of top quarks with the Large Hadron Collider (LHC) at CERN allows for a variety of accurate measurements of its properties. Of particular interest, the precise determination of its mass is a key to a deeper understanding of modern quantum-field theory (QFT). Most notably, the top-quark mass enters global electroweak fits which are important for consistency testing of the SM; it also strongly affects corrections to the Higgs quartic coupling, thus having a large impact on the stability of the SM vacuum. Finally, being the only quark with a lifetime surpassing the hadronization scale, it is the only *bare* colored particle produced in SM processes. In general, one has to choose an appropriate mass definition, be it a QFT-consistent definition like the pole mass (on-shell renormalized) and the $\overline{\text{MS}}$ mass (renormalized after the short-distance $\overline{\text{MS}}$ scheme), or the so-called Monte-Carlo (MC) mass.

Recently, the ATLAS and CMS experiments, using innovative approaches and analysis techniques, have been able to reduce the uncertainty of the measured MC top-quark mass to about $\Delta m_t \approx 0.5\,\text{GeV}$ in their respective combinations [5, 6] (see Fig. 1.1 for measurements at the LHC). Achieving a more precise determination of m_t constitutes a significant challenge for both the experimental and theoretical communities. While on the one hand, experimentalists have to find new ideas to drive down the mostly systematics-dominated uncertainties, theorists need to improve precision calculations by going to higher-order predictions and beyond formerly accepted approximations. The

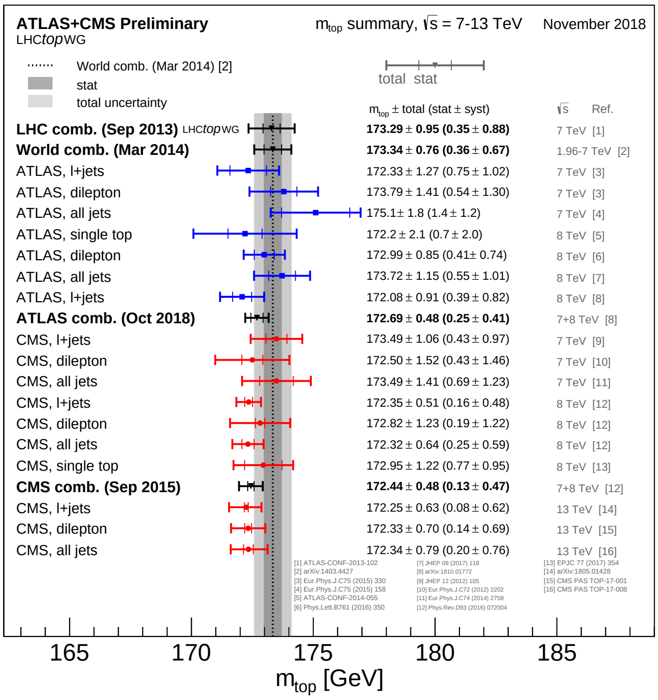

Figure 1.1: ATLAS and CMS combination of $\sqrt{s} = 7, 8, 13$ TeV data for measurements of the top-quark mass m_t. Figure taken from Ref. [4].

computation of higher-order corrections for on-shell top-quark pair ($t\bar{t}$) production has been a major success during the LHC era. The production of a pair of on-shell top quarks is referred to as the narrow-width approximation (NWA). Because the corrections to NWA calculations are expected to be small, of order $\mathcal{O}(\Gamma_t/m_t) < 1\%$ for inclusive cross-sections, most fixed-order predictions aim at computing higher-order QCD and EW corrections to top-quark pair production in this approximation.

The experimentalists, though, reconstruct the top-quark pair from their decay products, either from the dilepton, lepton+jets or allhadronic final-states, depending on the decay channel of the top and anti-top quarks. The fixed-order prediction of a fully-decayed $t\bar{t}$ final-state is computationally demanding: instead of a $2 \to 2$ process, the final-state phase-space becomes that of a $2 \to 4$ (for $pp \to W^+W^-b\bar{b}$) or a $2 \to 6$ process (including W-boson decay products). The full final-state prediction at next-to-leading order (NLO) comprises Feynman diagrams that are not present in the NWA: some do not contain doubly-resonant top quarks, and others include internal lines between the top-quark decay legs, which means the latter do not factorize. In fact, the additional interference terms can be of importance to distributions that are sensitive to higher-order and off-shell effects, for example in phase-space regions populated first at higher-order in QCD. The qualitative differences between NWA and full $W^+W^-b\bar{b}$ predictions shall be investigated later on.

Another issue concerns the theoretical definition of the top-quark mass in different renormalization schemes. Indeed, relations between schemes are known at 4-loop order [7]. This relation suffers from an infrared (IR) so-called renormalon singularity, which is associated with an intrinsically non-perturbative ambiguity in the definition of the top-quark pole mass. This inherent uncertainty was estimated to be of the order $\mathcal{O}(250\,\mathrm{MeV})$ [8–11]. Moreover, analyses that rely on simulated distributions (like the template fit method studied in the next chapters) measure the MC top-quark mass, not the pole mass. Although the discussion on the exact relation of the MC mass to the top-quark pole mass is still ongoing, the difference between both values is expected to be of the order $\mathcal{O}(300 - 500\,\mathrm{MeV})$ [12, 13].

In this work, the foundations of the SM are briefly presented, including the Higgs mechanism and the relation between the Higgs sector and the top quark, in Chapter 2. In Chapter 3, the basics of higher-order calculations are summarized: the appearance of UV and IR divergences in loop corrections and the way to deal with them, the perturbative expansion for QCD at high energies from the running of the strong coupling α_s, and the factorization theorem for hadron-hadron collisions are laid out in some detail. Finally, the focus point is set on MC event generators in Chapter 4, and the ingredients needed for particle-level event generation are explained. Switching to the experimental side, the LHC and in particular the ATLAS detector are presented in Chapter 5. After having sketched out these fundaments, the different theoretical descriptions of top-quark pair production are discussed in Chapter 6. With the example of top-quark pair predictions in the $e\mu$ dilepton channel, it is shown how higher-order and off-shell effects can have a sizable impact on an experimental MC top-quark mass extraction in Chapter 7. There, four different theoretical descriptions are compared with respect to an experimentally realistic top-quark mass extraction for $pp \to W^+(\to e^+\nu_e)W^-(\to \mu^-\bar{\nu}_\mu)b\bar{b}$. In the NWA, top-quark pair production is described at NLO QCD, and the top-quark decay is calculated at different accuracies: LO, respectively NLO QCD, as well as operated by a parton-shower. The NWA results are compared to a full $W^+W^-b\bar{b}$ computation at NLO QCD. Taking into account detector reconstruction efficiencies and bin migration effects, which are the subject of Chapter 8, the shift in the extracted top-quark mass is quantified in an exact ATLAS framework in Chapter 9, where distributions are folded up to detector level.

Looking at another sector entirely, top quarks also play an important role in calculations for the production of Higgs bosons at the LHC. Because the top quark is the heaviest SM particle and since the Higgs boson's coupling to fermions is proportional to their mass, higher-order corrections to Higgs processes mainly happen through top-quark loops. For instance, single Higgs production at the LHC is dominated by gluon fusion with a top-quark loop intermediate state (so-called loop-induced production). Higher-order corrections to $gg \to h$ thus start to contribute at two-loop level already. The same holds for the production of a pair of Higgs bosons: this process is of particular interest, since di-Higgs production is the main channel for probing the trilinear Higgs self-coupling. Although the Higgs couplings to heavy fermions and gauge bosons are currently reasonably constrained, as shown in Fig. 1.2, the best limit set on the Higgs self-coupling's ratio κ_λ to the SM-predicted value is given by ATLAS at

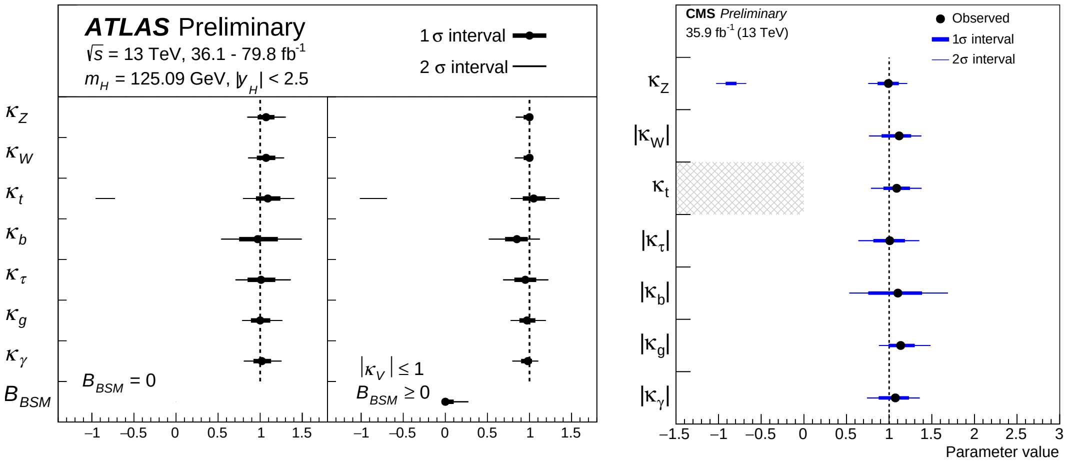

(a) ATLAS [14] **(b)** CMS [15]

Figure 1.2: Fit values of the Higgs coupling modifiers with respect to the SM-predicted coupling strength (in the $\kappa-$framework).

$-5.0 \leq \kappa_\lambda \leq 12.1$ [16]. In general, the Higgs sector is one of the more poorly explored experimentally, and it is important to have precise (at best model-independent) theoretical predictions for the case where the Higgs couplings are not SM-like. It is shown, within a non-linear Effective Field Theory (EFT) framework allowing to vary the Higgs couplings, that the full m_t-dependence of di-Higgs production at NLO QCD has important effects, especially on differential cross-section predictions. In Chapter 10, the EFT framework is introduced in the form of the Electroweak Chiral Lagrangian (EWChL). The results for di-Higgs cross-sections at NLO QCD and differential distributions with variations of the Higgs couplings are presented at a center-of-mass energy of 14 TeV for several benchmark points. Finally, the implementation of the full m_t-dependent NLO corrections for di-Higgs production into the POWHEG-BOX-V2 [17–19] event generator is the subject of Chapter 11. In this package, variations of the trilinear Higgs self-coupling and the top-Higgs Yukawa coupling are now possible. Studies comparing differential distributions for fixed-order NLO to parton-shower matched predictions are presented. Parton-shower related uncertainties are also discussed. Finally, the current state of the SM is summarized and future, potentially interesting developments in both top-quark and Higgs physics are outlined.

Part I

Theoretical and Experimental Setup

2 The Standard Model

The SM was developed and supplemented over five decades, and describes all elementary particles and their interactions via three of the four fundamental forces in a quantum-field theoretical framework: the electromagnetic, weak and strong interactions. Although it is known that the SM suffers from some theoretical shortfalls that are briefly described at the end of this chapter (like non-zero neutrino mass measurements [20]), there is, to date, no experimental evidence that directly contradicts it.

At the core, the discovery by Glashow, Salam and Weinberg [21–23] that the electromagnetic and weak interactions could be embedded in a unified theory constitutes the first stone of the SM edifice. What if all known forces and particles could be described by the same, unique theory? Later, the quantum chromodynamics (QCD) sector, describing the strong interaction, was correctly theorized to rely on a non-Abelian gauge symmetry group by Wilczek, Gross and Politzer [24, 25]. This group structure leads to the asymptotic freedom of color-charged particles. The addition of the Higgs mechanism, which generates mass terms for the fermions and gauge bosons, culminated in what is known today as the SM Lagrangian. The SM is one of the most successful theories up-to-date, and has been extensively tested against experimental data. A comprehensive comparison of computed cross-sections for SM processes to values measured by ATLAS, shown in Fig. 2.1, makes for a compelling argument in favor of the SM's predictive power.

2.1 Matter content and gauge interactions

The SM is a quantum-field gauge theory: the known elementary particles are interpreted as the excitations of quantized fields, and their interactions are described by the exchange of gauge bosons. Both matter and gauge fields obey certain rules under the corresponding gauge transformations: that is, they transform according to different representations of the underlying gauge group. The SM builds on the

$$SU(3)_C \times SU(2)_L \times U(1)_Y$$

gauge group. It is the product group of the QCD group $SU(3)_C$, and its corresponding color quantum number C, and the electroweak group $SU(2)_L \times U(1)_Y$, that distinguishes left- from right-handed particles as doublets, respectively singlets under the group transformation. The $U(1)_Y$ group's quantum number is the hypercharge Y. The fermionic matter fields are classified into left-handed leptons and quarks, both transforming as doublets under the $SU(2)_L$ group, and their singlet right-handed counterparts. There are furthermore three distinct copies, called generations, or families:

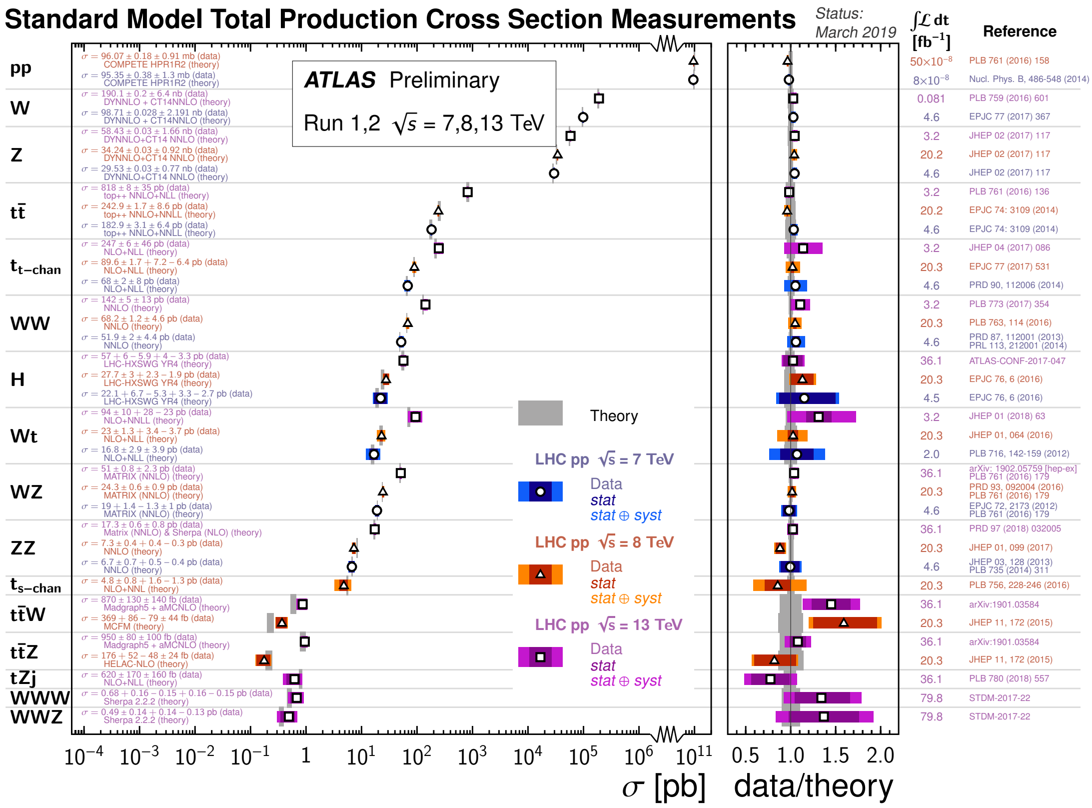

Figure 2.1: The predicted cross-sections (in gray, where bands represent the theoretical uncertainty) for SM production processes at LHC center-of-mass energies of $\sqrt{s} = 7, 8, 13\,\mathrm{TeV}$ are compared to their measured values at the ATLAS experiment (in color) [26]. The ratio of data to theory is shown to be compatible with 1.

$$\begin{pmatrix}\nu_e\\ e^-\end{pmatrix}_L, \quad \begin{pmatrix}u\\ d'\end{pmatrix}_L, \qquad \begin{pmatrix}\nu_\mu\\ \mu^-\end{pmatrix}_L, \quad \begin{pmatrix}c\\ s'\end{pmatrix}_L, \qquad \begin{pmatrix}\nu_\tau\\ \tau^-\end{pmatrix}_L, \quad \begin{pmatrix}t\\ b'\end{pmatrix}_L,$$

$$e^-_R, \quad u_R, \quad d'_R, \qquad \mu^-_R, \quad c_R, \quad s'_R, \qquad \tau^-_R, \quad t_R, \quad b'_R,$$

and their corresponding anti-particles. Here, e, μ, τ are the three lepton (ℓ) generations and their corresponding neutrinos ν_ℓ. The particles u, c, t, and d', s', b' are the up-type, respectively down-type quark weak eigenstates. The down-type eigenstates mix via the unitary Cabibbo-Kobayashi-Maskawa (CKM) matrix to give the physical mass eigenstates d, s, b:

$$\begin{pmatrix}d'\\ s'\\ b'\end{pmatrix} = \begin{pmatrix}V_{ud} & V_{us} & V_{ub}\\ V_{cd} & V_{cs} & V_{cb}\\ V_{td} & V_{ts} & V_{tb}\end{pmatrix}\begin{pmatrix}d\\ s\\ b\end{pmatrix}.$$

The quarks are the only matter fields carrying color charge, and live in the triplet (**3**), respectively anti-triplet ($\bar{\mathbf{3}}$) representations of the $SU(3)_C$ group. The color quantum numbers are defined as red, blue and green, respectively anti-red, anti-blue and anti-green. That is, for the up- and down-quark:

$$\begin{pmatrix} u_r \\ u_b \\ u_g \end{pmatrix} , \quad \begin{pmatrix} d_r \\ d_b \\ d_g \end{pmatrix} \in SU(3)_C \; .$$

Governing the interactions, the gauge bosons corresponding to each subgroup couple with a separate strength to the matter fields. There are:

- three W^a_μ, $a = (1, 2, 3)$, bosons belonging to $SU(2)_L$, coupling with strength $\propto g$,
- one B_μ boson belonging to $U(1)_Y$, coupling with strength $\propto g'$,
- eight gluon fields G^a_μ, $a = (1, ..., 8)$, belonging to $SU(3)_C$, with coupling $\propto g_s$.

By the principle of gauge covariance, the interaction terms between gauge bosons and the rest of the particle fields are given by promoting the 4-derivatives in the kinetic terms of the corresponding sector to covariant derivatives:

$$\partial_\mu \rightarrow D_\mu = \left[\partial_\mu + ig\frac{\sigma_a}{2}W^a_\mu + ig'\frac{Y}{2}B_\mu\right] \qquad \text{(EW)} \; , \tag{2.1}$$

$$\partial_\mu \rightarrow D_\mu = \left[\partial_\mu + ig_s T_a G^a_\mu\right] \qquad \text{(QCD)} \; , \tag{2.2}$$

where σ_a are the three Pauli matrices (the generators of the Lie algebra of $SU(2)_L$), and T_a are the eight generators of the Lie algebra of $SU(3)_C$. The covariant derivative also induces gauge boson self-coupling interactions.

Finally, analogously to the quarks, the electroweak gauge bosons mix to give rise to the physical charged- and neutral-current interaction bosons:

$$W^\pm = \frac{1}{\sqrt{2}}\left(W^1 \mp iW^2\right) \; , \tag{2.3}$$

$$\begin{pmatrix} \gamma \\ Z \end{pmatrix} = \begin{pmatrix} \cos(\theta_W) & \sin(\theta_W) \\ -\sin(\theta_W) & \cos(\theta_W) \end{pmatrix} \begin{pmatrix} B \\ W^3 \end{pmatrix} \; , \tag{2.4}$$

where θ_W is the Weinberg angle.

2.2 The Higgs mechanism

If one writes down the most general, renormalizable Lagrangian for the model above, two problems appear:

- the usual Dirac mass terms one can introduce in the fermionic sector are not invariant under $SU(2)_L$,
- mass terms for the $W^\pm$, Z bosons are not gauge-invariant.

So, in order to generate masses for the aforementioned particles, an external contraption is needed. The Brout-Englert-Higgs [27–29] mechanism proposed in 1964 introduces a new spin-0 fundamental $SU(2)_L$ doublet, called the Higgs field:

$$\phi(x) = \begin{pmatrix} \phi^+(x) \\ \phi^0(x) \end{pmatrix} . \tag{2.5}$$

It is colorless, and is charged under the electroweak $U(1)_Y$ symmetry. The $SU(3)_C \times SU(2)_L \times U(1)_Y$ Lagrangian gets completed by a (gauged) Higgs sector, where the covariant derivative D_μ is given by Eq. (2.1):

$$\begin{aligned} \mathcal{L}_h &= (D_\mu\phi)^\dagger (D^\mu\phi) + V(\phi) & (2.6)\\ &= (D_\mu\phi)^\dagger (D^\mu\phi) + \mu^2\phi^\dagger\phi - \lambda\left(\phi^\dagger\phi\right)^2, \qquad \lambda > 0 . & (2.7) \end{aligned}$$

Similarly to the case of superconductivity [30], the underlying $SU(2)_L \times U(1)_Y$ symmetry can be spontaneously broken if the Higgs potential $V(\phi)$ has a non-zero ground state. This is the case for the *Mexican-hat* potential given above, which is pictured in Fig. 2.2. When the Higgs field assumes one of the degenerate ground states with a vacuum expectation value at the minimum of the potential around $v = \mu/\sqrt{\lambda} \sim 246$ GeV, it spontaneously breaks the $SU(2)_L \times U(1)_Y$ symmetry of the Lagrangian.

Expanding the Higgs field from Eq. (2.5) around the vacuum and taking the EW covariant derivative from Eq. (2.1),

$$\phi(x) = \frac{1}{\sqrt{2}} \begin{pmatrix} 0 \\ v + h(x) \end{pmatrix} , \tag{2.8}$$

$$D_\mu\phi(x) = \frac{1}{\sqrt{2}} \begin{pmatrix} \frac{ig}{2}\left(W_\mu^1 - iW_\mu^2\right)(v + h(x)) \\ \partial_\mu h(x) + \frac{i}{2}\left(g' B_\mu - gW_\mu^3\right)(v + h(x)) \end{pmatrix} , \tag{2.9}$$

the Higgs field naturally couples to the gauge bosons. Then, the squared gauged kinematic term of the spontaneously broken Higgs field from Eq. (2.7) cane be computed (once the gauge fields are replaced with their physical rotated states from Eqs. (2.3), (2.4)) and gives:

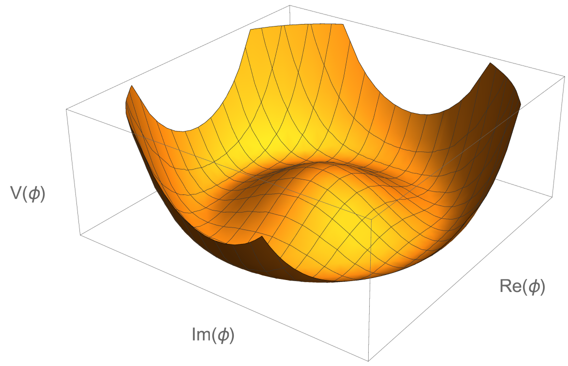

Figure 2.2: The $SU(2) \times U(1)$ symmetric Higgs Mexican-hat potential has a degenerate non-zero ground state at $v^2 = \langle \phi_0^\dagger \phi_0 \rangle \sim (246\ \text{GeV})^2$.

$$\begin{aligned}\mathcal{L} \supset \frac{1}{2}(\partial_\mu h)(\partial^\mu h) + \underbrace{\frac{g^2 v^2}{4}}_{m_W^2} W_\mu^+ W^{-\mu} + \frac{1}{2} \underbrace{\left(\frac{(g^2 + g'^2) v^2}{4} \right)}_{m_Z^2} Z_\mu Z^\mu \\ + \frac{1}{2} \underbrace{(2\lambda v^2)}_{m_h^2} h^2 + \lambda v h^3 + \frac{\lambda}{8} h^4 \, .\end{aligned} \tag{2.10}$$

The dynamic EW spontaneous symmetry breaking (EWSB) of the Higgs potential generates masses for the $W^\pm$, Z gauge bosons and identifying the mass terms in the Lagrangian leads to the following leading-order boson mass relations[1]:

$$\begin{aligned} m_H &= \sqrt{2\lambda} v \, , \\ m_W &= \frac{gv}{2} \, , & \cos(\theta_W) &= \frac{g}{\sqrt{g^2 + g'^2}} \, , \\ m_Z &= \frac{\sqrt{g^2 + g'^2} v}{2} \, , & \sin(\theta_W) &= \frac{g'}{\sqrt{g^2 + g'^2}} \, . \\ m_\gamma &= 0 \, , \end{aligned}$$

The $W^\pm$ and Z boson masses are related (at tree-level):

$$m_W = m_Z \cos(\theta_W) \, ,$$

with the experimentally measured values $m_W = 80.385$ GeV, $m_Z = 91.1876$ GeV and the Weinberg angle given by $\sin^2(\theta_W) = 0.2223$. Finally, considering the last two terms in Eq. (2.10), the Higgs couples to itself to produce the Feynman diagrams shown in Fig. 2.3.

[1]The introduction of the Higgs mechanism also allows for a fermionic gauge-invariant mass term, e.g. by the Yukawa coupling of fermions to the Higgs boson $\mathcal{L} \supset \frac{m_f}{2v} \bar{\psi}_f \psi_f h \xrightarrow{(h \to v)} \frac{1}{2} m_f \bar{\psi}_f \psi_f$.

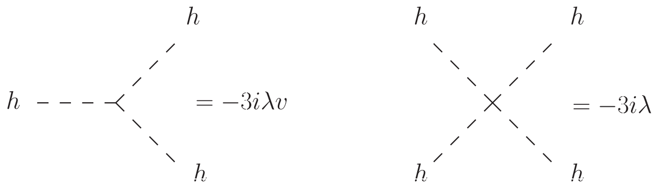

(a) Higgs trilinear self-coupling **(b)** Quartic coupling

Figure 2.3: The physical Higgs field couples to itself after EWSB. The Feynman rules are given for (a) the triple vertex and (b) the quartic vertex.

As a side note, expressing Eq. (2.5) with all available degrees of freedom would give, in polar coordinates,

$$\phi(x) = \frac{1}{\sqrt{2}} e^{\frac{i}{v}\chi_a(x)\sigma^a} \begin{pmatrix} 0 \\ v + h(x) \end{pmatrix} , \tag{2.11}$$

where the three real fields χ_a are the massless Goldstone bosons associated with the EWSB of $SU(2) \times U(1)$. Because they will anyhow disappear from the theory (their respective degrees of freedom are sacrificed to the W- and Z-boson longitudinal polarizations), they are not explicitly considered in the following. Combining the matter and gauge terms with the Higgs sector yields the final form of the SM Lagrangian:

$$\begin{aligned} \mathcal{L}_{\mathrm{SM}} = & -\frac{1}{2}\langle G_{\mu\nu}G^{\mu\nu}\rangle - \frac{1}{2}\langle W_{\mu\nu}W^{\mu\nu}\rangle - \frac{1}{4}B_{\mu\nu}B^{\mu\nu} \\ & + \sum_{\psi = q_L, \ell_L, q_R, \ell_R} \bar{\psi} i \not{D} \psi + \text{h.c.} \\ & + \bar{\ell}_L Y_\ell \ell_R \phi + \bar{q}_L Y_d d_R \phi + \bar{q}_L Y_u u_R \phi + \text{h.c.} \\ & + \left(D_\mu\phi\right)^\dagger \left(D^\mu\phi\right) + \mu^2 \phi^\dagger\phi - \lambda\left(\phi^\dagger\phi\right)^2 , \end{aligned} \tag{2.12}$$

where $\langle\cdot\rangle$ represents the trace and $\not{D} = \gamma^\mu \partial_\mu$. The first line contains the field-strength tensors of the corresponding gauge bosons, i.e. for a gauge group with structure functions f^{abc} defined by the generators $[T_a, T_b] =: i f^{abc} T_c$ of the corresponding Lie algebra, and general coupling strength $\tilde{g}$:

$$F^a_{\mu\nu} = \partial_\mu A^a_\nu - \partial_\nu A^a_\mu + \tilde{g} f^{abc} A^b_\mu A^c_\nu .$$

For the three SM subgroups:

- $SU(3)_C$
  - $\cdot$ $A^a_\mu := G^a_\mu$ the gluon fields in the adjoint representation,
  - $\cdot$ $\tilde{g} := g_s$ the strong coupling constant,
  - $\cdot$ $[T_a, T_b] =: i f^{abc} T_c$ with the generators given in Eq. (2.2).
- $SU(2)_L$
  - $\cdot$ $A^a_\mu := W^a_\mu$ the gauge fields defined in Eq. (2.1),
  - $\cdot$ $\tilde{g} := g$ the $SU(2)_L$ coupling constant,
  - $\cdot$ $[\sigma_a, \sigma_b] =: 2i\epsilon_{abc}\sigma_c$ with the Pauli matrices σ_i and the Levi-Civita symbol ϵ_{abc}.
- $U(1)_Y$
  - $\cdot$ $A^a_\mu := B_\mu$ the last gauge field appearing in Eq. (2.1),
  - $\cdot$ $\tilde{g} := g'$ the $U(1)_Y$ coupling constant,
  - $\cdot$ $f^{abc} = 0$ since the group is Abelian.

The second line of the SM Lagrangian in Eq. (2.12) contains the kinetic and interaction terms for the fermion fields. The third line contains the Yukawa interaction of all fermions with the Higgs boson for mass generation, and the last line is the unbroken SM Higgs boson sector.

The addition of just one Higgs doublet to the SM, like in Eq. (2.5), is a minimal choice. One could legitimately introduce further Higgs fields, as in the two-Higgs doublet model (2HDM) [31] or the Minimal Supersymmetric SM (MSSM) [32], which predict five physical scalar Higgs particles and which can assimilate the discovered Higgs boson at $m_h = 125\,\mathrm{GeV}$. These extensions of the SM predict in general different coupling strengths of the Higgs boson(s) to other particles and to itself. Precise experimental measurements of these couplings (and of the Higgs decay branching ratios) are needed in order to differentiate between models.

2.3 Top-Higgs interactions

Intrinsically, the top quark is tightly linked to the Higgs boson properties and has generally strong phenomenological implications for the Higgs sector. Because it is the heaviest SM elementary particle, and since the Yukawa coupling of the Higgs boson to fermions is proportional to their masses, the Higgs couples strongest to the top quark. It is especially important for Higgs production at the LHC: the predominant production mechanism is gluon fusion via a triangle top-quark loop. The theoretical cross-sections for single Higgs production are shown in Fig. 2.4. In comparison, other associated production modes have cross-sections that are more than one order of magnitude smaller. Representative Feynman diagrams for the main production channels at LHC are also depicted in Fig. 2.5.

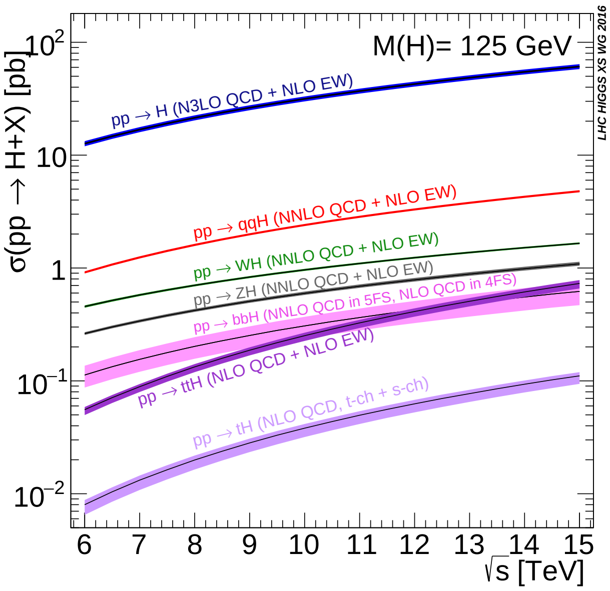

Figure 2.4: Theory prediction for $pp \to h + X$ production cross-sections as a function of the center-of-mass energy $\sqrt{s}$. Single Higgs production at the LHC is dominated by gluon fusion mediated by a top-quark loop. Figure taken from Ref. [33].

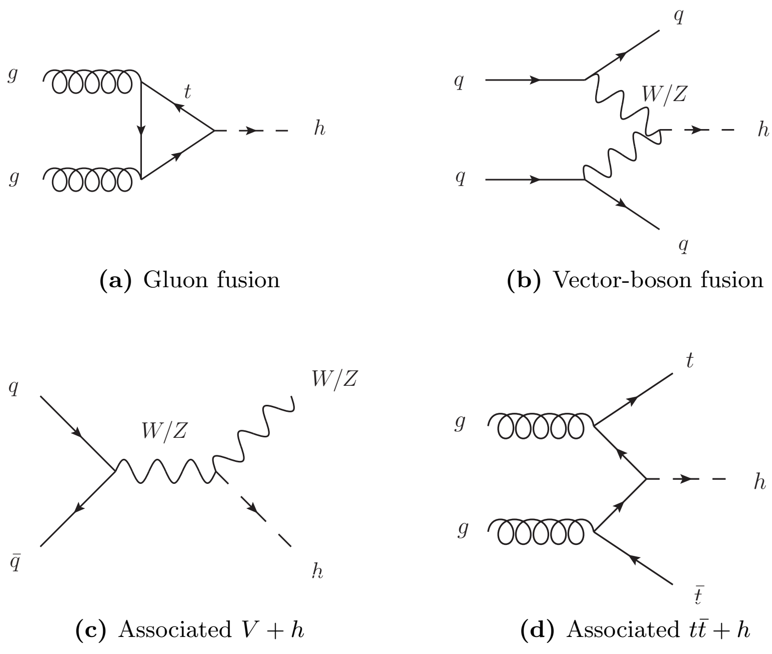

Figure 2.5: Leading-order diagrams for Higgs production by (a) gluon fusion, (b) vector-boson fusion, (c) associated vector production and (d) associated $t\bar{t}$ production.

In relation to both the measurement of the Higgs triple self-coupling and the importance of top-quark mass effects in Higgs production, the reader is referred to the extensive discussion laid out in Chapter 10. Not only do top quarks influence Higgs process cross-sections at collider experiments, but they also have a deeper connection to the Higgs potential. Indeed, the β-function of the Higgs quartic coupling (which governs the evolution of the coupling's value at different resolution scales, see Chapter 3) is sensitive to renormalization counterterms stemming from top-quark loops.

Eq. (2.13) gives the one-loop β-function for the Higgs quartic coupling [34]:

$$\mu^2 \frac{\mathrm{d}\lambda}{\mathrm{d}\mu^2} = \beta_\lambda(\lambda, y_t, g_s, \dots) = \frac{1}{16\pi^2}\left(12\lambda^2 + 6\lambda y_t^2 - 3y_t^4\right), \qquad y_t = \sqrt{2}\frac{m_t}{v} \sim 1\,, \tag{2.13}$$

where y_t is the top-Yukawa coupling and is proportional to the top-quark mass m_t.

Because the top-Yukawa coupling is of order $\mathcal{O}(1)$, small variations in the value of the top-quark mass modify the evolution of the Higgs quartic coupling λ in a non-trivial way. If $\lambda(\mu)$ was to become negative at scales much below the Planck scale, $M_P \sim 10^{18} - 10^{19}$ GeV (see Fig. 2.6a), the Higgs field could tunnel from the current false vacuum state to the true, absolutely stable vacuum ground state. Current measurements seem to support the fact that the SM is in a metastable state, as shown in Fig. 2.6b. For the existentially anxious reader, a state-of-the art calculation of the EW vacuum decay rate can be found in Ref. [35].

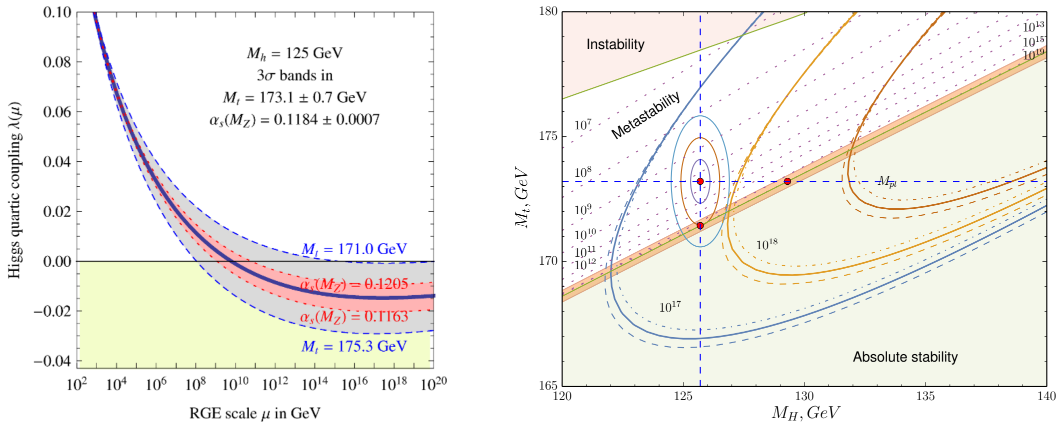

(a) Running of $\lambda(\mu)$ **(b)** Stability of the EW vacuum

Figure 2.6: (a) The evolution of the Higgs quartic coupling λ can lead to negative values at high energy scales (below the Planck scale M_P). This in turn makes the EW vacuum potentially unstable. The running is highly dependent on the top-quark mass and $\alpha_s(M_Z)$ values [36]. (b) The SM point, in red, is plotted in the (m_h, m_t) phase-space with 1-,2- and 3σ uncertainties. The pink dotted lines indicate contours where $\lambda(\mu) = 0$ for the indicated values of μ, and the parabolic curves where the beta-function $\beta_\lambda(\mu) = 0$ for chosen values of μ. The measured Higgs and top-quark masses point to a SM universe close to the metastable region [37].

2.4 Outstanding issues with the Standard Model

For all its successes, the SM is known to have some theoretical flaws. Below is a list of familiar shortcomings:

- **Massless neutrinos**: In the SM, neutrinos are naturally massless. Experiments [20] have shown that neutrinos can oscillate between the different families, and this requires a mixing of flavor states into mass eigenstates, similarly to the CKM mixing. Different mechanisms [38–40] were introduced to generate neutrino masses: a right-handed (so-called *sterile*) neutrino could exist, and would not interact with matter (since no right-handed neutrino was ever observed), or neutrinos could acquire a Majorana mass. Some R-parity violating supersymmetric (SUSY) models also produce neutrino masses [41, 42].

- **Gravity**: General relativity has yet to be quantized and incorporated into the SM under its current form, and a unified theory of all four interactions is still missing. As a first attempt, an exchange gravitational gauge boson can be introduced under the form of a spin-2 particle, called the graviton. The addition of corresponding terms to the SM Lagrangian spawns the apparition of UV divergences that cannot be handled by a finite number of counterterms [43–45], though, and the theory is not perturbatively renormalizable.

- **Dark matter**: The presence of dark matter in the Universe has been suggested from multiple cosmological observations [46–50]. Yet, the SM does not contain a good dark matter candidate particle. Some extensions of the SM, in particular SUSY, provide a heavy non-decaying particle (the lightest in the SUSY spectrum, called lightest supersymmetric particle) that turns out to be a good candidate.

- **Baryon asymmetry**: The SM predicts that matter and anti-matter should have been produced almost symmetrically at the Big Bang. Yet baryons are observed to be in overwhelming excess over anti-baryons in the visible part of the Universe [51, 52].

- **Hierarchy problem**: There is a manifest imbalance between the three unified forces of the SM and gravity, or between their respective mass scales. In particular, it is not clear why the Higgs boson mass is so small with respect to the Planck scale: basically, radiative corrections to the Higgs self-energy should blow up its mass, and the observed value of $m_h = 125$ GeV requires an incredible amount of fine-tuning to cancel radiative corrections. Again, SUSY models solve this problem by requiring every SM particle to have a supersymmetric partner which has the opposite spin-statistics: their contributions to the Higgs mass then cancel naturally [53].

Although all model extensions of the SM have respective advantages over the current theory, none of the particles predicted by them has been observed at the LHC or any other experiment yet.

3 Higher-order perturbative calculations in hadron-hadron collisions

The SM Lagrangian presented in the last chapter provides the Feynman rules to compute theoretical cross-sections. As will be explained in Section 3.1.3, the scattering amplitudes (at high-energies, for QCD) can be expanded to a perturbative series in the coupling constant: the interactions are represented by Feynman diagrams, and higher-order corrections generate loop diagrams that are most of the time divergent. Since the first successes of QFT in predicting basic energy spectrum properties and leading-order (LO) scattering amplitudes, there has always been a need for a more consistent framework in which higher-order corrections could be worked out. In this chapter, the important ingredients used in most theoretical computations nowadays are summarized, in particular in the context of high-energy hadron-hadron collisions. Most of the standard textbook content presented here is adapted from Refs. [54–58].

3.1 Divergences in Quantum-Field Theory

Going beyond Feynman tree diagrams in the computation of scattering matrix-elements, one encounters two classes of divergences. Consider a one-loop scalar massless two-point function, where the internal loop-momentum is integrated over:

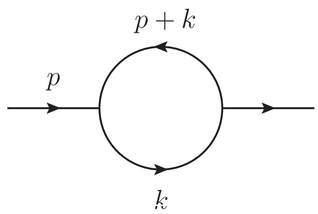

$$I_2(p^2;0,0) = \int_{-\infty}^{\infty} \frac{\mathrm{d}^4 k}{(2\pi)^4} \frac{1}{(k^2+i\delta)((p+k)^2+i\delta)} \ . \quad (3.1)$$

In the limit $|k| \to \infty$, the integral behaves as $I \propto \int \frac{\mathrm{d}|k|\,|k|^3}{|k|^2 \cdot |k|^2} = \int \frac{\mathrm{d}|k|}{|k|}$ which is logarithmically divergent. This is called an *ultraviolet* (UV) divergence. A divergence occuring when taking the small-momentum limit $|k| \to 0$ is called an *infrared* (IR) divergence.

As a solution to the infinities conundrum, the above integral has to be treated by the introduction of a UV regulator of some kind − this is a method called *regularization*. Then, the regularized infinities can be absorbed in a consistent way through the *renormalization* of the bare couplings and masses in the Lagrangian.

3.1.1 Regularization

A first attempt at controlling UV divergences consists in the introduction of a high-momentum regulator $|k|^2 < \Lambda^2$. Then, the loop integral given in Eq. (3.1) behaves as

$$I_2(p^2;0,0) \propto \int_\epsilon^\Lambda \frac{\mathrm{d}|k|}{|k|} \sim \log(\Lambda) \; , \tag{3.2}$$

and diverges logarithmically with the cutoff Λ. This is typical of renormalizable theories. Obviously, any physical observable should not depend on the value of the arbitrary cutoff, and in practice it does not.[1] As a theoretical downside, the introduction of the cutoff breaks gauge invariance. It also breaks translational invariance.

A possible gauge-invariant regularization method is the so-called Pauli-Villars regularization: a much more massive particle is introduced and its contribution subtracted from the ordinary propagator, that is:

$$\int \frac{\mathrm{d}^4k}{(2\pi)^4} \frac{1}{k^2+i\delta} \to \int \frac{\mathrm{d}^4k}{(2\pi)^4} \left(\frac{1}{k^2+i\delta} - \frac{1}{k^2-M^2+i\delta} \right) \; . \tag{3.3}$$

The Pauli-Villars technique cannot be applied to QCD because it is not gauge-covariant, though. On the same stance, it introduces an unphysical field that violates the spin-statistics theorem (it amounts to a spurious scalar field with Fermi statistics). One of the preferred regularization methods nowadays is dimensional regularization. It was worked out by 't Hooft and Veltman [60] to regularize any integral, is gauge-invariant and works for non-Abelian theories as well. The governing idea is that quantum-field theories in a smaller number of dimensions have a lower degree of divergence in the UV. The four dimensions of space-time are therefore analytically continued to $d = 4 - 2\epsilon$ dimensions, and the integral in Eq. (3.1) can be cast into the following form:

$$I_2(p^2;0,0) = \mu^{2\epsilon} \int \frac{\mathrm{d}^dk}{(2\pi)^d} \frac{1}{(k^2+i\delta)((p+k)^2+i\delta)} \; , \tag{3.4}$$

where the renormalization scale μ is a dimensionful parameter introduced to keep the integral dimensionless. Then the integral can be worked out by introducing Feynman parameters and Wick-rotating to give the analytical result

$$I_2(p^2;0,0) = \frac{1}{\epsilon} + \ln\frac{\mu^2}{-p^2-i\delta} + 2 + \mathcal{O}(\epsilon) \; . \tag{3.5}$$

The UV divergences now appear as (at most single, at one-loop level) poles in the dimensional regulator ϵ. A general dimensionally-regularized one-loop scalar integral with n external legs has the form:

[1] For a fun exercise of trying out different forms of cutoff (Gaussian, Dirac-delta,...), see Ref. [54] for the case of the vacuum polarization in the Casimir effect [59].

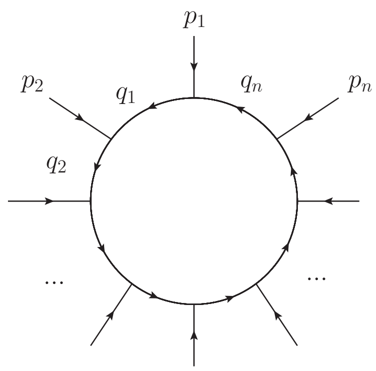

$$I = \mu^{n-d/2} \int \frac{\mathrm{d}^d k}{(2\pi)^d} \prod_{j=1}^{n} \frac{1}{(q_j^2 - m_j^2 + i\delta)} \,, \tag{3.6}$$

where the internal momenta $q_j = k + \sum_{i=1}^{j} p_i$ are expressed as a linear combination of the loop momentum k and the external momenta p_i. Feynman parameters can be introduced for the integral above, and generally it can be recast into the form

$$I = \Gamma(n - d/2) \prod_{i=1}^{n} \int_{0 \le x_i \le 1} \mathrm{d}x_i \delta \left(1 - \sum_{j=1}^{n} x_j\right) \frac{\mathcal{U}^{n-d}(\vec{x})}{\mathcal{F}^{n-d/2}(\vec{x}, p_i \cdot p_j, m_i^2)} \,. \tag{3.7}$$

The $x_1, \ldots, x_n$ are the Feynman parameters, and $\mathcal{U}$, $\mathcal{F}$ are the first, respectively second Symanzik polynomials.[2] Then, one needs only perform the integration over the Feynman parameters. For tensor integrals where the numerator of Eq. (3.6) contains Lorentz indices, there exist methods for their reduction to a set of scalar integrals, like the systematic Passarino-Veltman method [61] which uses a form factor expansion to factorize the indices. Most importantly, all one-loop integrals can be reduced to a linear combination of a set of *master integrals* that are at most box-diagrams, which are all known analytically and implemented in integral libraries. For the interested reader, Refs. [62–67] supply a comprehensive examination of various techniques for reducing and evaluating Feynman integrals.

Dimensional regularization has lots of benefits, and the algebra is quite straightforward. Its major disadvantage is that the Dirac algebra for fermions has to be analytically extended to $d = 4 - 2\epsilon$ space-time dimensions as well, which is not trivial. The Dirac matrices can be made to obey an analytically continued Clifford algebra

$$\{\gamma^\mu, \gamma^\nu\} = 2g^{\mu\nu} \,, \tag{3.8}$$

with a d-dimensional metric, $g^{\mu\nu} g_{\mu\nu} = d$, where it is unclear what happens to the Dirac matrix $\gamma_5 = i\gamma_0\gamma_1\gamma_2\gamma_3$. The different ways of treating γ_5 and the helicities of external and internal particle fields lead to different regularization schemes. Note that physical observables do not depend on the chosen scheme. In the dimensional reduction scheme (DRED) which is used for the predictions given in Chapters 6−11, the Dirac algebra is left to $d = 4$ dimensions, and the same holds for all external momenta and helicities. Only the internal momenta are analytically continued to d dimensions.

[2] Eq. (3.7) can also be generalized to a Feynman integral for l loops and n external momenta.

3.1.2 Renormalization

As a way to treat the infinities arising from the UV region of integration, the bare parameters of the Lagrangian are redefined to absorb the divergent contributions. Although this seems mathematically ill-defined, it is remarkable that the redefinition of a finite number of parameters allows for the treatment of divergences order-by-order and for all Feynman diagrams contributing to the amplitude of a renormalizable theory. In practice, renormalization of the Lagrangian is achieved by rewriting the bare masses and couplings m_0 and g_0 as a physical (measurable) parameter and a counterterm, as well as the fields themselves ψ_0, as

$$\begin{aligned} m_0 &= Z_m m = m + \delta m \;, \\ g_0 &= Z_g g = g + \delta g \;, \\ \psi_0 &= \sqrt{Z}\psi \;. \end{aligned} \tag{3.9}$$

The only requirement is that diagrams corresponding to the counterterms should cancel UV divergences stemming from the bare Lagrangian. In principle, the procedure does not define how to handle the finite terms accompanying these diagrams: depending on the additional criteria, several renormalization schemes can be chosen (on-shell, MS, $\overline{\mathrm{MS}}$, or others). Here as well, the physical observables should be independent of the choice of scheme (the top-quark mass is a fringe example and will be discussed summarily in Chapter 6).

The physical parameters entering the Lagrangian, e.g. the masses and couplings m, g, have to be determined by experiment. By definition, they are measured at a given energy scale. Colloquially, a renormalization starting point is chosen: the couplings/masses can then be evolved to a different scale in a well-defined way. Notably, the parameters of the renormalized field theory run according to the Callan-Symanzik [68–70] equation, which governs the dependence of the n-point correlation functions $G_0^{(n)}(x_1, ..., x_n; m_0, g_0)$ on the model's parameters:

$$\left(m\frac{\partial}{\partial m} + \beta(g)\frac{\partial}{\partial g} + n\gamma \right) G^{(n)}(x_1, ..., x_n; m, g) = 0 \;, \tag{3.10}$$

where the β-function of the theory is defined as $\beta(g) = \frac{m}{\delta m}\delta g$, and the anomalous dimension is given by $\gamma = \frac{m}{\delta m}\frac{\delta\sqrt{Z}}{\sqrt{Z}}$. Eq. (3.10) is an example of a broad class of evolution equations called renormalization group equations (RGE).

3.1.3 Perturbative expansion of Quantum Chromodynamics

From the running of the strong coupling constant given by the QCD β-function,

$$\mu_R^2 \frac{\partial \alpha_s}{\partial \mu_R^2} = \beta(\alpha_s) = -\left(b_0\alpha_s^2 + b_1\alpha_s^3 + \dots \right), \tag{3.11}$$

one sees that because of the negative sign in Eq. (3.11), the strong coupling $\alpha_s(\mu_R^2)$ becomes smaller at higher scales μ_R^2. This running is manifest in Fig. 3.1, which shows measurements of the strong coupling α_s at different energy scales Q, in agreement with the QCD theory prediction. Thus, with the measured value of the strong coupling at intermediate scales $\alpha_s(M_Z) \approx 0.118$, the interactions at high-energy hadron colliders can be treated perturbatively in α_s. For any partonic cross-section $\sigma_{ab\to X}$, where a, b, and X are freely propagating initial-, respectively final-states, one can expand the cross-section in a Taylor series,

$$\hat{\sigma}_{ab\to X} = \alpha_s^k(\mu_R^2)\left(\hat{\sigma}_{\mathrm{LO}}(p_i, p_f; \mu_R^2) + \alpha_s(\mu_R^2)\hat{\sigma}_{\mathrm{NLO}}(p_i, p_f; \mu_R^2) + \mathcal{O}(\alpha_s^2(\mu_R^2))\right) \ . \quad (3.12)$$

At each order in the strong coupling α_s, the cross-section can be computed and will depend on the choice of the renormalization scale. In general, it is chosen close to the expected momentum exchange Q^2. The systematic uncertainty related to the arbitrary choice of the scale is then usually estimated by varying the renormalization scale by factors of $\frac{1}{2}$ and 2.

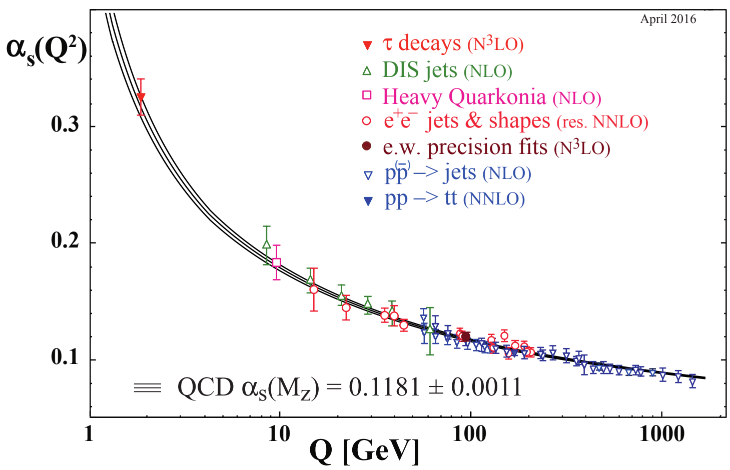

Figure 3.1: Various measurements of the strong coupling $\alpha_s(Q^2)$ at different energy scales Q show the running behavior typical of QCD, with a coupling strength that becomes smaller at higher energies, and a Landau pole at the hadronization scale $Q = \Lambda \sim$ 1 GeV. Figure taken from Ref. [1].

The accuracy of a computation is given by the truncation order of the perturbative series in Eq. (3.12). In certain regions of phase-space, though, large prefactors can be introduced at all orders, when two far-away scales Q and q are involved. This usually spawns the appearance of large logarithms of the form $\ln^n(Q^2/q^2)$, which have to be resummed to a given *logarithmic* accuracy across all orders. Some details will be given in Section 4.2.

3.2 Infrared divergences

Starting from an example, let us consider the case of QED higher-order corrections to $e^+e^- \to \mu^+\mu^-$ annihilation, where $m_e = m_\mu = 0$. Feynman diagrams contributing up to $\mathcal{O}(\alpha^3)$ at cross-section level are shown in Fig. 3.2.

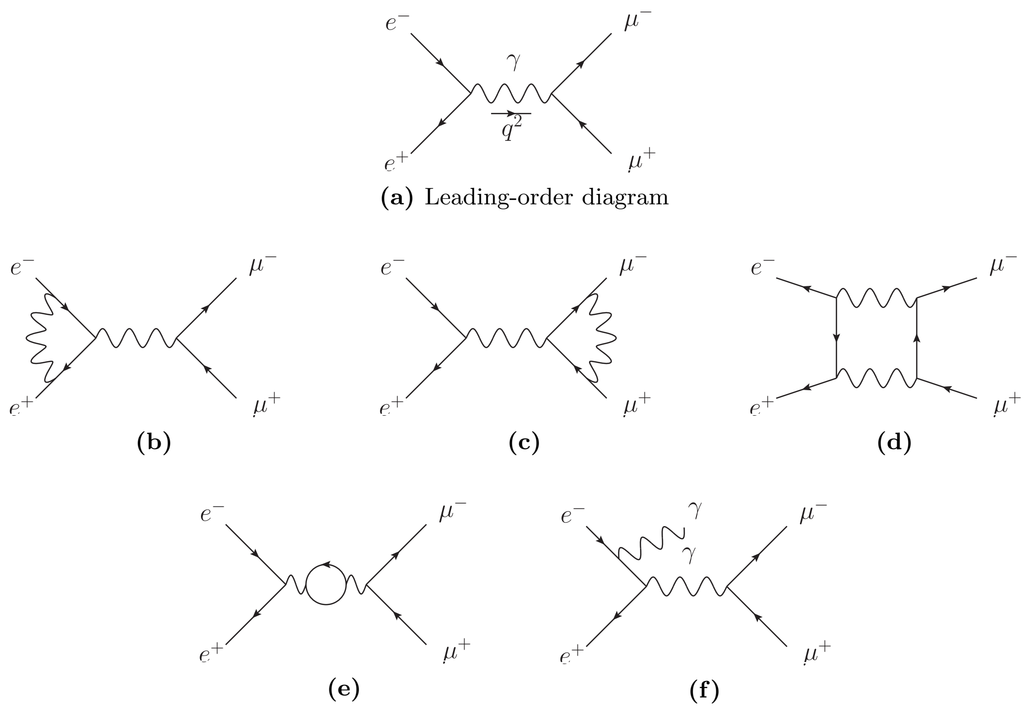

Figure 3.2: Feynman diagrams for $e^+e^- \to \mu^+\mu^-$. (a) The only leading-order diagram, with a photon in the s-channel, (b-e) virtual one-loop corrections and (f) a real-emission diagram.

At leading-order, the cross-section is given by

$$\sigma_{\text{LO}} = \int_\Phi \mathrm{d}\Phi |\mathcal{M}_0|^2 = \frac{4\pi\alpha^2}{3q^2} \,, \tag{3.13}$$

where the squared amplitude $|\mathcal{M}_0|^2$ has to be integrated over the phase-space Φ, and q^2 is the momentum carried by the exchanged photon. Let us assume the UV divergences have been handled by the introduction of appropriate counterterms.[3] Computing the amplitude, one realizes there is also an IR divergence coming from the massless photon propagator in the loops, and from the soft photon radiation.

First, the IR divergence needs regularizing. The simplest way to do that is to give the photon a small, non-zero mass, $m_\gamma > 0$, and to take the limit $m_\gamma \to 0$ at the end of

[3]The Ward identity [71, 72] in QED relates the renormalization terms together and ensures the cancellation of UV divergences at all orders.

the calculation. In this way, the nature of the IR pole is made explicit. Computing the virtual contribution, $\sigma_V \propto \left(\mathcal{M}_V^\dagger \mathcal{M}_0 + \text{ h.c.}\right)$, one arrives at the result

$$\sigma_V = \frac{2}{3}\pi^2 \frac{\alpha^3}{q^2}\left(\frac{\pi^2}{5} - \frac{7}{2} - \ln^2\left(\frac{m_\gamma^2}{q^2}\right) - 3\ln\left(\frac{m_\gamma^2}{q^2}\right)\right) . \tag{3.14}$$

The IR divergence is still present but it is explicit in $\ln(m_\gamma)$.[4] For the perturbative expansion to be consistent, real-emission diagrams contributing to $\mathcal{O}(\alpha^3)$ at cross-section level have to be included, that is diagrams of the sort pictured in Fig. 3.2f, where a photon is radiated either from the initial- or the final-state. Doing so, one gets a contribution of the form $\sigma_R \propto |\mathcal{M}_R|^2$:

$$\sigma_R = \frac{2}{3}\pi^2 \frac{\alpha^3}{q^2}\left(-\frac{\pi^2}{5} + 5 + \ln^2\left(\frac{m_\gamma^2}{q^2}\right) + 3\ln\left(\frac{m_\gamma^2}{q^2}\right)\right) . \tag{3.15}$$

Combining the different contributions to the cross-section, the IR divergences cancel between the virtual one-loop and the real-emission matrix-elements to give a finite correction to the leading-order cross-section:

$$\sigma_{\text{NLO}} = \sigma_{\text{LO}} + \sigma_V + \sigma_R = \sigma_{\text{LO}}\left(1 + \frac{3}{4\pi}\alpha\right) . \tag{3.16}$$

This behavior is symptomatic of IR divergences and falls under the purview of the Kinoshita–Lee–Nauenberg (KLN) theorem, which states that sufficiently inclusive observables are always IR-finite.

Although the cancellation of IR divergences is ensured by the KLN theorem, it is non-trivial to realize it numerically (for example in the context of a Monte-Carlo event generator). Section 4.1.2 will briefly develop this point.

3.3 The factorization theorem

The collision of composite states like the protons used at LHC implies interactions of highly non-perturbative objects. It is not clear at first how to handle these theoretically: color confinement does not allow for free quarks or gluons to be observed, thus the initial-state in hadron colliders cannot a priori be defined perturbatively. At high energy, though, the interaction with the highest momentum exchange takes place over time scales that are far smaller than the typical time scale at which the proton's constituents interact among themselves. The description of such a collision can therefore be *factorized* in long- and short-distance (or short- and long-time scale) physics: a hard collision of two freely propagating partons, and non-perturbative interactions within hadrons.

[4] The divergent terms are called Sudakov double logarithms and are systemic of collinear/soft emission (see Chapter 4).

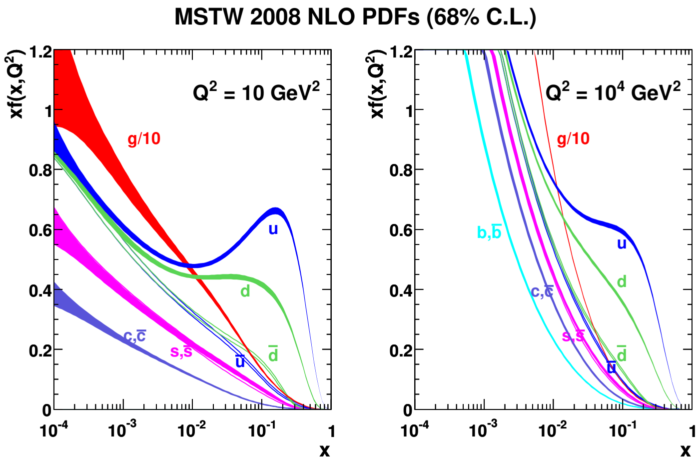

Figure 3.3: The MSTW 2008 NLO proton PDFs [73] as a function of the parent proton's momentum fraction x at resolution scales $Q^2 = 10$ GeV^2 (left), $Q^2 = 10^4$ GeV^2 (right).

Mathematically, the cross-section $\sigma_{pp\to X}$ for the production of a state X from the collision of two protons can be written in this approach as

$$\sigma_{pp\to X} = \sum_{ab} \int \mathrm{d}x_a f_{a/p}(x_a, \mu_F^2) \int \mathrm{d}x_b f_{b/p}(x_b, \mu_F^2) \cdot \hat{\sigma}_{ab\to X}(x_a p_1, x_b p_2; \mu_F^2) \ , \tag{3.17}$$

where a and b are possible constituents of the parent protons (sea or valence quarks and gluons), $f_{a/p}$, $f_{b/p}$ are encoding the non-perturbative origin of the partons in the parent protons, and $\hat{\sigma}_{ab\to X}$ is the cross-section for the production of the final-state X from the collision of the free partons a and b, which can now be computed perturbatively in QCD. Eq. (3.17) is called the *QCD factorization theorem*, and sets the basis for all cross-section predictions at LHC. The functions $f_{a/p}$, $f_{b/p}$, which are called *parton distribution functions* (PDF), depend on the momentum fraction x_a, x_b carried away by the parton from the parent proton, and on the resolution scale Q^2. Crudely said, the partonic content of the protons depends on the scale at which they are resolved.[5] The PDFs by definition cannot be computed perturbatively in QCD, but they can be measured from experimental data. As a matter of fact, a precise measurement of the proton's PDF is crucial, and constitutes one of the main sources of uncertainty in theoretical predictions at the LHC. Fig. 3.3 depicts the measurement of the proton PDFs by the MSTW collaboration from a global fit of hard-scattering data [73].

[5]The PDFs also obey an evolution equation similar to the RGE called DGLAP equation: this evolution runs from a central scale choice, namely the *factorization scale* μ_F.

4 Monte-Carlo (MC) event generators

To be able to compare a theory prediction for hadron colliders to an experimental measurement released by e.g. the ATLAS experiment, theorists and experimentalists meet on a common ground: the cross-section σ. The cross-section can be inclusive, and represents the total number of events for a given process after applying cuts and correcting for the detector acceptance, or it can be a differential cross-section $\mathrm{d}\sigma/\mathrm{d}\mathcal{O}$ with respect to some kinematic variable, where $\mathcal{O}$ is any event observable. On one side, the theorists need to compute a cross-section from a QFT starting point, namely from the Lagrangian. At the most basic level, this means implementing Fermi's golden rule:

$$\sigma = \frac{1}{4E_a E_b v} \int \prod_f \left(\frac{d^3 p_f}{(2\pi)^3} \frac{1}{2E_f} \right) |\mathcal{M}_{fi}|^2 \, (2\pi)^4 \delta^4(p_a + p_b - \sum_f p_f) \, , \tag{4.1}$$

where E_a and E_b are the energies of the incoming particles a and b, the constant $v = |\vec{v}_a - \vec{v}_b|$ is given by the relative 3-velocities of the particles in the beam and p_f, E_f are the 3-momenta and energies of all final-states. As a matter of fact, the infinitesimal volume element above is relativistically invariant. Ultimately, the relativistic matrix-element squared $|\mathcal{M}_{fi}|^2$ has to be integrated over the whole phase-space while enforcing 4-momentum conservation. On the other side, experimentalists have to count events and correct for detector acceptance and resolution:

$$\sigma = \frac{N_{\text{events}}}{\epsilon \cdot \mathcal{L}_{\text{int}}} \, , \tag{4.2}$$

Here, the cross-section is equal to the event count N_{events}, corrected for phase-space acceptance, detector resolution (represented here by an overall factor ϵ) and normalized by the integrated luminosity $\mathcal{L}_{\text{int}}$. For the case of differential distributions, the formula becomes more complicated, as binned events migrate depending on the detector resolution. The discussion of this case is postponed to Chapter 8.

There are two issues with the picture at hand. First, the matrix-element for a given process can typically be computed only up to $\mathcal{O}(\text{few})$ external legs. Because the multiplicity of final-state particles in a collider experiment like the LHC is of the order $\mathcal{O}(10^2 - 10^3)$, it is in practice impossible to calculate such amplitudes. Second, the perturbative expansion and the factorization presented in Chapter 3 break down when colored particles are produced with small energies. In particular, around energy scales where free final-state partons fall in the realm of non-perturbative interactions, they hadronize to form the observable colorless bound states demanded by color confinement. Therefore, the structure of the whole collision has to be broken down into pieces across the several scales involved, and the theoretical treatment of each piece is valid only in these subdomains and subjected to different levels of approximation. The theory community developed the necessary ingredients to improve the description of each stage and assembled them into mostly-automated programs called *Monte-Carlo (MC) event generators*.

MC event generators basically simulate the particle collisions as they would happen at the interaction points of an experiment like ATLAS or CMS. The MC program has to match multi-scale physics to simulate a collision, taking into account non-perturbative (PDF and quark fragmentation, hadron decay, underlying event, proton beam remnants) as well as perturbative (matrix-element and parton-shower matching) phenomena, as shown in Fig. 4.1.

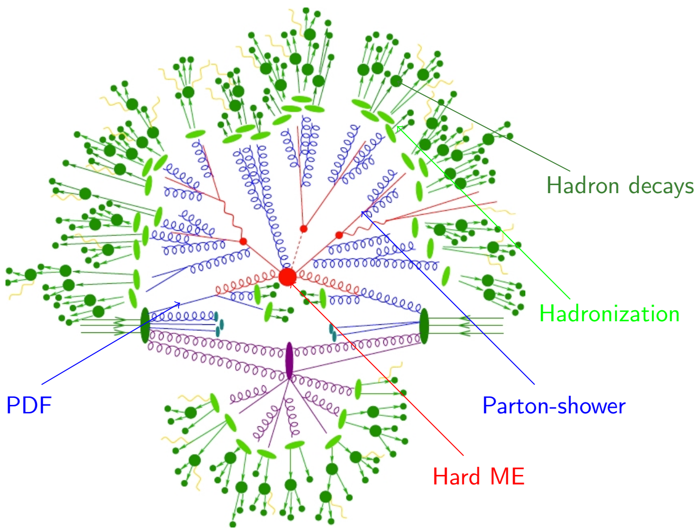

Figure 4.1: A typical MC event. Figure adapted from Ref. [74].

Under the hood of any Monte-Carlo program, the ingredients are essentially the same:

- **Monte-Carlo integrator**: The phase-space is sampled, usually with the help of an adaptive Monte-Carlo integration algorithm, to numerically perform the integral given in Eq. (4.1). As a notable example, the `Cuba` library [75] implements four multi-dimensional integration algorithms: `Vegas` [76], `Divonne` [77], `Suave` [75, 78] and `Cuhre` [79] (although `Cuhre` is deterministic and not properly a MC integrator).
- **PDFs**: There is an extensive amount of PDF measurements varying in the used datasets, theoretical precision, combination strategy, handling of α_s, or flavor thresholds. The `LHAPDF6` package [80] interpolates PDF values from discrete measurement points in the (x, Q^2) phase-space and can be interfaced to the MC generator.

- **Hard matrix-element (ME)**: The core of the calculation is the computation of the matrix-element $\mathcal{M}_{fi}$. It determines the theoretical accuracy of the prediction to a given order in the corresponding couplings. More details are given in Section 4.1.

- **Parton-shower**: As stated above, the high-multiplicity final-state is evolved from the few-parton hard matrix-element through subsequent radiative emission by a parton-shower algorithm. These routines are based on first-principles QCD (and QED), but contain inherent approximations and parametric degrees of freedom that generate an uncertainty associated with the choice of algorithm. Section 4.2 will expand on the topic.

- **Hadronization and hadron decay**: Once the shower evolution is brought down to energies of the order of the hadronization scale (of order $\mathcal{O}(1\ \text{GeV})$), the free partons bind to form colorless states. This is handled by a model on the only assumption that it should describe data to the best possible extent. Commonly, these models have a certain number of free parameters that are *tuned* to data. In Section 4.3, the Lund string and the cluster model are briefly detailed.

- **Multiple partonic interaction and underlying event**: Especially at small momentum fractions, it is possible that more than one parton from the same parent proton contributes to the interaction. The description of this phenomenon is also mostly based on MC modeling and has to be tuned to experimental data.

4.1 Matrix-element providers

The first programs for generating the matrix-element $\mathcal{M}_{fi}$ needed in Eq. (4.1) were highly specialized. They would handle one specific process and would be mostly analytically hard-coded. At some point, authors from the theory community started to make their code available and the corresponding libraries would be assembled into multi-process packages. This is the example of the `MCFM` [81], `VBFNLO` [82–84] and `BlackHat` [85] packages. Nowadays, after a paradigm shift, the computation of the hard process matrix-element is decidedly automated at one-loop level: general programs like MadLoop [86–89], OpenLoops [90, 91], GoSam [92, 93], Recola [94, 95] and `HELAC-NLO` [96] can be interfaced directly to most MC generators and provide the amplitude given any phase-space point. Other programs focus on specific processes, as for example NJet [97], which calculates multijet amplitudes at NLO in massless QCD, `VBFNLO` for vector-boson fusion in a number of processes, or HJets++ [98] for Higgs boson production in association with one or more jets in the high-energy limit. The program GoSam-2.0 is used in all subsequent NLO computations, thus its mode of operation is detailed in the next section.

4.1.1 GoSam: MC interfacing of one-loop amplitudes

GoSam is a general-purpose package that computes one-loop amplitudes automatically and interfaces to any MC generator, provided it supports the Binoth-Les Houches Accord (BLHA1 [99] or BLHA2 [100]) format. The workflow of GoSam is shown in Fig. 4.2.

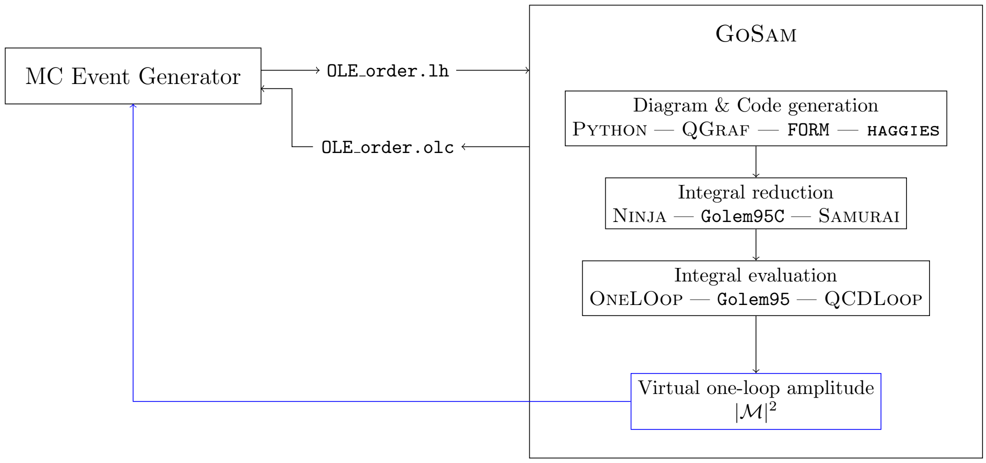

Figure 4.2: GoSam relies on external packages to compute virtual one-loop amplitudes. Feynman diagrams are generated by QGraf, and `fortran` code containing the terms relevant to each diagram is automatically written out by `FORM`. The various integral families are then reduced and the basis integrals evaluated using external libraries.

Any process can be defined in the GoSam input card, where only incoming and outgoing particles as well as the desired order in α, α_s have to be given for the generation of the Feynman diagrams. The Python executable `gosam.py` is then called and a series of external packages handle the different steps of the computation: QGraf [101] generates the Feynman diagrams, and filters for vertices or propagators can be applied, as well as manual removal of diagrams. Then, `FORM` [102] code containing the relevant expressions is generated automatically for all diagrams and helicities. Integral reduction is operated by any of three programs, namely Ninja [103], `Golem95C` [104, 105] or Samurai [106]. Finally, the evaluation of the set of basis integrals is performed using one of the three external integral libraries QCDLoop [107], OneLOop [108] or `Golem95C`.

On a higher level, in compliance with the BLHA format, the MC generator produces an order file `OLE_order.lh` containing the subprocesses to be computed by GoSam. The latter is called and generates routines for all subprocesses. After checking the order file, GoSam validates the order and returns a contract file `OLE_order.olc`. The generated libraries for all helicities are linked, and common functions are written in a `matrix.f90` file to be called by the MC generator. The physics parameters, like particle masses and couplings, can be set by an external call to the `OLP_Option` function. Then, for a set of 4-momenta $(p_i)_{i=1,\dots,n}$, the matrix-element is provided by calling the `OLP_EvalSubProcess`($\{p_i\}$) function, which returns the full one-loop amplitude coefficients $c_{(-2)}$, $c_{(-1)}$ and c_0 (double, single pole and finite terms) as given in the Laurent series:

$$\mathrm{Re}\{\mathcal{M}_V^\dagger \mathcal{M}_0\} = g_1^{n_1} \dots g_q^{n_q} \frac{\alpha_s}{2\pi} \frac{(4\pi)^\epsilon}{\Gamma(1-\epsilon)} \left(\frac{c_{(-2)}}{\epsilon^2} + \frac{c_{(-1)}}{\epsilon} + c_0 + \mathcal{O}(\epsilon) \right) , \tag{4.3}$$

where $g_i^{n_i}$ are the coupling constants appearing in the tree-level matrix-element. GoSam is a very flexible package, and allows high-level control over the various subtleties of higher-order computations (e.g. choice of regularization scheme, renormalization counterterms, and so on). A rescue system for phase-space points that are numerically badly behaved can be activated, and the amplitude for these is recomputed either in quadruple precision or with a different method.

4.1.2 Infrared divergence cancellation

Having acquired the virtual contribution to the amplitude, one has to combine the Born, virtual and real-emission contributions together. As was shown in Section 3.2, the singularities appearing in both virtual loop calculations and in soft/collinear configurations of real emissions should combine to give finite quantities for any IR-safe observable.[1] Although this is analytically true, in the case of MC computations, the different contributions are first sampled over different phase-spaces, and only then combined. Symbolically, for the NLO cross-section σ^{NLO}:

$$\sigma^{\mathrm{NLO}} = \int_{\Phi_m} \mathrm{d}\sigma^{\mathrm{B}} + \int_{\Phi_m} \mathrm{d}\sigma^{\mathrm{V}} + \int_{\Phi_{m+1}} \mathrm{d}\sigma^{\mathrm{R}}, \tag{4.4}$$

where $\mathrm{d}\sigma^{\mathrm{B}}$, $\mathrm{d}\sigma^{\mathrm{V}}$ and $\mathrm{d}\sigma^{\mathrm{R}}$ are the Born, virtual and real contributions. Note that the singularities in virtual and real contributions only cancel after integration. Numerically, the cancellation of IR divergences is thus non-trivial. At NLO, there are two kinds of algorithms to implement IR divergence cancellation: phase-space slicing and subtraction methods. The Catani-Seymour (CS) [109] and Frixione-Kunzst-Signer (FKS) [110, 111] automated subtraction algorithms of IR divergences are mostly used nowadays in NLO MC generators. The CS algorithm is outlined below and is used in all calculations present in Chapters 6−10, while the Powheg framework in Chapter 11 uses the FKS scheme.

Consider the addition of a subtraction term $\mathrm{d}\sigma^{\mathrm{S}}$ which approximates the ($d = 4 - 2\epsilon$ regularized) real contribution and reproduces its IR singularity pattern in d dimensions:

$$\mathrm{d}\sigma^{\mathrm{V}} + \mathrm{d}\sigma^{\mathrm{R}} = \mathrm{d}\sigma^{\mathrm{V}} + \mathrm{d}\sigma^{\mathrm{S}} + \left(\mathrm{d}\sigma^{\mathrm{R}} - \mathrm{d}\sigma^{\mathrm{S}}\right). \tag{4.5}$$

The ($d = 4$)-dimension limit can be taken directly for the integration of the real-emission and the local counterterm cancels the divergence in the phase-space integrand. The total NLO cross-section then takes the form:

$$\sigma^{\mathrm{NLO}} = \int_{\Phi_m} \mathrm{d}\sigma^{\mathrm{B}} + \int_{\Phi_m} \left(\mathrm{d}\sigma^{\mathrm{V}} + \int_{\Phi_1} \mathrm{d}\sigma^{\mathrm{S}} \right)_{\epsilon=0} + \int_{\Phi_{m+1}} \left(\mathrm{d}\sigma^{\mathrm{R}}\big|_{\epsilon=0} - \mathrm{d}\sigma^{\mathrm{S}}\big|_{\epsilon=0} \right), \tag{4.6}$$

[1] Generally, at NLO, regularized poles appear either as double poles (soft and collinear), or single poles (soft, collinear, or UV).

where all integrals are now separately finite. The CS dipole formalism is a factorization framework that permits the automatic generation of the subtraction term $\mathrm{d}\sigma^{\mathrm{S}}$. Universal dipole factors are introduced for any process, and setting the subtraction term to

$$\mathrm{d}\sigma^{\mathrm{S}} = \sum_{\text{dipoles}} \mathrm{d}\sigma^{\mathrm{B}} \otimes \mathrm{d}V_{\text{dip}}, \tag{4.7}$$

$$\int_{\Phi_{m+1}} \mathrm{d}\sigma^{\mathrm{S}} = \sum_{\text{dipoles}} \int_{\Phi_m} \mathrm{d}\sigma^{\mathrm{B}} \otimes \int_{\Phi_1} \mathrm{d}V_{\text{dip}} =: \int_{\Phi_m} \mathrm{d}\sigma^{\mathrm{B}} \otimes \mathbf{I} \tag{4.8}$$

allows one to compute the cross-section σ^{NLO} of any process:

$$\int_{\Phi_m} \mathrm{d}\sigma^{\mathrm{B}} + \int_{\Phi_m} \left(\mathrm{d}\sigma^{\mathrm{V}} + \mathrm{d}\sigma^{\mathrm{B}} \otimes \mathbf{I}\right)_{\epsilon=0} + \int_{\Phi_{m+1}} \left(\mathrm{d}\sigma^{\mathrm{R}}\big|_{\epsilon=0} - \sum_{\text{dipoles}} \mathrm{d}\sigma^{\mathrm{B}} \otimes \mathrm{d}V_{\text{dip}}\big|_{\epsilon=0} \right) \tag{4.9}$$

with $\mathbf{I}$ the integrated CS insertion operator. The universal dipole factors are obtained by considering the soft/collinear limits of a one-emission matrix-element with respect to the Born configuration:

$$|\mathcal{M}_{m+1}|^2 = \sum_{k \neq i,j} \mathcal{D}_{ij,k}(p_1, \ldots, p_{m+1}) + (\text{regular in } p_i \cdot p_j \to 0) \tag{4.10}$$

$$\begin{aligned} &= - \sum_{k \neq i,j} \frac{1}{2 p_i \cdot p_j} \mathcal{M}_m^{\dagger}(i, j \to \widetilde{ij}, \tilde{k}) \left(\frac{\mathbf{T}_k \cdot \mathbf{T}_{ij}}{\mathbf{T}_{ij}^2} \mathbf{V}_{ij,k} \right) \mathcal{M}_m(i, j \to \widetilde{ij}, \tilde{k}) \\ &\quad + (\text{regular in } p_i \cdot p_j \to 0) \end{aligned} \tag{4.11}$$

where the singular terms are collected in the dipoles $D_{ij,k}$. The $\mathbf{T}_i$ are the generators of the color algebra and $\mathcal{M}_m$ is a general matrix-element corresponding to an m-particle final-state, $\mathcal{M}_m = |1, \ldots, m\rangle$. Then, Eq. (4.11) states that the matrix-element corresponding to an $(m+1)$-particle final-state factorizes into dipole factors $\mathbf{V}_{ij,k}$ convoluted with an underlying Born configuration where partons i and j are assembled into one parton $(\widetilde{ij})$ (the so-called *emitter*), and parton $\tilde{k}$ (the *spectator*) absorbs the residual 4-momentum. The formulae for the universal dipoles $\mathbf{V}_{ij,k}$ are very closely related to the Altarelli-Parisi splitting functions, see Section 4.2.

In the case of the presence of initial-state hadrons like at the LHC, Eq. (4.11) is modified and an additional dipole term has to be added in Eq. (4.8), $\mathrm{d}V_{\text{dip}} \to \mathrm{d}V_{\text{dip}} + \mathrm{d}V'_{\text{dip}}$. Eq. (4.8) then becomes

$$\int_{\Phi_{m+1}} \mathrm{d}\sigma^{\mathrm{S}} = \int_{\Phi_m} \mathrm{d}\sigma^{\mathrm{B}} \otimes \mathbf{I} + \int_0^1 \mathrm{d}x \int_{\Phi_m} \mathrm{d}\sigma_B(xp) \otimes (\mathbf{P} + \mathbf{K})(x), \tag{4.12}$$

where xp is the proton momentum fraction carried away by the parton, and $\mathbf{P}$, $\mathbf{K}$ are insertion operators appearing from the convolution with the PDF.

4.2 Parton-shower models

4.2.1 The Altarelli-Parisi splitting functions

Parts of the following section are adapted from Ref. [112]. Inherently, the few-parton, high-energy final-state generated by the hard process matrix-element further produces QCD and QED radiation. The parton-shower algorithm evolves partons from the collision scale Q^2 via further radiation to a cutoff scale Q^2_{min} that is set around the hadronization scale. At that point, the shower terminates and the final-state is passed on to the hadronization model. Schematically, the simplest shower algorithms are based on the so-called Dokshitzer–Gribov–Lipatov–Altarelli–Parisi (DGLAP) kernels [113–115] for $1 \to 2$ collinear particle splitting $P_{a\to bc}$, as given in Fig. 4.3.

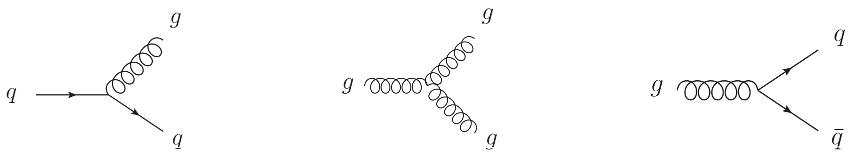

(a) $q \to qg$ **(b)** $g \to gg$ **(c)** $g \to q\bar{q}$

Figure 4.3: The QCD vertices for $1 \to 2$ splittings allow to calculate the leading-order kernels appearing in the DGLAP evolution equation.

The (unregularized) LO kernels can be computed from the QCD interaction vertices as:

$$P_{q\to qg}(z) = C_F \frac{1+z^2}{1-z} \;, \tag{4.13}$$

$$P_{g\to gg}(z) = 2C_A \left(\frac{1-z}{z} + z(1-z) + \frac{z}{1-z} \right) \;, \tag{4.14}$$

$$P_{g\to q\bar{q}}(z) = T_R(1-2z(1-z)) \;, \tag{4.15}$$

with $0 \leq z \leq 1$, the longitudinal momentum fraction of the parent parton a. Note the undefined behavior of $P_{q\to qg}$ and $P_{g\to gg}$ for $z \to 1$. The splitting functions can be regularized from general constraints to:

$$P_{q\to qg}(z) = C_F \left(\frac{1+z^2}{(1-z)_+} + \frac{3}{2}\delta(z-1) \right) \;, \tag{4.16}$$

$$P_{g\to gg}(z) = 2C_A \left(\frac{1-z}{z} + z(1-z) + \frac{z}{(1-z)_+} + \left(\frac{11}{12} - \frac{1}{3}\frac{T_R}{C_A} \right) \delta(z-1) \right) \;, \tag{4.17}$$

$$P_{g\to q\bar{q}}(z) = T_R(1-2z(1-z)) \;. \tag{4.18}$$

The factor $(1-z)^{-1}$ is regularized in being interpreted as a plus-distribution $(1-z)^{-1}_+$ such that for any test function $f(z)$ sufficiently regular at $z = 0$, $z = 1$,

$$\int_0^1 \frac{\mathrm{d}z\, f(z)}{(1-z)_+} = \int_0^1 \frac{f(z)-f(1)}{1-z} \,. \tag{4.19}$$

The master equation governing the evolution of the collinear splitting of a parton a from a scale q^2 to a scale $q^2 + \mathrm{d}q^2$ is then given by

$$\mathrm{d}P_{a\to bc} = \frac{\mathrm{d}q^2}{q^2}\frac{\alpha_s}{2\pi}P_{a\to bc}(z)\,\mathrm{d}z \ , \tag{4.20}$$

where q^2 is an arbitrary strong-ordered evolution variable. For example, one can choose the azimuthal angle of emission $E_a^2\theta^2$, or the particle's virtuality m^2, or an appropriate definition of the transverse momentum p_T^2. Different shower algorithms implement different choices of the evolution variable. This will be of importance when considering parton-shower related uncertainties, see Chapters 7 and 11.

4.2.2 The Sudakov form factor

Going from the one-emission to the multiple-emission case, and using broad assumptions[2], the probability of no-emission between scales Q^2 and $Q^2_{\max}$ is given by the *Sudakov form factor*:

$$\mathrm{d}P_{a\to bc}\,(z) = \frac{\mathrm{d}q^2}{q^2}\frac{\alpha_s}{2\pi}P_{a\to bc}(z)\,\mathrm{d}z \times \exp\left(-\sum_{b',c'}\int_{Q^2}^{Q^2_{\max}}\frac{\mathrm{d}q'^2}{q'^2}\int\frac{\alpha_s}{2\pi}P_{a\to b'c'}(z')\,\mathrm{d}z'\right) \,. \tag{4.21}$$

As explained in Section 3.1.3, the perturbative expansion of the cross-section in α_s can suffer from large enhancements in the soft/collinear regions of phase-space. In general, double logarithms of the form $\alpha_s^n \log^{2n}(Q^2/q^2)$ appear when a soft particle is emitted, or when it becomes collinear to one of the incoming partons. Here, q^2 is the scale describing the soft/collinear emission, and Q^2 is the global scale of the process. Generally, this tower of large logarithms can be analytically resummed to all orders in α_s. Instead, the parton-shower algorithm offers the possibility of resumming soft and collinear contributions within the Monte-Carlo framework. Nowadays, most parton-showers only guarantee leading-logarithmic (LL) accuracy, although recent studies [116] have found differences at LL (subleading number of colors N_C), and NLL (leading-N_C) between parton-showers and analytic resummations.

4.2.3 Parton-shower matching

The shower algorithm should respect the theoretical accuracy of the hard matrix-element, and at the same time conserve the logarithmic accuracy of the parton-shower resummation in their respective limits. In particular, the cross-section after showering should be

[2] Namely that the time between emissions can be sliced, and unitarity as well as multiplicativity (meaning the shower has no memory of past emissions) hold.

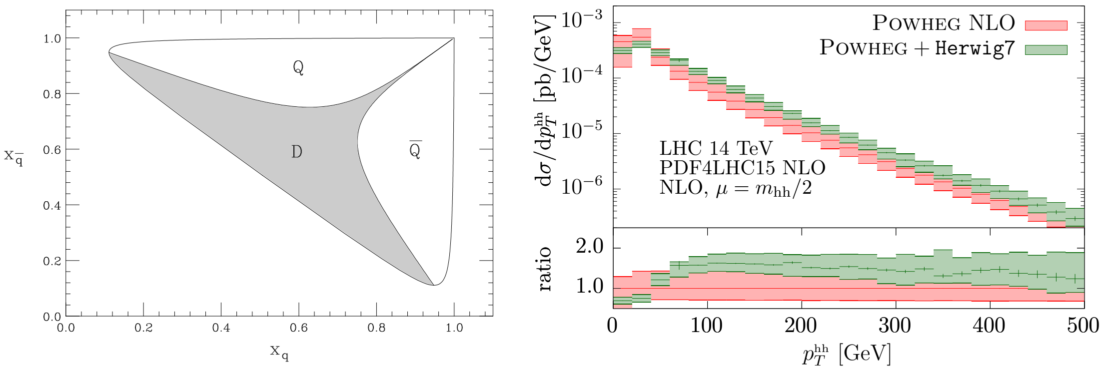

(a) $Q\bar{Q}g$ phase-space **(b)** hh NLO matching

Figure 4.4: (a) Phase-space for a heavy-quark pair emitting a gluon, depicted as a function of the Dalitz plot variables $(x_Q, x_{\bar{Q}})$. Figure adapted from Ref. [120]. (b) The transverse momentum p_T^{hh} of the Higgs pair system in di-Higgs production is compared for the fixed-order NLO prediction to a parton-shower matched calculation.

identical to the fixed-order cross-section. Kinematic configurations that belong simultaneously to the hard matrix-element and the parton-shower final-states should not be double-counted. These requirements form part of a procedure which is called *matching*.

At NLO, the matching of the parton-shower algorithm to the fixed-order matrix-element handles both these issues. Roughly said, it interpolates between the two kinematic regions where the hard matrix-element, respectively the parton-shower, generate their dominant contributions. As an example, the phase-space for the production of two heavy quarks and one gluon-emission $Q\bar{Q}g$ is given in Fig. 4.4a. The soft/collinear emission regions (where $x_Q \to 1$ or $x_{\bar{Q}} \to 1$, with $x_j = 2p\cdot q_j/p^2$, and p is the initial center-of-mass 4-momentum) can be covered by the parton-shower while the dead region (shaded) describes a hard gluon-emission. In a correct matching, these regions should not overlap. An illustration of this fact is shown in Fig. 4.4b for the case of $gg \to hh$ production, where a fixed-order NLO calculation is matched to the HERWIG7 [117] parton-shower. There, the parton-shower correctly reproduces the NLO computation at high-transverse momentum and softens the low-momentum region (Sudakov suppression). Among the various matching procedures that keep in line with the above criteria, the subtractive `MC@NLO` [118] and the multiplicative POWHEG [119] schemes are among the most used ones.

As examples of available parton-shower algorithms mostly used by the physics community, the PYTHIA8 [121, 122] and HERWIG7 codes implement a p_T-ordering, respectively an angular-ordering in the choice of the evolution variable. HERWIG also uses a dipole shower as an alternative algorithm (which is based on a Catani-Seymour dipole formulation of $2 \to 3$ splitting kernels). The `Sherpa` [123] generator implements two alternative parton-shower algorithms based on variations of the CS dipoles.

4.3 Hadronization

Once particles have been showered down to the hadronization scale, the hadronization model takes over. By far, the two most used hadronization models are the Lund string model and the cluster model.

4.3.1 The Lund hadronization string model

The Lund string model [124] is based on the principle of quark color confinement. When two quarks are separated by a distance r, the potential takes the form:

$$U(r) = -\frac{4}{3}\frac{\alpha_s}{r} + \kappa r \ , \tag{4.22}$$

and the linear confinement contribution dominates for larger distances, with $\kappa \sim 1$ GeV/fm. In analogy to a classical elastic potential, the field lines build up a stretched *string*. When the distance between a quark-pair increases, the string tension grows until the string breaks: the freed energy creates another quark-antiquark pair appearing from the vacuum. The creation of the quark-pair happens with a Gaussian probability (similarly to quantum tunneling) in the quark transverse mass $m_T^2 = m^2 + p_T^2$. From Lorentz invariance, causality and left-right symmetry, the fragmentation function $f(z)$ can be constrained and fixes the longitudinal momentum fraction z carried away by the created hadron:

$$\mathcal{P} \propto \exp\left(-\frac{\sigma m_T^2}{\kappa}\right), \qquad f(z) \propto \frac{(1-z)^a}{z}\exp\left(-\frac{b m_T^2}{z}\right) \ . \tag{4.23}$$

The Lund string model is implemented in the Pythia8 generator and the main parameters a, b, σ are determined by tuning to data. For the more complex case of baryons, the three quarks can be pictured in a quark-diquark frame. Finally, the gluons appear as kinks on strings. For more details and improvements to the model, see the Pythia manual [125].

4.3.2 The cluster hadronization model

Instead of building on color confinement, the cluster model [126, 127] makes the assumption that gluons can be viewed as carrying color and anti-color and behaving as a $q\bar{q}$ pair. Color singlets usually obey a mass spectrum that peaks at low mass due to the property of preconfinement of the parton-shower [128], i.e. they are closer to one another in phase-space. The model then clusters these color singlets together and splits them per the following procedure: if a cluster of mass M, with parton constituents of masses m_1, m_2, satisfies

$$M^{C_{\mathrm{pow}}} > C_{\max}^{C_{\mathrm{pow}}} + (m_1 + m_2)^{C_{\mathrm{pow}}}, \tag{4.24}$$

the algorithm splits it and the masses get redistributed. To split a cluster, the model pops a $q\bar{q}$ pair from the vacuum and forms two new clusters with one original parton each, and masses distributed according to

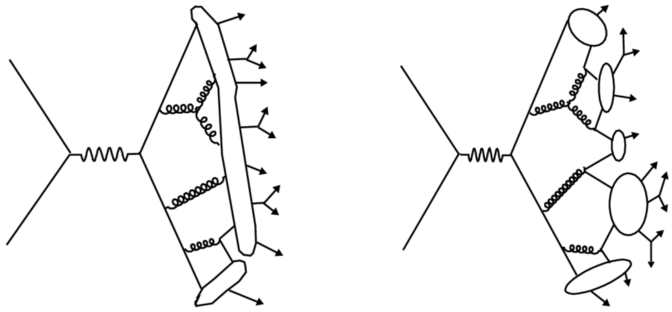

(a) Lund string model **(b)** Cluster model

Figure 4.5: A pictorial representation of both hadronization models. (a) In the Lund model, the potential energy from the color field between two quarks increases linearly with the distance, like in a string. When a string breaks, a new quark-antiquark pair is created. (b) The cluster model groups color-connected partons together into clusters and lets them decay isotropically.

$$M_{1,2} = m_{1,2} + (M - m_{1,2} - m_q)\mathcal{R}_{1,2}^{P_{\text{split}}} , \tag{4.25}$$

with $\mathcal{R}_{1,2} \in [0, 1]$ two random numbers. Again, the parameters C_{pow}, C_{max} and P_{split} have to be tuned to data.

Notice that the cluster model does not propagate any spin information: the hadronized clusters therefore decay isotropically. Historically, the cluster model was implemented in the Herwig event generator. Fig. 4.5 summarizes the conceptual differences between the Lund string and the cluster model.

As a concluding remark, the MC event generators represent the basis of a large fraction of experimental measurements. They are quite complex systems whose constituents are all intercorrelated: the different pieces interact and the matching between all appearing physical scales is not always explicit at the end of the simulation. Typically, the parton-shower output influences the hadronization tune, and it is in general difficult to disentangle their respective contributions. As such, variations in the MC setup are linked to large uncertainties which should, in principle, be taken into account with their full correlations.

5 The LHC and the ATLAS detector

The Large Hadron Collider (LHC) is currently the most powerful particle accelerator worldwide and is located at the Centre Européen pour la Recherche Nucléaire (CERN) on the French-Swiss border, near Geneva. Historically, it replaced the Large Electron-Positron (LEP) collider after it was decommissioned in 2000, and is being housed in the same tunnel. In this chapter, the main working parts of the accelerator complex are briefly reviewed, and the structure of the ATLAS detector is presented in more detail. A short overview of the trigger and data acquisition system, as well as the MC simulation in ATLAS, will close the subject.

5.1 The Large Hadron Collider

The LHC's main collider ring [129–131] is installed in a circular tunnel of ~ 27 km circumference and a depth varying between 45 m and 170 m under ground level. It is designed to accelerate protons up to an energy of 7 TeV, reaching a design center-of-mass energy of 14 TeV at a peak luminosity of 10^{34} cm^{-2} s^{-1}. As a side note, the LHC can also accelerate heavy ions, and in the past a few runs of lead-lead, proton-lead and xenon-xenon collisions have also given interesting complementary physics results.

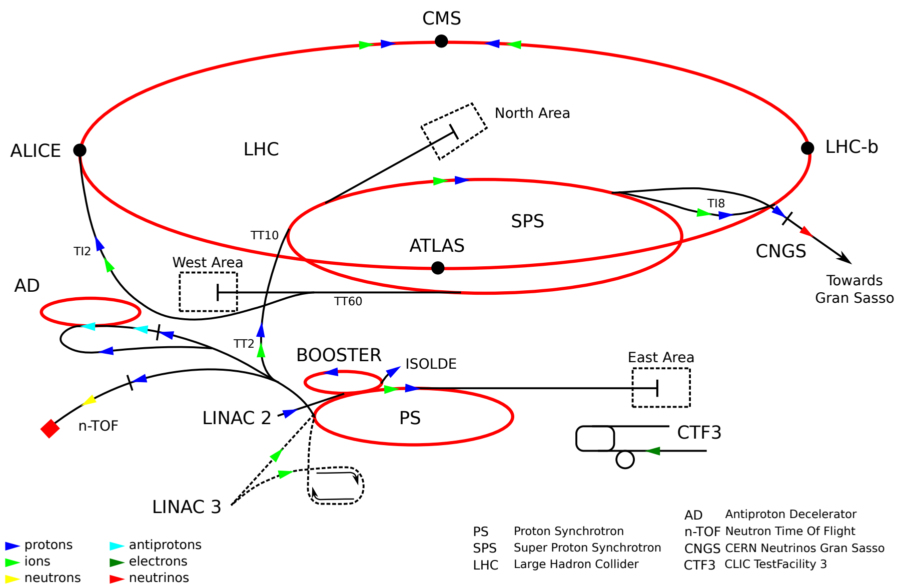

Figure 5.1: The LHC accelerator complex [132].

To accelerate protons to these high energies, a sequence of pre-accelerators boosts the proton beams before injecting them into the next link. A schematic of the full accelerator complex is presented in Fig. 5.1. Upon being produced and pre-collimated, the protons are accelerated to 50 MeV in the Linac2, then to 1.4 GeV in the Proton Synchrotron (PS) Booster, and to 26 GeV in the PS. Within the PS, the protons are collimated into 25 ns-spaced (7.5 m) bunches of around $1.15 \cdot 10^{11}$ protons per bunch. From there, the Super Proton Synchrotron (SPS) ramps up the energy to 450 GeV, and injects both beams in opposite directions into the LHC itself. After approximately 20 minutes of acceleration in the main LHC beampipe by 16 radiofrequency cavities, the proton bunches achieve the current energy of 6.5 TeV per beam.

Equipped with 1232 superconducting main dipole magnets, the LHC operates with magnetic fields of ~ 8.3 T to keep the proton bunches on their circular trajectory. The main dipole magnets are supplemented by higher-multipole magnets to correct for edge imperfections in the dipole field. Along the LHC beam path, 392 main quadrupole magnets are used to re-focus the proton beams.

Once at the nominal energy, the two circulating proton beams are brought to collision at four different interaction points, corresponding to the four largest LHC experiments: ATLAS, CMS, ALICE and LHCb. Out of these, ATLAS and CMS are general-purpose detectors designed to discover higher-mass particles like the Higgs boson or possible supersymmetric resonances, as well as to produce high-precision measurements of particles like the top quark. On the other hand, ALICE is dedicated to studies of heavy-ion collisions and focuses on high-density QCD bound states, while LHCb is optimized to investigate heavy-flavor physics. From the start of Run II in 2015 until the Long Shutdown of December 2018, the LHC delivered a total integrated luminosity of 147 fb^{-1} at a maximal center-of-mass energy of 13 TeV and a peak luminosity of $2.1 \cdot 10^{34}$ cm^{-2} s^{-1}, even surpassing the design value. The next section concentrates on the ATLAS detector substructure.

5.2 The ATLAS detector

A Toroidal LHC ApparatuS (ATLAS) [133] aims for high-energy precision measurements of the SM in all possible sectors: with the help of the enormous amount of data produced at LHC and the precision of the tracking detectors and calorimeters, it allows for measurements of particle masses, SM couplings or cross-section measurements, but also the observation of rare SM processes (like $t\bar{t}h$ production [134], light-by-light scattering [135] or $B_s^0 \to \mu^+\mu^-$ decays [136]). These high-precision tests of the SM are intrinsically linked to searches for Beyond the SM (BSM) physics: higher-scale BSM particles participating in loop corrections to the SM can have an impact on the cross-sections or kinematic observables, and any observed deviation from the SM predictions would hint at New Physics at higher scales. In general, though, direct searches are employed to look for potential high-mass resonances.

The ATLAS detector, situated at the LHC beam interaction point 1 near Meyrin, Switzerland, has an onion-shell structure comprised of particle trackers, electromagnetic and hadronic calorimeters, and a muon detector: from inner to outer radii, the produced particles encounter the Inner Detector (ID), the Liquid Argon (LAr) and the Tile Calorimeter (TileCal), and finally the Muon Spectrometer (MS). The detector itself is 44 m long and has a diameter of 25 m, and weighs more than 7000 tons. Fig. 5.2 shows a sketch of the ATLAS detector. To bend the charged-particle tracks for momentum measurement, ATLAS relies on four magnets: a 2 T central solenoid [137] close to the interaction point, an 8-coil barrel toroid [138] that is cylindrically placed around the detector generating a peak magnetic field of 4 T, and two other 8-coil toroid magnets at the detector endcaps [139] which provide a peak magnetic field of 4 T on the superconductor ($0.2 - 3.5$ T in the bore). The geometry of the magnet coils is shown in Fig. 5.3.

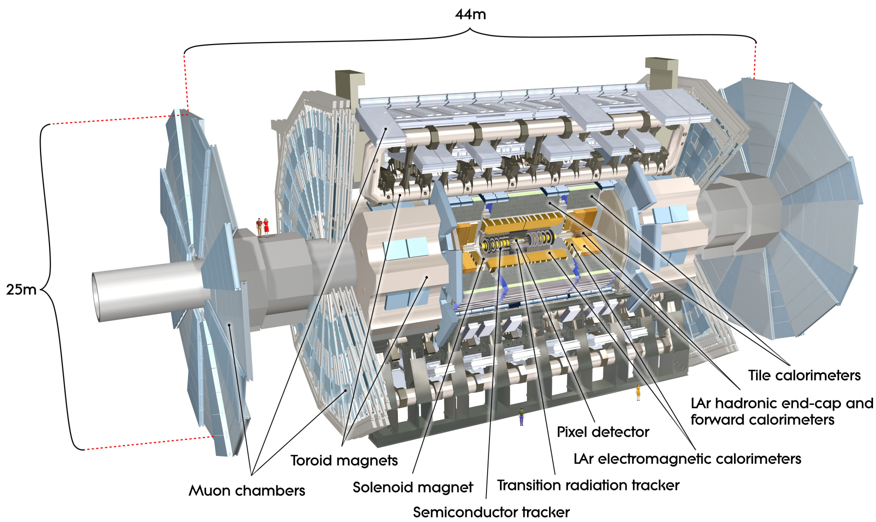

Figure 5.2: A cut-away view of the ATLAS detector. Figure from Ref. [133].

The ATLAS coordinate system is defined as right-handed and centered at the interaction point, with the beam axis chosen as the z-axis, the x-axis pointing towards the center of the LHC ring, and the y-axis pointing upwards.

5.2.1 The Inner Detector

Being the detector closest to the beampipe, the Inner Detector (ID) [140, 141] must fulfill several criteria for the reconstruction of charged-particles 4-momenta, as well as for the identification of secondary vertices due to the decay of bottom-flavored hadrons or τ leptons, and for the measurement of the impact parameter. The ID is further divided into a silicon Pixel Detector [142], a Semiconductor Tracker (SCT) [143] and a Transition Radiation Tracker (TRT) [144, 145]. In Fig. 5.4, the structure of the ID is presented in a cut view along the beampipe.

The Pixel Detector has a total of $8.6 \cdot 10^7$ channels and is the device closest to the interaction point. Four concentric layers of silicon pixel detectors are laid out around the beam axis in so-called barrel layers. The innermost layer is called the insertable B-layer

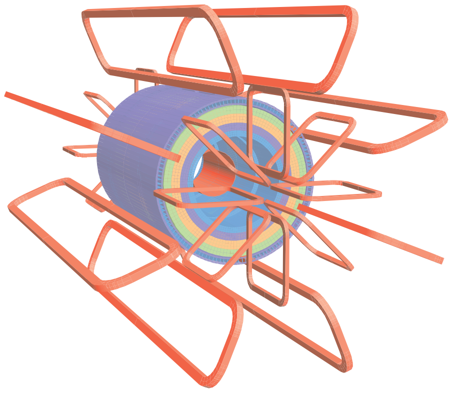

Figure 5.3: The geometry of the coils used to produce the magnetic field in the ATLAS detector. A solenoid magnet (2 T) is installed cylindrically around the beampipe, surrounded by a toroid magnet (4 T) and two endcap toroid magnets (4 T). Figure from Ref. [133].

(IBL) [146, 147] and was installed during the first Long Shutdown. It is only 3.3 cm away from the nominal interaction region and improves measurements of (secondary) vertex positions. It was designed to work in a high-radiation environment. Three other layers are disposed concentrically around the beampipe, and additionally three pixel disks are mounted on each endcap. The Pixel Detector reaches a resolution of $\sim 10\,\mu\text{m} \times 75\,\mu\text{m}$ [148, 149] in the transverse and longitudinal $(R \cdot \phi, z)$ directions.

At intermediate radius, the SCT is a silicon microstrip tracker and provides, using $6.2 \cdot 10^6$ readout channels, a measurement of the (R, ϕ, z) track points. Four SCT barrel layers are disposed at radii between 299 mm and 514 mm away from the beampipe, while 18 more planar discs are placed at the endcaps. The strips are placed back-to-back and rotated with a stereo angle of 40 mrad with respect to each other, so as to deliver tracking information also in the longitudinal direction. The barrel modules have a resolution of $17\,\mu\text{m} \times 570\,\mu\text{m}$ [143, 150].

Finally, at the outer layer, the TRT is made of thin-walled straw tubes and gives information for distinguishing electrons from pions, as well as contributes to the transverse position measurement for a total of $3.5 \cdot 10^5$ readout channels. A straw tube is a 4 mm-diameter cylinder filled with gaseous xenon and a gold-plated tungsten wire strung through the center. The inner tube wall serves as cathode and the wire as an anode. A high voltage of 1.5 kV is applied, and charged particles passing through ionize the gas. The freed electrons then drift to the wire, and the drift time can be used to determine the distance of the particle from the anode. Moreover, electron identification succeeds by transition-radiation photons created between the straws and converted in the xenon gas. The probability of transition radiation is proportional to the relativistic γ-factor, which is usually highest for electrons and positrons. The TRT determines the transverse position at a resolution of $\sim 110 - 130\,\mu\text{m}$ [151].

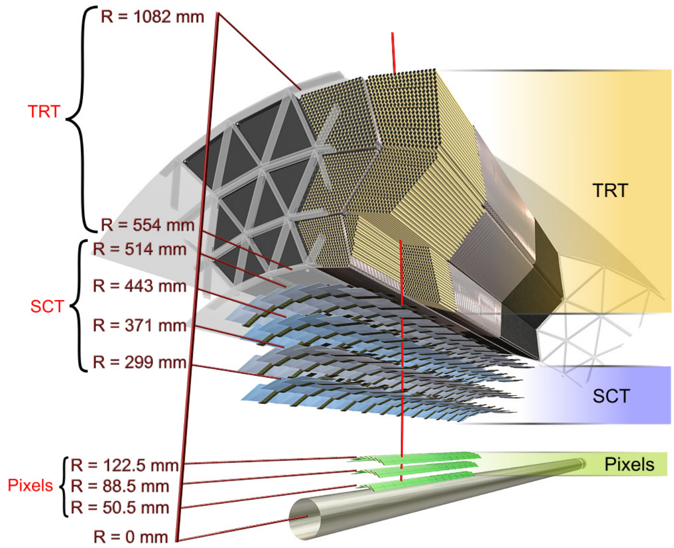

Figure 5.4: Cross-sectional view of the Inner Detector (ID). The ID particle tracker is made of the Pixel Detector, the microstrip Semiconductor Tracker (SCT), and the Transition Radiation Tracker (TRT). Figure from Ref. [133].

5.2.2 Calorimeters

The primary goal of calorimeters is to measure the energy deposited by the particles, but they also contribute to position measurements and particle identification as well as to the measurement of the missing transverse energy. ATLAS uses so-called sampling calorimeters with a *sandwich* structure. These detectors are made from alternating layers of high-density passive absorbers (Pb, Fe, Cu, . . .) and active material (scintillating plastic, liquid argon, Si, . . .) producing a detectable signal. The energy measurement is a destructive process: the incoming particle initiates secondary showers, and all produced particles deposit energy and radiate further until the total initial energy is absorbed. These energetic showers have different topologies depending on the type of incoming particle, namely whether they are leptonic (and photonic) or hadronic.

A passing electron/positron or a photon produces an electromagnetic (EM) shower in the absorber mainly through bremsstrahlung and electron-positron pair creation. EM showers are characterized by a rapid energy loss. A given detector material is described by the radiation length X_0, which is the distance after which the incoming particle has deposited $1/e$ of its total energy.

In comparison, charged and neutral hadrons generate further hadronic activity by inelastic nuclear reactions through spallation and excitation. The secondary neutral mesons also generate additional EM shower activity. Furthermore, hadronic showers are generally wider than EM ones, and hadronic calorimeters are correspondingly much bulkier. They are characterized by the nuclear absorption length λ_a, for which 95% of the total energy is absorbed in a cylinder of radius λ_a. In ATLAS, both the EM and the hadronic calorimeters are found between the ID and the Muon Spectrometer.

5.2.2.1 The Liquid Argon (LAr) Calorimeter

Fig. 5.5 depicts the Liquid Argon (LAr) calorimeters [152] in yellow, which are closest to the ID and enveloped by the Tile Calorimeter. The LAr calorimeters contain both EM and hadronic detectors. The LAr calorimeters function as a system of alternating lead/stainless steel absorbers and electrodes measuring the signal drift-time, with the whole system immersed in liquid argon which plays the role of active medium.

The electromagnetic barrel (EMB, $|\eta| < 1.475$) and endcap (EMEC, $1.375 < |\eta| < 3.2$) calorimeters use the same absorber material and geometry. In the forward region (FCal) at rapidities $3.1 < |\eta| < 4.9$, a copper-based absorber covers EM activity while a tungsten module provides measurement of hadronic energy deposition. A hadronic LAr calorimeter is also placed at the endcaps (HEC) and complements readings from the Tile Calorimeter. The EM calorimeters have an energy resolution of $\sigma_E/E = 10\%/\sqrt{E} + 0.7\%$, while the FCAL subdetector fares more poorly with a resolution of $\sigma_E/E = 100\%/\sqrt{E} + 10\%$. Finally, the hadronic HEC subdetector reaches an energy resolution of $\sigma_E/E = 50\%/\sqrt{E} + 3\%$ [153].

5.2.2.2 The Tile Calorimeter (TileCal)

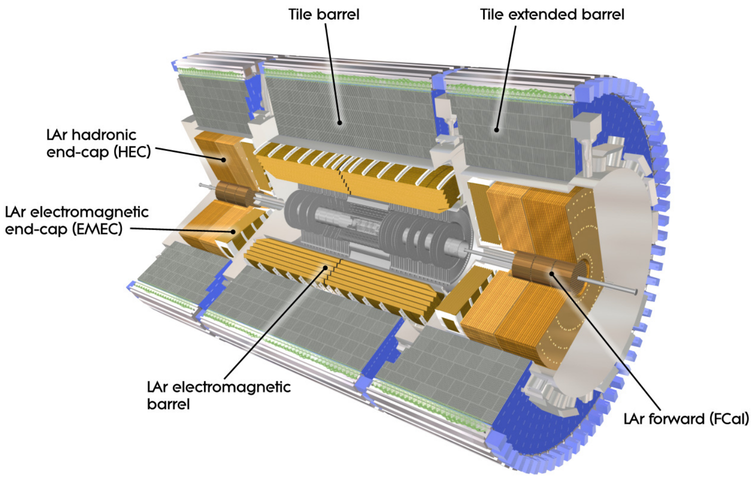

Figure 5.5: The ATLAS calorimetry system is composed of the inner Liquid Argon calorimeter (yellow) and the outer Tile Calorimeter (gray). Figure from Ref. [133].

The central and two extended barrel regions are covered by the TileCal [154], which is cylindrically disposed around the beampipe (see Fig. 5.5) and is made of iron plate absorbers and plastic scintillators as the active medium. The scintillating light created by hadronic energy deposition is wavelength-shifted and led to photomultiplier tubes that amplify the signal. The TileCal has a total energy resolution of $\sigma_E/E = 50\%/\sqrt{E} + 3\%$ for single pions [155].

5.2.3 The Muon Spectrometer (MS)

At the outermost layer of the ATLAS detector, the MS [156] is designed to deliver high-precision measurements of the muon transverse momenta. It uses four different techniques to trigger and detect the produced muons: resistive-plate chambers (RPC) [157], cathode strip chambers (CSC) [158], monitored drift tubes (MDT) [159] and thin-gap chambers (TGC) [160], shown in Fig. 5.6. The muon tracks are bent by three air-core toroid magnets for a rapidity-dependent bending power between $1 - 7.5$ Tm. This amounts to a resolution of $\sim 10\%$ in the transverse momentum of high-energy muons at around 1 TeV. Both the RPCs and the TGCs are used as a first-level trigger on well-resolved, high-p_T muons in the barrel region, respectively the endcaps. On the other hand, the MDTs which are located in the barrel and endcap regions, and the CSCs in the forward region, measure the position of the incoming muons in the bending plane.

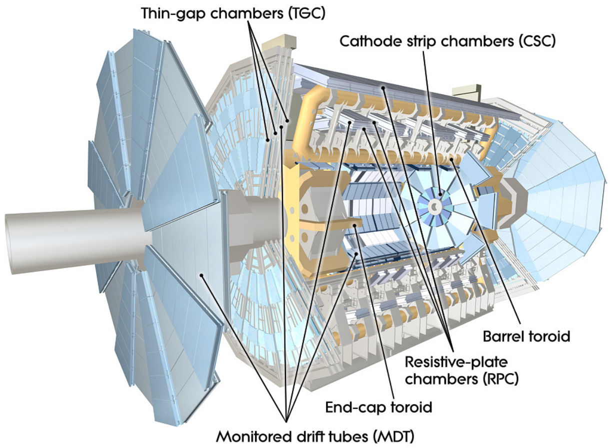

Figure 5.6: The ATLAS Muon Spectrometer. Figure from Ref. [133].

5.2.4 Trigger and data acquisition

The collision rate at high-energy collider experiments like ATLAS poses enormous computing and storage requirements. At the LHC, the proton-bunch crossing-rate at the current luminosity towers at a monumental 40 MHz. With a data content of ~ 1.6 MB per event, the storage of all events would produce ~ 60 TB per second. Thus, the event rate needs to be reduced to an affordable storage and readout rate. The ATLAS trigger and data acquisition system [161, 162] lowers the stored event rate using certain quality criteria from the detectors. The trigger system is organized in three sublevels:

- **Level 1**: The first trigger is implemented at the hardware level already, and uses both calorimetry information (cluster energy sum / isolation criteria) and data from the muon trigger chambers to reduce the event rate from 40 MHz to ~ 75 kHz. It also identifies regions-of-interest (ROI) characterized by specific signatures deemed physically relevant.

- **Level 2**: At the software level, the Level 2 Trigger uses the ROIs identified by Level 1 and combines information from all subdetectors to focus on the physics objects. The event rate is then reduced from 75 kHz to ~ 1 kHz.

- **Event Filter**: The full events are analyzed offline and the Level 2 selection is refined by the Event Filter (EF), which can also perform full event reconstruction at this stage. Accepted events are then stored permanently on disk at a rate of ~ 200 Hz for an acceptable total storage rate of around 300 MB per second.

Since Run II, the ATLAS software trigger comprises a single high-level trigger (HLT) farm, instead of the separate Level 2 and EF trigger levels, reducing the Level 1 total event rate from 100 kHz to $1 - 1.5$ kHz. The raw data are then stored first in the central CERN data center. The LHC Computing Grid is composed of several levels, or tiers. After the central CERN data center at Tier-0, the data are redistributed to 13 other computer storage and analysis sites forming the Tier-1, which store and process the raw data into refined formats and distributes them along to Tier-2 computer sites (university/institute clusters). Tier-3 sites are composed of local computers for analysis purposes. Mostly, analysers use pre-processed data that simplify the description of physics objects.

5.2.4.1 Data formats

From the raw data saved on-site to the final format available to analysers, several levels of data processing and reconstruction are implemented to derive a meaningful identification of physics objects that can be used in an analysis. Below, the successive file formats and their content are presented:

- **RAW**: The raw data from the trigger output are stored as primary information from the subdetectors: these complete events contain partially redundant information and metadata for the final analyses.

- **ESD**: The detector output present in the RAW events is fed to the reconstruction algorithm, and all the information needed for particle identification, track fitting, jet calibration is summarized in so-called Event Summary Data (ESD) files.

- **xAOD**: More information is pruned away, and only the physics objects (electrons, muons, jets, MET, ...) are summarized in containers and saved as ROOT [163] files called Analysis Object Data (xAOD).

- **DxAOD**: The xAOD files are further reduced to analysis-dependent (Top, Higgs, SUSY ...) event subsets, the derived AODs (DxAOD). The goal is to reduce file size and analysis computing times. Derived AODs are produced by either removing uninteresting events (so-called *skimming*), eliminating entire variables or object collections from all events (*slimming*), or removing particular objects in some events (*thinning*). Analyses handle directly the derived xAOD files as input.

5.2.4.2 MC simulation in ATLAS

Common MC event generation was explained in Chapter 4. In the following, a *parton level* event is defined as the set of particles (with their well-defined 4-momenta) produced by the hard-scattering matrix-element or by the parton-shower algorithm applied to the hard collision, but before hadronization. Both cases will be explicitly discerned when necessary. Such parton-level events are unphysical since they do not obey color confinement. The output of a full-fledged MC program after hadronization is a collection of events at *particle level*: this is usually the point of comparison between theory and experiment. Finally, accounting for the further evolution of particles in the magnetic field of a specific experiment, as well as for geometric acceptance and detection efficiencies, defines measurable events at *detector level*. Fig. 5.7 illustrates the event-level definitions. The full process of producing sets of events at detector level from the theory input will be referred to as MC simulation.

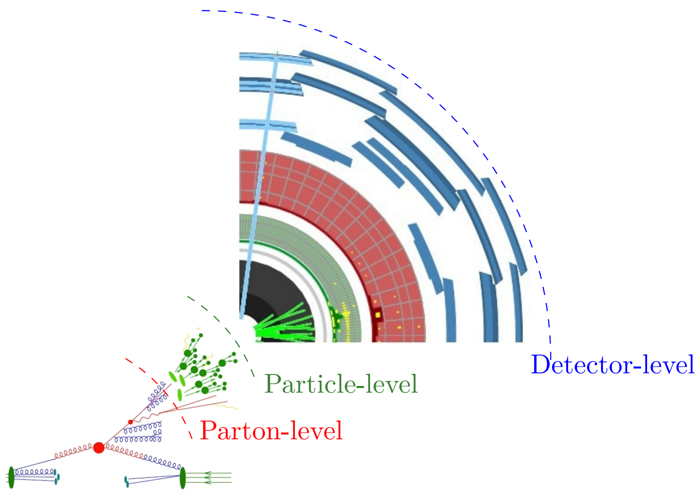

Figure 5.7: Definition of event levels: parton level after the hard collision (and including parton-showering), particle level after hadronization and detector level after the evolution in the ATLAS magnetic field, digitization and reconstruction.

In the ATLAS experiment, this production chain is implemented in the `Athena` framework, and comprises several steps outlined in Fig. 5.8. The event output at each stage is identified by a tag. For a given process, the first step consists of basic MC production using the programs available on the market (Sherpa [123], Herwig7 [117], Pythia8 [121, 122], and so on). The `AthGeneration` subpackage handles the interfacing of public MC programs in the ATLAS infrastructure, so as to ensure the use of common parameters, like particle masses and decay widths, and to facilitate reproducibility. From job option scripts at the user-level, the interface writes the standard input cards readable by the MC programs, and launches the event generation itself. The intermediate output at parton level (from the hard ME) is saved as Les Houches Event (LHE) files [164], and the generation of fully-showered and hadronized particle-level events (`EVNT`/`e`-tag) is referred to as `evgen`. Next, the simulation of events from particle to detector level happens in two phases: `simul` (`s`/`a`-tags) and `reco` (`r`-tag). The actual simulation (the evolution of the particles in the ATLAS magnetic field and the generation of the detector response) is handled by the GEANT4 [165] program: it contains the detector geometry and reproduces the particle hits in the subdetectors, accounting for detection efficiency. Because of the enormous computing time needed to produce hits from the hundreds of particles at play, an alternative is to parametrize the detector response without running a full event simulation (so-called ATLFAST [166] simulation). The output of the `simul` step is a `HITS` file. Then, as happens with the real data in the `reco` stage, signals simulated in the subdetectors are digitized, and the physics objects reconstructed to produce the xAOD format mentioned above. DxAODs derivations can be constructed for the latter and serve as input to the analyses, like the MC event sets which will be introduced in Chapter 9.

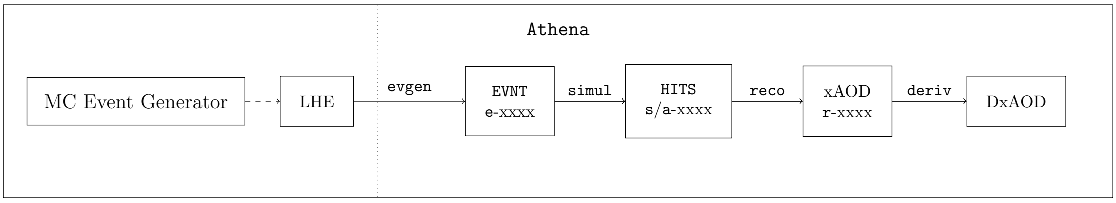

Figure 5.8: The `Athena` workflow for MC event generation and simulation.

Part II

Top-Quark Mass Determinations

6 Theoretical predictions for $t\bar{t}$ final-states

The top-quark pairs created in high-energy particle collisions, e.g. at the LHC, are not observable *per se*: the top quark has a short lifetime of $\sim 0.5 \cdot 10^{-24}$ s [1]. Thus, the only directly measurable quantities are the properties of its decay products. The top quark has a decay branching ratio of 99.8% for $t \to W^+b$, $\bar{t} \to W^-\bar{b}$. The $t\bar{t}$ final-state contains two b-jets that can be experimentally tagged, and depends only on the decay mode of the W bosons. In the case of top-quark pair production, both W bosons can decay either hadronically or leptonically, with branching ratios $\Gamma(W \to q\bar{q}') = 0.67$, $\Gamma(W \to \ell\nu_\ell) = 0.33$: the final-state is either dileptonic, monoleptonic (lepton+jets) or allhadronic, and the top-quark properties must then be reconstructed from the measured final-states. Fig. 6.1 depicts the topology of the three decay channels and Table 6.1 gives an overview of their respective cross-sections and major features.

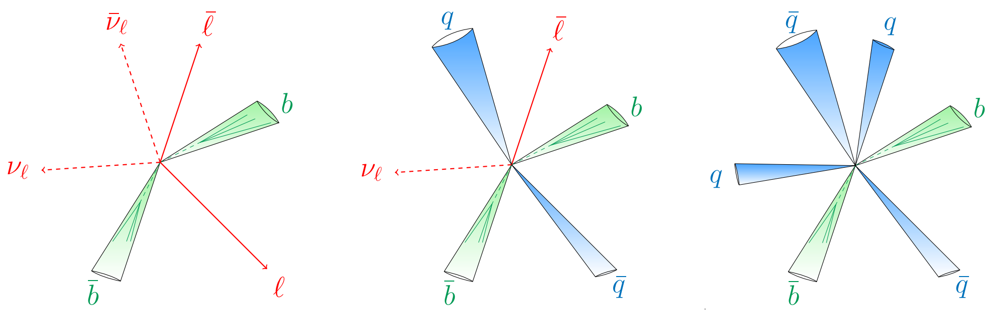

(a) Dilepton **(b)** Lepton+jets **(c)** Allhadronic

Figure 6.1: Topologies for $t\bar{t}$ events are characterized by either (a) dileptonic, (b) monoleptonic or (c) allhadronic decays.

A precise computation for the top-quark pair production cross-section and differential observables is paramount for the extraction of top-quark properties. Most theoretical systematic uncertainties are well under control and have been the subject of various studies [176–179]. In this chapter, the different theoretical descriptions of $t\bar{t}$ final-states are reviewed. The most important issues are summarized, and their potential impact on the extraction of top-quark properties from data are discussed. To do so in a realistic and quantitative way, an analysis close to the ATLAS 8 TeV top-quark mass extraction in the dilepton channel [180] is set up. The dilepton channel is a clean-signature decay mode, with the possibility of requiring two well-reconstructed, high-momentum leptons and a minimal threshold for missing transverse energy. It benefits from a small background (mainly fake leptons, diboson and Z+jets production), but suffers from the small branching fraction ($\Gamma \sim 0.048$ for e/μ in the final-state) and the impossibility to fully

Final-state X	dilepton (w. $\tau^+\tau^-$)	ℓ+jets (w. $\tau + j$)	allhadronic	all channels
$\Gamma(t\bar{t} \to X)$ [%]	10.89	44.02	44.89	100.0
σ_{NNLO} [pb]	27.42	110.82	113.02	$251.76^{+2.54\%}_{-3.44\%}$
Advantages	Clean signature	Full reconstruction	Largest BR	
Drawbacks	No full reconstruction	Jet-scale uncertainties	QCD background	
References	[167–169],[170, 171]	[168, 172],[5]	[173],[174]	

Table 6.1: The inclusive theoretical cross-sections at NNLO+NNLL QCD are computed for the $t\bar{t}$ decay channels with the `Top++` program [175] for a top-quark mass of $m_t = 172.5$ GeV and the MSTW2008nnlo68cl PDF set [73] in pp collisions at $\sqrt{s} = 13$ TeV. Advantages and drawbacks of (any) top-quark measurement in said channel are given. References for ATLAS measurements of the top-quark mass in particular are also laid out for each subchannel for the top-quark pole mass (in black), and for the MC mass (in blue) from template fits.

reconstruct the event, due to the two neutrinos escaping the detector. Cross-sections for all considered theoretical descriptions of $t\bar{t}$ final-states are given at the end of the chapter for the fiducial cuts employed in the analysis.

6.1 The narrow-width approximation (NWA)

Considering the intermediate state $W^+W^-b\bar{b}$, it makes sense at first to approximate it and examine only on-shell, doubly-resonant top-quark diagrams: the cross-section contribution stemming from non-resonant diagrams is expected to be of the order of $\mathcal{O}(\Gamma_t/m_t) \leq 1\%$, and usually neglecting other contributions is fine. This description is called the *narrow-width approximation* (NWA), and it builds on the limit $\Gamma_t \to 0$, where the top-quark propagator can then be written as

$$\lim_{\Gamma_t \to 0} \frac{1}{(p^2 - m_t^2) + m_t^2\Gamma_t^2} = \frac{\pi}{m_t\Gamma_t}\delta(p^2 - m_t^2) + \mathcal{O}\left(\frac{\Gamma_t}{m_t}\right) . \tag{6.1}$$

That is, top-quark production and decay entirely factorize, i.e.:

$$\begin{aligned} \mathcal{M}_{pp\to W^+W^-b\bar{b}} &= \mathcal{M}^{\text{NWA}}_{pp\to t\bar{t}\to W^+W^-b\bar{b}} + \mathcal{O}(\Gamma_t/m_t) \\ &= \mathcal{P}_{pp\to t\bar{t}} \otimes \mathcal{D}_{t\to W^+b} \otimes \mathcal{D}_{\bar{t}\to W^-\bar{b}} + \mathcal{O}(\Gamma_t/m_t) , \end{aligned} \tag{6.2}$$

where $\mathcal{P}$ denotes the $t\bar{t}$ production and $\mathcal{D}$ the top-quark decay dynamics, and the spin correlations are correctly taken into account as indicated by the symbol $\otimes$. The corresponding three LO Feynman diagrams, as well as a few examples of one-loop diagrams for $gg \to t\bar{t}$ production, are shown in Fig. 6.2. Nowadays, most of the theoretical predictions used for the extraction of top-quark properties in experimental analyses rely on NLO matrix-elements for top-quark pair production only. The top-quark decay and all subsequent radiation is left to the MC generator, with the approximations it entails:

particle decay predictions usually only have LO accuracy, spin correlations (in particular in the parton-shower) were only recently implemented, and resummation is as good as the shower algorithm's accuracy. Even so, there exists a number of more complete MC implementations for $t\bar{t}$ production in the NWA: the effects of NLO corrections to both production and decay were investigated in the POWHEG-BOX-V2 [17–19] framework called `ttb_NLO_dec` [181]. The HERWIG7.1 MC generator supports a new multijet merging algorithm adapted to $t\bar{t}$ production at NLO [182], and finally the SHERPA generator allows for the matching of the CS shower to production of $t\bar{t}$ associated with 1-, 2- and 3-jets at NLO [183, 184].

Furthermore, some dedicated calculations have appeared over the years. In particular, QCD NNLO corrections for $t\bar{t}$ production have been calculated for differential distributions [185–187], and combined with NLO EW corrections [188]. For a review of NLO EW effects, see Refs. [189–191]. Leaving corrections to top-quark pair production aside, it was later shown that higher-order corrections to the top-quark decay have a measurable impact on differential distributions in certain regions of phase-space. NLO radiative corrections to the top-quark decays were computed [192–194] and completed by NNLO QCD corrections [195, 196], NNLL resummation and other improvements above higher-order corrections in α_s [197–202]. Within the NWA, the calculation of QCD NNLO + NNLL' (soft-gluon and small-mass resummation) corrections for differential distributions was combined with NLO EW corrections and is the most complete fixed-order calculation up-to-date [203].

For the results shown in Section 6.5 in the NWA, the top-quark pair production is described at NLO QCD and factorizes from the top-quark decay. Furthermore, only the $e\mu$ dilepton channel is considered, that is $pp \to (e^+\nu_e)(\mu^-\bar{\nu}_\mu)b\bar{b}$ production, in the analysis presented in Chapter 7. The top-quark decay accuracy is handled in three different ways:

(1) The top-quark decay at LO is realized in the fixed-order SHERPA setup, as in Ref. [204] (referred to as $\mathbf{NLO^{LOdec}_{NWA}}$ from now on).

(2) The top-quark decay at NLO is computed in Ref. [193], and is shortly described below ($\mathbf{NLO^{NLOdec}_{NWA}}$).

(3) The top-quark decay is handled by the parton-shower, namely through the SHERPA `CSS` shower ($\mathbf{NLO_{PS}}$).

The $\mathrm{NLO}^{\mathrm{NLOdec}}_{\mathrm{NWA}}$ calculation in the NWA is based on the formula from Ref. [193], where top-quark pair production and decay factorize. Taking the perturbative expansion of Eq. (6.2) to NLO gives

$$\begin{aligned}\mathcal{M}^{\text{NWA, NLO}}_{ij\to t\bar{t}\to b\bar{b}2\ell 2\nu} = \quad & \mathcal{P}^{\text{LO}}_{ij\to t\bar{t}} \otimes \mathcal{D}^{\text{LO}}_{t\to b\ell^+\nu} \otimes \mathcal{D}^{\text{LO}}_{\bar{t}\to \bar{b}\ell^-\bar{\nu}} + \mathcal{P}^{\delta\text{NLO}}_{ij\to t\bar{t}} \otimes \mathcal{D}^{\text{LO}}_{t\to b\ell^+\nu} \otimes \mathcal{D}^{\text{LO}}_{\bar{t}\to \bar{b}\ell^-\bar{\nu}} \\ + \quad & \mathcal{P}^{\text{LO}}_{ij\to t\bar{t}} \otimes \left(\mathcal{D}^{\delta\text{NLO}}_{t\to b\ell^+\nu} \otimes \mathcal{D}^{\text{LO}}_{\bar{t}\to \bar{b}\ell^-\bar{\nu}} + \mathcal{D}^{\text{LO}}_{t\to b\ell^+\nu} \otimes \mathcal{D}^{\delta\text{NLO}}_{\bar{t}\to \bar{b}\ell^-\bar{\nu}}\right) \ , \end{aligned} \qquad (6.3)$$

where LO (δNLO) represent the LO (NLO) contributions to the $t\bar{t}$ production and top-quark decays, respectively. [1]

[1] The product $\mathcal{P}^{\delta\text{NLO}} \otimes \mathcal{D}^{\delta\text{NLO}}$ is formally of higher order.

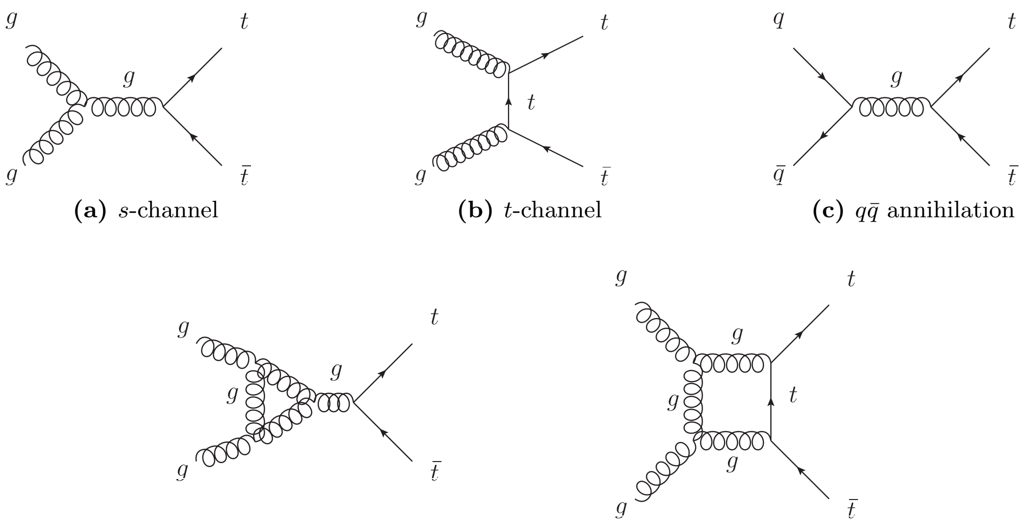

(a) s-channel **(b)** t-channel **(c)** $q\bar{q}$ annihilation

(d) **(e)**

Figure 6.2: (a-c) Leading-order diagrams for $t\bar{t}$ production and (d-e) two examples of NLO QCD one-loop diagrams for $gg \to t\bar{t}$.

As mentioned above, the NWA is expected to be precise enough for most calculations and yet, NLO and off-shell effects in the top-quark decay can have an important impact on sensitive regions of phase-space. In practice, experimental analyses do account for part of the non-doubly-resonant contributions: they usually include single-top quark production in the signal, since it contributes to the same final-state at NLO, or they subtract it consistently as background. Taking care of the interference between $t\bar{t}$ and single-top diagrams is generally accomplished with the help of a diagram subtraction (DS) or diagram removal (DR) scheme [205]. This procedure is not entirely free of quirks and violates gauge invariance. To get an entirely consistent theoretical prediction, it is therefore preferable to produce the full intermediate state $pp \to W^+W^-b\bar{b}$, which contains the complete set of Feynman diagrams at NLO.

6.2 $W^+W^-b\bar{b}$ production: review of existing calculations

The full calculation of $W^+W^-b\bar{b}$ at NLO in QCD contains all doubly-resonant top-quark diagrams, but also non-doubly resonant as well as non-factorizing contributions. Fig. 6.3 illustrates some of the additional Feynman diagrams.

At LO, the full $W^+W^-b\bar{b}$ final-state including the non-resonant diagrams has been computed in Refs. [204, 206–208]. In general, the calculation of NLO corrections poses some technical problems because of the existence of b-quarks in both initial- and final-state. In the 5-flavor scheme (5FNS), where b-quarks are treated as massless, collinear $g \to b\bar{b}$ splittings contribute to the final-state and the corresponding IR divergence has to be handled. Considering massive b-quarks (4FNS) has the advantage of allowing

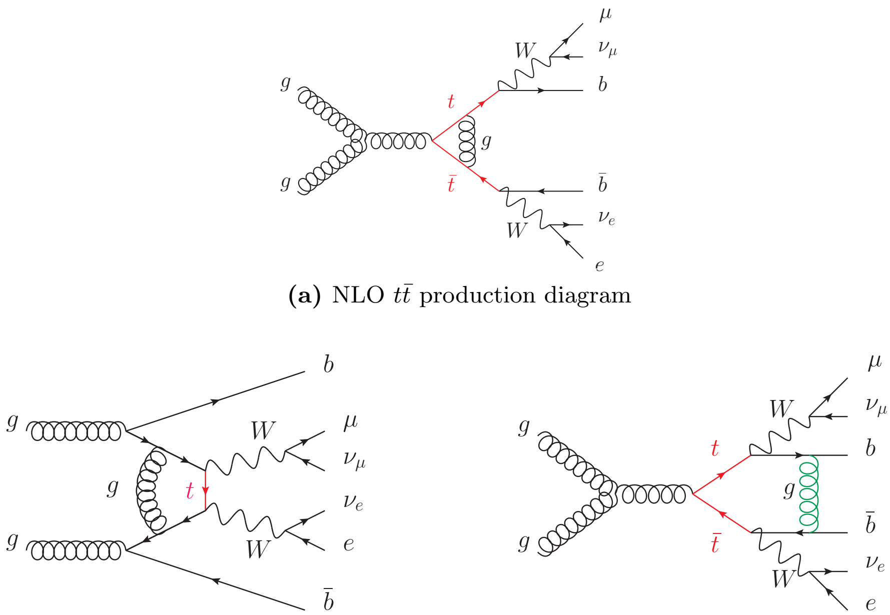

(a) NLO $t\bar{t}$ production diagram

(b) Non-doubly resonant diagram

(c) Non-factorizing diagram

Figure 6.3: One-loop diagrams for $pp \to W^+W^-b\bar{b}$ production contain (a) NLO corrections to standard NWA $t\bar{t}$ production, but also (b) diagrams with one or no top-quark propagators and (c) resonant diagrams with non-factorizing legs.

any phase space restrictions on the b-quarks without endangering infrared safety. It is therefore possible to consider exclusive 0-, 1- and 2-jet bins for $pp \to (e^+\nu_e)(\mu^-\bar{\nu}_\mu)b\bar{b}$ in the same setup. On the other hand, massive b-quarks are accompanied by an additional mass scale to the one-loop integrals and thus renders the integral evaluation less straightforward. In Refs. [209, 210], NLO calculations in the 4FNS have been performed.

Often, the $W^+W^-b\bar{b}$ prediction differs from the NWA in phase-space regions accessible only at NLO or sensitive to the top-quark decay kinematics. In Ref. [204], particular emphasis has been put on the impact of the non-factorizing contributions on the top-quark mass measurements in the dilepton channel. Recently the calculation of the NLO QCD corrections to $W^+W^-b\bar{b}$ production with full off-shell effects has also been achieved in the lepton+jets channel [211].

6.3 $W^+W^-b\bar{b}$ calculation setup at NLO QCD

Inclusive and differential cross-sections (along with results for top-quark mass determinations) were published in Ref. [212]. The calculation is analogous to the one described in Ref. [204]. The NLO QCD corrections to the $pp \to W^+W^-b\bar{b} \to (e^+\nu_e)(\mu^-\bar{\nu}_\mu)b\bar{b}$ process are computed, i.e. up to $\mathcal{O}(\alpha_s^2\alpha^2)$, in the 5FNS. This means that interference from (massless) b-quarks in the initial-state is taken into account. Top-quark finite width effects are fully included. The complex mass scheme is used to incorporate the width in a gauge-invariant way, where the top-quark mass is replaced by a complex number μ_t:

$$\mu_t^2 = m_t^2 - i m_t \Gamma_t \; . \tag{6.4}$$

The W and intermediate Z bosons also acquire a complex mass. Note that only resonant W-boson diagrams are taken into account: non-resonant contributions and finite-W-width effects were found to be small compared to top-quark effects [213]. The calculation is realized at parton level within the Sherpa v2.2.3 framework [123],[2] where tree-level and real amplitudes are computed by the Sherpa matrix-element generators Comix [215–217] and Amegic [218]. The one-loop amplitudes are compiled by GoSam and linked to Sherpa via the BLHA2 interface. Finally, the IR divergences are subtracted with the help of the Catani-Seymour dipole formalism as automated in Sherpa.

There are 334 diagrams contributing to the $q\bar{q} \to W^+W^-b\bar{b}$ virtual corrections, where q are the light quarks (u, d, s, c), and 1068 diagrams contributing to $gg \to W^+W^-b\bar{b}$. Additionally, because of the b-quarks present in the initial-state, 668 one-loop diagrams contribute to $b\bar{b} \to W^+W^-b\bar{b}$.

In the results presented in Chapters 7 and 8, the full $pp \to W^+W^-b\bar{b} \to (e^+\nu_e)(\mu^-\bar{\nu}_\mu)b\bar{b}$ QCD NLO prediction is compared with various $t\bar{t}$ predictions in the NWA. One of the goals of this study is to disentangle the effects from production and decay corrections, as well as from extra radiation in a parton-shower resummed approximation. The four theoretical descriptions considered in the next chapter are summarized again for completeness:

$\mathbf{NLO_{full}}$: full NLO corrections to $pp \to W^+W^-b\bar{b}$ with leptonic W-decays,

$\mathbf{NLO_{NWA}^{NLOdec}}$: NLO $t\bar{t}$ production $\otimes$ NLO decay,

$\mathbf{NLO_{NWA}^{LOdec}}$: NLO $t\bar{t}$ production $\otimes$ LO decay,

$\mathbf{NLO_{PS}}$: NLO $t\bar{t}$ production+shower $\otimes$ decay via parton-showering.

Note that the three first theoretical descriptions are not matched to a parton-shower. The PDF4LHC15_nlo_30_pdfas sets [219] are interfaced to Sherpa via `LHAPDF6` and events are produced at a center-of-mass energy of $\sqrt{s} = 13\,\text{TeV}$. The central top-quark mass was set to $m_t = 172.5\,\text{GeV}$ and the G_μ−electroweak scheme was used with the following numerical values:

$$G_\mu \;=\; 1.16637\cdot 10^{-5}\,\text{GeV}^{-2}, \qquad M_W \;=\; 80.385\,\text{GeV}, \qquad M_Z \;=\; 91.1876\,\text{GeV}, \tag{6.5}$$

$$\begin{aligned} \Gamma_t^{\text{LO}} &= 1.4806\,\text{GeV}, & \Gamma_t^{\text{NLO}} &= 1.3535\,\text{GeV}, \\ \Gamma_W^{\text{LO}} &= 2.0454\,\text{GeV}, & \Gamma_W^{\text{NLO}} &= 2.1155\,\text{GeV}, \\ \Gamma_Z &= 2.4952\,\text{GeV}, \end{aligned} \tag{6.6}$$

where the LO (NLO) widths were used for the LO (NLO) decays, respectively.

[2] A patched version [214] was used for the `CSS` shower, with the correct eikonal expressions for radiating off massive top quarks (relevant only for the NLO_{PS} description).

6.4 Event requirements

To study the differences between these predictions and their impact on the top-quark mass determination, an analysis similar to the ATLAS top-quark mass measurement at 8 TeV in the dilepton channel [180] is performed. In the following, the trigger cuts on leptons and jets are adapted to the ATLAS 13 TeV standards. For details of the analysis, the reader is referred to Chapter 7. The following event requirements are applied:

- The number of b-jets $n_{b,\mathrm{jets}} = 2$ with $p_T^{\mathrm{jet}} > 25\,\mathrm{GeV}$ and $|\eta^{\mathrm{jet}}| < 2.5$. Jets are clustered with the anti-k_T algorithm [220] as implemented in `FastJet` [221, 222] using a jet distance parameter of $R = 0.4$. In the analysis, a jet is considered a b-jet if it contains a B-hadron (or its decay products).

- Exactly two oppositely charged leptons are required with $p_T^{\mu} > 28$ GeV, $|\eta^{\mu}| < 2.5$ for muons and $p_T^{e} > 28$ GeV, $|\eta^{e}| < 2.47$. For electrons, the crack region $1.37 < |\eta^{e}| < 1.52$ between barrel and endcap EM calorimeters is excluded. For charged leptons a separation of $\Delta R(\ell, \mathrm{jet}) > 0.4$ to any jet is required: otherwise, the event is vetoed entirely.

- $p_T^{\ell b} > 120\,\mathrm{GeV}$. Using the same lepton-$b$-jet assignments as for $m_{\ell b}$, the value of $p_T^{\ell b}$ is defined as the average transverse momentum of both lepton-b-jet systems.

For the MC calculation, the central renormalization and factorization scales are set to $\mu_R = \mu_F = m_t$. The scale variation bands are obtained by varying $\mu_{R,F} = c_{R,F} \cdot m_t$, with $(c_R, c_F) \in \{(0.5, 0.5),\, (2, 2)\}$.[3]

In the NWA parton-showered results, the central scale was also compared to a dynamic scale called $\mu_{t\bar{t}}$. The latter is a “color-flow inspired” QCD scale suggested in Ref. [223]. For the Mandelstam invariants s, t and u, the dynamic scale is given by

$$\mu_{t\bar{t}}^2(q\bar{q} \to t\bar{t}) \;=\; 2\,p_q p_t \;=\; m_t^2 - t \;, \tag{6.7}$$

$$\mu_{t\bar{t}}^2(\bar{q}q \to t\bar{t}) \;=\; 2\,p_q p_t \;=\; m_t^2 - u \;, \tag{6.8}$$

$$\mu_{t\bar{t}}^2(gg \to t\bar{t}) \;=\; \left\{ \begin{array}{lcl} m_t^2 - t & & w_1 \propto \frac{u-m_t^2}{t-m_t^2} + \frac{m_t^2}{m_t^2-t}\left\{\frac{4\,t}{t-m_t^2} + \frac{m_t^2}{s}\right\} \\ & \text{with weight} & \\ m_t^2 - u & & w_2 \propto \frac{t-m_t^2}{u-m_t^2} + \frac{m_t^2}{m_t^2-u}\left\{\frac{4\,u}{u-m_t^2} + \frac{m_t^2}{s}\right\} \;, \end{array} \right. \tag{6.9}$$

the value of $\mu_{t\bar{t}}$ being chosen with a probability proportional to the two weights w_1, w_2 for the gg channel.

---

[3]Also, 7-point variations were considered but the simultaneous variations are identical to their envelope.

6.5 Total cross-section results

The fiducial cross-sections after applying the aforementioned cuts are given in Table 6.2 for all considered predictions, where production at LO accuracy is also added for completeness. The renormalization and factorization scale uncertainties are given in percent.

	X=LO [fb]	X=NLO [fb]
$\mathbf{X_{full}}$	$(739.5 \pm 0.3)^{+31.5\%}_{-22.4\%}$	$(914 \pm 3)^{+2.1\%}_{-7.6\%}$
$\mathbf{X^{LOdec}_{NWA}}$	$(727.3 \pm 0.2)^{+31.4\%}_{-22.3\%}$	$(1029 \pm 1)^{+10.4\%}_{-11.5\%}$
$\mathbf{X^{NLOdec}_{NWA}}$	-	$(905 \pm 1)^{+2.3\%}_{-7.7\%}$
$\mathbf{X_{PS}}, \mu = m_t$	$(637.7 \pm 0.9)^{+29.7\%}_{-21.0\%}$	$(886 \pm 1)^{+8.5\%}_{-9.3\%}$
$\mathbf{X_{PS}}, \mu = \mu_{t\bar{t}}$	$(499.7 \pm 0.7)^{+27.6\%}_{-19.3\%}$	$(805.2 \pm 0.9)^{+12.3\%}_{-10.9\%}$

Table 6.2: Cross-sections for all predictions at LO, respectively NLO in production, where the top-quark mass $m_t = 172.5\,\text{GeV}$. The uncertainty stemming from MC integration is given in parentheses, and scale variation uncertainties are shown in percent.

While the cross-sections for NLO_{full} and $\text{NLO}^{\text{NLOdec}}_{\text{NWA}}$ agree with each other within uncertainties, the $\text{NLO}^{\text{LOdec}}_{\text{NWA}}$ cross-section is about 13% higher than the latter. The NLO_{PS} cross-section, in comparison, is smaller because of the softening of b-jets in the parton-shower which leads to a higher rejection rate when taking jet requirements into account. The $\mu_{t\bar{t}}$ scale is larger than the central scale m_t, thus the even smaller cross-section for this scale choice. Notice also the reduction in the renormalization and factorization scale uncertainties when including NLO corrections to the top-quark decay. Usually, rather than total inclusive cross-sections, the most sensitive top-quark mass measurements rely on differential distributions, where mostly the distributions for $t\bar{t}$ final-states are MC-generated and *fitted* to extract the top-quark mass (see the full explanation of the method in Chapter 7). One caveat of considering differential distributions is that the measured top-quark mass is rather represented by the MC input top-quark mass parameter m_t^{MC}, instead of the top-quark pole mass determined in inclusive $t\bar{t}$ measurements.

Leaving the difference between heavy-quark mass schemes aside, the exact procedure used in current ATLAS analyses for measuring the MC top-quark mass is explained in the next chapter, along with quantitative comparisons of the theoretical predictions outlined above.

7 NWA versus $W^+W^-b\bar{b}$: Top-quark mass uncertainties at parton level

This chapter shall investigate quantitatively the effect of using the different theoretical predictions presented above in a top-quark mass extraction. The measurement method is based on the ATLAS 8 TeV analysis in the dilepton channel [180], where the ATLAS cuts are adapted to the 13 TeV center-of-mass energy. This chapter first introduces the template fit method that was used in the experimental measurement. After a short discussion of important features of the considered observables, the results for the fit of the top-quark mass and its dependence on the different theoretical descriptions of the $t\bar{t}$ dilepton final-state are laid out.

7.1 The template fit method

In the dilepton channel, the top-quark momenta cannot be fully reconstructed in the experiment because of the two-particle spectrum spread given by the neutrinos from both W decays. One successful method is to use a differential distribution that is sensitive to the top-quark mass instead, and which can be defined without having to properly reconstruct the top-quark intermediate states. The procedure is the following:

- Choose a distribution that is sensitive to the theoretical top-quark mass: for example, the average invariant mass of the lepton-b-jet system $m_{\ell b}$ (which consists of the visible top-quark decay products) is chosen as a function of the top-quark mass set in the MC event generator.

- Generate distributions for different input top-quark masses m_t^{in}. These are called *template* distributions.

- Individually fit the template distributions simulated for the input masses m_t^{in} with an appropriate function. Considering the simple example of a Gaussian fit, this gives:

$$\mathcal{G}(A,\mu,\sigma;m_t^{\text{in}}) = A(m_t^{\text{in}})\exp\left(-\frac{\left(\mu(m_t^{\text{in}}) - m_t^{\text{in}}\right)^2}{2\sigma^2(m_t^{\text{in}})}\right) \,, \tag{7.1}$$

  where the parameters A, μ, σ are fitted to the distributions generated for each input mass.

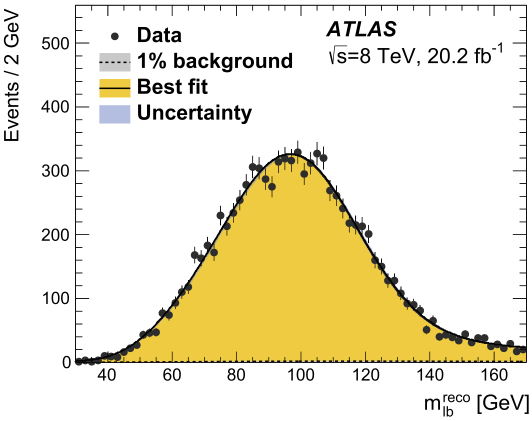

(a) Fit of the $m_{\ell b}$ template to ATLAS data

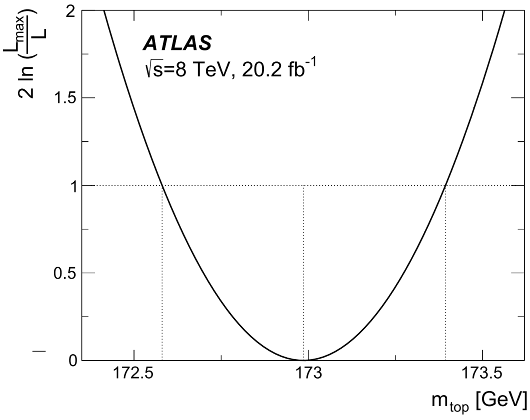

(b) Log-likelihood for m_t

Figure 7.1: (a) The ATLAS 8 TeV analysis generates parametrized template distributions for $m_{\ell b}$ for different input top-quark masses. The parametrized function is then fitted to data. (b) The likelihood function for m_t is maximized in an fit to the measured $m_{\ell b}$ distribution to extract the top-quark mass. Figures from Ref. [180].

This step is called *calibration* in the following paragraphs, and the functions for each of the input top-quark masses are called calibration functions. The dependence of the parameters on m_t^{in} is assumed to be linear, a fact that is checked against the MC prediction. Once it is confirmed, the linear dependence is imposed (in this example, $A(m_t^{\text{in}}) = a + b \cdot m_t^{\text{in}}$ with a and b fixed, and analogously for $\mu(m_t^{\text{in}})$, $\sigma(m_t^{\text{in}})$). The underlying linear parameters are then kept constant, and the only free parameter is the top-quark mass $m_t = m_t^{\text{out}}$ to be measured. This function can then be used directly in an unbinned likelihood fit to the distribution measured in experimental data, as shown in Fig. 7.1 as an illustration from the ATLAS 8 TeV measurement.

For a satisfying modeling of the $m_{\ell b}$ distribution, the sum of a Gaussian and a Landau distribution is used in the analysis. In practice, the overall normalization factor is fixed to the measured data. In the rest of this chapter, the extraction is repeated from a custom analysis implemented in `Rivet` [224] similar to the one performed by ATLAS. Predictions from the four different theoretical setups presented in Chapter 6 are used at parton level (after parton-showering for the NLO$_{\text{PS}}$ results). Different observables are also compared in addition to $m_{\ell b}$.

7.2 Definition of the observables

The results presented in the rest of this chapter were published in Ref. [212]. The reader is referred to the latter for details that are omitted in the following. A list of observables is studied that should in principle be maximally sensitive to the top-quark mass while minimally sensitive to theoretical systematic uncertainties (that is, including differences between NWA and full $W^+W^-b\bar{b}$ predictions):

- $m_{\ell b}$ – the invariant mass of the two lepton- and b-jet systems

$$m_{\ell b}^2 \;=\; (p_\ell + p_b)^2 \; . \tag{7.2}$$

Since both top quarks decay leptonically and there is no possibility to determine the charge of the b-jets experimentally, there is an ambiguity in the assignment of the lepton and b-jet to the two top quarks. Here, the same criterion is used as in the ATLAS analysis: the two possible pairs for the lepton-b-jet system $(\ell^+ b_1, \ell^- b_2)$ are tried out, and the pairing that minimizes the sum of the two $m_{\ell b}$ values per event is chosen. The final value is set to the average of both $m_{\ell b}$ values.

- m_{T2} – following Refs. [225, 226] in the case of the final-state $(e^+\nu_e)(\mu^-\bar{\nu}_\mu)b\bar{b}$, the definition of this variable is given by

$$m_{T2}^2 \;=\; \min_{p_T^{\nu_1}+p_T^{\nu_2}=p_T^{\text{miss}}} \left[\max\left\{ m_T^2\left(p_T^{(\ell^+ b_1)}, p_T^{\nu_1}\right), m_T^2\left(p_T^{(\ell^- b_2)}, p_T^{\nu_2}\right)\right\}\right] \; . \tag{7.3}$$

The same pairing as for $m_{\ell b}$ is chosen for the lepton and b-jet systems, and the transverse mass is defined as

$$m_T^2\left(p_T^{(\ell b_i)}, p_T^{\nu_i}\right) = m_{(\ell b_i)}^2 + 2\left(E_T^{(\ell b_i)} E_T^{\nu_i} - p_T^{(\ell b_i)} p_T^{\nu_i}\right) \; , \tag{7.4}$$

with $E_T = \sqrt{|p_T|^2 + m^2}$ and $m_{\nu_i} = 0$.

- $E_T^{\Delta R}$ – the lepton transverse energy weighted by the angular distance to the corresponding b-jet

$$E_T^{\Delta R} \;=\; \frac{1}{2}\left(E_T^{\ell^+}\Delta R(\ell^+, b_1) + E_T^{\ell^-}\Delta R(\ell^-, b_2)\right) \; , \tag{7.5}$$

where again the above $m_{\ell b}$ criterion is used.

- $m_{\ell\ell}$ – the invariant mass of the two-lepton system.

For the $\text{NLO}_{\text{NWA}}^{\text{LOdec}}$, $\text{NLO}_{\text{NWA}}^{\text{NLOdec}}$ and NLO_{full} calculations, only the parton level is considered, including the decay products from the W bosons. The b-jets are identified with the b-quarks in that case. For the NLO_{PS} prediction, the cuts and observables are defined on the parton-level output of the shower algorithm, before any hadronization but with the full-particle final-state. Sets of MC samples were produced for the input top-quark masses

$$m_t \in \{165.0, 172.5, 180.0\}\,[\,\text{GeV}] \; . \tag{7.6}$$

The dependence on the input top-quark mass m_t is shown for all four observables in Fig. 7.2. Whereas $m_{\ell b}$ and m_{T2} are the most sensitive to the input m_t with a ratio to the central choice of the order $\mathcal{O}(2-3)$, the dependence of the $E_T^{\Delta R}$ and $m_{\ell\ell}$ observables on the top-quark mass is rather weak.

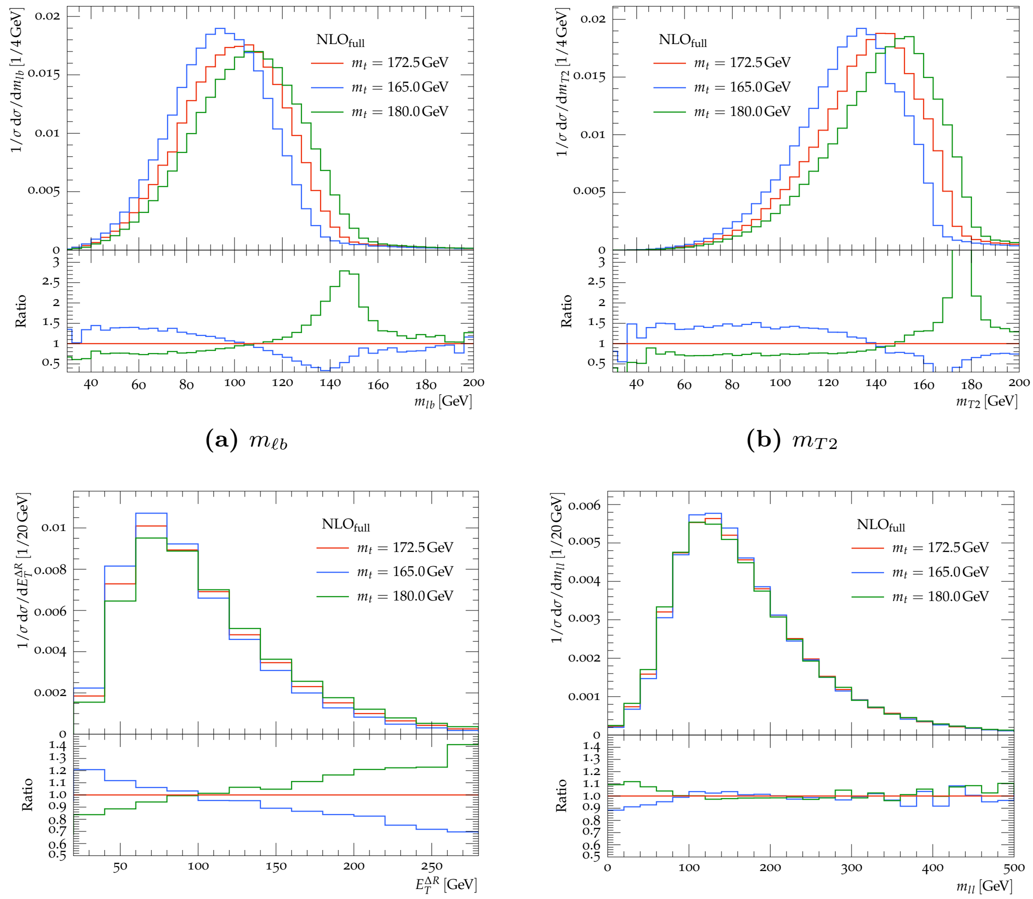

(a) $m_{\ell b}$ **(b)** m_{T2}

(c) $E_T^{\Delta R}$ **(d)** $m_{\ell\ell}$

Figure 7.2: Differential observables are shown for three different top-quark mass points chosen symmetrically around $m_t = 172.5$ GeV for the full $W^+W^-b\bar{b}$ NLO prediction. While the (a) $m_{\ell b}$ and the (b) m_{T2} observables show the highest top-mass dependence, the observables (c) $E_T^{\Delta R}$ and (d) $m_{\ell\ell}$ are not sensitive enough to be considered for the template fit. Figures from Ref. [212].

7.3 Comparison of the different theoretical descriptions

The normalized differential cross-section for the $m_{\ell b}$ observable is outlined in Fig. 7.3 for the four theoretical predictions presented in Chapter 6. The ratio to the complete $W^+W^-b\bar{b}$ NLO$_{\text{full}}$ calculation is shown, where the latter's scale uncertainties are represented by gray bands in the plot. Note that the $m_{\ell b}$ distribution has a sharp kinematic edge at $m_{\ell b}^{\text{edge}} = \sqrt{m_t^2 - m_W^2} \sim 153\,\text{GeV}$. Beyond the kinematic edge, the bins are only populated by wrong lepton-b-jet pairing, additional radiation from the initial-state clustered along the lepton-b-jet system, and non-resonant contributions. The LO cross-section for $t\bar{t}$ production vanishes in this phase-space region. Thus, because NLO corrections represent the first non-trivial order contributing to this region, differences between the theoretical descriptions considered here are expected to be sizable around and above this kinematic edge. On the other hand, as seen in Fig. 7.2, this region also displays the highest sensitivity to the top-quark mass.

In Fig. 7.3, all predictions for $m_{\ell b}$ agree within a few percent in the bulk of the distribution, $40\,\text{GeV} \leq m_{\ell b} \leq 140\,\text{GeV}$, except for $\text{NLO}_{\text{NWA}}^{\text{LOdec}}$. The latter introduces a positive slope around and above the peak with differences of $\mathcal{O}(-10\%)$ at small masses up to $+20\%$ at $\sim 140\,\text{GeV}$, effectively shifting the peak to higher values of $m_{\ell b}$. This translates into an artificially higher extracted mass for the top quark when using LO decay predictions. In contrast, $\text{NLO}_{\text{NWA}}^{\text{NLOdec}}$ is found within 4% of the NLO_{full} prediction for the bulk of the distribution, starting to differ above the kinematic edge and stagnating at -50% of the full prediction in the tail, as expected. Finally, for the NLO_{PS} case, the tail at high $m_{\ell b}$-values is populated by the additional radiation from the parton-shower, and is driven closer to NLO_{full} while it mostly lies between $\text{NLO}_{\text{NWA}}^{\text{LOdec}}$ and $\text{NLO}_{\text{NWA}}^{\text{NLOdec}}$ in the rest of the distribution.

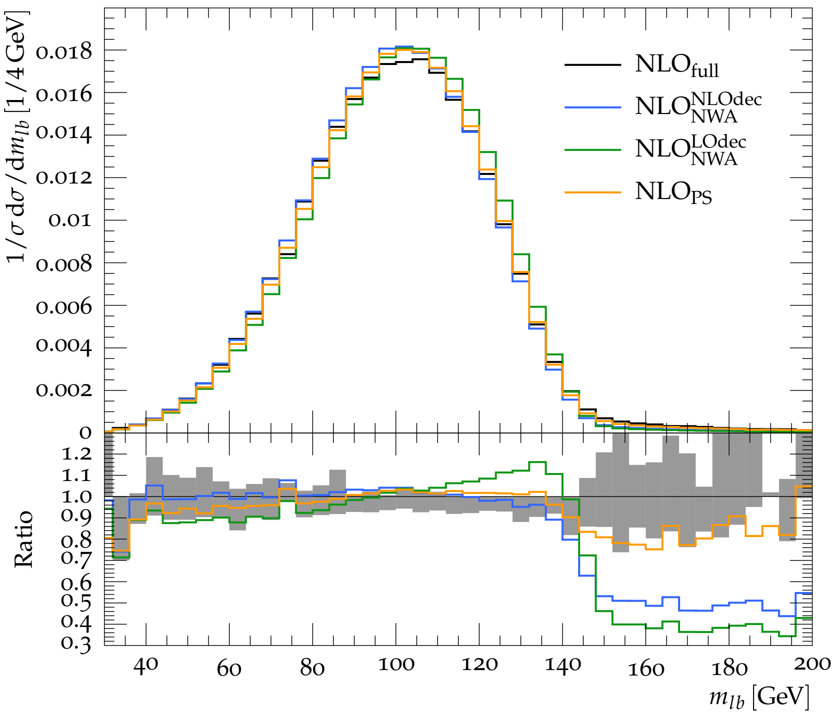

Figure 7.3: The normalized differential lepton-b-jet system invariant mass $m_{\ell b}$ is shown for all four theoretical predictions considered at 13 TeV, with their ratio to the NLO_{full} prediction. The gray band represents the latter's scale variation uncertainty. Figure from Ref. [212].

Similar features can be observed for the normalized distribution of m_{T2} in Fig. 7.4 on a larger range up to the kinematic edge at $m_{T2}^{\text{edge}} = m_t$. In Figs. 7.5a and 7.5b, the normalized $E_T^{\Delta R}$ and $m_{\ell\ell}$ distributions show smaller differences between the theoretical predictions, with maximal deviations of $\mathcal{O}(10 - 12\%)$ in the regions of lowest cross-section. Since they are much less sensitive to the top-quark mass, though, they are not considered for the template fitting procedure in the results below.

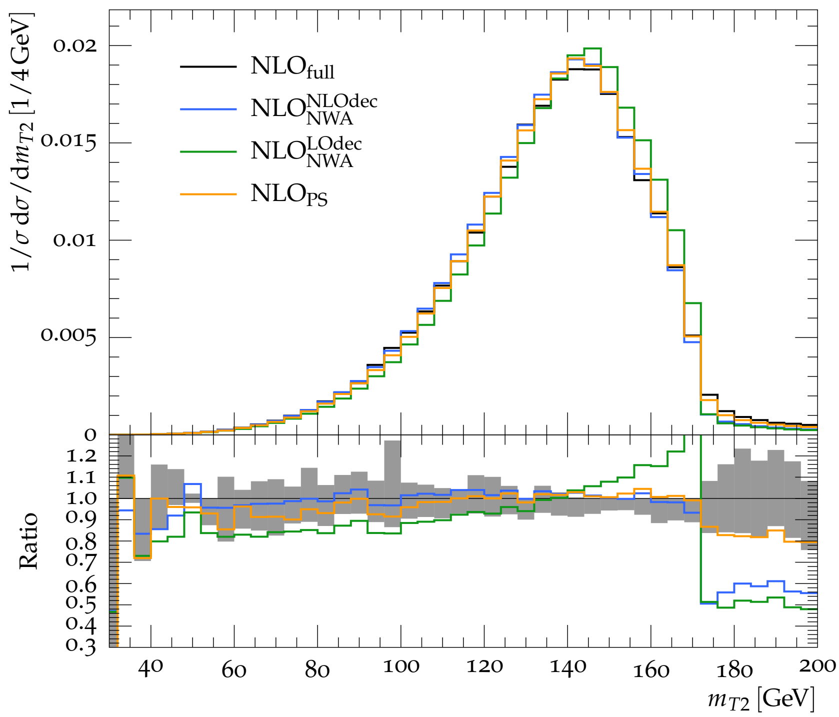

Figure 7.4: The normalized m_{T2} distribution is depicted for the four theoretical predictions, and shows a behavior similar to $m_{\ell b}$. Figure from Ref. [212].

It is also enlightening to look at the scale dependence of the four theoretical descriptions for LO and NLO production. In Fig. 7.6a, the ratio of the $W^+W^-b\bar{b}$ prediction NLO$_{\text{full}}$ to LO$_{\text{full}}$ is shown for the $m_{\ell b}$ observable. Although large corrections are expected above the kinematic edge when going from LO to NLO in production, one finds unexpectedly important corrections in the low-mass region as well, where differences between both orders of accuracy in production are not covered by the scale uncertainties. In the NWA case shown in Fig. 7.6b, the NLO corrections to the top-quark decay also push the prediction out of the NLO$_{\text{NWA}}^{\text{LOdec}}$ scale uncertainties. The differences between the NLO$_{\text{NWA}}^{\text{LOdec}}$ and NLO$_{\text{NWA}}^{\text{NLOdec}}$, respectively NLO$_{\text{PS}}$ are also not covered around the kinematic edge. In general, scale uncertainties for $t\bar{t}$ production in the NWA are shown to be misguidedly small in the tails of the $m_{\ell b}$ and m_{T2} distributions. The behavior of scale-varied predictions is depicted for m_{T2}, $E_T^{\Delta R}$ and $m_{\ell\ell}$ in Figs. 7.7–7.9.

Taking into account the mass sensitivity (Fig. 7.2a) and the systematic differences between predictions (Fig. 7.6a), the template fit strategy should be optimized to maximize

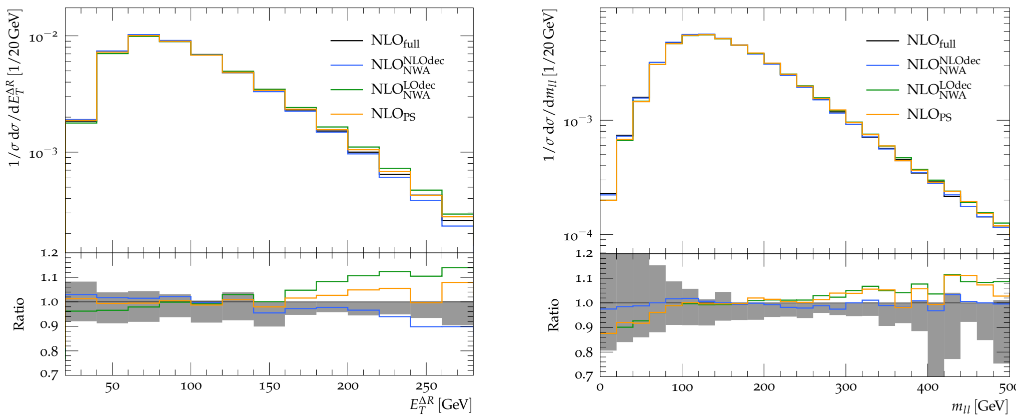

(a) **(b)**

Figure 7.5: The normalized differential cross-sections for the (a) $E_T^{\Delta R}$ and (b) $m_{\ell\ell}$ distributions with all four theoretical predictions. Figures from Ref. [212].

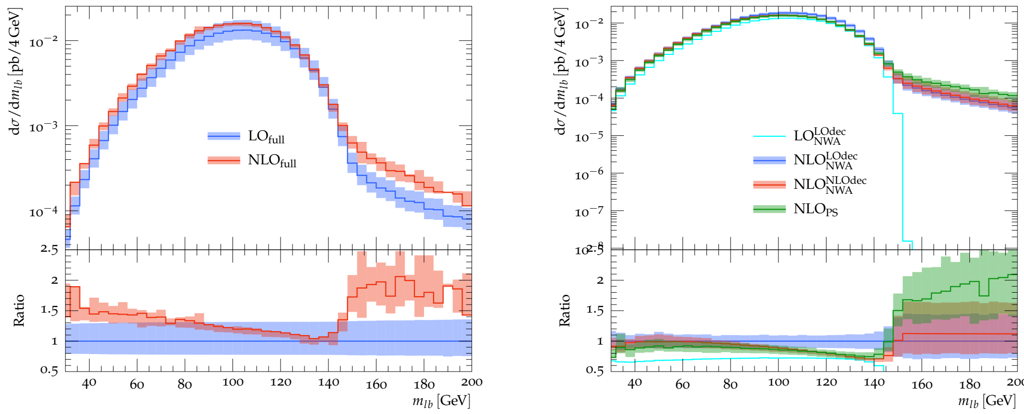

(a) **(b)**

Figure 7.6: Results including scale variation bands for m_{lb}, for (a) the $\mathrm{LO_{full}}$ and $\mathrm{NLO_{full}}$ calculations, (b) the calculations based on the NWA. The ratios with respect to (a) $\mathrm{LO_{full}}$ and (b) $\mathrm{NLO_{NWA}^{LOdec}}$ are also shown. Figures from Ref. [212].

the top-quark mass sensitivity while keeping the systematic uncertainty associated to the theoretical predictions to a minimum. The fit range is chosen to be

$$\begin{aligned} 40\text{ GeV} \leq m_{\ell b} \leq 160\text{ GeV}\ , \\ 80\text{ GeV} \leq m_{T2} \leq 180\text{ GeV}\ . \end{aligned} \tag{7.7}$$

The exact dependence on the fit range was investigated, where the results were reproduced with a restricted range of $m_{\ell b} \leq 140$ GeV, and numerical values were found to be stable.

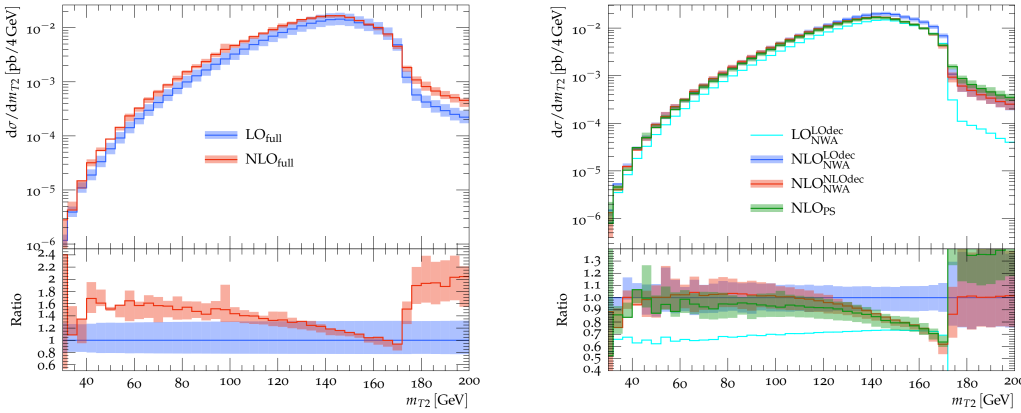

(a) **(b)**

Figure 7.7: Results including scale variation bands for m_{T2}, for (a) the $\mathrm{LO_{full}}$ and $\mathrm{NLO_{full}}$ calculations, and (b) the calculations based on the NWA. The ratios are defined as in Fig. 7.6. Figures from Ref. [212].

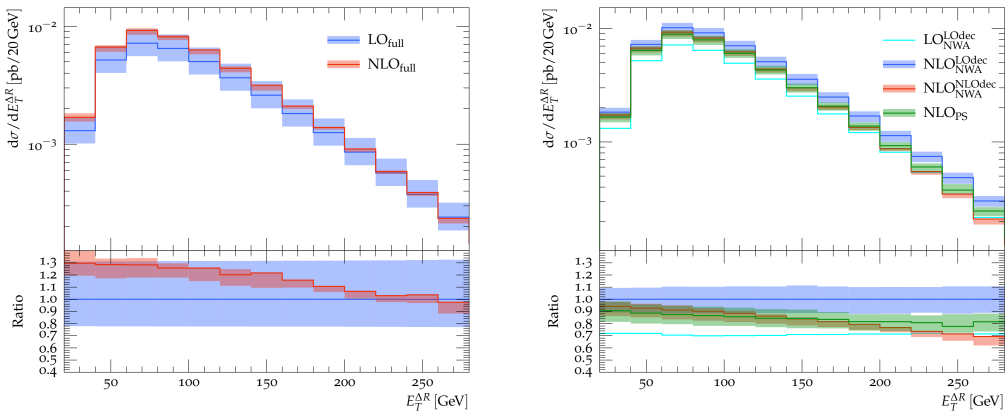

(a) **(b)**

Figure 7.8: Results including scale variation bands for $E_T^{\Delta R}$ for (a) the $\mathrm{LO_{full}}$ and $\mathrm{NLO_{full}}$ calculations, and (b) the calculations based on the NWA. The ratios are defined as in Fig. 7.6. Figures from Ref. [212].

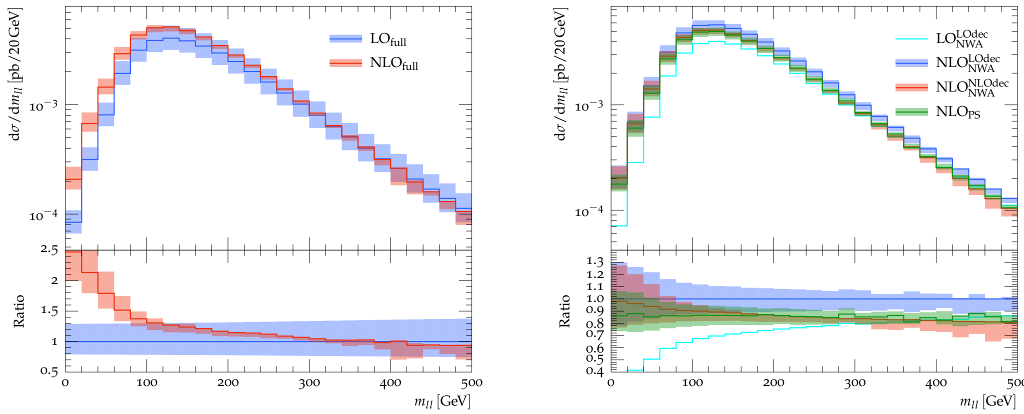

(a) **(b)**

Figure 7.9: Results including scale variation bands for $m_{\ell\ell}$, for (a) the $\mathrm{LO_{full}}$ and $\mathrm{NLO_{full}}$ calculations, and (b) the calculations based on the NWA. The ratios are defined as in Fig. 7.6. Figures from Ref. [212].

7.4 Template fit results

After the qualitative discussion of differential distributions in the last section, results from the template fitting procedure are shown and numerical values compared for the extracted top-quark mass from the different theoretical descriptions. To this effect, since no data were available to compare to, the procedure outlined in Section 7.1 is adapted and the following approach is applied to produce plots like the one displayed in Fig. 7.10:

- **Simulation** : The distributions for $m_{\ell b}$ and m_{T2} are produced at parton level with the three input top-quark masses m_t^{in} for all theoretical descriptions.
- **Template calibration**: The template distributions produced in the first step are individually fitted to the sum of a Gaussian and a Landau function. The theoretical description used as a basis for the distribution is called the *calibration set*. In the example of Fig. 7.10a, the two calibration sets are described by the red/blue reference points in the legend.
- **Pseudo-data**: From the different theoretical descriptions, a subset of events is drawn and labeled as *pseudo-data*. This sample corresponds to a luminosity of 50 fb^{-1}. In Fig. 7.10a, the theoretical description used for producing pseudo-data is given at the top of the plot. In general, the pseudo-data set is drawn from the more complete of the two predictions, which should be closer to real data. For a given theory prediction, pseudo-experiments are performed by repeating the random drawing of the pseudo-data 1000 times from the subset of all events.
- **m_t extraction**: For each of the input top-quark masses m_t^{in}, an unbinned likelihood fit is applied to the pseudo-data, using the corresponding calibration set, to determine the extracted value of the top-quark mass m_t^{out}.

The normalization of the histograms is chosen to reproduce the pseudo-data cross-section in the fit range, so that the result of template fits depends only on differences in the distribution shape. Taking again Fig. 7.10a as reference, the red/blue points indicate the offset of the extracted top-quark mass with respect to the MC input mass $\Delta m_t^{\mathrm{MC}} = m_t^{\mathrm{out}} - m_t^{\mathrm{in}}$. When considering the calibration function generated from the same theoretical prediction as used to produce the pseudo-data, the offset Δm_t should be close to zero and serves as a cross-check that no systematic bias exists in the fitting procedure. The error bars indicate the statistical uncertainty associated with the finite size of the pseudo-data sample. The numerical offset Δm_t given in the legend is calculated as the average of the offsets from the three mass points. Finally, the systematic uncertainty bands are provided by fitting the calibration set to the scale-varied pseudo-data.

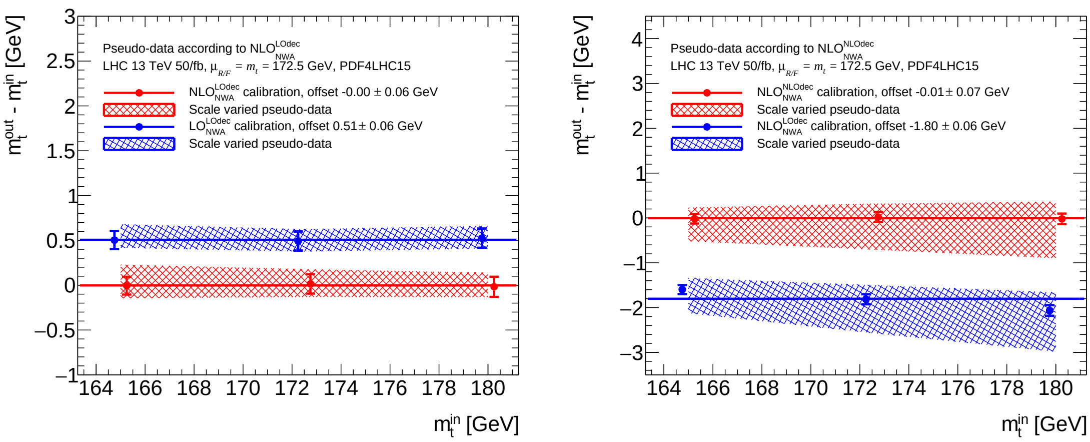

(a) **(b)**

Figure 7.10: Pseudo-data are drawn from the (a) NLO$^{\mathrm{LOdec}}_{\mathrm{NWA}}$ and (b) NLO$^{\mathrm{NLOdec}}_{\mathrm{NWA}}$ samples, and the difference between the input mass and the fit output is shown for each mass point. The calibration set from the same prediction (red) is used to show the absence of systematic bias in the template fit. The calibration set from (a) LO$^{\mathrm{LOdec}}_{\mathrm{NWA}}$ and (b) NLO$^{\mathrm{LOdec}}_{\mathrm{NWA}}$ yields an offset (blue) in the top-quark mass extracted from the theoretically more complete respective pseudo-data. Figures from Ref. [212].

The predictions are considered in order of increasing complexity. Fig. 7.10a shows the offset between extracted and input top-quark masses when generating pseudo-data according to the NLO$^{\mathrm{LOdec}}_{\mathrm{NWA}}$ prediction, and using the calibration function fitted from LO$^{\mathrm{LOdec}}_{\mathrm{NWA}}$ MC templates in blue. The offset in m_t produced by going from LO to NLO in $t\bar{t}$ production amounts to 0.51 GeV. For comparison, Fig. 7.10b gives the offset from fitting the NLO$^{\mathrm{NLOdec}}_{\mathrm{NWA}}$ pseudo-data with the NLO$^{\mathrm{LOdec}}_{\mathrm{NWA}}$ calibration function: higher-order corrections solely in the top-quark decay lead to an offset of -1.80 GeV. Moreover, the NLO decay corrections in Fig. 7.10b lead to larger uncertainty bands, because the scale variations produce non-uniform shape differences. These results already highlight the importance of higher-order corrections to the top-quark decay in mass measurements based on $m_{\ell b}$.

Considering higher-order corrections in both production and decay simultaneously, the offsets in the extracted top-quark masses are given in Fig. 7.11a for the NWA case, and in Fig. 7.11b for the full $W^+W^-b\bar{b}$ case. The factorization of production and decay in the NWA approximation yields an offset of -1.38 GeV, corresponding to the sum of the offsets in NLO production and in NLO decay separately shown in Fig. 7.10a, respectively Fig. 7.10b. This serves as a check of the factorization properties in the NWA.

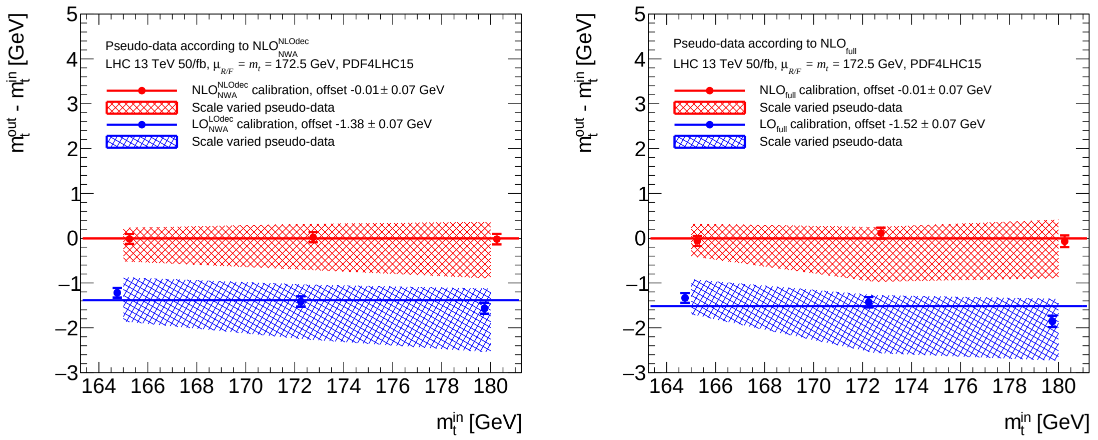

(a) (b)

Figure 7.11: From fitting the $m_{\ell b}$ distribution, the offset for the extracted top-quark mass based on (a) $\mathrm{NLO}^{\mathrm{NLOdec}}_{\mathrm{NWA}}$ and (b) $\mathrm{NLO}_{\mathrm{full}}$ pseudo-data underlines the effect of taking NLO contributions for production and decay into account. Figures from Ref. [212].

After these basic considerations, the top-quark mass offsets stemming from the most complete predictions are discussed. The offset in m_t produced when fitting the $\mathrm{NLO}_{\mathrm{full}}$ pseudo-data set with the calibration from the $\mathrm{NLO}^{\mathrm{NLOdec}}_{\mathrm{NWA}}$ prediction is shown in Fig. 7.12a. Although it still yields a sizable offset of 0.83 GeV with respect to the more complete $W^+W^-b\bar{b}$ prediction, the uncertainty bands now overlap. The fit of the calibration function from $\mathrm{NLO}_{\mathrm{PS}}$ to the $\mathrm{NLO}_{\mathrm{full}}$ pseudo-data is displayed in Fig. 7.12b. In this case, the offset is compatible with zero within statistical uncertainties. Although the $\mathrm{NLO}_{\mathrm{PS}}$ prediction does not describe the top-quark decay at NLO accuracy beyond the soft limit, it still largely reproduces the full $W^+W^-b\bar{b}$ description for the most part of the $m_{\ell b}$ fit range (as can be seen in Fig. 7.3). Further studies were performed to understand if the discrepancy between $\mathrm{NLO}^{\mathrm{NLOdec}}_{\mathrm{NWA}}$ and $\mathrm{NLO}_{\mathrm{PS}}$ originates in the genuine NLO-accurate description of the decay. More details are given in Appendix A, where the parton-shower number of emissions in both production and decay is gradually restricted, and offsets in m_t are compared to the $\mathrm{NLO}^{\mathrm{NLOdec}}_{\mathrm{NWA}}$ prediction. Reducing the number of emissions to one in the production and decay showers moves the $\mathrm{NLO}_{\mathrm{PS}}$ fitted m_t-value close to the $\mathrm{NLO}^{\mathrm{NLOdec}}_{\mathrm{NWA}}$ prediction. This suggests that it is the general softening of $m_{\ell b}$ around the kinematic edge, originating in the successive emissions from the parton-shower, that drives the top-quark mass fitted from the $\mathrm{NLO_{PS}}$ prediction towards the $\mathrm{NLO_{full}}$ value.

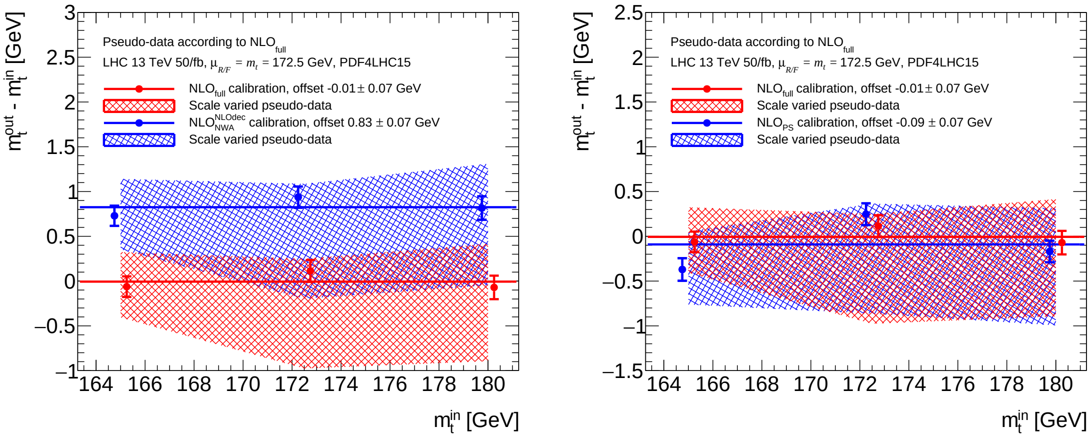

(a) **(b)**

Figure 7.12: Top-quark mass offsets from $m_{\ell b}$ for pseudo-data generated from the $\mathrm{NLO_{full}}$ prediction are reduced when considering the case of (a) $\mathrm{NLO_{NWA}^{NLOdec}}$ and (b) $\mathrm{NLO_{PS}}$ calibration functions. Figures from Ref. [212].

Similar results are shown for the m_{T2} distribution in Appendix A. The numerical offsets for all comparisons are summarized in Table 7.1, together with a combined χ^2 computed from both $m_{\ell b}$ and m_{T2} offsets for the same theoretical predictions. The value of χ^2 is defined as $\chi^2 = (o_1 - o_2)^2/(u_1^2 + u_2^2)$, with $i = 1, 2 = m_{\ell b}, m_{T2}$ and $o_i \pm u_i$ are the corresponding offsets and their (uncorrelated) uncertainties. While almost all χ^2 values are consistent with zero, the comparison between $\mathrm{NLO_{NWA}^{NLOdec}}$ and $\mathrm{NLO_{PS}}$ differs significantly: therefore, the m_{T2} estimator for the top-quark mass is concluded to be less sensitive to differences between the two latter predictions.

In conclusion, this study shows that higher-order corrections to the top-quark decay are at least as important as corrections to $t\bar{t}$ production, considering a top-quark mass extraction based on the $m_{\ell b}$ distribution. Moreover, the theoretical scale uncertainties in the NWA with LO top-quark decay seem to be underestimated. Yet, even the inclusion of the NLO corrections to the top-quark decay falls short of describing the full final-state. The comparisons presented above suffer from a few shortcomings: in particular, further showering and hadronization effects, as well as detector resolution, are expected to partly wash out the differences observed in the extracted top-quark mass at detector level. This is the subject of Chapter 9, which treats the topic in a more realistic experimental setup with the help of a folding procedure in the ATLAS framework.

		Offset [GeV]		Figure		
Pseudo-data	Calibration	$m_{\ell b}$	m_{T2}	$m_{\ell b}$	m_{T2}	χ^2
$\mathrm{NLO}^{\mathrm{LOdec}}_{\mathrm{NWA}}$	$\mathrm{LO}^{\mathrm{LOdec}}_{\mathrm{NWA}}$	$+0.51 \pm 0.06$	$+0.48 \pm 0.04$	7.10a	A.4a	0.17
$\mathrm{NLO}^{\mathrm{NLOdec}}_{\mathrm{NWA}}$	$\mathrm{NLO}^{\mathrm{LOdec}}_{\mathrm{NWA}}$	-1.80 ± 0.06	-1.67 ± 0.04	7.10b	A.4b	3.25
$\mathrm{NLO}^{\mathrm{NLOdec}}_{\mathrm{NWA}}$	$\mathrm{LO}^{\mathrm{LOdec}}_{\mathrm{NWA}}$	-1.38 ± 0.07	-1.24 ± 0.05	7.11a	A.4c	2.65
$\mathrm{NLO}_{\mathrm{full}}$	$\mathrm{LO}_{\mathrm{full}}$	-1.52 ± 0.07	-1.62 ± 0.05	7.11b	A.4d	1.35
$\mathrm{NLO}_{\mathrm{full}}$	$\mathrm{NLO}^{\mathrm{NLOdec}}_{\mathrm{NWA}}$	$+0.83 \pm 0.07$	$+0.60 \pm 0.06$	7.12a	A.4e	6.22
$\mathrm{NLO}_{\mathrm{full}}$	$\mathrm{NLO}_{\mathrm{PS}}$	-0.09 ± 0.07	-0.07 ± 0.06	7.12b	A.4f	0.05
$\mathrm{NLO}_{\mathrm{PS}}$	$\mathrm{NLO}^{\mathrm{LOdec}}_{\mathrm{NWA}}$	-0.92 ± 0.07	-1.17 ± 0.05	A.3a	A.4g	8.45
$\mathrm{NLO}_{\mathrm{PS}}$	$\mathrm{NLO}^{\mathrm{NLOdec}}_{\mathrm{NWA}}$	$+0.96 \pm 0.07$	$+0.68 \pm 0.05$	A.3b	A.4h	10.59
$\mathrm{NLO}_{\mathrm{PS}}$	$\mathrm{NLO}_{\mathrm{PS}}$ $(\mu_{t\bar{t}})$	-0.03 ± 0.07	$+0.02 \pm 0.05$	A.5b	A.5d	0.34

Table 7.1: The offsets from the top-quark mass extraction are given in GeV for pairs of the considered theoretical descriptions, from which the pseudo-data are generated, respectively the calibration function produced. The results are given for both the $m_{\ell b}$ and m_{T2} distributions, along with the corresponding plot references (see also Appendix A). A χ^2-value is computed between the offsets procured from fits of $m_{\ell b}$ and m_{T2}. Table from Ref. [212].

8 Folding of predictions to detector level

In the following chapter, the results outlined in Chapter 7 are reproduced with full particle-level predictions and the NLO$_{\text{full}}$ calculation is compared to $t\bar{t}$ results in the ATLAS framework at detector level. To study the extracted values of the top-quark mass from reconstructed events in a fast-simulation style, all distributions are folded from particle level to detector level in a custom implementation. Top-quark mass determinations focus entirely on the dilepton channel in this chapter, but the folding setup can be used in any decay channel.

8.1 Inverse problems

Usually, when performing a measurement, background contributions are first subtracted from data, and the corresponding signal distributions are unfolded to particle level [227] so that available measurements can be compared to predictions. The unfolding procedure is a particular example of so-called inverse problems: having a true distribution $f(x)$ for some observable Ω, $x \in [\Omega_{\text{min}}, \Omega_{\text{max}}]$, the measured distribution $g(y)$ is given by the Fredholm integral equation [228]:

$$g(y) = \int_{\Omega_{\text{min}}}^{\Omega_{\text{max}}} K(x,y) f(x) \mathrm{d}x \, , \tag{8.1}$$

where the kernel $K(x, y)$ is a continuous function. For binned results, discretizing Eq. (8.1) gives a linear equation for $\mathbf{x}$, $\mathbf{y}$ the n-, respectively m-bin histograms corresponding to the true, respectively the measured distribution:

$$y_j = \sum_{i=1}^{n} A_{ij} x_i, \quad j \in \{1, \ldots, m\} \, , \tag{8.2}$$

where $\mathbf{A}$ is the bin migration matrix. The problem of inverting Eq. (8.2), that is to uncover the true distribution $\mathbf{x}$ of an observable Ω from the measured signal distribution $\mathbf{y}$, is the foundation of unfolding procedures. Because noise in the measured function can lead to instabilities in the inversion of the response matrix $\mathbf{A}$, the procedure has to be regularized. There are two distinct unfolding methods: direct unfolding procedures, which usually implement some regularization parameter for a smooth inversion of Eq. (8.2), and iterative methods. For a short review of unfolding methods in particle physics, see Refs. [229, 230].

Conversely, instead of unfolding the data to particle level, the chosen strategy for the 13 TeV ATLAS top-quark mass analysis is to produce the distribution templates and perform the likelihood fit only at detector level. To do so, all samples are simulated up to detector level. This procedure avoids the complications of the unfolding problem. In contrast, the main disadvantage of the direct method lies in the computing time: all MC samples (systematics-varied samples and background) have to be simulated up to detector level. Here, a complementary approach is employed with the use of direct folding, as in Eq. (8.2), to provide distributions at detector level from the samples generated at particle level. Thus, the costly ATLAS simulation is performed only once and one can quickly quantify effects of theoretical uncertainties, on e.g. the extracted top-quark mass.

8.2 Folding setup in the ATLAS framework

Considering the results of Chapter 7, the primary goal is to use the folding setup within the ATLAS standard analysis package to quantify the uncertainty in using the incomplete $t\bar{t}$ prediction instead of a full parton-showered $W^+W^-b\bar{b}$ event set. It is clear that simulating all MC samples from particle to detector level is time-consuming: with one theoretical central prediction (for example POWHEG+PYTHIA8) and one parameter for the template fit (e.g. the top-quark mass m_t), one already has to produce and simulate samples for a number of top-quark mass points.

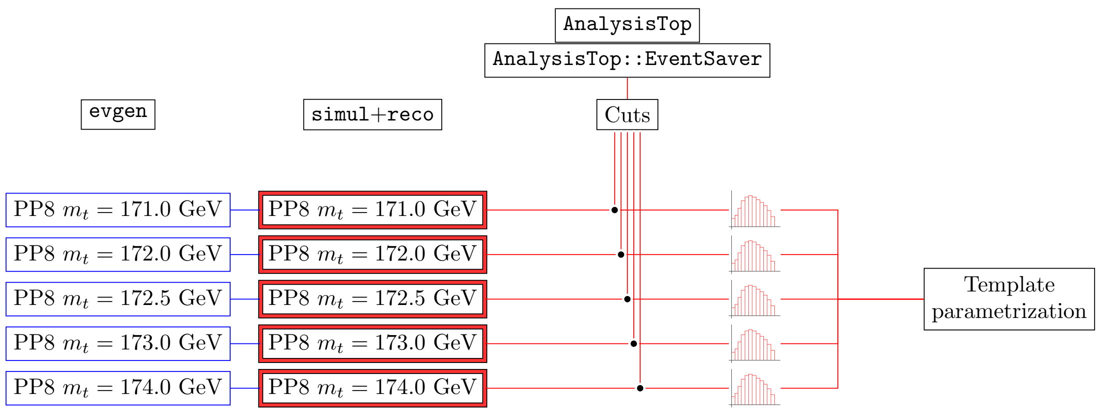

Figure 8.1: The workflow for a template fit of the central prediction POWHEG+PYTHIA8 (PP8) and five top-quark mass points.

Fig. 8.1 illustrates the current analysis workflow for five top-quark mass points. Each of the samples is produced at particle level first (`evgen` in blue on the far left) and is then simulated and reconstructed (`simul+reco` in red). In the ATLAS 13 TeV analysis, all samples entering the template fit parametrization are fast-simulated with the ATLFAST [166] package. A custom software package applies the analysis cuts outlined later in Section 8.5. Histograms of the $m_{\ell b}$ distribution for all individual mass points are then fed to the template parametrization.

To estimate systematic uncertainties, MC variation samples currently go through the same routine. For example, MC samples with variations of radiative parameters (e.g. `hdamp` in POWHEG, or a variation of the shower and hadronization algorithm) are also simulated and parametrized, and the result of the template fit is taken as a systematic uncertainty on the central sample for the extracted top-quark mass. In the following, for a swifter evaluation of the associated systematics, histograms of varied samples are directly folded from particle to detector level, and the output in the template fit is used to estimate the systematic uncertainty on the extracted top-quark mass.

A simple version of Eq. (8.2) is introduced, where pure bin migrations are implemented by a right stochastic matrix **A**, and the detector efficiencies are represented by two bin-by-bin probability vectors ϵ^{eff} and f^{acc}:

$$\mathcal{R}_i = \frac{1}{f_i^{\text{acc}}} A_{ij} \times \left(\mathcal{P}_j \, \epsilon_j^{\text{eff}} \right) \, , \tag{8.3}$$

where $\mathcal{R}_i$ is the number of events at detector level in bin i (for an arbitrary differential distribution), and $\mathcal{P}_j$ is the number of events at particle level in bin j. The migration matrix entry A_{ij} is the probability for an event in bin j at particle level to be reconstructed in bin i at detector level. The efficiency ϵ_j^{eff} is the probability for an event in bin j at particle level to be reconstructed at detector level. The factor $1/f_i^{\text{acc}}$ is the probability of an event in bin i at detector level to stem from a fake signal (i.e. its counterpart at particle level does not pass the fiducial cuts).[1] The migration matrices and detector efficiencies shall encode the experimental resolution simulated by ATLFAST.

The migration matrices and efficiencies can be expressed in terms of the usual definitions of acceptance A_i, purity P_i and stability S_i [229]:

$$A_i = \frac{\mathcal{R}_i}{\mathcal{P}_i}, \qquad P_i = \frac{\mathcal{P}_i A_{ii} \epsilon_i^{\text{eff}}}{\mathcal{R}_i}, \qquad S_i = \mathcal{P}_i A_{ii} \, . \tag{8.4}$$

The folding procedure is depicted in Fig. 8.2. The central POWHEG+PYTHIA8 (PP8) sample is simulated once: histograms at both detector level (in red) and particle level (in blue) are fed to the custom folding package (green nodes). From the distributions at both levels, a script produces the migration matrices and detector efficiencies defined above. In principle, for a given top-quark mass, pure theoretical uncertainties can then be estimated by applying the migration matrices and efficiencies from the central sample to variation samples, since detector effects do not depend on the MC theory variations themselves. The folding framework implements Eq. (8.3) and generates folded detector-level histograms from the particle-level MC-varied samples. They are also saved for subsequent use in the template fit. Moreover, consistency and statistical cross-checks are performed. In principle, this procedure can be applied to all **theoretical** uncertainties. Thus, in addition to the usual systematic variations, an estimate is computed for the uncertainty stemming from the non-resonant and non-factorizing diagrams in the full $W^+W^-b\bar{b}$ calculation.

[1] This ansatz is similar to the one used in other ATLAS analyses, see e.g. the unfolding procedure in Ref. [231].

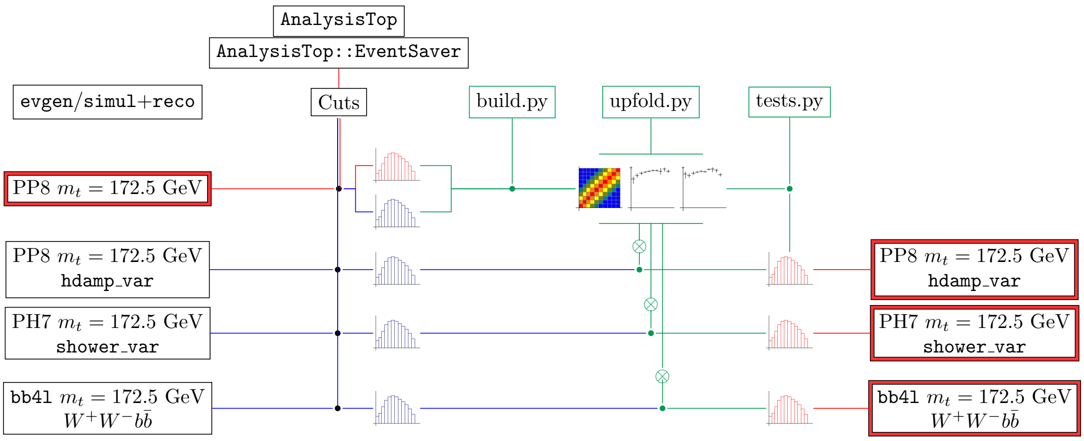

Figure 8.2: The folding package builds migration matrices and bin-by-bin efficiencies from the simulated detector and particle levels of a central sample, for example Powheg + Pythia8 with $m_t = 172.5$ GeV. They are used to fold particle-level histograms from MC-varied samples to detector level.

8.3 Theoretical descriptions of the signal

The MC derivation samples (DxAOD) used for all subsequent studies were produced officially by ATLAS during the `MC16a` campaign (optimized to describe the 2015/2016 data) and are summarized in Appendix B. The nominal samples for NLO $t\bar{t}$ in the NWA are generated by Powheg (for the matrix-element) and parton-showered with Pythia8 for five different mass points.[2] These samples are simulated up to detector level with the AtlFast algorithm, but a cross-check is done with respect to the full Geant4 simulation for one mass point. For a fairer comparison of the full $W^+W^-b\bar{b}$ prediction to the $t\bar{t}$ NWA description, the single-top Wt channel (with diagram removal) is added to the $t\bar{t}$ sample. In order to generate the $W^+W^-b\bar{b}$ predictions at particle level, the following setup is used:

- **Parton-level production**: The full dilepton final-state $(e^+\nu_e)(\mu^-\bar{\nu}_\mu)b\bar{b}$ events are produced at parton level with a local installation of the `bb4l` generator [232] in Powheg-BOX-RES [233]. They are generated outside of the ATLAS framework since the implementation of the `bb4l` program has not been validated yet. The matrix-element is computed by `OpenLoops` [90, 91], and LHE files are written out by Powheg for subsequent showering.

- **Particle-level production**: The Pythia8 parton-shower is applied in the ATLAS framework to the parton-level events produced with `bb4l`. Hadronization is also handled in Pythia8 by the Lund string model.

[2] Samples with nine top-quark mass points were officially produced, but only the same mass points as for $W^+W^-b\bar{b}$ samples are used in this study.

- **Analysis pre-step**: The MC simulation step in ATLAS produces a so-called event (EVNT) file containing the particle information and kinematics. To be able to run the `AnalysisTop` routine on the sample, one needs to transform it to a DxAOD derivation format. The truth information is propagated to the derivation level, which contains thinned MC truth information.

Altogether, predictions for five m_t values are generated for the $t\bar{t}$ NWA and the $W^+W^-b\bar{b}$ configurations (as well as for single-top Wt samples), with:

$$m_t \in \{171, 172, 172.5, 173, 174\}\,[\,\mathrm{GeV}\,]\ . \tag{8.5}$$

8.4 Object definition

In ATLAS, the measured data and the MC simulation output are fed to reconstruction algorithms. These algorithms rely on well-defined physics objects at detector level. The Level-1 trigger identifies well-resolved candidate physics objects, like electrons, photons, muons and jets. The Level-2 trigger cuts are designed to refine this selection. Without entering into much detail, trigger and reconstruction algorithms for electrons and photons [234], muons [235], jets [236], taus [237] and MET [155, 238] mostly use information from calorimeter energy clusters matched to one or several tracks identified in the Inner Detector. More about the exact object selection can be found in Ref. [239].

8.4.1 Electrons

Electron reconstruction matches tracks identified in the Inner Detector to energy deposits in the EM calorimeter within $(\Delta\eta, \Delta\phi) = (0.05, 0.05)$. The electron candidates must satisfy the kinematic requirements $p_T > 28\,\mathrm{GeV}$ and $|\eta| < 2.47$, where the transition region between the barrel and endcap calorimeters $1.37 < |\eta| < 1.52$ is excluded. For electrons and photons at the Level-1 trigger, a minimal transverse energy requirement $E_{T,\mathrm{min}}$ is used. In order to distinguish possible fake signals, a veto can be applied on the activity in the hadronic calorimeter behind the identified cluster in the EM calorimeter. To originate from the primary interaction vertex, electrons have to fulfill $|z_0 \cdot \sin(\theta)| < 0.5$ mm and $|d_0|/\sigma_{d_0} < 5$. Here, z_0 and d_0 are the longitudinal and transverse impact parameters, θ is the azimuthal angle, and σ_{d_0} is the transverse impact parameter resolution.

A multivariate algorithm [240] is used for calibrating the measured cluster energy. Then, electrons are identified with a likelihood (LH) discriminant that defines three working points: `Loose`, `Medium` and `Tight` [241, 242]. In this analysis, electrons have to satisfy a `Tight` requirement. Finally, a p_T- and η-dependent isolation criterion (described in Ref. [235]) is applied. To ensure a good separation with other types of activity, an overlap procedure is defined on the identified objects. Any electron sharing a track with a muon is removed. Any jet found within $\Delta R < 0.2$ of a reconstructed electron is discarded. Subsequently, any electron found within $\Delta R < 0.4$ of a jet is also removed.

8.4.2 Muons

Information from the MDT detectors in the Muon Spectrometer is used to fit the track of the muon candidate. The track is then extrapolated back to the interaction vertex and combined with tracks identified in the Inner Detector. The muon candidate has to satisfy $p_T > 28$ GeV and $|\eta| < 2.5$. To be assigned to the primary vertex, the muon tracks need to fulfill $|z_0 \cdot \sin(\theta)| < 0.5$ mm and $|d_0|/\sigma_{d_0} < 3$.

Muons are reconstructed with a minimal requirement on the transverse momentum. Depending on the quality and isolation requirements, they are classified in `VeryLoose`, `Loose`, `Medium`, `Tight` or `High-`p_T containers [235]. In Chapter 9, `Medium` muons are selected. Additionally, an optional isolation criterion for low-p_T muons can be applied. As muons can leave a trace in the calorimeter that might be misidentified as a jet, any jet with less than three associated tracks found within $\Delta R < 0.2$ of a muon is removed. Subsequently, any muon found within $\Delta R < 0.4$ of a jet is also discarded.

8.4.3 Jets and b-tagging

The anti-k_T jet algorithm [220] is applied (with a distance parameter $R = 0.4$ for small-R jets) to topological clusters identified in the calorimeter. These topo-clusters are reconstructed from the full set of calorimeter clusters. Jets are required to satisfy $p_T >$ 25 GeV and $|\eta| < 2.5$. The identified jets have to be calibrated, and correction factors are applied to retrieve their correct 4-momentum and origin vertex. The determination of jet energy scale (JES) factors and uncertainties comprises several steps, and usually includes comparisons between MC and data. In the ATLAS jet calibration, a MC-based comparison is followed by an *in situ* energy calibration step.[3] To reduce pile-up contributions, a multivariate jet-vertex tagger [243] is used for jets with $p_T < 60$ GeV and $|\eta| < 2.4$, and a pile-up correction factor derived with a jet area method [244, 245] is applied on all jets. Especially for the case of the ATLAS top-quark mass analysis in the lepton+jets channel (which is not covered in this work), the jet- and b-jet energy scale systematics dominate the total measurement uncertainty. For a comprehensive study of jet reconstruction and associated uncertainties, the reader is referred to Ref. [246].

Finally, jets stemming from b-quarks can be discriminated against light-quark jets. This feature is crucial in several analyses, including the measurement of the top-quark mass. Mostly, the identification of a b-jet (so-called b-tagging) relies on the observation of a displaced vertex from which the jet originates. There exist multiple b-tagging algorithms: impact-based (IP2D and IP3D [247, 248]), secondary vertex identification (SV [249]) and decay chain multi-vertex (JetFitter [250]). In ATLAS, the output from all three procedures are combined in a multivariate likelihood algorithm (MV2 [238]). A point in the likelihood discriminant can be chosen and defines the tagging efficiency. In the following chapter, a 70% b-tagging efficiency is chosen, corresponding to a rejection rate of ~ 8 for c-jets and ~ 313 for light jets.

[3] This type of energy calibration uses events where a well-known reference object recoils against one measured jet, e.g. $Z(\to \ell\ell) + j$ or $\gamma + j$.

8.5 Trigger and event requirements

The `AnalysisTop` package in the ATLAS framework contains all the subpackages that are necessary for general top-quark measurements. It defines and applies the calibration, correction factors, scale factors and their systematic variations to MC events and data. Here, `AnalysisTop` version `21.2.61` is used. The following requirements are applied on the events in the $e\mu$ dilepton channel:

- At least one primary vertex exists in the event.
- Two oppositely charged leptons with exactly one electron and one muon which fulfill $p_T^\ell > 28$ GeV, and $|\eta| < 2.47$ for electrons, $|\eta| < 2.5$ for muons. For electrons, the crack region $1.37 < |\eta| < 1.52$ is excluded. For reconstructed events, the lepton requirements from the high-level trigger (HLT) depend on the luminosity and are different for 2015 and 2016 data. They are set to the following values for 2015, respectively 2016 data:

Trigger cut	Object	Min. [GeV]	LH	Isolation	L-1
`HLT_e24_lhmedium_L1EM20VH`	$e^\pm$	$E_T > 24$	`Medium`	–	VH
`HLT_e60_lhmedium`	$e^\pm$	$E_T > 60$	`Medium`	–	–
`HLT_e120_lhloose`	$e^\pm$	$E_T > 120$	`Loose`	–	–
`HLT_mu20_iloose_L1MU15`	$\mu^\pm$	$p_T > 20$	–	$\sum p_T^{\text{track}}/p_T^e < 0.1 (R = 0.2)$	–
`HLT_mu50`	$\mu^\pm$	$p_T > 50$	–	–	–
`HLT_e26_lhtight_nod0_ivarloose`	$e^\pm$	$E_T > 26$	`Tight`	$\sum p_T^{\text{track}}/p_T^e < 0.1$	$\not{d}_0$
`HLT_e60_lhmedium_nod0`	$e^\pm$	$E_T > 60$	`Medium`	–	$\not{d}_0$
`HLT_e140_lhloose_nod0`	$e^\pm$	$E_T > 140$	`Loose`	–	$\not{d}_0$
`HLT_mu26_ivarmedium`	$\mu^\pm$	$p_T > 26$	–	$\sum p_T^{\text{track}}/p_T^\mu < 0.07$	–
`HLT_mu50`	$\mu^\pm$	$p_T > 50$	–	–	–

  The electrons are designated by their likelihood discriminant (LH). An isolation cut can be applied, where a maximum is set on the scalar sum of the transverse momentum in a cone around an object track (with variable size for the 2016 Run). Finally, an additional Level-1 trigger (L-1) veto can be applied on the hadronic activity behind the EM clusters (VH). For 2016 data, no impact parameter requirement is set on the electron tracks.

- $H_T = \sum_i p_{T,i} > 120$ GeV, the scalar transverse momentum sum of all particles.
- $n_{\text{jets}} \geq 2$ for the total number of jets with $p_T^{\text{jet}} > 25$ GeV and $|\eta| < 2.5$.
- Exactly two b-jets with $p_T^{\text{jet}} > 25$ GeV, $|\eta| < 2.5$. For reconstructed events, a 70% b-tagging working point is chosen for the `MV2c10` [247, 251] b-tagging algorithm. A b-jet is defined within particle-level events using the `JET_N_GHOST` criterion (so-called ghost association [245]), for which a jet is b-tagged if it contains a B-hadron.
- $m_{\ell\ell} > 15$ GeV for the invariant mass of the two-lepton system.

9 Determination of the top-quark mass at detector level

The simulated $t\bar{t}$ and single-top NWA predictions are presented, after applying the object selection and event requirements laid out in Chapter 8. The template parametrization of the $t\bar{t}$+single-top samples is performed. To compare these results to the $W^+W^-b\bar{b}$ prediction, a setup is introduced in an ATLAS framework for folding histograms generated at particle level. Migration matrices derived from the simulated $t\bar{t}$ samples are plotted. After some simple cross-checks of the setup, the $W^+W^-b\bar{b}$ folded results and template parametrization are presented, along with numerical comparisons of both theoretical descriptions for the extraction of the top-quark mass. A preliminary fit to ATLAS data from $t\bar{t}$+single-top and $W^+W^-b\bar{b}$ templates is performed. The results shown here are based on an ongoing implementation of the ATLAS 13 TeV analysis [252].

9.1 NWA predictions and template parametrization

The signal contains $t\bar{t}$ dilepton and single-top Wt events, where the interference terms contributing to the final-state are taken into account by the diagram removal scheme [205]. The nominal sample is produced in the Powheg-BOX generator [17–19] matched to Pythia8 [122] (PP8) for parton-showering and hadronization. The matrix-element is convoluted with the NNPDF3.0 NLO sets [253] and the parton-shower uses parameters from NNPDF2.3 LO. The parton-shower parameters in Pythia8 are set according to the A14 tune [254]. A central value `hdamp` $= 1.5 \cdot m_t$ is chosen for the `hdamp` resummation parameter in Powheg that was found to improve the description of the $t\bar{t}$ kinematics [255]. Moreover, the definition of the $m_{\ell b}$ observable is identical to the one given in Chapter 7 (see Eq. (7.2)): the lepton-b-jet pairing that minimizes the sum of both $m_{\ell b}$-values per event is chosen, and the $m_{\ell b}$ observable is defined as their average. The leptons and b-jets entering the definition are the objects reconstructed using the prescriptions given in Sections 8.4-8.5.

In Fig. 9.1, distributions of the $m_{\ell b}$ observable are shown at five different MC top-quark mass points for the $t\bar{t}$+single-top predictions. In all plots, the distributions are normalized to unity since, as in Chapter 7, only normalized distributions are input to the default ATLAS template fit. The ratio is displayed in the lower panel with respect to the central top-quark mass, and error bars indicate MC statistical uncertainties. The predictions are shown at particle level in Fig. 9.1a and at detector level in Fig. 9.1b. It is observed that the sensitivity to the input top-quark mass decreases visibly when comparing the particle and detector levels.

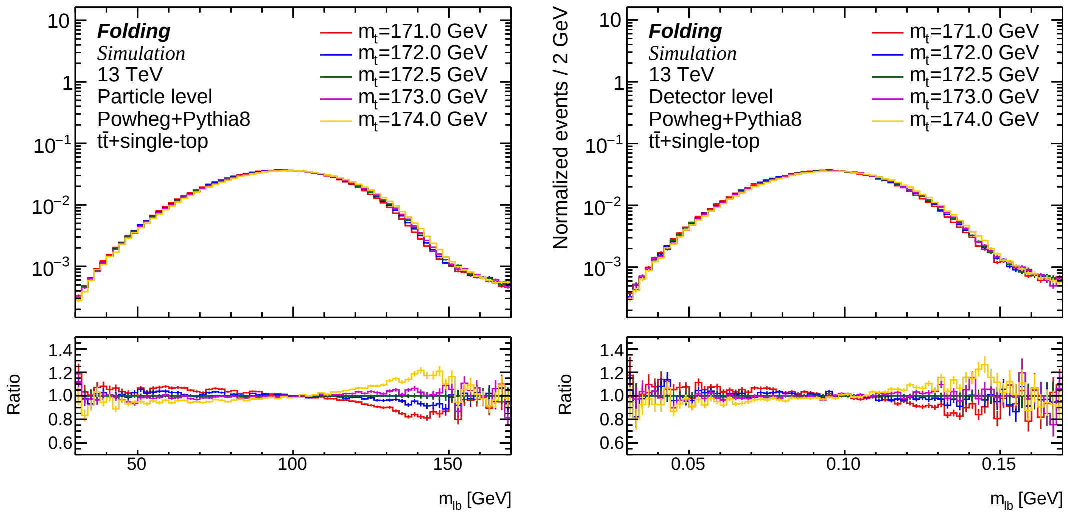

(a) **(b)**

Figure 9.1: The normalized $m_{\ell b}$ distribution from the PP8 $t\bar{t}$+single-top NWA predictions is shown for five top-quark mass points at (a) particle level and (b) detector level.

The template fit method is now applied to these predictions analogously to Chapter 7. It is performed in the framework of the ATLAS analysis at 13 TeV, which is currently under development [252], and is based on the work conducted in Refs. [5, 180, 256, 257]. The $m_{\ell b}$ template distributions for all five input top-quark masses are parametrized separately. In this case, a sum of three Gaussian distributions is used for a total of 18 parameters (9 functional parameters $\times$ 2 linear parametrizations as a function of m_t). The fit is performed with MINUIT [258] within `ROOT` [163], and the fit range is set to

$$m_{\ell b} \in [40\,\text{GeV}, 148\,\text{GeV}]\ . \tag{9.1}$$

Fig. 9.2a shows the $m_{\ell b}$ distribution from the central MC sample and the fitted function. The chosen functions satisfactorily describe the distributions. In Fig. 9.2b, the histograms and fit functions for three mass points are displayed together.

As explained in Section 7.1, the linear dependence of the functional parameters on the top-quark mass is then fixed. The mass itself is left as the only free parameter.[1] This function can now be used in an unbinned likelihood fit to data (or pseudo-data). The likelihood function $\mathcal{L}$ depends only on the top-quark mass m_t. For N events with weights w_i, the following function is minimized with respect to m_t:

$$-2\log(\mathcal{L}) = -2\sum_{i=1}^{N} w_i \cdot \log \mathcal{G}(m_{\ell b,i}|m_t)\ , \tag{9.2}$$

[1] The linear dependence of the different functional parameters on the input top-quark mass is shown in Appendix C.

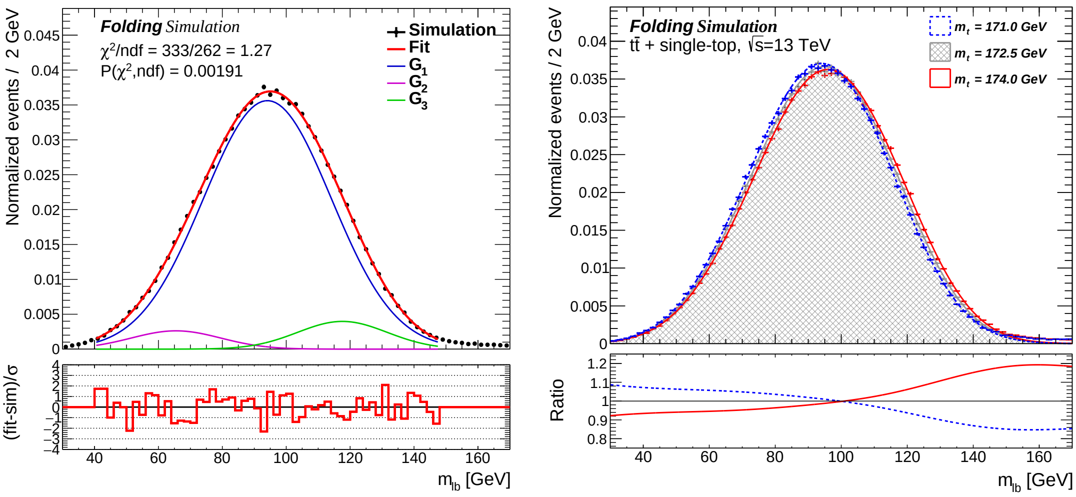

(a) **(b)**

Figure 9.2: (a) The $m_{\ell b}$ distribution and the three Gaussian fit functions are shown for $m_t =$ 172.5 GeV. The difference between the fit function and the simulated sample is given below in units of standard deviation. (b) The template histograms and the fit functions are shown for $m_t = 171$ GeV (blue), $m_t = 172.5$ GeV (gray) and $m_t = 174$ GeV (red). The ratio with respect to the central top-quark mass is shown in the lower plot.

where $\mathcal{G}$ is the sum of the three Gaussian functions derived from the MC generated templates. Pseudo-experiments are drawn, and the difference between the MC input top-quark mass and the mean of the output top-quark mass determined by the fit to pseudo-data is plotted.[2] Because of the limited number of events available in the MC samples, a correction factor for oversampling is applied [260]. A closure test is realized by fitting the template fit function derived from the $t\bar{t}$+single-top sample to pseudo-data drawn from the same sample in 1000 pseudo-experiments. The result is displayed in Fig. 9.3. The offsets between the extracted top-quark mass and the input MC mass are given for each mass point. The average result is an offset of $\Delta m_t = (-0.01 \pm 0.02)$ GeV compatible with zero.

For the final result, theoretical and experimental systematic uncertainties are considered. To estimate the impact of theoretical systematic uncertainties on the top-quark mass, 100 pseudo-experiments are drawn from the MC-varied samples. Again, the calibration function generated from the nominal $t\bar{t}$+single-top sample is fitted to the varied pseudo-data. Experimental uncertainties are estimated from the central sample with a similar procedure, where event weights are applied according to parameter variations of the reconstruction algorithm. For one-sided variations, the difference between the

[2] Pseudo-experiments are especially useful for determining statistical uncertainties and correlations on the systematic variations [5, 259] and to test the validity of this method.

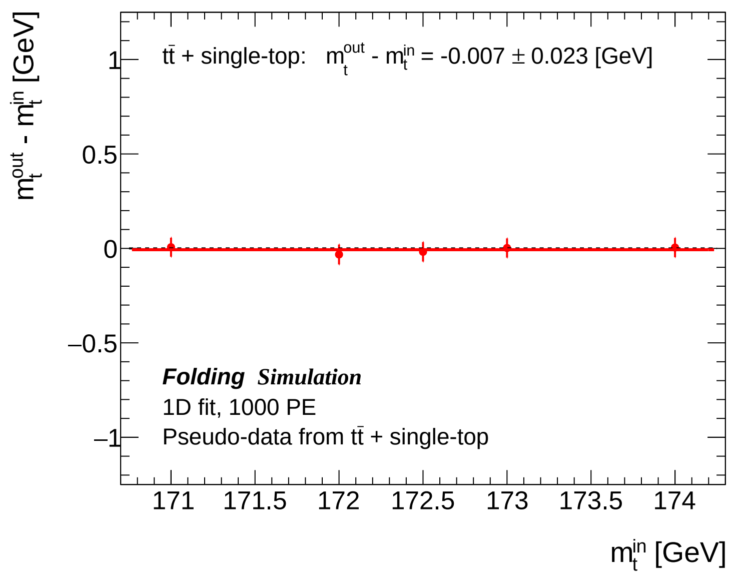

Figure 9.3: The fit function determined from the $t\bar{t}$+single-top predictions is used in an unbinned likelihood fit to pseudo-data drawn from the same samples in 1000 pseudo-experiments. The average difference between the MC input top-quark mass and the value extracted from the fit is plotted. The offset is consistent with zero, indicating the absence of bias in the fit procedure.

top-quark mass obtained from the nominal and the varied sample is taken as systematic uncertainty. For two-sided variations, the systematic uncertainty is set to half the difference between up- and downwards variations. The different systematic components are discussed next.

Systematic uncertainties for $t\bar{t}$ modeling

- **MC Signal Generator**

  The signal MC generator uncertainty is estimated by comparing a MG5_aMC@NLO v2.6.0 [261] $t\bar{t}$ event sample parton-showered with Pythia8.230 using the A14 tune to the central Powheg+Pythia8 sample. The sample uses the same PDF sets as the nominal PP8 generation.

- **Parton-shower and hadronization**

  The parton-shower and hadronization uncertainties are derived by a 2-point variation of Powheg interfaced to Herwig7 and Pythia8, respectively.

- **ISR/FSR**

  Initial-state QCD radiation uncertainties are estimated by comparing the nominal PP8 sample to two variation samples: for the upwards variation, the factorization and renormalization scales μ_R/μ_F are multiplied by a factor of 0.5, the POWHEG parameter `hdamp` is set to $3\cdot m_t$ and the `Var3c up` variation of the A14 tune is used. For the downwards variation, μ_R and μ_F are varied by a factor of 2, `hdamp` $= 1.5\cdot m_t$ is left to its nominal value, and the `Var3c down` variation of A14 is used. Final-state radiation uncertainties are determined by varying μ_R by factors of 0.5 and 2 in the running of the strong coupling α_S^{FSR} in the parton-shower splitting kernels.

Experimental uncertainties

- **(b)-JES**

  For jet reconstruction, the experimental jet energy scale (JES) uncertainties are estimated by varying jet energies within ranges derived from the comparison of MC simulation and in-situ jet calibration [244]. The JES uncertainties include 27 separate components (stemming from Z+jet, γ+jet, pile-up, single-particle response, and others). To take into account the remaining discrepancy between b-jets and light jets after the JES is applied, an uncorrelated uncertainty component is assigned additionally to the relative b-to-light-jet energy scale.

- **JER**

  The uncertainty on the jet energy resolution is derived by smearing the energy of the jets to match the resolution of an in-situ measurement in dijet events to MC simulation [244, 262]. The uncertainties are given as a function of p_T and η and contain 8 separate components.

- ***b*-tagging**

  A systematic uncertainty is assigned to the b-tagging efficiency working point: p_T-dependent b-tagging scale factors are derived from measurements of dileptonic $t\bar{t}$ events [263] and applied to the MC samples per jet. The scale factors are varied within $\pm 1\sigma$ and the template fit is repeated. Altogether, 20 different components (from b-jets, c-jets, light jets and two extrapolations) contribute to the b-tagging uncertainty.

The results of the fit to MC-varied pseudo-data are shown in Table 9.1. Note that for the present work, only the dominant systematic uncertainties are estimated. Considering the corresponding ATLAS 8 TeV analysis in the dilepton channel [180], other systematic uncertainties (underlying event, color reconnection, lepton scale factors, ...) have been found to be negligible.

It is noted that the matrix-element MC generator is currently the dominating source of systematic uncertainty, with $\Delta m_t = 1.28$ GeV. Yet, the signal MC generator uncertainty estimated from the comparison to MG5_aMC@NLO should not be taken at face value: the generator suffers from tuning issues in the matching to PYTHIA8 [179]. The total uncertainty is thus expected to be reduced in the future once the generator tune is improved.

Systematic uncertainty	$\lvert\Delta m_t\rvert$
Theory	
Signal MC Generator	1.28 GeV
Parton-shower and hadronization	0.71 GeV
ISR/FSR	0.26 GeV
Experiment	
JES (light jets)	0.72 GeV
b-JES	0.43 GeV
Jet energy resolution	0.45 GeV
b-tagging	0.13 GeV
Total	**1.77 GeV**

Table 9.1: A partial list of systematic uncertainties for the $t\bar{t}$+single-top signal is given for the top-quark mass extraction. Theoretical uncertainties are estimated by fitting the calibration function generated from the nominal sample to MC-varied pseudo-data. For experimental uncertainties, weights derived from the experimental calibration and reconstruction resolution are applied to the simulated events (see text).

The same comment applies to the parton-shower and hadronization uncertainty. The experimental systematics are dominated by the JES, b-JES and JER uncertainties. In the ATLAS top-quark mass analysis at 8 TeV, the main experimental uncertainties are the JES and b-JES uncertainties, with $\Delta m_t(\text{JES}) = 0.54$ GeV and $\Delta m_t(b\text{-JES}) = 0.30$ GeV. There, the JER uncertainty is equal to $\Delta m_t(\text{JER}) = 0.09$ GeV. The total systematic uncertainty in the 8 TeV analysis amounts to 0.74 GeV, which is compared to the current total systematic uncertainty of 1.75 GeV on the top-quark mass. This discrepancy reflects the fact that the analysis presented here is not yet at the level of precision of the 8 TeV result. Note that a cut on the transverse momentum $p_T^{\ell b}$ of the lepton-b-jet system is applied at 8 TeV, whose value is optimized to minimize the total uncertainty on the top-quark mass [264].

9.2 Migration matrices and efficiencies from the nominal $t\bar{t}$ (PP8) sample

As stated in Section 8.2, the $W^+W^-b\bar{b}$ predictions are to be folded from particle to detector level using the $t\bar{t}$ migration matrices. The migration matrices and detector efficiencies are reconstructed for the $m_{\ell b}$ distribution and two other observables. Histograms are pictured at particle and detector level for the $t\bar{t}$ sample at $m_t = 172.5$ GeV. In Fig. 9.4a, the distribution of the angular separation between the two leptons $\Delta R_{\ell\ell}$ is shown. The total number of events corresponds to the full MC sample. The migration matrix $\mathbf{A}_{ij}$ is pictured in Fig. 9.4b. The migration matrix rows are normalized to unity. They are shown here within a restricted range for better visualization. For distributions relying on well-reconstructed objects, like $\Delta R_{\ell\ell}$, the migration matrix diagonal elements are very close to unity. The efficiency ϵ^{eff} and inverse fake rate f^{acc} are displayed in Fig. 9.4c and Fig. 9.4d, respectively. The overall efficiency is low with an average of $\sim$ 26% due to the reconstruction trigger cuts at detector level, which do not exist at particle level. This was checked in cutflows for a subset of MC events.

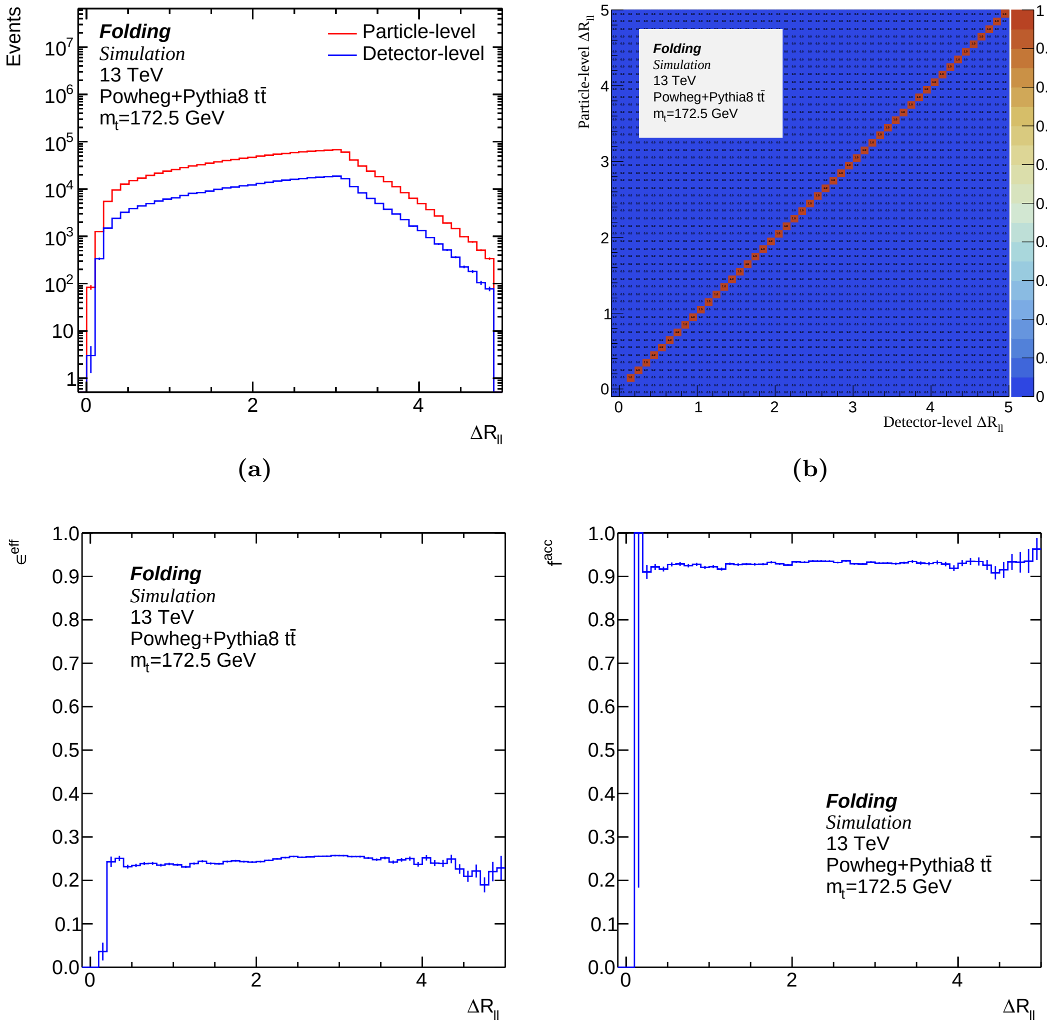

(a) (b) (c) (d)

Figure 9.4: The angular separation between both leptons $\Delta R_{\ell\ell}$ for the PP8 $t\bar{t}$ sample at $m_t = 172.5\,\mathrm{GeV}$ with (a) differential distributions at particle and detector level, (b) migration matrix $\mathbf{A}_{ij}$, (c) efficiency ϵ^{eff} and (d) inverse fake rate f^{acc} as defined in Eq. (8.3).

Jets are in general more difficult to reconstruct than charged leptons. Fig. 9.5 gives histograms, migration matrices and detector efficiencies for the number of jets n_{jets}. Some migration to the next bins (and next-to-next bins for higher jet multiplicities) can be observed. Bins with $n_{\text{jets}} > 8$ have large statistical uncertainties. While for $\Delta R_{\ell\ell}$ both the efficiency and the fake rate are almost constant (see Fig. 9.4), for n_{jets} some bin dependence of the fake rate is observed, as displayed in Fig. 9.5d.

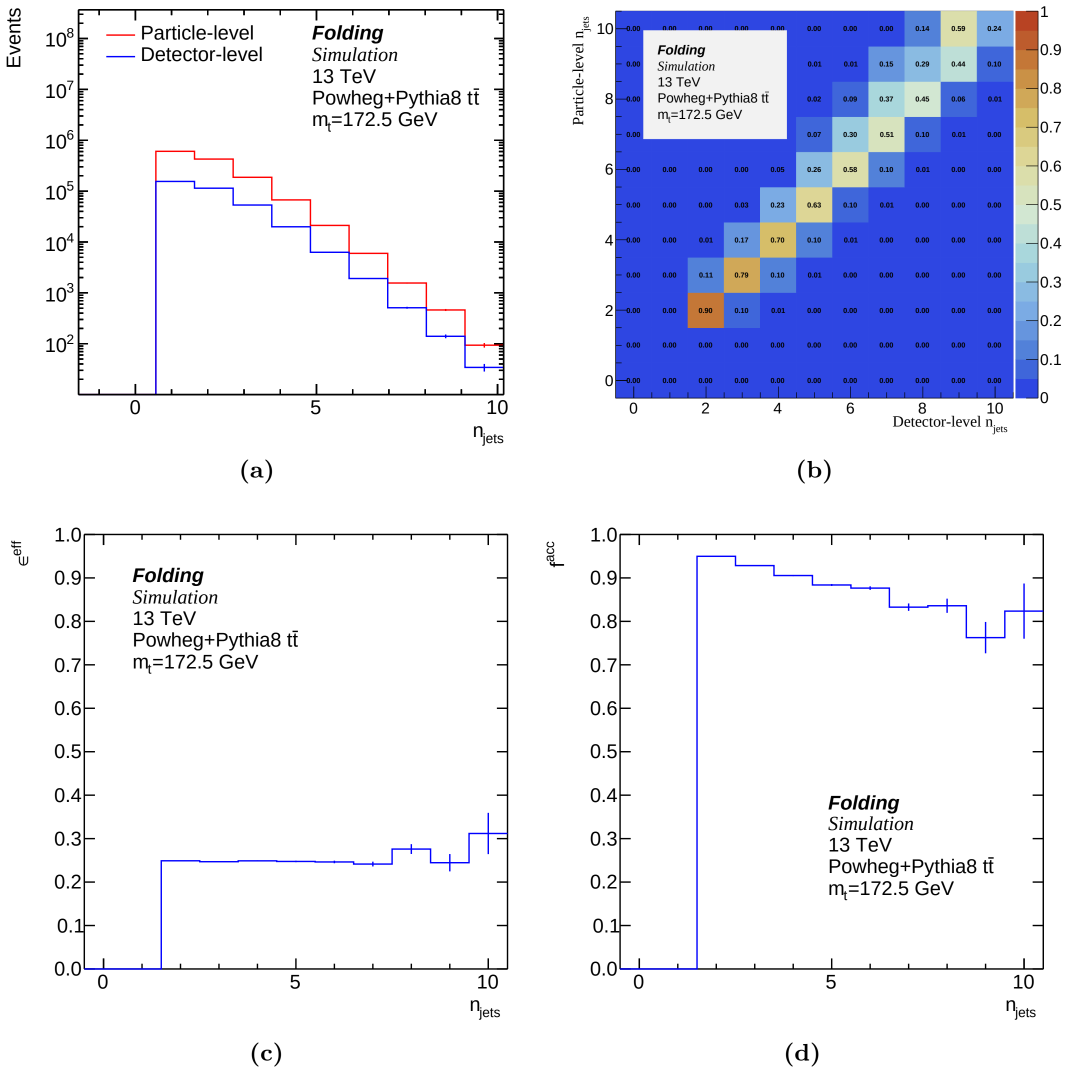

Figure 9.5: The number of jets n_{jets} for the PP8 $t\bar{t}$ sample at $m_t = 172.5\,\text{GeV}$, with (a) differential distributions at particle and detector level, (b) migration matrix $\mathbf{A}_{ij}$, (c) efficiency ϵ^{eff} and (d) inverse fake rate f^{acc} as defined in Eq. (8.3).

For the $m_{\ell b}$ distribution, the same quantities are shown in Fig. 9.6. The migration matrix has larger off-diagonal elements: this is because the b-jets are difficult to reconstruct, and the pairing of the lepton and b-jet systems at the particle and detector levels might not be identical. The efficiency is highest below the kinematic edge, which corresponds to well-separated, on-shell top-quark pairs.

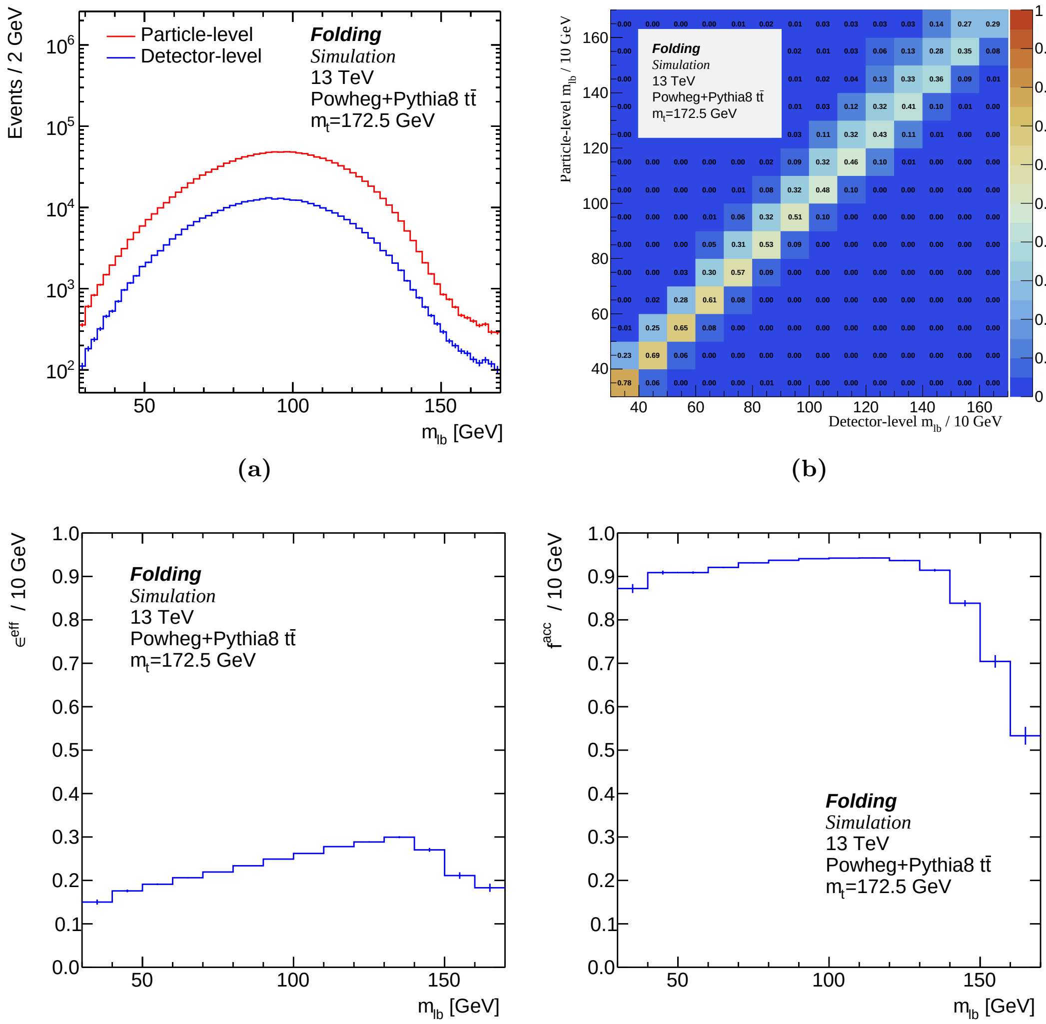

(a) (b) (c) (d)

Figure 9.6: The lepton-b-jet invariant mass $m_{\ell b}$ for the PP8 $t\bar{t}$ sample at $m_t = 172.5$ GeV with (a) differential distributions at particle and detector level, (b) migration matrix $\mathbf{A}_{ij}$, (c) efficiency ϵ^{eff} and (d) inverse fake rate f^{acc} as defined in Eq. (8.3). Here, the migration matrices were rebinned for better visibility.

9.3 Statistical and systematic cross-checks

Several cross-checks are performed in order to test statistical and systematic biases that could appear in the folding procedure. To ensure that statistical uncertainties are propagated correctly, only half of the sample for the $t\bar{t}$ prediction at $m_t = 172.5$ GeV is used to derive migration matrices and efficiencies. The folding matrices from this reduced sample, called symbolically $\frac{1}{2}A_S$, are then applied to the particle-level sample S_P with full statistics. The $m_{\ell b}$ distribution obtained at detector level (folded from the subset sample) is compared to the full simulated distribution at detector level S in Fig. 9.7a. The differences between both are covered by the statistical uncertainties with no significant bias. In Fig. 9.7b, the $m_{\ell b}$ distribution is compared at detector level for the GEANT4 (FullSim) and the ATLFAST (AFII) algorithms. Although some structure in the tail of the distribution seems to indicate a softer spectrum for ATLFAST than for the full simulation, both distributions still agree within statistical uncertainties.

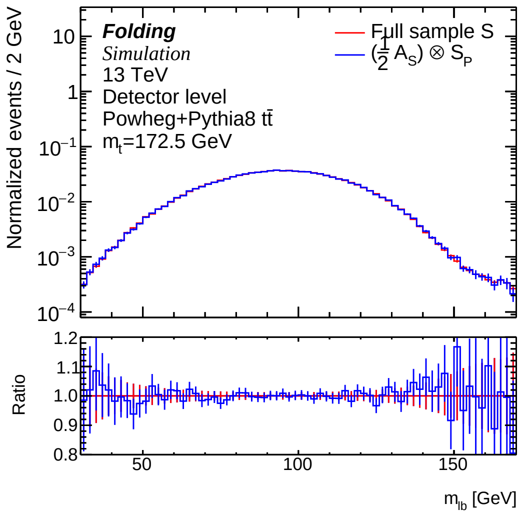

(a)

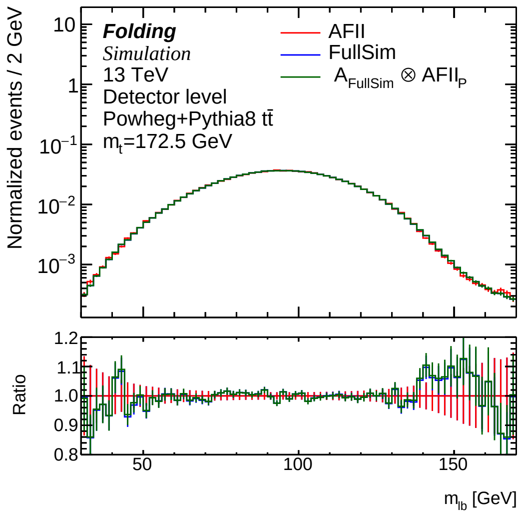

(b)

Figure 9.7: Migration matrices from one sample are used to fold another sample's particle-level $m_{\ell b}$ distribution for statistical and systematic cross-checks. (a) A statistical subset is used to derive migration matrices $\frac{1}{2}A_S$ and fold the full sample S_P. (b) Same for the GEANT4 (SIM) and ATLFAST (AFII) simulated samples.

In the final results, migration matrices are consistently chosen to use the same input top-quark mass as the sample to be folded. Still, it is checked that the input top-quark mass does not introduce any visible systematic bias in the folded distributions: in Fig. 9.8a, the migration matrices from the $m_t = 174$ GeV sample are used to fold the $m_t = 171$ GeV prediction to detector level. The folded and simulated distributions for $m_t = 171$ GeV agree very well. The same should be true of any theoretical MC variation. Conventionally, the h_{damp} parameter in POWHEG, which regulates the amount of hard radiation, is taken as such a variation. The central value is chosen as $h_{\mathrm{damp}} = 1.5\, m_t =: h_1$. The variation sample uses $h_{\mathrm{damp}} = 3\, m_t := h_2$. Folding the varied sample at particle level $h_{2,P}$ with the migration matrices A_{h_1} from the central sample leads to good agreement at detector level, as shown in Fig. 9.8b.

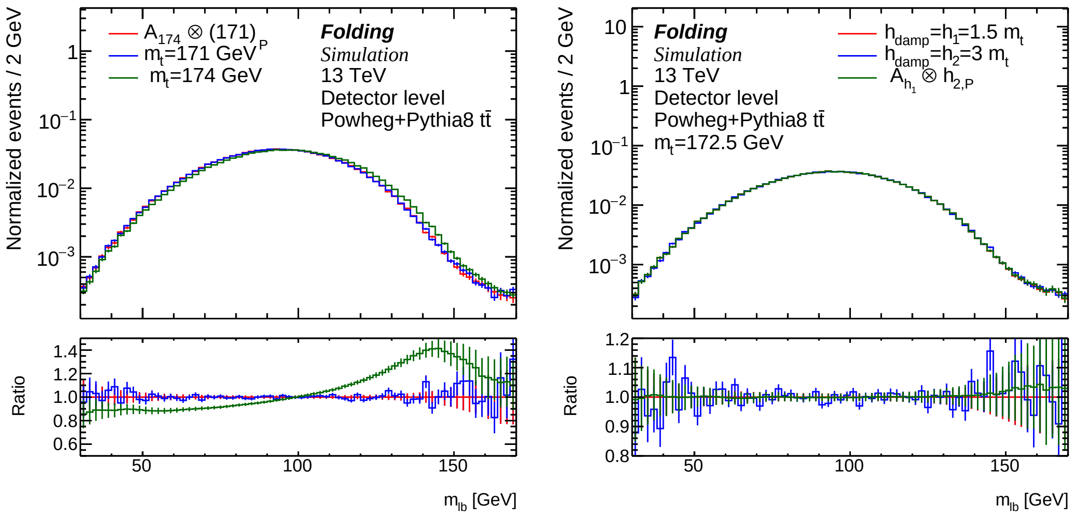

(a) (b)

Figure 9.8: (a) Same as Fig. 9.7, where the $m_t = 174$ GeV sample is used to fold the $m_t = 171$ GeV prediction. (b) Same for the central, respectively varied values of the h_{damp} parameter.

In another study, a comparison is made between the Pythia8 and Herwig7 parton-showers, displayed at particle level in Fig. 9.9a. Usage of different parton-shower algorithms leads to significantly dissimilar spectra. Once detector effects are taken into account, the discrepancy is much less pronounced, although a small slope is still visible, as shown in Fig. 9.9b.

This feature can be traced back to the difference in simulated predictions for both parton-showers. The fact that Pythia8 produces harder radiation than Herwig7 is well-known (see Chapter 11 for the case of Higgs pair production).[3] As can be seen with the example of the transverse momentum of jets and leptons given in Appendix D, the data are not always well-described by the Pythia8 parton-shower.

This mismodeling in the simulated samples propagates to the derived efficiencies. Fig. 9.10a gives the efficiency ϵ^{eff} and inverse fake rate f^{acc} for the $m_{\ell b}$ distribution. Essentially, the efficiency is higher for the simulated Pythia8 sample than for Herwig7. Furthermore, their ratio is not constant: the Pythia8 sample is more efficient for small $m_{\ell b}$-values, a fact that is reflected in Fig. 9.9b. In contrast, the inverse fake rates shown in Fig. 9.10b are identical. The migration matrices of both samples are also consistent within statistical uncertainties. The slope in Fig. 9.9b leads to a bias in the

[3] The effect on the top-quark mass was investigated in the Powheg-BOX-RES framework recently [265].

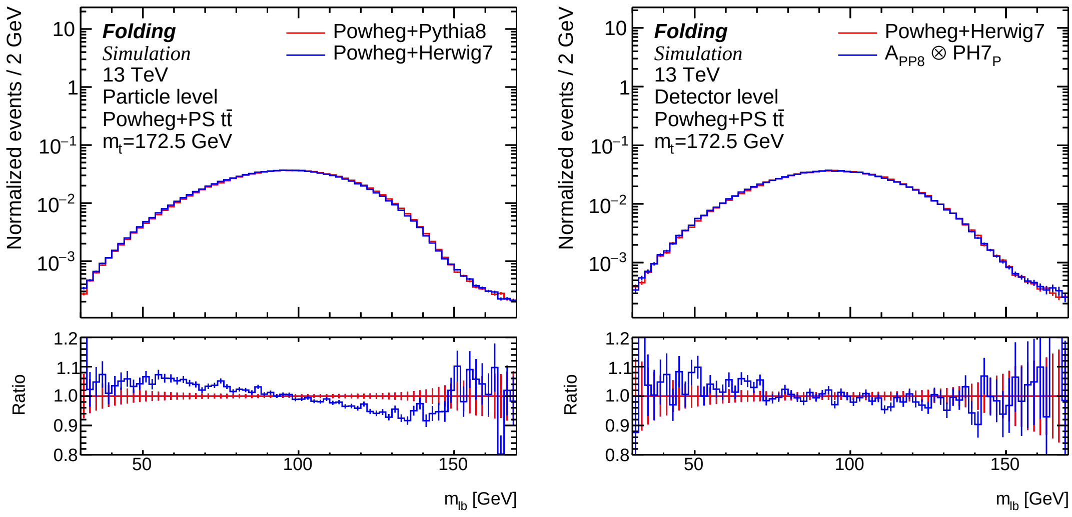

(a) **(b)**

Figure 9.9: (a) The Pythia8 (PP8) and Herwig7 (PH7) parton-showered samples are compared at particle level for a fixed top-quark mass $m_t = 172.5$ GeV. (b) Same as Fig. 9.7 for the PP8 and PH7 samples.

top-quark mass; however, the uncertainty is already taken into account by the parton-shower/hadronization uncertainty. Thus, it is not a folding uncertainty *per se*, and it should not be double-counted.

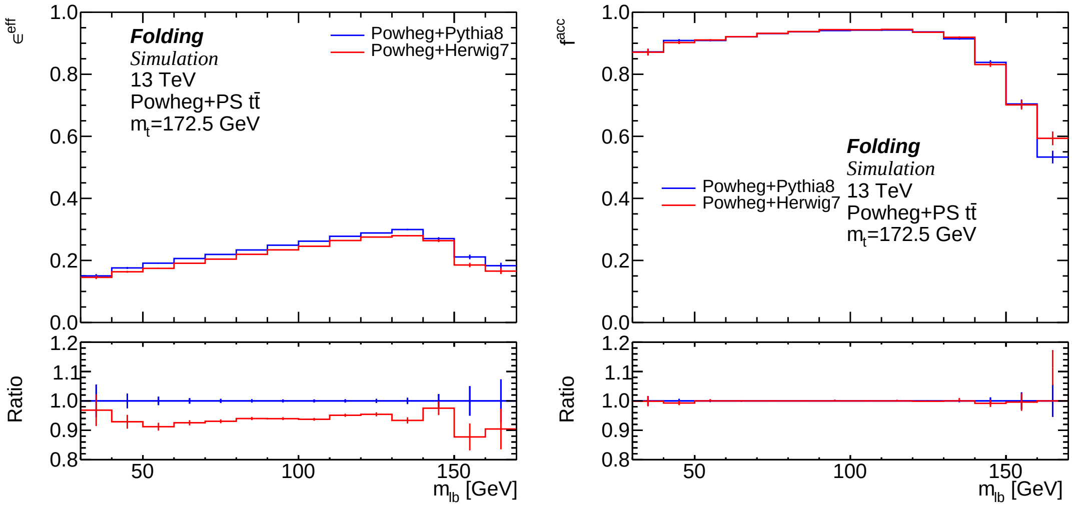

(a) **(b)**

Figure 9.10: (a) The efficiency ϵ^{eff} for PP8 and PH7. (b) Same for the inverse fake rate f^{acc}.

To test if a residual bias exists, the following procedure is performed: the $m_{\ell b}$ distribution from the PYTHIA8 samples at particle level is folded with the migration matrix and fake rate from HERWIG7. The efficiencies, though, are replaced by the ones derived from PYTHIA8. The folded histogram then agrees very well with the fully-simulated PYTHIA8 distribution. The template functions derived from these histograms are used to fit the simulated PYTHIA8 pseudo-data: the offset in the output top-quark mass then vanishes within statistical uncertainties.

9.4 Folded $W^+W^-b\bar{b}$ results and template parametrization

The $W^+W^-b\bar{b}$ prediction from the `bb4l` event generator is folded to detector level using the migration matrices obtained with PP8. Fig. 9.11a displays the particle-level $m_{\ell b}$ distribution for the full $W^+W^-b\bar{b}$ prediction at NLO QCD matched to the PYTHIA8 parton-shower, as a function of the five input top-quark masses. In Fig. 9.11b, the same comparison is made at detector level with the folded predictions. The distributions are smoothed out by the folding procedure. Moreover, the relative statistical uncertainties can decrease in certain bins from particle level to detector level, if the statistical covariance matrix has large off-diagonal elements. These cannot be displayed on the plot. In general, the statistical precision of the $W^+W^-b\bar{b}$ samples is limited: the `bb4l` MC generator is demanding in terms of resources for both the MC integration and the event generation. This might be optimized further by adjusting generation parameters.

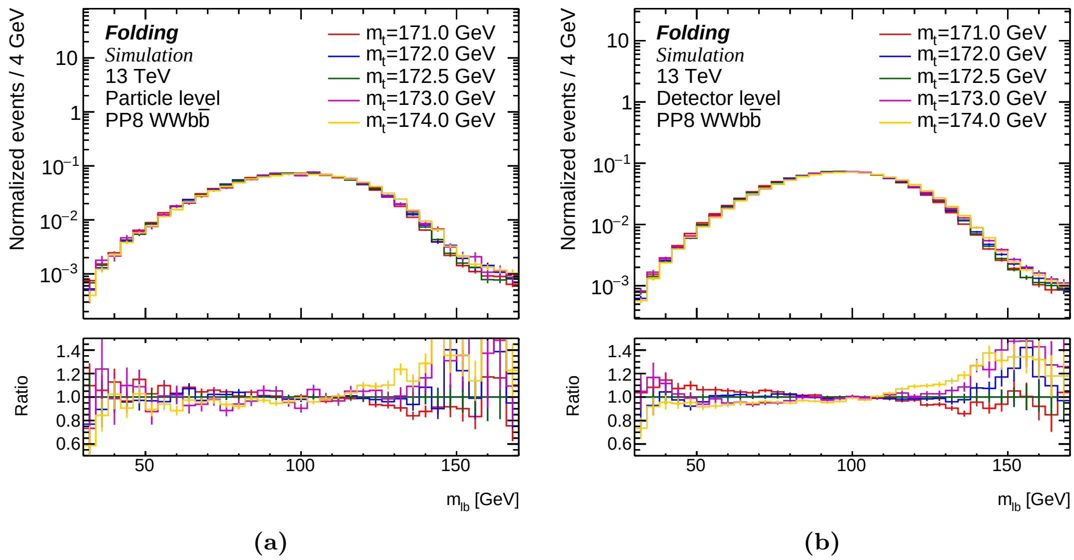

Figure 9.11: The normalized $m_{\ell b}$ distribution for the generated $W^+W^-b\bar{b}$ events for the five different input top-quark masses at (a) particle level and (b) detector level.

The primary goal is to quantify the shift in the extracted top-quark mass generated by using the $t\bar{t}$+single-top, respectively $W^+W^-b\bar{b}$ predictions at NLO QCD. In Fig. 9.12, the normalized $m_{\ell b}$ distribution is shown for the signal ($t\bar{t}$ and single-top in the Wt channel) and the folded $W^+W^-b\bar{b}$ predictions at detector level for an input top-quark mass $m_t = 172.5$ GeV. Note that the single-top contribution starts populating the region above the kinematic edge $m_{\ell b}^{\text{edge}} \sim 153$ GeV. The same samples are then compared to pseudo-data drawn in a single pseudo-experiment from the $t\bar{t}$+single-top sample for comparison. The $m_{\ell b}$ distribution from the corresponding $W^+W^-b\bar{b}$ sample introduces a bias (in green), which shall be quantified in the top-quark mass extraction. The $m_{\ell b}$ distribution from the parton-showered $W^+W^-b\bar{b}$ sample is shifted towards higher values. Thus, the extracted top-quark mass will be lower for $W^+W^-b\bar{b}$ than for $t\bar{t}$+single-top.

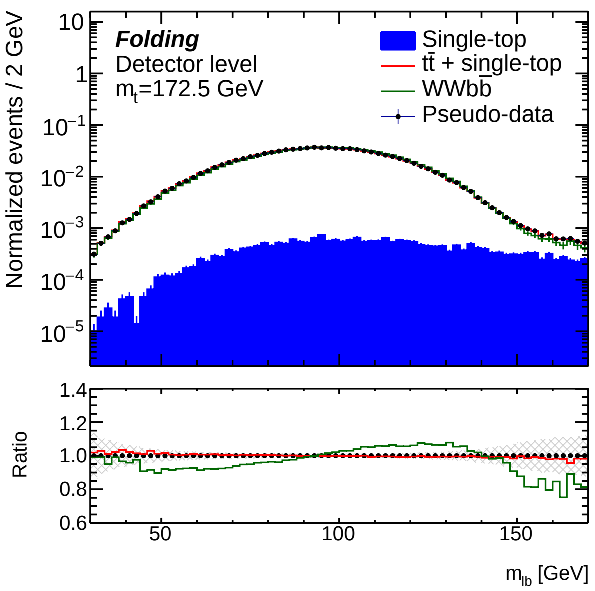

Figure 9.12: The normalized $m_{\ell b}$ distribution for $m_t = 172.5$ GeV is shown for the $t\bar{t}$+single-top sample, as well as for the $W^+W^-b\bar{b}$ prediction folded to detector level. Pseudo-data drawn from the central $t\bar{t}$+single-top sample in a single pseudo-experiment are given for a qualitative comparison. The lower plot shows the ratio to pseudo-data (with statistical uncertainties as hatched error bars).

Similarly to Chapter 7, the calibration functions determined from the $W^+W^-b\bar{b}$ predictions are used to fit pseudo-data drawn from the $t\bar{t}$+single-top samples with 1000 pseudo-experiments (PE). The template fit to pseudo-data gives an offset in the extracted top-quark mass, $\Delta m_t = m_t^{\text{out}} - m_t^{\text{in}}$. This offset quantifies the difference between the incomplete $t\bar{t}$+single-top and the full $W^+W^-b\bar{b}$ prediction.

Fig. 9.13 displays the result of the template fit. Again, the use of $t\bar{t}$+single-top fit functions yields an offset close to zero (in red), serving as a cross-check that no bias exists in the fitting procedure. The use of the $W^+W^-b\bar{b}$ calibration functions (in blue) results in an average value $\Delta m_t = -0.33 \pm 0.02$ GeV. The second uncertainty is the statistical uncertainty on the systematic offset Δm_t.

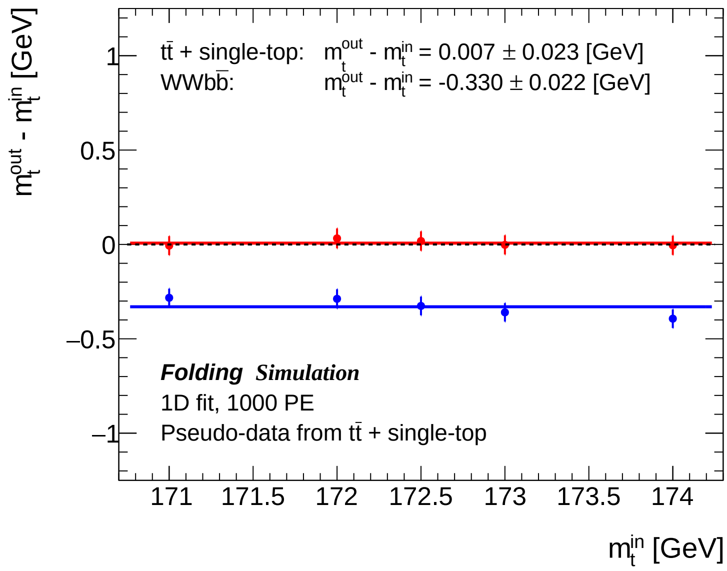

Figure 9.13: A comparison similar to the ones performed in Chapter 7 is presented at detector level. The folded $W^+W^-b\bar{b}$ prediction is used to fit pseudo-data drawn from $t\bar{t}$+single-top samples. This introduces an average offset of $\Delta m_t = -0.330 \pm 0.022$ GeV in the top-quark mass extraction.

The theoretical systematic uncertainties for the $W^+W^-b\bar{b}$ prediction would be estimated in a slightly different way than for $t\bar{t}$+single-top. Most of them require dedicated runs, and were not quantified in this study.[4] Conceptual definitions are proposed next, and some preliminary systematic uncertainties are estimated from general considerations. The experimental uncertainties are identical to the $t\bar{t}$ uncertainties: this was checked by fitting the $W^+W^-b\bar{b}$ calibration function to the $t\bar{t}$ pseudo-data weighted by the different experimental uncertainty components.

Systematic uncertainties for $W^+W^-b\bar{b}$ modeling

Theoretical uncertainties

- **MC Signal Generator**

  The signal MC generator uncertainty cannot be estimated by a 2-point variation of the event generator, since `bb4l` is the only existing full-fledged out-of-the-box generator to produce a $W^+W^-b\bar{b}$ dilepton final-state at NLO QCD, at the moment.[5]

[4] Since the generation of $W^+W^-b\bar{b}$ events is computing-intensive, the mentioned MC variations were not yet performed in this work.

[5] One could use a matrix-element provider (e.g. GoSam) to interface to a suitable MC generator.

For the full prediction with bb4l, conventional well-defined theoretical uncertainties can be estimated by renormalization and factorization scale variations, as an alternative representation of the signal MC generator uncertainty. This requires dedicated samples for a 7-point scale variation and subsequent folding to detector level. If they are assumed to be of smaller magnitude at detector level than at parton level, an upper bound would be of the order $\mathcal{O}(700\,\text{MeV})$, as illustrated e.g. in Fig. 7.12.

- **Parton-shower and hadronization**

  The parton-shower and hadronization uncertainties would be derived by a 2-point variation of Powheg interfaced to Herwig7 and Pythia8. Because of the particularities of the Powheg-BOX-RES generator, parton-shower matching has to be implemented carefully. A class called ShowerVeto has been introduced in the default Herwig7 shower to that effect since v.7.1. Once it is implemented and fully validated in the ATLAS framework, the parton-shower and hadronization uncertainties could be estimated in the usual way. Studies of the different matching prescriptions and vetoing possibilities in bb4l [265] point to a difference in the position of the W-b-jet invariant mass $m_{Wb_{\text{jet}}}$ of $\mathcal{O}(1\,\text{GeV})$ between both showers. This uncertainty is expected to decrease at detector level. Moreover, the $m_{\ell b}$ distribution is less sensitive to the input top-quark mass than $m_{Wb_{\text{jet}}}$ (which corresponds to the fully-reconstructed top-quark mass). In the following, a conservative uncertainty of 1 GeV for the top-quark mass is taken as a first guess of the combination of parton-shower and hadronization systematics.

- **ISR/FSR** The same prescription given for the estimate of ISR/FSR modeling uncertainties in $t\bar{t}$ can be implemented for the $W^+W^-b\bar{b}$ prediction (variation of the Pythia8 tune, renormalization and factorization scales and hdamp parameter). These uncertainties should not be overly sensitive to the non-doubly resonant contributions in the matrix-element. Thus, they are expected to be of the same order as for the $t\bar{t}$ prediction.

The preliminary (partially conjectured) list of systematic uncertainties for the $W^+W^-b\bar{b}$ prediction at NLO QCD can be found in Table 9.2.

9.5 Numerical results for the top-quark mass in ATLAS data

The calibration functions from the $t\bar{t}$+single-top and $W^+W^-b\bar{b}$ predictions are now fitted to ATLAS pp collision data at a center-of-mass energy of $\sqrt{s} = 13$ TeV. The data were recorded in 2015 and 2016 for a total integrated luminosity of 36.2 fb^{-1}. Control plots can be found in Appendix D for a few observables. It is stressed again that these results are preliminary. No background is simulated, but the fiducial contribution is expected to be of $\mathcal{O}(1\%)$. The full ATLAS analysis, including the latest Run II data recorded in

Est. systematic uncertainty	$\lvert\Delta m_t\rvert$
Theory	
Signal MC Generator	≤ 0.70 GeV
Parton-shower and hadronization	≤ 1 GeV
ISR/FSR	0.26 GeV
Experiment	
JES (light jets)	0.72 GeV
b-JES	0.43 GeV
Jet energy resolution	0.45 GeV
b-tagging	0.13 GeV
Total	**1.57 GeV**

Table 9.2: A partial list of estimated systematic uncertainties is given for the top-quark mass extraction, using the $W^+W^-b\bar{b}$ prediction at NLO QCD (see the text for details).

2017 and 2018, is expected to yield improved results and lead to a significantly lower uncertainty.

The template functions from the $t\bar{t}$+single-top and the full $W^+W^-b\bar{b}$ predictions are used in a direct unbinned likelihood fit to data. In Eq. (9.2), the weights are equal to one. The data and the fit functions are shown in Fig. 9.14a. The fit describes data best for an input value of $m_t = 172.90$ GeV for the $t\bar{t}$+single-top, respectively $m_t = 172.54$ GeV for the $W^+W^-b\bar{b}$ fit functions. Fig. 9.14b displays the log-likelihood as a function of the top-quark mass m_t.

The central offset introduced by the $W^+W^-b\bar{b}$ fit function is very close to the value $\Delta m_t = -0.330$ GeV found when fitted to the $t\bar{t}$+single-top pseudo-data. A summary plot of the results is also given in Fig. 9.15, with the published ATLAS 8 TeV result in the dilepton channel for comparison. Note that the statistical uncertainties from this preliminary analysis are greatly reduced in comparison to the 8 TeV result, thanks to the higher cross-section and integrated luminosity at $\sqrt{s} = 13$ TeV. The values are all in good agreement. Altogether, the difference between the NWA and the full $W^+W^-b\bar{b}$ theoretical predictions is not as large as it was at parton level in Chapter 7. It is distinctly covered by the systematic uncertainties evaluated per the ATLAS recommendations. Once the systematic uncertainties are under control (in particular from the MC signal generator) and the extensive 147 fb^{-1} of Run II data are analyzed, the total top-quark mass uncertainty can be expected to shrink further.

Additional studies are still warranted. Since the validation of the analysis framework is still in progress, a detailed account of the systematic uncertainties is beyond the scope of this work. Part of the systematics for the central $t\bar{t}$+single-top prediction will decrease once generators are better tuned. Moreover, as already mentioned, the theoretical uncertainties for the $W^+W^-b\bar{b}$ prediction were only roughly estimated in this study. A careful definition and computation of the systematics might reveal somewhat different values than those presented here. Once a full set of systematic variations is

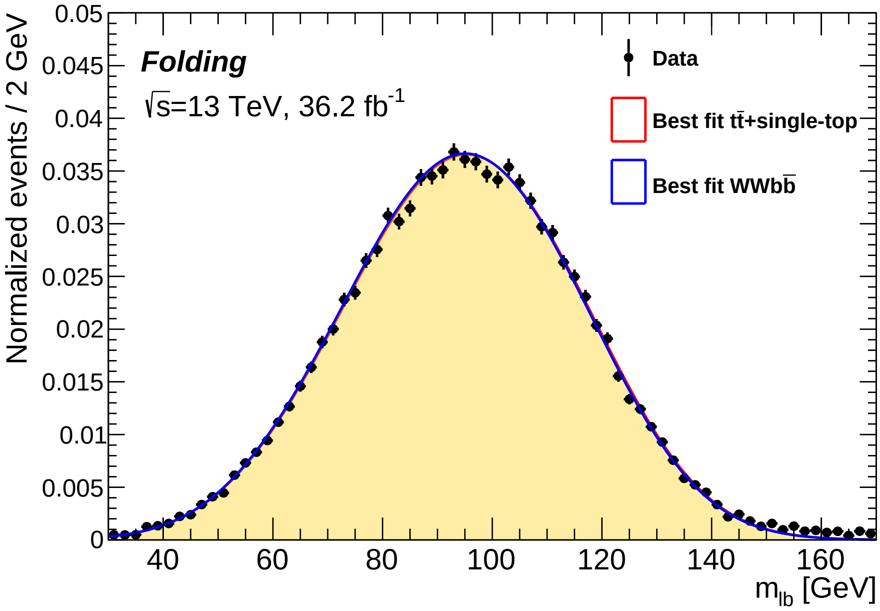

(a)

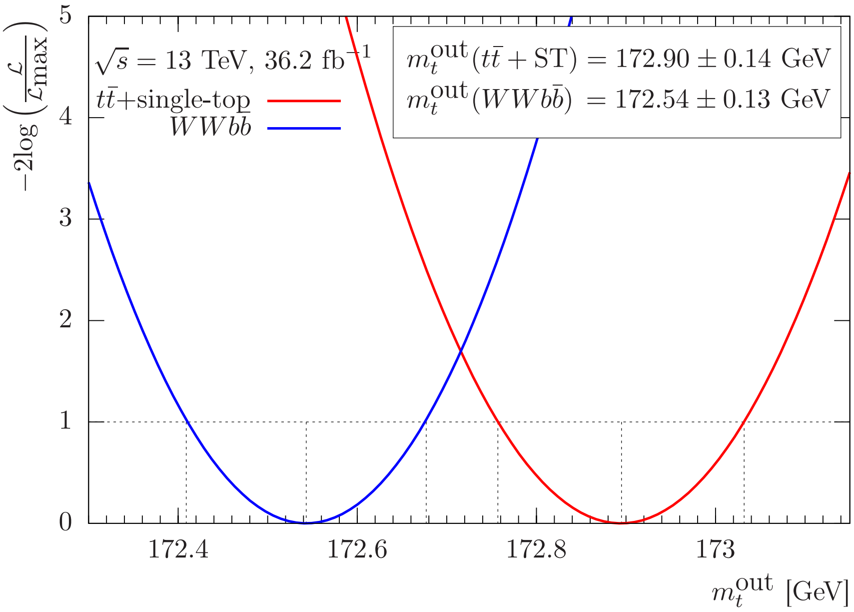

(b)

Figure 9.14: (a) The best fit generated by the $t\bar{t}$+single-top and $W^+W^-b\bar{b}$ predictions is compared to data recorded by ATLAS, for an integrated luminosity of 36.2 fb^{-1}. (b) The log-likelihood for the $t\bar{t}$+single-top (ST) and $W^+W^-b\bar{b}$ fit functions, with 1σ statistical errors.

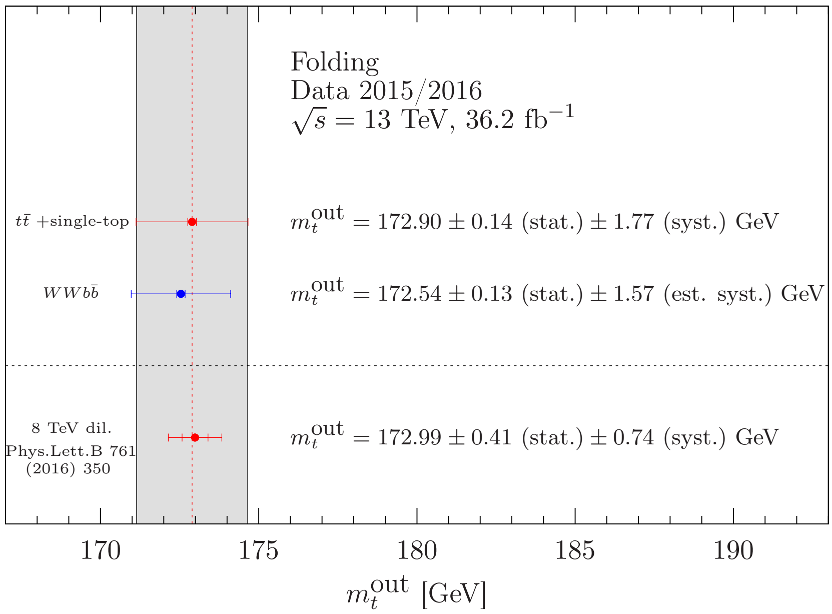

Figure 9.15: The outcome of the extraction of the top-quark mass is summarized: results from the fit of the template functions generated from the $t\bar{t}$+single-top and $W^+W^-b\bar{b}$ folded samples are indicated by red, respectively blue points. The systematic uncertainties were evaluated only partly (see text). For comparison, the ATLAS 8 TeV result in the dilepton channel is given below.

produced, it will be interesting to place the $t\bar{t}$+single-top and $W^+W^-b\bar{b}$ predictions on a same footing, and compare their impact on the extracted top-quark mass in the full analysis (with the inclusion of background processes and the evaluation of all systematic uncertainties).

Although the central value derived from the $W^+W^-b\bar{b}$ prediction does not differ much from the currently used $t\bar{t}$+single-top signal, two points are worth mentioning. First, there is an uncertainty associated to the ill-defined diagram removal/subtraction of interference terms between $t\bar{t}$ and single-top Wt contributions. When using $W^+W^-b\bar{b}$ predictions, this uncertainty is not present. As a matter of fact, the definition of the top-quark mass itself (at least at the matrix-element level) is perfectly consistent, in a perturbative sense, for the full prediction only. Secondly, the fit range used in the analysis ends before the tail of the $m_{\ell b}$ distribution. Although this choice might improve systematic uncertainties, some sensitivity to the input top-quark mass is lost. It might be interesting to optimize the fit range for the $W^+W^-b\bar{b}$ prediction, which offers a more robust description of the region above the kinematic edge for the $m_{\ell b}$ distribution. The inclusion of the full $W^+W^-b\bar{b}$ process in the ATLAS top-quark mass analysis constitutes an important step towards higher-precision measurements. Now that the necessary theoretical tools are available, efforts for implementing and validating them in ATLAS will prove useful in the race for more accurate top-quark mass measurements.

Part III

Top-Quark Mass Effects in Higgs Pair Production

10 Top-quark mass dependence in Higgs pair production at NLO

The top-quark mass has substantial effects in the Higgs sector. After the discovery of the Higgs boson by both ATLAS [266] and CMS [267] experiments in 2012, which was the crowning completion of one of LHC's foremost goals, the experimental community set to measure its properties to further test if it was compatible with the SM-predicted Higgs boson. As of today, some of the Higgs boson properties are very well-measured (as for the example of its mass, spin, or couplings to heavier fermions and gauge bosons). Still, because of lower branching ratios and irreducible backgrounds, the measurement of the Higgs boson couplings to light fermions, as well as the Higgs self-coupling, is still accompanied by large uncertainties of the order of $\mathcal{O}(100\%)$ in the case of the trilinear self-coupling. This leaves room for New Physics to appear. The latest ATLAS constraint on the Higgs boson self-coupling, in ratio to its predicted value from the SM $c_{hhh} = \lambda/\lambda_{\text{SM}}$, is $-5.0 \leq c_{hhh} \leq 12.1$ [16] at 95% confidence level (CL), from a combination of three searches for the hh final-states $b\bar{b}b\bar{b}$, $b\bar{b}\tau^+\tau^-$ and $b\bar{b}\gamma\gamma$. These limits assume the other Higgs couplings to be SM-like. In the future, with the accumulation of data at high-luminosity (HL)-LHC, the experimental bounds are expected to improve. The measurement of differential distributions (with a small number of total events) is even conceivable. In the rest of this chapter, the theoretical standpoint of hh production is reviewed, and the way in which New Physics can affect this process is presented in the framework of a non-linear EFT.

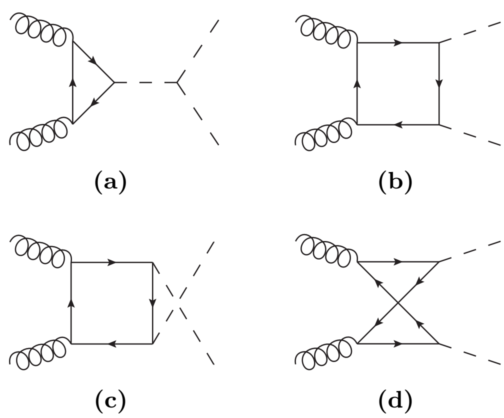

Figure 10.1: (a-d) LO Feynman diagrams for hh production by gluon fusion.

10.1 Theoretical descriptions of Higgs pair production

At the LHC, Higgs bosons (and in particular Higgs boson pairs, which are considered in the next chapters) are produced mainly via a top-quark loop. Fig. 10.1 displays the LO Feynman diagrams for di-Higgs production in gluon fusion: diagrams that contain the Higgs self-coupling λ are called *triangle*-like (as in Fig. 10.1a), and diagrams that do not *box*-like (as in Figs 10.1b-10.1d).[1] Because $gg \to hh$ production is loop-induced, NLO corrections start at two-loop order already and pose a challenge to compute. The matrix-element for $g(p_1, \mu, a) + g(p_2, \nu, b) \to h(p_3) + h(p_4)$ production decomposes into two form factors (with p_i the 4-momenta, Greek letters for the Lorentz indices and Roman letters for the color indices):

$$\mathcal{M}_{ab}^{\mu\nu} = \frac{\alpha_s}{8\pi v^2}\delta_{ab}\epsilon_\mu\epsilon_\nu \left(F_1(\hat{s}, \hat{t}, m_h^2, m_t^2, d)T_1^{\mu\nu} + F_2(\hat{s}, \hat{t}, m_h^2, m_t^2, d)T_2^{\mu\nu}\right), \tag{10.1}$$

where the Lorentz structure is contained in the tensors T_1, T_2 and the functions F_1, F_2 depend on four physical scales altogether (two kinematic invariants and both particle mass scales, as well as on the analytically-continued dimension d). Moreover, the first form factor can be further split into a contribution stemming only from triangle-like diagrams, respectively only box-like diagrams:

$$F_1 = F_\triangle + F_\Box , \tag{10.2}$$

and the box diagrams contribute to both $F_\Box$ and F_2. Historically, the LO one-loop total cross-section has been known analytically for some time [268], and the triangular form factor given in Eq. (10.2), for $\tau = 4m_t^2/\hat{s}$, takes the form

$$F_\triangle = \frac{6m_h^2\lambda\hat{s}}{\hat{s} - m_h^2}\tau\left(1 + (1-\tau)f(\tau)\right) , \tag{10.3}$$

$$f(\tau) := \begin{cases} \arcsin^2(\frac{1}{\sqrt{\tau}}) & \tau \geq 1 \\ -\frac{1}{4}\left(\log\left(\frac{1+\sqrt{1-\tau}}{1-\sqrt{1-\tau}}\right) - i\pi\right)^2 & \tau < 1 . \end{cases}$$

The triangle diagrams can be reduced to single Higgs production and subsequent attachment of the triple Higgs vertex, where all the NLO integrals (massive two-loop up to three-point) have been computed with the full top-mass dependence [269–271]. The two-loop massive four-point integrals to $gg \to hh$ are known analytically only partly [272–274]. Some computations exist with expansions in given kinematic limits (large top-quark mass [272], top-quark threshold [275], small Higgs transverse momentum [276], and high-energy expansion [277, 278]). In the following, only the heavy-top limit $m_t \to \infty$ is considered, without any expansion in $1/m_t^{2n}$, as well as several approximations that include part of the full-theory result at NLO QCD.

[1] At two-loop level, some diagrams do not contain the coupling λ but have triangular topologies, see e.g. the last diagram in Fig. 10.4.

10.1.1 Approximations in the heavy-top limit ($m_t \to \infty$)

To circumvent the direct computation of the difficult NLO QCD corrections to $gg \to hh$, one neat approach that was applied successfully in Higgs production (as well as in a whole collection of other processes) is to collapse one top-quark loop to an effective coupling between gluons and Higgs bosons within a so-called Effective Field Theory (EFT). This constitutes the heavy-top limit (HTL). EFTs are usually employed to describe physics entering at a higher scale than the typical scales of the process at hand. In an agnostic approach, one assumes nothing about new particles and instead computes effective couplings between known particles, that are only indirectly affected by more massive particles. Their exact degrees of freedom are thus integrated out of the calculation. This was for example the basic framework of the Fermi theory before W and Z bosons were discovered, where one assumes a 4-particle interaction vertex between fermions coupling with strength G_F. In the case of di-Higgs production, the top-quark degrees of freedom are integrated out and an effective coupling between gluons and Higgs bosons is introduced. There exist different consistent formulations of a theory with effective coupling vertices between gluons and Higgs bosons: usually, one introduces higher-dimension contact operators into the SM Lagrangian, with an EFT expansion in the New Physics scale $1/\Lambda$.[2] Another EFT formulation will be introduced in Section 10.2.

In the next sections, comparisons are shown between predictions for the full theory at QCD NLO and various approximations based on the heavy-top limit for variations of the Higgs couplings.[3] In order of increasing accuracy, these are:

- **Pure HTL**: all top-quark loops are shrunk to an effective vertex between gluons and Higgs bosons. At LO, the form factors given in Eqs. (10.1), (10.3), for $\tau \to \infty$, reduce to

$$F_\triangle \to \frac{3m_h^2\lambda}{\hat{s}-m_h^2}\left(\frac{4}{3}\hat{s}\right) , \tag{10.5}$$

$$F_\Box \to -\frac{4}{3}\hat{s} , \tag{10.6}$$

$$F_2 \to 0 . \tag{10.7}$$

  At NLO, they are at most given by one-loop diagrams.

- **Born-improved HTL**: the virtual and real contributions are calculated within the HTL, but reweighted on an event-by-event basis with the ratio of the full-theory Born to the HTL Born contribution,

$$\mathrm{d}\sigma_{V,R}^{\text{B.-i.}} = \mathrm{d}\sigma_{V,R}^{\text{HTL}} \frac{\mathrm{d}\sigma_B^{\text{FT}}}{\mathrm{d}\sigma_B^{\text{HTL}}} . \tag{10.8}$$

[2] Mostly, nowadays, analyses consider only dimension-6 operators, because the only dimension-5 operator violates lepton number conservation.

[3] In the SM case, there are already important differences between the considered approximations [279].

- **$\mathbf{FT_{approx}}$** : the same prescription as given in Eq. (10.8) is applied for the virtual contribution, but the real-emission matrix-element is computed in the full theory (these are at most one-loop diagrams).

- **Full theory**: the real and two-loop virtual contributions are computed with full m_t-dependence.

10.1.2 Two-loop contribution in the SM

The first full computation of NLO QCD corrections to $gg \to hh$ production in the SM was presented in Ref. [279]. All BSM results shown in Sections 10.3 and 11.2 are based on two-loop amplitudes calculated numerically for the SM.

As a brief description of the calculation, the two-loop contribution to the SM amplitude was generated by an extended version of GoSam called GoSam-2loop. The reduction to master integrals was operated with Reduze 2 [280] as far as possible, and the integral evaluation performed with the help of sector decomposition in SecDec 3 [281–283]. In particular, the integration itself was implemented within a rank-one lattice quasi-Monte-Carlo rule (QMC) that is described in more detail in Refs. [284, 285]. The Higgs and the top-quark mass are fixed, so that the integrals depend only on the two kinematic invariants $\hat{s}$ and $\hat{t}$.[4]

Examples of the SM two-loop Feynman diagrams are given in the first, third and last rows of Fig. 10.4. The amplitude was calculated for a pre-sampled set of 5372 phase-space points in $(\hat{s}, \hat{t})$ at 14 TeV and 1343 points at 100 TeV. IR subtraction was performed within the CS dipole formalism, where for the gg channel, the insertion operator $\mathbf{I}$ is given by

$$\mathbf{I}_{gg} = \frac{\alpha_s}{2\pi} \frac{(4\pi)^\epsilon}{\Gamma(1-\epsilon)} \left(\frac{\mu_R^2}{2p_1 \cdot p_2} \right)^\epsilon \cdot 2 \left(\frac{C_A}{\epsilon^2} + \frac{\beta_0}{2\epsilon} - C_A \frac{\pi^2}{3} + \frac{\beta_0}{2} + K_g \right) , \tag{10.9}$$

with $\beta_0 = \frac{11}{6} C_A - \frac{2}{3} T_R N_f$ and $K_g = \left(\frac{67}{18} - \frac{\pi^2}{6} \right) C_A - \frac{10}{9} T_R N_f$. As a side note, the IR singular pattern is the same between the SM and the BSM case presented below. When inserting the CS operator into the Born term, see Eq. (4.8), the poles from the virtual contribution should cancel. To get the correct finite terms, thus, the Born has to be expanded up to $\mathcal{O}(\epsilon^2)$. The explicit cancellation of poles in ϵ is checked numerically.

10.2 The Electroweak Chiral Lagrangian

Regarding variations of the Higgs couplings, one class of extensions of the SM called the Electroweak Chiral Lagrangian (EWChL) [287, 288] is considered, which is a non-linear realization of an EFT. The EWChL, to leading-order, is given as

[4] The top-quark mass is renormalized on-shell. Dependence of the numerical results on the top-mass scheme are investigated in Ref. [286].

$$
\begin{aligned}
\mathcal{L}_2 \;\; = \;\; & -\frac{1}{2}\langle G_{\mu\nu}G^{\mu\nu}\rangle - \frac{1}{2}\langle W_{\mu\nu}W^{\mu\nu}\rangle - \frac{1}{4}B_{\mu\nu}B^{\mu\nu} + \sum_{\psi=q_L,l_L,u_R,d_R,e_R} \bar{\psi} i \not{D} \psi \\
& + \frac{v^2}{4}\,\langle D_\mu U^\dagger D^\mu U\rangle\,(1+F_U(h)) + \frac{1}{2}\partial_\mu h \partial^\mu h - V(h) \\
& - v\left[\bar{q}_L\left(Y_u + \sum_{n=1}^{\infty} Y_u^{(n)}\left(\frac{h}{v}\right)^n\right) U P_+ q_R + \bar{q}_L\left(Y_d + \sum_{n=1}^{\infty} Y_d^{(n)}\left(\frac{h}{v}\right)^n\right) U P_- q_R \right. \\
& \left. \quad + \bar{l}_L\left(Y_e + \sum_{n=1}^{\infty} Y_e^{(n)}\left(\frac{h}{v}\right)^n\right) U P_- l_R + \text{h.c.}\right] , \qquad (10.10)
\end{aligned}
$$

where $U = \exp(2i\phi^a T^a/v)$ is the Goldstone matrix and contains the electroweak Goldstone fields ϕ^a, and T^a are the generators of $SU(2)_L$. Here, $P_\pm = 1/2 \pm T_3$ are the chiral projection operators, and the Higgs sector is characterized by an order-by-order expansion in the Higgs EW singlet h, given by the functions

$$
F_U(h) = \sum_{n=1}^{\infty} f_{U,n}\left(\frac{h}{v}\right)^n , \qquad V(h) = v^4 \sum_{n=2}^{\infty} f_{V,n}\left(\frac{h}{v}\right)^n . \qquad (10.11)
$$

The coefficients $f_{U,n}$, $V_{U,n}$ and $Y^{(n)}_{u,d,e}$ are in principle free parameters and can be of $\mathcal{O}(1)$. The SM case is retrieved when

$$
f_{U,1} = 2, \quad f_{U,2} = 1, \quad f_{V,2} = f_{V,3} = \frac{m_h^2}{2v^2}, \quad f_{V,4} = \frac{m_h^2}{8v^2}, \quad Y_f^{(1)} = Y_f . \qquad (10.12)
$$

Now, this Lagrangian is structured not in terms of canonical dimensions for the quantum fields and couplings, but rather in terms of *chiral* dimensions (as in the case of the chiral EFT of pions in QCD). The chiral dimension assigned to fields, derivatives and couplings are

$$
d_\chi(A_\mu, \varphi, h) = 0 , \qquad d_\chi(\partial, \bar{\psi}\psi, g, y) = 1 , \qquad (10.13)
$$

with A_μ being any gauge field, g representing any of the SM gauge couplings, and y any weak coupling (like the Yukawa couplings). The ordering in the chiral dimension d_χ is equivalent to counting the number of loops L, $d_\chi = 2L + 2$. In summary, the NLO (in α_s) QCD corrections to hh production stem from one-loop diagrams in the leading (in d_χ) EWChL $\mathcal{L}_2$ and from tree diagrams in the next-to leading part $\mathcal{L}_4$. All of these contributions are of chiral dimension $d_\chi = 4$. Then, in the Higgs sector, the effective Lagrangian reduces to

$$
\mathcal{L} \supset \underbrace{-m_t\left(c_t\frac{h}{v} + c_{tt}\frac{h^2}{v^2}\right)\bar{t}\,t - c_{hhh}\frac{m_h^2}{2v}h^3}_{\mathcal{L}_2} + \underbrace{\frac{\alpha_s}{8\pi}\left(c_{ggh}\frac{h}{v} + c_{gghh}\frac{h^2}{v^2}\right)G^a_{\mu\nu}G^{a,\mu\nu}}_{\mathcal{L}_4} . \qquad (10.14)
$$

The EWChL introduces five anomalous couplings to the SM and the corresponding LO Feynman diagrams are given in Fig. 10.2.

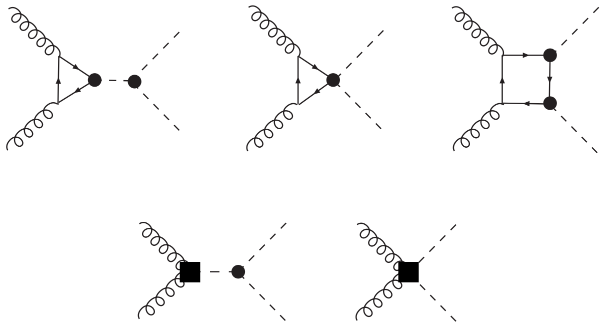

Figure 10.2: LO diagrams for the various terms from the EWChL Lagrangian. Both vertices from $\mathcal{L}_2$ (black dots) and local contact terms from $\mathcal{L}_4$ (black squares) contribute.

Diagrams that are of higher chiral dimension (or do not belong to $\mathcal{O}(\alpha_s^4\alpha^2)$) are systematically neglected, like the ones given in Fig. 10.3. The full virtual amplitude is then given by two-loop contributions (Fig. 10.4), one-loop diagrams that contain one effective coupling from $\mathcal{L}_4$ (Fig. 10.5), and one tree-diagram containing exactly two effective vertices between gluons and Higgs bosons (Fig. 10.6). Note that all two-loop diagrams with non-SM values of the Higgs couplings can be retrieved from their SM counterparts by rescaling them at amplitude-level:

$$
\begin{aligned}
\mathcal{M}_V(\triangle_1) &\to \mathcal{M}_V^{\mathrm{SM}}(\triangle_1)\cdot c_t\, c_{hhh} && (1^{\mathrm{st}} \text{ row in Fig. 10.4})\\
\mathcal{M}_V(\triangle_2) &\to \mathcal{M}_V^{\mathrm{SM}}(\triangle_1)\cdot \frac{\hat{s}-m_h^2}{3m_h^2} c_{tt} && (2^{\mathrm{nd}} \text{ row in Fig. 10.4})\\
\mathcal{M}_V(\square) &\to \mathcal{M}_V^{\mathrm{SM}}(\square)\cdot c_t^2 && (3^{\mathrm{rd}}, 4^{\mathrm{th}} \text{ rows in Fig. 10.4})\ ,
\end{aligned}
$$

where $\mathcal{M}_V(\triangle_1)$ are the triangle diagrams from the 1st row of Fig. 10.4, $\mathcal{M}_V(\triangle_2)$ from the 2nd row (given by the corresponding diagrams from the 1st row where the s-channel Higgs propagator is pinched), and $\mathcal{M}_V(\square)$ are the box-diagrams from the 3rd row. Accordingly, the amplitudes computed in Ref. [279] are used for the pre-sampled set of phase-space points and are simply rescaled.

Finally, real-emission diagrams contain five-point one-loop diagrams with SM-like topologies, as well as tree diagrams carrying one effective coupling between gluons and Higgs bosons from $\mathcal{L}_4$ (Fig. 10.7).

10.3 Total cross-sections for BSM benchmark points

All results for total and differential cross-sections presented in this chapter can be found in Ref. [289]. To summarize, all HTL contributions were computed analytically with

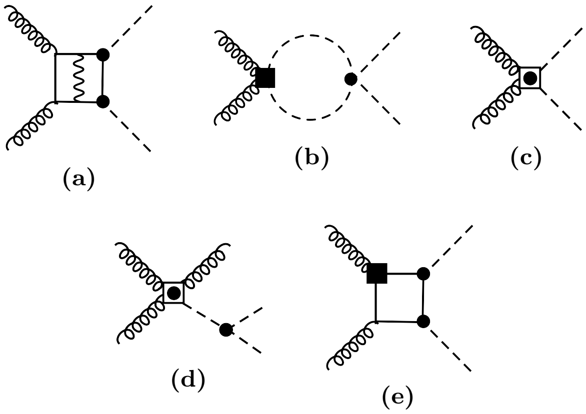

Figure 10.3: (a-d) Diagrams that do not scale like α_s^4 are consistently neglected. (e) The chromomagnetic operator $Q_{ttG} = c_t g_s \bar{t}_L \sigma_{\mu\nu} G^{\mu\nu} t_R$ only contributes at two-loop order at least ($d_\chi = 6$).

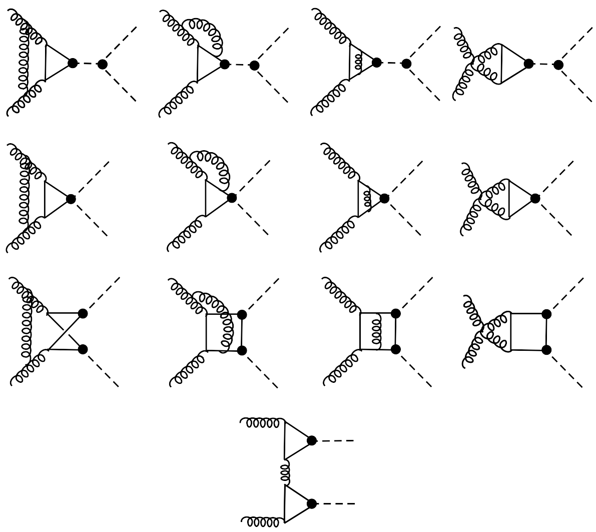

Figure 10.4: Two-loop diagrams generated by the EWChL at NLO QCD. They can all be computed by rescaling from the corresponding SM diagrams (see text).

`FORM`. In $\mathrm{FT}_{\mathrm{approx}}$ and in the full theory predictions, the real radiation is provided by GoSam [92, 93]. A Universal FeynRules Output (UFO) model [290] for the EWChL was produced with FeynRules [291, 292] and interfaced to GoSam to produce all tree and one-loop diagrams. The various parts are assembled into a `C++` code which performs the phase-space integration with Vegas [76] as interfaced through the Cuba package [75].

The results shown below are produced at a center-of-mass energy of $\sqrt{s} = 14\,\mathrm{TeV}$, where the PDF4LHC15_nlo_100_pdfas set [219] is used and interfaced through `LHAPDF6`. The corresponding value of $\alpha_s(\mu)$, with $\alpha_s(m_Z) = 0.118$, is consistently employed

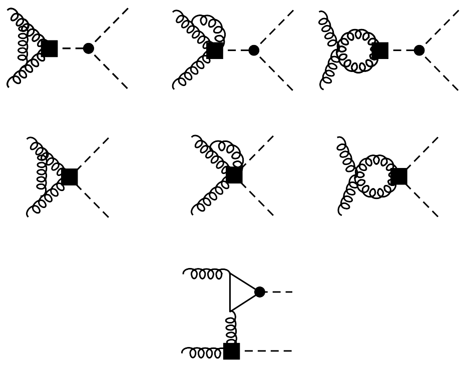

Figure 10.5: One-loop virtual contributions at NLO QCD: these diagrams contain exactly one effective contact coupling from $\mathcal{L}_4$.

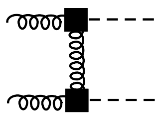

Figure 10.6: Tree diagram at NLO QCD containing exactly two effective couplings from $\mathcal{L}_4$.

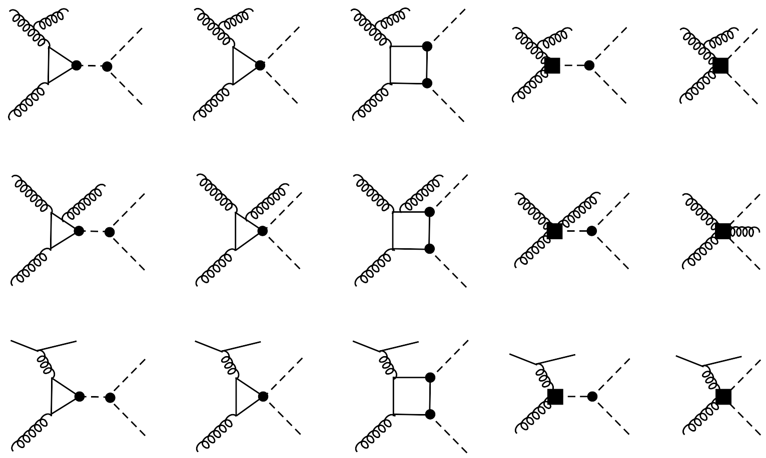

Figure 10.7: Real-emission contributions that are either one-loop diagrams without effective contact coupling, or tree diagrams with exactly one such coupling.

throughout the calculation. The Higgs boson and top-quark masses are set to $m_h = 125\,\mathrm{GeV}$ and $m_t = 173\,\mathrm{GeV}$, as the two-loop amplitudes were computed with these values, and both their widths are set to zero. Finally, the renormalization and factorization scales are set to $\mu_R = \mu_F = \mu_0 = m_{hh}/2$ and uncertainties are estimated according to 7-point scale variations $\mu_{R,F} = c_{R,F}\mu_0$ with $(c_R, c_F) \in \{0.5, 1, 2\} \times \{0.5, 1, 2\} \setminus \{(0.5, 2), (2, 0.5)\}$.

To characterize the 5-dimensional BSM space, the set of Higgs coupling variations used in the following part is based mostly on the definition of benchmark (BM) points presented in Ref. [293]. There, the BSM space is scanned for different values of the Higgs anomalous couplings and clustered into blocks that manifest a similar behavior in differential distributions. The set of BM points is defined in Table 10.1, and the total cross-sections, K-factors and uncertainties are shown in Table 10.2.

First, looking at Table 10.2, the NLO cross-sections can become quite sizable depending on the BM point considered (of $\mathcal{O}(100)$ times the SM cross-section), and some are even excluded considering recent bounds on hh production from experimental limits. With the ATLAS current limit [16] on the observed non-resonant hh production cross-section of 220 fb at 95% CL, several BM points would indeed be excluded already. Second, the full m_t-dependent NLO corrections are important, with K-factors between 1.66 and 2.34, and are accompanied by large scale uncertainties of $\mathcal{O}(15-20\%)$ (similarly to single Higgs production at NLO QCD [294, 295]). Finally, the K-factors themselves depend substantially on the considered BM point. This is illustrated in Fig. 10.8, where only one parameter is varied at a time. In fact, studies realized in the heavy-top limit suggest the dependence of the K-factors on the different couplings to be quite small [296] (of $\mathcal{O}(5\%)$ or less for all considered coupling variations). Once full top-quark loop corrections are taken into account, though, the K-factors for c_{hhh}, c_{tt} and c_t vary by more than 30% (55% for c_{tt}). Later on, in Section 10.4, it will be shown that this feature is especially prominent around the top-quark pair $2m_t$ threshold when considering differential distributions.

BM	c_{hhh}	c_t	c_{tt}	c_{ggh}	c_{gghh}
1	7.5	1.0	-1.0	0.0	0.0
2	1.0	1.0	0.5	$-\frac{1.6}{3}$	-0.2
3	1.0	1.0	-1.5	0.0	$\frac{0.8}{3}$
4	-3.5	1.5	-3.0	0.0	0.0
5	1.0	1.0	0.0	$\frac{1.6}{3}$	$\frac{1.0}{3}$
6	2.4	1.0	0.0	$\frac{0.4}{3}$	$\frac{0.2}{3}$
7	5.0	1.0	0.0	$\frac{0.4}{3}$	$\frac{0.2}{3}$
8a	1.0	1.0	0.5	$\frac{0.8}{3}$	0.0
9	1.0	1.0	1.0	-0.4	-0.2
10	10.0	1.5	-1.0	0.0	0.0
11	2.4	1.0	0.0	$\frac{2.0}{3}$	$\frac{1.0}{3}$
12	15.0	1.0	1.0	0.0	0.0
SM	1.0	1.0	0.0	0.0	0.0

Table 10.1: Different BM points in the 5-dimensional Higgs coupling space are analyzed below at inclusive, respectively differential cross-section level.

Furthermore, the ratio of the cross-section to the SM can be parametrized [293, 297] in terms of the anomalous Higgs couplings: the cross-section ratio is expressed as a polynomial whose coefficients correspond to all squared/interference terms from the various diagrams. At LO, this gives 15 possible combinations:

BM	σ_{NLO} [fb]	K-factor	scale uncertainties [%]	stat. uncertainties [%]	$\frac{\sigma_{\text{NLO}}}{\sigma_{\text{NLO,SM}}}$
B_1	194.89	1.88	${}^{+19}_{-15}$	1.6	5.915
B_2	14.55	1.88	${}^{+5}_{-13}$	0.56	0.4416
B_3	1047.37	1.98	${}^{+21}_{-16}$	0.15	31.79
B_4	8922.75	1.98	${}^{+19}_{-16}$	0.39	270.8
B_5	59.325	1.83	${}^{+4}_{-15}$	0.36	1.801
B_6	24.69	1.89	${}^{+2}_{-11}$	2.1	0.7495
B_7	169.41	2.07	${}^{+9}_{-12}$	2.2	5.142
B_{8a}	41.70	2.34	${}^{+6}_{-9}$	0.63	1.266
B_9	146.00	2.30	${}^{+22}_{-16}$	0.31	4.431
B_{10}	575.86	2.00	${}^{+17}_{-14}$	3.2	17.48
B_{11}	174.70	1.92	${}^{+24}_{-8}$	1.2	5.303
B_{12}	3618.53	2.07	${}^{+16}_{-15}$	1.2	109.83
SM	32.95	1.66	${}^{+14}_{-13}$	0.1	1

Table 10.2: The total cross-sections for the considered BM points, with their respective K-factors, scale and (MC) statistical uncertainties, as well as the ratio to the SM cross-section $\sigma_{\text{NLO,SM}} = 32.95$ fb.

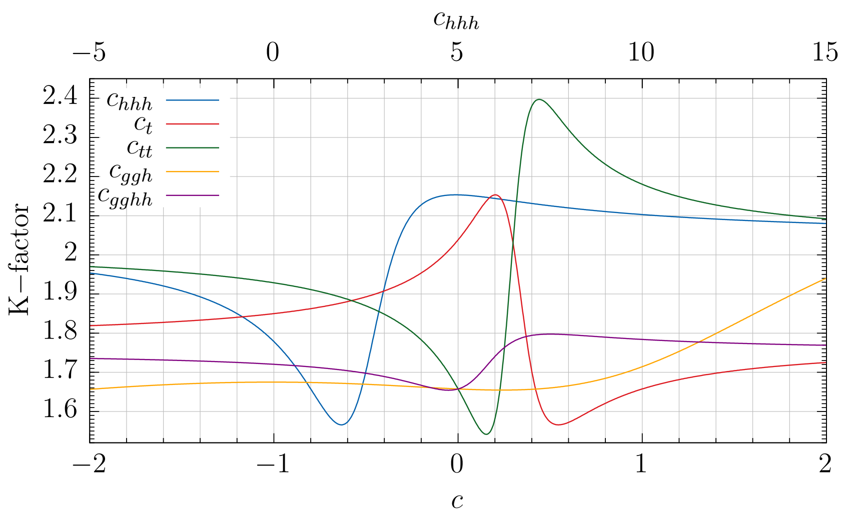

Figure 10.8: The K-factor is shown as a function of c_{hhh} on the top axis, and of the other couplings on the lower axis.

$$\begin{aligned}\sigma/\sigma_{SM} = {} & A_1\, c_t^4 + A_2\, c_{tt}^2 + A_3\, c_t^2 c_{hhh}^2 + A_4\, c_{ggh}^2 c_{hhh}^2 + A_5\, c_{gghh}^2 + A_6\, c_{tt} c_t^2 \\ & + A_7\, c_t^3 c_{hhh} + A_8\, c_{tt} c_t\, c_{hhh} + A_9\, c_{tt} c_{ggh} c_{hhh} + A_{10}\, c_{tt} c_{gghh} \\ & + A_{11}\, c_t^2 c_{ggh} c_{hhh} + A_{12}\, c_t^2 c_{gghh} + A_{13}\, c_t c_{hhh}^2 c_{ggh} \\ & + A_{14}\, c_t c_{hhh} c_{gghh} + A_{15}\, c_{ggh} c_{hhh} c_{gghh}\,. \end{aligned} \tag{10.15}$$

The coefficients A_1 to A_{15} are corrected at NLO, and 8 new coefficients appear from genuine NLO diagrams:

$$\begin{aligned}\Delta\sigma/\sigma_{SM} &= A_{16}\, c_t^3 c_{ggh} + A_{17}\, c_t c_{tt} c_{ggh} + A_{18}\, c_t c_{ggh}^2 c_{hhh} + A_{19}\, c_t c_{ggh} c_{gghh} \\ &\quad + A_{20}\, c_t^2 c_{ggh}^2 + A_{21}\, c_{tt} c_{ggh}^2 + A_{22}\, c_{ggh}^3 c_{hhh} + A_{23}\, c_{ggh}^2 c_{gghh}\,. \end{aligned} \tag{10.16}$$

These coefficients can be determined by dedicated event generation runs for a set of the 5-dimensional parameter space, and by projecting out a system of equations, or by a simple fit of the polynomial in Eq. (10.16) to the calculated set of cross-sections. The results for the NLO coefficients A_1 to A_{23} at $\sqrt{s} = 14$ TeV are given in Table E.1. Interestingly, once the cross-section coefficients are computed, the parametrization given in Eqs. (10.15), (10.16) yields the cross-section for any point of the BSM space. This allows to produce iso-contour plots where curves represent configurations in the BSM space which lead to the same cross-section, see Figs. 10.9−10.11. In the latter, two BSM couplings are simultaneously varied (within bounds still approximately allowed by experimental measurements), and iso-curves for the ratio of the predicted cross-section to the SM cross-section at LO (red), respectively NLO (black), are shown.

The cross-section iso-curves are given for c_{tt} against c_{gghh} in Fig. 10.9a, respectively against c_{ggh} in Fig. 10.9b. In both cases, the cross-section varies sizably with respect to the SM value, and is generally more sensitive to changes in c_{tt}. The NLO corrections to hh production introduce important shifts in the iso-curves (reflected by the large K-factors). Fig. 10.10 shows iso-contours for variations of c_{hhh} versus c_{ggh}, respectively c_{tt}. Again, the curves are much more dependent on c_{hhh} than on the Higgs contact coupling, as exhibited by Fig. 10.10a. In comparison, the dependence of the cross-section on c_{hhh} and c_{tt} is large, with ratios to the SM cross-section going up to a factor $\mathcal{O}(\sim 100)$. Finally, iso-contours are also plotted for simultaneous variations of c_t versus c_{tt} and c_{hhh} in Fig. 10.11.

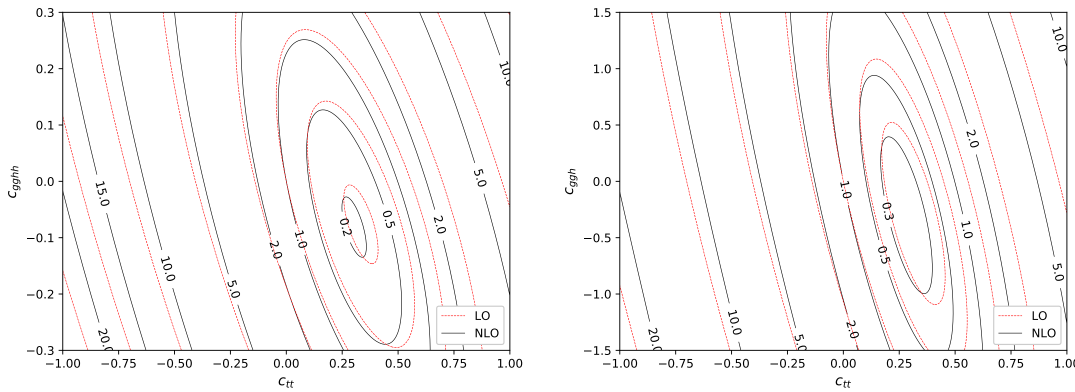

(a) (b)

Figure 10.9: Iso-contours of σ/σ_{SM}: (a) c_{gghh} and (b) c_{ggh} versus c_{tt}.

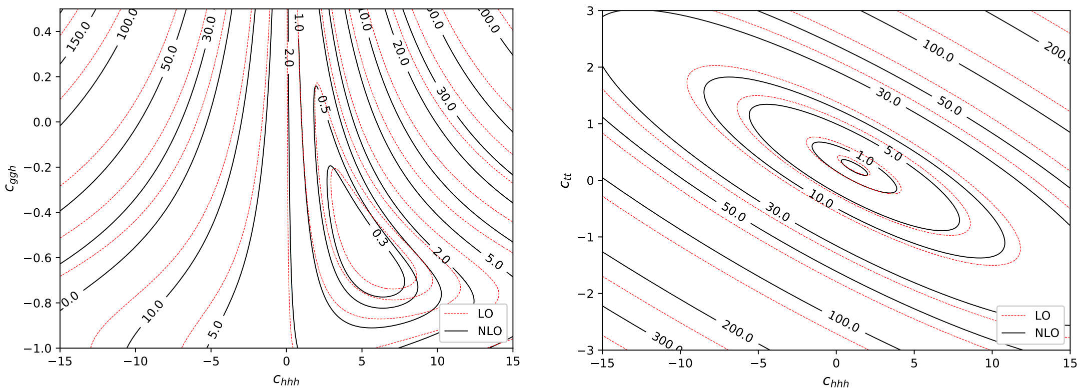

(a) **(b)**

Figure 10.10: Iso-contours of σ/σ_{SM}: (a) c_{ggh} and (b) c_{tt} versus c_{hhh}.

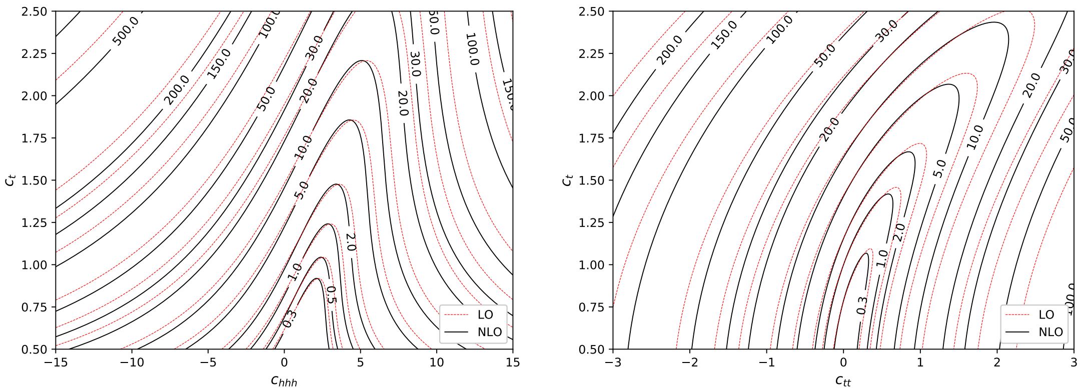

(a) **(b)**

Figure 10.11: Iso-contours of σ/σ_{SM}: (a) c_t versus c_{hhh} and (b) c_t versus c_{tt}.

10.4 Differential cross-sections and HTL approximations

Next, differential cross-sections are compared for the various approximations laid out in Section 10.1.1. Distributions are shown for the invariant mass of the Higgs boson pair system m_{hh} and the transverse momentum of one (any) Higgs $p_{T,h}$, for a subset of the BM points defined in Table 10.2.

In Fig. 10.12, both distributions are displayed for the BM point 6: the SM distributions are plotted against the the BSM Born-improved, $\mathrm{FT}_{\mathrm{approx}}$ and full predictions, respectively, both at LO and NLO. While the inclusive cross-section for B_6 is similar to the SM value for all considered NLO approximations, the interference pattern between triangle- and box-like diagrams is very different. The m_{hh} observable in Fig. 10.12a manifests a dip around $m_{hh} = 370\,\mathrm{GeV}$,[5] which would be a characteristic sign of BSM physics at the differential level. As a matter of fact, the chosen value of $c_{hhh} = 2.4$ corresponds to an approximately maximal destructive interference between triangle- and box-like contributions when the other couplings are kept fixed at their SM values. Secondly, the differential K-factor shown in the first ratio plot (in red), which is found to be relatively flat in the usual HTL approximations, varies by more than 70% for the full m_t-dependent NLO prediction. Finally, while both the Born-improved and $\mathrm{FT}_{\mathrm{approx}}$ descriptions show the largest difference to the full NLO calculation around the top-quark pair threshold (see the purple and green curves in the second ratio plot), they describe the tail of the m_{hh} distribution rather well. The same considerations apply to the $p_{T,h}$ distribution plotted in Fig. 10.12b.

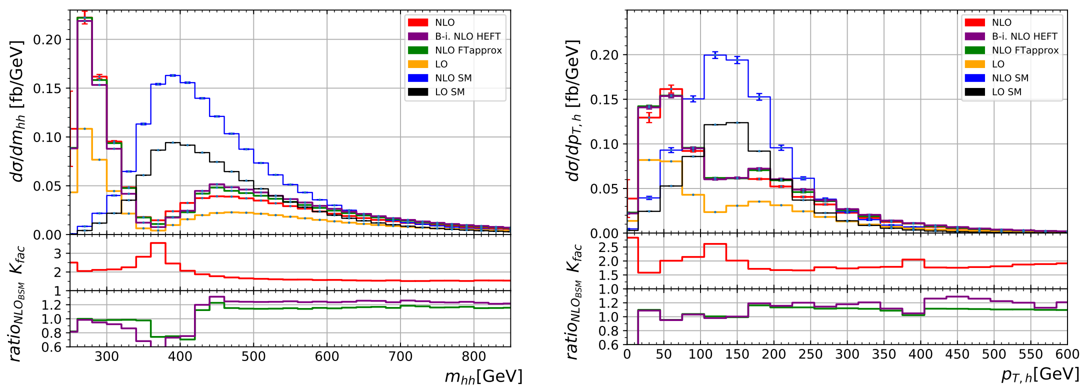

(a) **(b)**

Figure 10.12: (a) Higgs boson pair invariant mass and (b) Higgs transverse momentum for BM point 6 ($c_{hhh} = 2.4, c_t = 1, c_{tt} = 0, c_{ggh} = 2/15, c_{gghh} = 1/15$) with all considered hh production approximations.

The same differential distributions are plotted for the BM point 9 in Fig. 10.13, which is characterized by SM values for c_{hhh}, c_t and non-zero values of c_{tt} and gluon-Higgs couplings c_{ggh}, c_{gghh}. In this case, the cross-section is much larger than the SM value. The anomalous gluon-Higgs coupling values also enhance the tail of both distributions (the dependence of the c_{gghh} term grows proportionally to the invariant $\hat{s}$ in the limit $\hat{s} \to \infty$). Both NLO approximations fall short of describing the full prediction around the top-quark pair threshold and in the middle-range region of the m_{hh} distribution.

Renormalization and factorization scale uncertainties are given along the central prediction for the BM point 5 in Fig. 10.14. This BM point is one example where, contrary to the SM case, the envelope is not given by the two most extreme scale variations $c_{R,F} \in \{(0.5, 0.5), (2, 2)\}$, which both give downwards deviations. As for the SM point, the NLO BM prediction is not covered by the LO scale uncertainties. All BM points not shown here are given in Appendix E for completeness.

[5] The LO pure HTL amplitude vanishes at $m_{hh} = 429\,\mathrm{GeV}$.

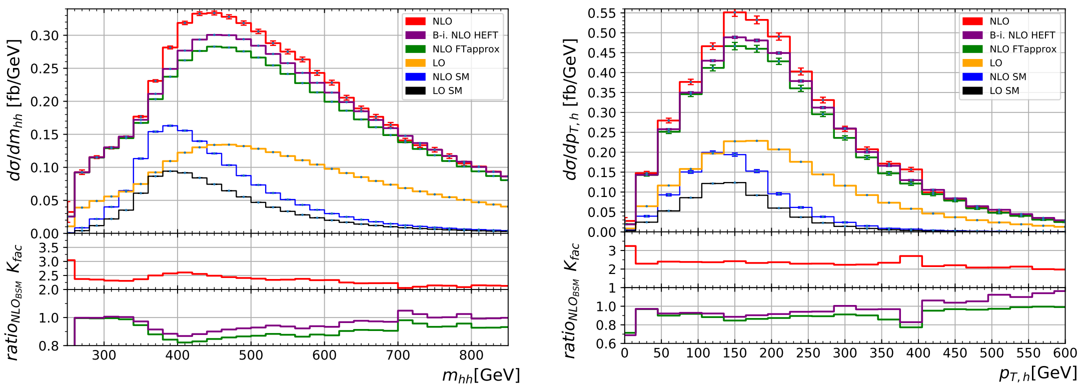

(a) **(b)**

Figure 10.13: (a) Higgs boson pair invariant mass and (b) Higgs transverse momentum for BM point 9 ($c_{hhh} = 1, c_t = 1, c_{tt} = 1, c_{ggh} = -0.4, c_{gghh} = -0.2$).

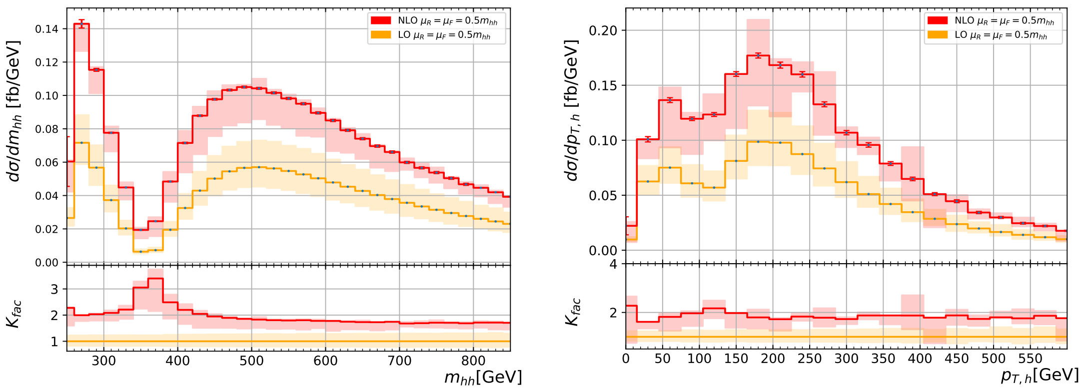

(a) **(b)**

Figure 10.14: The (a) m_{hh} and (b) $p_{T,h}$ distributions for BM point 5 ($c_{hhh} = 1, c_t = 1$, $c_{tt} = 0, c_{ggh} = 8/15, c_{gghh} = 1/3$), along with μ_R/μ_F scale uncertainties.

Note that both BM points 5 and 9 assume values of c_{ggh} that are already excluded by CMS for $c_t = 1$ [298]. Generally, the full m_t-dependent NLO prediction introduces a high dependence of the K-factor on both the anomalous Higgs couplings and at the differential level in distribution bins. For some BM points, the Born-improved and $\mathrm{FT}_{\mathrm{approx}}$ approximations fare rather poorly and should be replaced by the full theory prediction when comparing to experimentally measured cross-sections, for maximal exclusion limits on anomalous couplings. In particular, it should help identify updated BM points in the BSM space of anomalous Higgs couplings. In this prospect, part of the EWChL setup presented above is incorporated next into a MC event generator available to experimentalists.

11 Variations of the triple Higgs coupling and parton-shower effects

Having considered the extension of the SM through the EWChL and the effects of the full NLO QCD corrections due to the top-quark loops in hh production, its implementation in a full-fledged MC event generator is presented. Numerical results and differential distributions are given in more detail in Ref. [299]. A version of the m_t-dependent prediction at NLO was already implemented in the case of the SM in the Powheg-BOX-V2 package `UserProcesses-V2/ggHH`. It is extended to allow for variations of both the Higgs boson trilinear self-coupling λ and the top-Higgs Yukawa coupling y_t: the result is a public MC generator that permits full particle-level production. In particular, Higgs bosons are allowed to decay, and the fixed-order calculation can be matched to a parton-shower and hadronization package. In this chapter, the workflow of the Powheg-BOX MC generator is briefly presented. The interfacing of the two-loop contribution to hh production (including the aforementioned coupling variations) is explained, and NLO cross-sections at $\sqrt{s} = 13, 14, 27$ TeV, as well as differential distributions at $\sqrt{s} = 14$ TeV are shown. Finally, the matching of the fixed-order NLO calculation to a parton-shower is studied in more depth, and shower-related systematic uncertainties are estimated.

11.1 The Powheg-BOX framework

The Powheg-BOX framework [17–19] is a `fortran` MC event generator skeleton that handles MC integration and event production for any arbitrary NLO process, supposing the user grants the few necessary input ingredients for the calculation, namely a parametrization of phase-space and the different contributions to the amplitude. The Powheg-BOX also constitutes a repository of previously calculated processes which are made publicly available. In the following, the second version of the program Powheg-BOX-V2 is used. The Powheg formalism is based on the following formula for the hardest emission:

$$\mathrm{d}\sigma_{\mathrm{NLO}} = \mathrm{d}\Phi_m \bar{B}(\Phi_m) \left(\Delta(p_{T,\min}, \mu^2) + \int_{p_{T,\min}} \mathrm{d}\Phi_1 \Delta(p_T, \mu^2) \frac{R(\Phi_{m+1})}{B(\Phi_m)} \Theta(\mu^2 - p_T) \right) , \tag{11.1}$$

where $p_{T,\min}$ is the parton-shower IR cutoff, μ^2 is the shower starting scale, B and R are the Born and the real-emission matrix-elements, and $\bar{B}$ represents the Born underlying configuration. Note that in general, the transverse momentum could be replaced by any other shower evolution variable. The function Δ is the Sudakov form factor (see

Section 4.2.2) yielding the probability of no-emission above a given scale. In the Powheg notation, it is written as:

$$\Delta(t_0, t) = \exp\left(-\int \mathrm{d}\Phi_1 \frac{R(\Phi_{m+1})\Theta(t-t_0)}{B(\Phi_m)}\right) . \tag{11.2}$$

For more details, the reader is referred to Ref. [18]. The workflow is quite simple and separates into four stages:

- An importance sampling grid for the integration is determined: if run in parallel mode, Powheg generates importance sampling grids for each seed and subsequently combines them into one and stores the result in a `pwgxgrid.dat` file.
- The integration is performed, and an upper bounding envelope is determined for the underlying Born kinematics cross-section $\bar{B}$ and stored into a `pwggrid.dat` file.
- The upper bound for the normalization of the radiation function $R(\Phi_{m+1})/B(\Phi_m)$ is found, and stored into a `pwgubound.dat` file.
- Events can be generated in the LHE format, and run in parallel. Files `pwgevents.lhe` are produced and can then be fed to a parton-shower algorithm later on.

11.2 Interfacing two-loop contributions

The grid of the amplitude at pre-sampled PS points used for producing the results of Chapter 10 is stored and has to be interfaced to Powheg. First, the program has to be able to call the virtual amplitude at any phase-space point (without having to recompute the expensive two-loop integrals for any possible kinematics $(\hat{s}, \hat{t})$). In the SM `ggHH` program [300], this is handled by setting up a `Python` interface that interpolates the 2-dimensional grid: first, the $(\hat{s}, \hat{t})$ phase-space is re-parametrized into new variables (x, c_θ) to produce an almost uniform distribution of phase-space points. This is achieved by choosing

$$x = f(\beta(\hat{s})), \quad c_\theta = |\cos(\theta)| = \left|\frac{\hat{s} + 2\hat{t} - 2m_h^2}{\hat{s}\beta(\hat{s})}\right|, \quad \beta = \sqrt{1 - \frac{4m_h^2}{\hat{s}}} \tag{11.3}$$

with f any monotonic function. In this case, $f(\beta(\hat{s}))$ is chosen to be the cumulative distribution function of the phase-space points generated in Ref. [279]. A uniform grid in the (x, c_θ) space is generated, and the result at each point is set by linearly interpolating the amplitude using the neighboring points computed by SecDec. The amplitude at any phase-space points is then interpolated using the Clough-Tocher scheme [301] in `SciPy` [302], which allows for a high numerical stability. For details on the grid performance and caveats, the reader is referred to Ref. [299, 300].

The implementation of variations of the Higgs trilinear self-coupling λ bases on a simple observation: at all orders (in QCD), the squared amplitude for di-Higgs production is a second-order polynomial in λ,

$$M_\lambda \equiv |\mathcal{M}_\lambda|^2 = A + B\,\lambda + C\,\lambda^2\ . \tag{11.4}$$

Thus knowing the amplitude for three values of λ allows to interpolate the matrix-element to any other arbitrary value. In this case, grids of the virtual amplitudes are produced for $\lambda \in \{-1, 0, 1\}$. Before starting the POWHEG run, the three grids are combined to a new grid containing the virtual amplitude for the user-given value of the Higgs self-coupling by simple Lagrange interpolation,

$$M_\lambda = M_{\lambda=0}\,(1-\lambda^2) + \frac{M_{\lambda=1}}{2}\,(\lambda+\lambda^2) + \frac{M_{\lambda=-1}}{2}\,(-\lambda+\lambda^2)\ , \tag{11.5}$$

where the uncertainties on the three amplitudes are added in quadrature. This grid is then further propagated to the Clough-Tocher interpolation routine. Note that in the BSM case, points at 100 TeV are also included in the grid to further improve statistics at higher center-of-mass energies, and by extension, in the tails of the distributions. On the other hand, because BSM distributions differ in shape from the SM case (for example, see Fig. 11.2), phase-space regions that could well be populated for certain values of the anomalous couplings are not always well-sampled by the SM grid.

11.3 Total and differential cross-sections at fixed-order

The PDF4LHC15_nlo_30_pdfas sets [219] are used and interfaced to POWHEG-BOX-V2 through `LHAPDF6`. Jets are clustered by the anti-k_T algorithm [220] as implemented in `FastJet`, with a jet distance parameter of $R = 0.4$ and a minimum transverse momentum $p_{T,\min}^{\mathrm{jet}} = 20\,\mathrm{GeV}$. Otherwise, the same setup presented in Section 10.3 is used for the next results. Note that the nomenclature is different, with respect to Chapter 10, for variations of the Higgs trilinear coupling and the top-Higgs Yukawa coupling: the Higgs self-coupling ratio to the SM value, formerly called c_{hhh}, is replaced by κ_λ (in reference to the widely-used experimental κ framework), and the top-Higgs Yukawa coupling ratio c_t is now named y_t.

Total cross-sections for various values of $\kappa_\lambda = \lambda/\lambda_{\mathrm{SM}}$ were computed for $\sqrt{s} = 13, 14$ and 27 TeV and are displayed in Table 11.1. Note again that the cross-section has a minimum around $\kappa_\lambda \sim 2.4$, for which the interference between triangle- and box-like diagrams is at its most destructive. The K-factor is plotted in Fig. 11.1 as a function of the Higgs self-coupling, this time ranging over the full, not yet excluded region for κ_λ.

The distributions of the invariant mass of the Higgs boson pair m_{hh} are shown for the considered values of κ_λ in Fig. 11.2 with their respective scale uncertainties. For values of κ_λ that lead to a minimal cross-section, the interference pattern is well-recognizable with a dip around $m_{hh} \sim 350\,\mathrm{GeV}$, near the top-pair threshold. For greater values of

$\lambda_{\rm BSM}/\lambda_{\rm SM}$	$\sigma_{\rm NLO}$@13TeV [fb]	$\sigma_{\rm NLO}$@14TeV [fb]	$\sigma_{\rm NLO}$@27TeV [fb]	K-factor@14TeV
-1	$116.71^{+16.4\%}_{-14.3\%}$	$136.91^{+16.4\%}_{-13.9\%}$	504.9	1.86
0	$62.51^{+15.8\%}_{-13.7\%}$	$73.64^{+15.4\%}_{-13.4\%}$	275.29	1.79
1	$27.84^{+11.6\%}_{-12.9\%}$	$32.88^{+13.5\%}_{-12.5\%}$	$127.7^{+11.5\%}_{-10.4\%}$	1.66
2	$12.42^{+13.1\%}_{-12.0\%}$	$14.75^{+12.0\%}_{-11.8\%}$	59.10	1.56
2.4	$11.65^{+13.9\%}_{-12.7\%}$	$13.79^{+13.5\%}_{-12.5\%}$	53.67	1.65
3	$16.28^{+16.2\%}_{-15.3\%}$	$19.07^{+17.1\%}_{-14.1\%}$	69.84	1.90
5	$81.74^{+20.0\%}_{-15.6\%}$	$95.22^{+19.7\%}_{-11.5\%}$	330.61	2.14

Table 11.1: The cross-sections for di-Higgs production at full NLO QCD are given for $\sqrt{s} = 13, 14$ and 27 TeV with scale uncertainties for several values of $\kappa_\lambda = \lambda/\lambda_{\rm SM}$.

$|\kappa_\lambda|$, this dip completely disappears and the enhanced triangle-like contribution tends to populate the lower m_{hh}-region. A similar behavior is observed for the transverse momentum of one (any) Higgs boson, as presented in Fig. 11.3, although the effect is partly washed out.

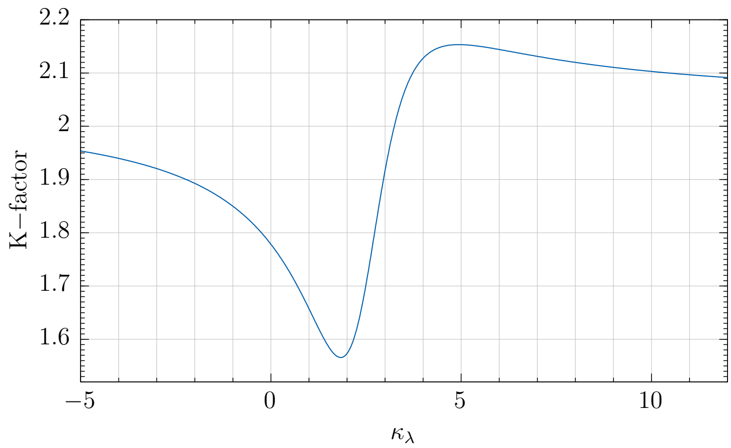

Figure 11.1: The full-theory NLO QCD K-factor is plotted as a function of the trilinear Higgs self-coupling κ_λ.

Furthermore, variations of the top-Higgs Yukawa coupling y_t can be recovered by a trick: allowing for y_t variations changes Eq. (11.4) into

$$|\mathcal{M}|^2 = y_t^4 \left[\mathcal{M}_B \mathcal{M}_B^* + \frac{\lambda}{y_t}(\mathcal{M}_B \mathcal{M}_T^* + \mathcal{M}_T \mathcal{M}_B^*) + \frac{\lambda^2}{y_t^2} \mathcal{M}_T \mathcal{M}_T^* \right] , \tag{11.6}$$

where $\mathcal{M}_B$ is the box- and $\mathcal{M}_T$ is the triangle contribution, and only the ratio $\frac{\lambda}{y_t}$ appears up to an overall factor. So, it suffices to generate events with the value of λ

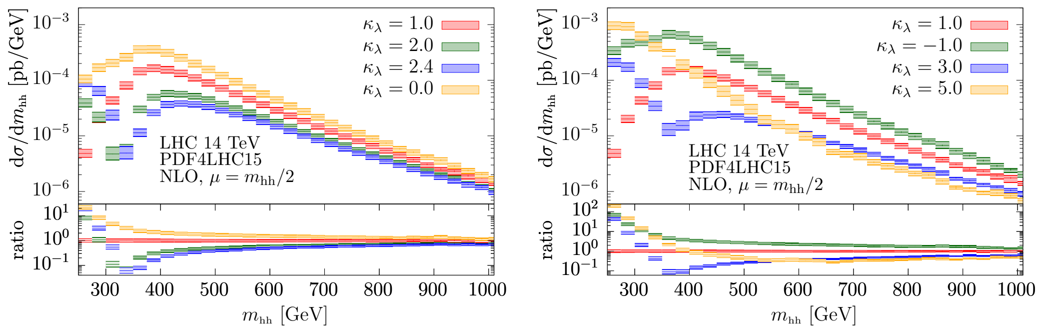

(a) (b)

Figure 11.2: The Higgs boson pair invariant mass distributions for different values of κ_λ are given at $\sqrt{s} = 14\,\text{TeV}$.

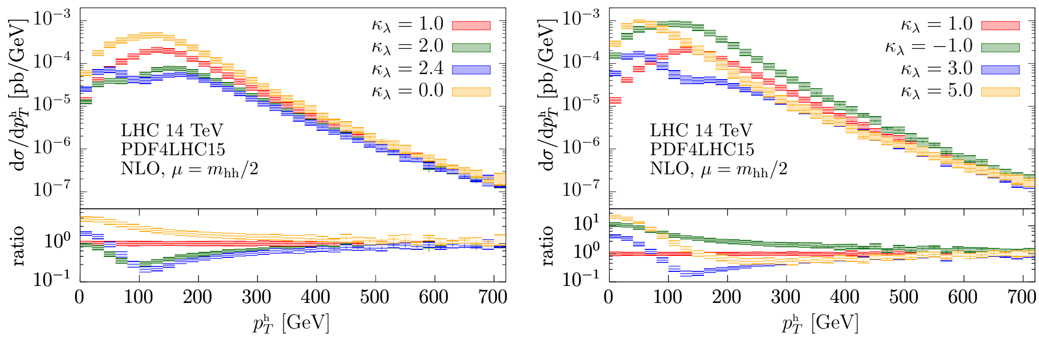

(a) (b)

Figure 11.3: The transverse momentum of one (any) Higgs boson is shown for several values of κ_λ at $\sqrt{s} = 14\,\text{TeV}$.

corresponding to the desired value of the ratio $\frac{\lambda}{y_t}$, and finally rescale all results by y_t^4. For example, to produce results for $\kappa_\lambda = 1, y_t = 0.8$, the cross-section is given by

$$\mathrm{d}\sigma_{\mathrm{NLO}}\left(\kappa_\lambda = 1, y_t = 0.8\right) = (0.8)^4 \cdot \mathrm{d}\sigma_{\mathrm{NLO}}\left(y_t = 1\,, \kappa_\lambda = \frac{1}{0.8} = 1.25\right)\,. \tag{11.7}$$

Both m_{hh} and p_T^h distributions are displayed for y_t-values close to the currently excluded region in Fig. 11.4.

11.4 Parton-shower matched predictions at NLO

For use by experimentalists in a full simulation, the fixed-order calculation is matched to a parton-shower (where the final-state can also be hadronized later on) within Powheg. In the fourth generation stage presented in Sec. 11.1, Powheg generates full parton-level events and stores them in LHE files. These events can then be used as input to

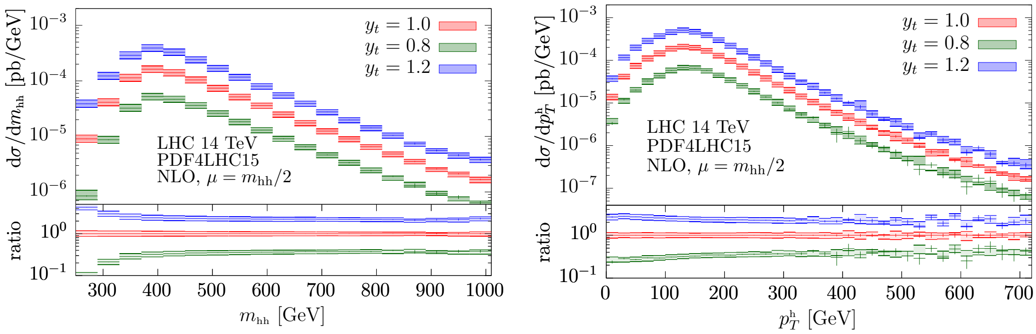

(a) **(b)**

Figure 11.4: (a) The invariant mass of the Higgs boson pair system and (b) the transverse momentum of one Higgs boson are shown for three values of y_t. The procedure for generating y_t-varied events is explained in the text.

most modern parton-shower programs. For this purpose, two different parton-shower programs are employed, namely Pythia 8.235 and Herwig7.1.4. Additionally, both the angular-ordered (so called $\tilde{q}$) and the dipole shower algorithms present in Herwig are applied. The interfacing of both programs to Powheg is mostly automated: the standard `UserHooks` based on the `main31` LHE showering routine from Pythia are used to set the shower p_T definitions and vetoes (see Appendix F). For Herwig7, a process-independent interface library is present since revision `r3591` of the Powheg-BOX-V2 which sets the `LHEReader` class and handles the Herwig output for the event analysis. Finally, in both showers, the tunes are left to their default values. Note that the Sudakov form factor is automatically included by Powheg when producing LHE files. The Powheg h_{damp} parameter is kept fixed throughout the next section and set to $h_{\text{damp}} = 250\,\text{GeV}$.

In Fig. 11.5a, the transverse momentum of one (any) Higgs boson p_T^h is shown for the fixed-order NLO prediction, as well as the matched predictions to the three different shower algorithms: Pythia8 (PP8), and both the angular-ordered $\tilde{q}$ shower (PH7-$\tilde{q}$) and the dipole shower (PH7-dipole) from Herwig. For variables that are inclusive in the additional radiation, like p_T^h, all predictions are largely identical. In the case of variables that are sensitive to real emission, like the angular distance of both Higgs bosons $\Delta R^{hh} = \sqrt{(\eta_1 - \eta_2)^2 + (\phi_1 - \phi_2)^2}$ shown in Fig. 11.5b, the showered predictions differ from the NLO calculation. There, the Sudakov exponent effectively resums radiation around $\Delta R^{hh} = \pi$, where the Higgs bosons are close to a back-to-back configuration. In addition, the parton-shower starts populating the region $\Delta R^{hh} < \pi$. Also, differences between the Pythia and Herwig parton-showers are already visible: while both Herwig showers produce very similar results, Pythia overshoots their prediction by $\sim 50\%$.

The differences between both parton-shower programs become more obvious when considering the transverse momentum of the Higgs boson pair system p_T^{hh}, displayed in Fig. 11.6 for two values of the Higgs trilinear coupling $\kappa_\lambda = 1$, $\kappa_\lambda = 2.4$. In that case, both Pythia and Herwig agree at low transverse momentum, until they start to deviate

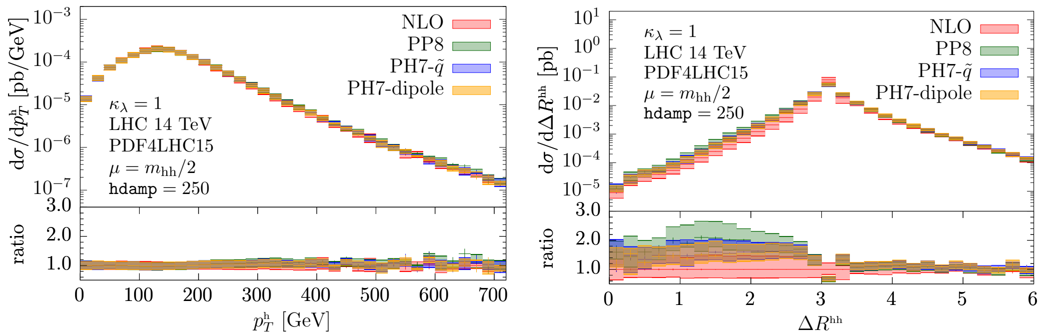

(a) (b)

Figure 11.5: For the SM case $\kappa_\lambda = 1$, (a) the transverse momentum of one Higgs boson, and (b) the angular distance between both Higgs bosons are shown for the fixed-order NLO case, as well as for the three different parton-shower algorithms. The parton-level events from POWHEG are matched to PYTHIA8 (PP8), and to both the angular-ordered $\tilde{q}$-shower (PH7-$\tilde{q}$) and the dipole shower (PH7-dipole) from HERWIG7.

at $p_T^{hh} \sim 100$ GeV already. Then, while both HERWIG showers correctly reproduce the hard NLO emission in the high-p_T^{hh} region, the PYTHIA parton-shower produces much harder radiation and its ratio to the fixed-order prediction stagnates at ~ 2 over the remaining range. In di-Higgs production, the harder spectrum from PYTHIA was found to be due to too hard sub-leading jets produced solely in the shower [303] as compared to the older PYTHIA6 parton-shower. In other processes, like $t\bar{t}$ production, sizable differences between PYTHIA and HERWIG had also already been observed [304].

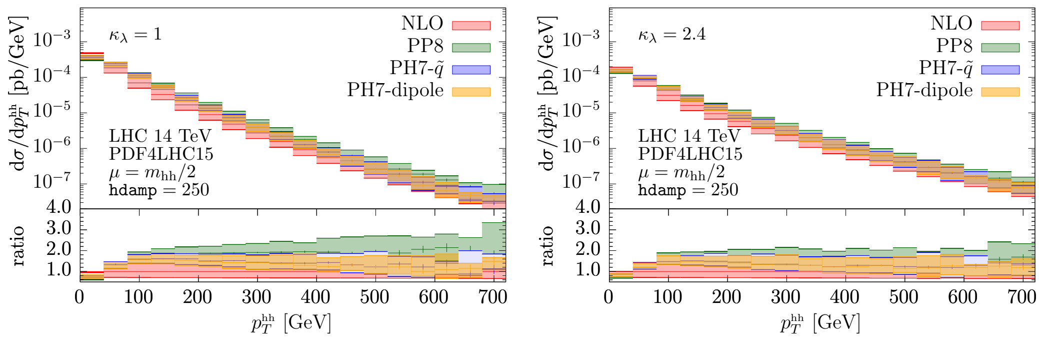

(a) (b)

Figure 11.6: The NLO fixed-order prediction is compared to results from the three parton-shower algorithms with respect to the transverse momentum of the Higgs boson pair system p_T^{hh} for (a) $\kappa_\lambda = 1$ and (b) $\kappa_\lambda = 2.4$.

As a way to estimate shower-matching uncertainties, the maximal transverse momentum allowed for shower emissions can be set in HERWIG by varying the so-called hard scale μ_Q. The parameter `HardScaleFactor` is varied to $c_Q = 0.5$, $c_Q = 2$ and applied on the central hard shower scale separately for the up- and down-variations of the renormalization and factorization scales $\mu_{R,F}$. In Fig. 11.7, the result is presented for the di-Higgs transverse momentum p_T^{hh} and the angular separation between the Higgs bosons ΔR^{hh}. The shower scale variations add to the renormalization/factorization scale uncertainties, bringing their common envelope to a corresponding 50% − 100% overall systematic uncertainty in the far-p_T^{hh} region of the distribution. The differences between the central PYTHIA and HERWIG predictions are then partly covered by the hard shower scale variations.

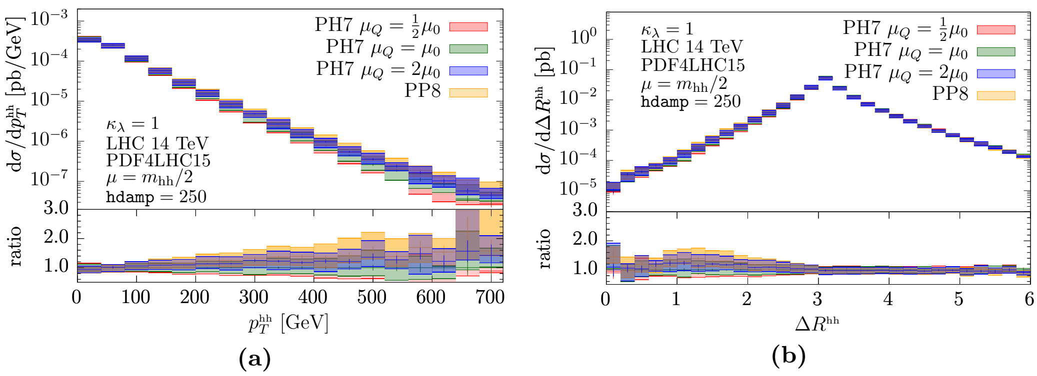

Figure 11.7: (a) The di-Higgs transverse momentum p_T^{hh} and (b) the angular separation ΔR^{hh} between the Higgs bosons are shown for variations of the HERWIG hard shower scale, which regulates the maximal allowed transverse momentum of shower emissions. The hard scale $\mu_Q = c_Q \mu_0$ is varied by $c_Q \in \{\frac{1}{2}, 2\}$ with respect to the default scale μ_0.

All in all, considering both scale and parton-shower uncertainties, the Higgs pair production process underlines the necessity of computing higher-order corrections in both fixed-order *and* logarithmic accuracy. In the future, it will be informative to study parton-shower (as well as other non-perturbative, e.g. hadronization) modeling effects in loop-induced color singlet production and try to reduce the sizable associated uncertainties.

12 Conclusion and Outlook

A precise determination of the top-quark mass is important for several reasons. Experimentally, its value is used in global electroweak fits, which are one of the most stringent tests of the SM. Theoretically, it largely affects the running of the Higgs quartic coupling and thus the stability of the SM vacuum. It also plays a role in many BSM models. Nowadays, experimental measurements have reduced the top-quark mass uncertainty to the point where new questions have to be asked. In particular:

- Are the theoretical descriptions of the $t\bar{t}$ final-state used in MC simulations for experimental analyses good enough?
- Do the uncertainties correctly cover the unknown higher-order corrections and other neglected contributions?
- What is the exact nature of the measured MC top-quark mass, and how does it relate to other mass schemes?

The answer to these questions requires a lot of effort from both the experimental and theoretical sides. One specific assumption made in most $t\bar{t}$ analyses relies on the factorization of top-quark pair production and decay: such a treatment is called the narrow-width approximation (NWA). In automated particle-level MC event generators, this description usually contains NLO QCD production of a $t\bar{t}$ pair and LO decay of the top quarks. The full parton-level final-state is then handed over to the parton-shower and hadronization algorithms. It was shown that for certain observables, higher-order and off-shell effects can lead to important differences. Specifically, NLO QCD corrections to the top-quark decay can have sizable effects on the kinematics of its decay products.

To reach a quantifiable answer to the first and second questions stated above, the determination of the top-quark mass in the dilepton channel is taken as an example. Experimentally, the template fit method provides an extraction of the MC top-quark mass. Following the same procedure, template distributions for $pp \to (e^+\nu_e)(\mu^-\bar{\nu}_\mu)b\bar{b}$ are produced at $\sqrt{s} = 13$ TeV using four different theoretical descriptions of the final-state at parton level. Starting from top-quark pair production at NLO QCD, three different levels of accuracy for the top-quark decay are investigated: LO, respectively NLO QCD, as well as decay by a parton-shower. These three NWA predictions are compared to a $W^+W^-b\bar{b}$ calculation at NLO QCD at parton level. The latter contains Feynman diagrams that are not present in the NWA, namely diagrams with top-quark legs that do not factorize, and diagrams with zero or one top-quark propagator only.

In an implementation similar to the ATLAS analysis, distributions of the lepton and b-jet invariant mass $m_{\ell b}$ are parametrized separately for a set of MC input top-quark masses. Once the parameters are fixed, only the top-quark mass is left as a free quantity to be determined by a fit to data. To compare the different calculations two-by-two, the parametrization from one theoretical prediction is used in an unbinned likelihood fit to pseudo-data drawn from another prediction. The offsets obtained in the extracted top-quark mass represent the systematic uncertainty accompanying the use of the incomplete set of diagrams. It is shown that NLO corrections to the top-quark decay in the NWA have an important effect on the extracted top-quark mass. In fact, the offset in the top-quark mass is opposite in sign and higher in absolute value than from NLO corrections to $t\bar{t}$ production. When comparing the NLO top-quark decay to the full $W^+W^-b\bar{b}$ computation, the offset is reduced to (0.83 ± 0.07) GeV. More importantly, the offset stemming from renormalization/factorization scale variations now overlap. These comparisons suggest that the scale uncertainties in $t\bar{t}$ production with LO top-quark decay are underestimated. While the NLO corrections to the top-quark decay describe correctly the emission of a hard jet from the final-state, the parton-shower is formally of LO accuracy in QCD. Yet, because it produces additional radiation as the parton level is fully showered down to hadronization scales, it comes close to the top-quark mass extracted from $W^+W^-b\bar{b}$ samples, with an offset of (-0.09 ± 0.07) GeV.

The studies presented above suffer from two complications: first, they were realized at parton level, and it is unclear if the bias in the extracted top-quark mass is as important at detector level. Second, they only compared pure $t\bar{t}$ predictions to the full $W^+W^-b\bar{b}$ computation, while usually single-top production in the Wt channel is also included in the signal. As a first attempt at curing both issues, a setup implemented in the ATLAS framework is presented, where particle-level distributions can be folded up to detector level. Bin migration matrices and detector efficiencies are derived from simulated $t\bar{t}$ samples produced at five different top-quark mass points. In parallel, $W^+W^-b\bar{b}$ samples are generated using the `bb4l` MC generator present in the Powheg-BOX-RES framework, and matched to the Pythia8 parton-shower. This time, the folding matrices from the $t\bar{t}$ prediction are used to bring the $W^+W^-b\bar{b}$ distribution of $m_{\ell b}$ to detector level. The same procedure of template parametrization and fit to pseudo-data is repeated at detector level, and the templates from $t\bar{t}$ and single-top Wt are compared to the full $W^+W^-b\bar{b}$ calculation. This procedure is fast, and avoids the need to simulate all MC variation samples. The offset in the extracted top-quark mass between $W^+W^-b\bar{b}$ and $t\bar{t}$+single-top predictions amounts to (-0.330 ± 0.022) GeV. A first preliminary fit to ATLAS data recorded in 2015 and 2016 (amounting to 36.2 fb^{-1}) is performed for both theoretical descriptions. The extracted top-quark mass from $t\bar{t}$ and $W^+W^-b\bar{b}$ calibration functions is equal to 172.90 ± 0.14 (stat.) $\pm$ 1.77 (syst.) GeV, respectively 172.54 ± 0.13 (stat.) $\pm$ 1.57 (est. syst.) GeV. The evaluation of systematic uncertainties is not complete yet, and the total uncertainty is expected to decrease once MC-related mismodeling is under better control. In relation to the third question given above, the folding setup might be useful to estimate the top-quark mass IR-dependence on e.g. the shower cutoff scale Q_0 in Herwig: in turn, this would help shed some light on the controversial relations between different mass definitions.

The top-quark mass also has sizable theoretical effects in the computation of Higgs boson pair production in gluon-gluon fusion at the LHC. This process is important since it is the golden channel to experimentally constrain the trilinear Higgs self-coupling. At LO, Higgs pair production takes place via an intermediate top-quark loop. At NLO, the virtual contributions are thus of two-loop order and the Feynman integrals contain up to four mass scales. Only part of the master integrals are known analytically at this point. Nevertheless, these integrals were evaluated numerically with the full top-quark mass dependence using sector decomposition. To allow for variations of the Higgs boson couplings to the QCD sector, a non-linear EFT framework is introduced in the form of the Electroweak Chiral Lagrangian (EWChL). At NLO in QCD, this class of extensions contains five couplings parametrizing variations from the SM: the top-Higgs Yukawa coupling c_t and the trilinear Higgs self-coupling c_{hhh}, as well as effective couplings for two-top-two-Higgs c_{tt}, gluon-gluon-Higgs c_{ggh} and two-gluons-two-Higgs c_{gghh} vertices.

The setup is based on a grid of virtual two-loop amplitudes for pre-sampled phase-space points in the SM. Cross-section results are then presented for Higgs pair production at NLO QCD with full top-quark mass dependence in the EWChL framework. Both inclusive and differential cross-sections are produced at $\sqrt{s} = 14$ TeV for several benchmark points characterizing the BSM parameter space. Inclusive cross-sections exhibit large K-factors up to ~ 2.34 depending on the considered benchmark point. In particular, once the full top-quark loops are taken into account, a sizable dependence of the K-factors on the top-quark couplings c_t and c_{tt} is found, as well as on the trilinear coupling c_{hhh}.

Finally, a MC event generator is put forward for use by experimentalists in Higgs pair searches. Within the Powheg-BOX-V2 framework, the MC generator `ggHH` for Higgs pair production in the SM at NLO QCD is extended with the possibility of varying the trilinear Higgs self-coupling and the top-Higgs Yukawa coupling. In this program, the hard NLO matrix-element can be matched to both Pythia8 and Herwig7 parton-showers. Some first studies suggest that there are considerable uncertainties associated to the parton-shower.

Challenging prospects and developments are still awaiting in top-quark and Higgs-boson physics. In consideration of the major advances and successes met in the last years, the question arises whether there is still hope to unveil New Physics at the LHC. While the LHC started as a discovery machine, it is now, perhaps surprisingly, regarded as a well-suited instrument for precision measurements. With the advent of the HL-LHC, the large amount of expected data will drive down statistical uncertainties. Increasingly, all questions examined in this work will gain in importance. Further approximations used in theoretical descriptions will need improving, and more fundamental issues need closer scrutiny − like the heavy-quark mass definition problem. These refinements will prove of extreme use in the measurement of the properties of the Higgs boson, especially of the true form of its potential. Precision might be crucial to disentangle BSM Higgs models, if deviations from the SM were to be discovered. Finally, new generations of colliders will hopefully see the light sooner or later, and keep the physics community hard at work for years to come. As *Star Trek* character Captain Jean-Luc Picard said, "Our mission is to go forward. [...] There's still much to do; still so much to learn."

Bibliography

[1] Particle Data Group collaboration, M. Tanabashi et al., *Review of Particle Physics*, *Phys. Rev. D* **98** (2018) 030001.

[2] CDF collaboration, F. Abe et al., *Observation of Top Quark Production in $\overline{p}p$ Collisions with the Collider Detector at Fermilab*, *Phys. Rev. Lett.* **74** (1995) 2626–2631.

[3] D0 collaboration, S. Abachi et al., *Observation of the top quark*, *Phys. Rev. Lett.* **74** (1995) 2632–2637.

[4] "LHC Top Working Group." `https://twiki.cern.ch/twiki/bin/view/LHCPhysics/LHCTopWG`.

[5] ATLAS collaboration, M. Aaboud et al., *Measurement of the top quark mass in the $t\bar{t} \to$ lepton+jets channel from $\sqrt{s} = 8$ TeV ATLAS data and combination with previous results*, *Submitted to: Eur. Phys. J.* (2018) [arXiv:`1810.01772`].

[6] CMS collaboration, V. Khachatryan et al., *Measurement of the top quark mass using proton-proton data at $\sqrt{s} = 7$ and 8 TeV*, *Phys. Rev.* **D93** (2016) 072004 [arXiv:`1509.04044`].

[7] P. Marquard, A.V. Smirnov, V.A. Smirnov et al., *Quark Mass Relations to Four-Loop Order in Perturbative QCD*, *Phys. Rev. Lett.* **114** (2015) 142002 [arXiv:`1502.01030`].

[8] M. Beneke and V.M. Braun, *Heavy quark effective theory beyond perturbation theory: Renormalons, the pole mass and the residual mass term*, *Nucl. Phys.* **B426** (1994) 301–343 [arXiv:`hep-ph/9402364`].

[9] I.I.Y. Bigi, M.A. Shifman, N.G. Uraltsev et al., *The Pole mass of the heavy quark. Perturbation theory and beyond*, *Phys. Rev.* **D50** (1994) 2234–2246 [arXiv:`hep-ph/9402360`].

[10] M. Beneke, *More on ambiguities in the pole mass*, *Phys. Lett.* **B344** (1995) 341–347 [arXiv:`hep-ph/9408380`].

[11] A.H. Hoang, C. Lepenik and M. Preisser, *On the Light Massive Flavor Dependence of the Large Order Asymptotic Behavior and the Ambiguity of the Pole Mass*, *JHEP* **09** (2017) 099 [arXiv:`1706.08526`].

[12] A.H. Hoang and I.W. Stewart, *Top Mass Measurements from Jets and the Tevatron Top-Quark Mass*, *Nucl. Phys. Proc. Suppl.* **185** (2008) 220–226 [arXiv:`0808.0222`].

[13] A.H. Hoang, S. Plätzer and D. Samitz, *On the Cutoff Dependence of the Quark Mass Parameter in Angular Ordered Parton Showers*, *JHEP* **10** (2018) 200 [arXiv:`1807.06617`].

[14] ATLAS collaboration, *Combined measurements of Higgs boson production and decay using up to 80 fb^{-1} of proton-proton collision data at $\sqrt{s} = 13$ TeV collected with the ATLAS experiment*, Tech. Rep. ATLAS-CONF-2018-031, CERN, Geneva, Jul 2018.

[15] CMS collaboration, *Combined measurements of the Higgs boson's couplings at $\sqrt{s} = 13$ TeV*, Tech. Rep. CMS-PAS-HIG-17-031, CERN, Geneva, 2018.

[16] ATLAS collaboration, *Combination of searches for Higgs boson pairs in pp collisions at 13 TeV with the ATLAS experiment.*, Tech. Rep. ATLAS-CONF-2018-043, CERN, Geneva, Sep 2018.

[17] P. Nason, *A New method for combining NLO QCD with shower Monte Carlo algorithms*, *JHEP* **11** (2004) 040 [arXiv:`hep-ph/0409146`].

[18] S. Frixione, P. Nason and C. Oleari, *Matching NLO QCD computations with Parton Shower simulations: the POWHEG method*, *JHEP* **11** (2007) 070 [arXiv:`0709.2092`].

[19] S. Alioli, P. Nason, C. Oleari et al., *A general framework for implementing NLO calculations in shower Monte Carlo programs: the POWHEG BOX*, *JHEP* **06** (2010) 043 [arXiv:`1002.2581`].

[20] Super-Kamiokande collaboration, Y. Fukuda et al., *Evidence for oscillation of atmospheric neutrinos*, *Phys. Rev. Lett.* **81** (1998) 1562–1567.

[21] S.L. Glashow, *The renormalizability of vector meson interactions*, *Nuclear Physics* **10** (1959) 107 – 117.

[22] S. Weinberg, *A model of leptons*, *Phys. Rev. Lett.* **19** (1967) 1264–1266.

[23] A. Salam and J.C. Ward, *Weak and electromagnetic interactions*, *Il Nuovo Cimento* **11** (1959) 568–577.

[24] D.J. Gross and F. Wilczek, *Ultraviolet behavior of non-abelian gauge theories*, *Phys. Rev. Lett.* **30** (1973) 1343–1346.

[25] H.D. Politzer, *Reliable perturbative results for strong interactions?*, *Phys. Rev. Lett.* **30** (1973) 1346–1349.

[26] ATLAS collaboration, *Standard Model Summary Plots Spring 2019*, Tech. Rep. ATL-PHYS-PUB-2019-010, CERN, Geneva, Mar 2019.

[27] F. Englert and R. Brout, *Broken symmetry and the mass of gauge vector mesons*, *Phys. Rev. Lett.* **13** (1964) 321–323.

[28] P.W. Higgs, *Broken symmetries and the masses of gauge bosons*, *Phys. Rev. Lett.* **13** (1964) 508–509.

[29] G.S. Guralnik, C.R. Hagen and T.W.B. Kibble, *Global conservation laws and massless particles*, *Phys. Rev. Lett.* **13** (1964) 585–587.

[30] J. Bardeen, L.N. Cooper and J.R. Schrieffer, *Theory of superconductivity*, *Phys. Rev.* **108** (1957) 1175–1204.

[31] T.D. Lee, *A Theory of Spontaneous T Violation*, *Phys. Rev. D* **8** (1973) 1226–1239.

[32] S. Dimopoulos and H. Georgi, *Softly Broken Supersymmetry and SU(5)*, *Nucl. Phys.* **B193** (1981) 150–162.

[33] LHC Higgs Cross Section Working Group collaboration, D. de Florian et al., *Handbook of LHC Higgs Cross Sections: 4. Deciphering the Nature of the Higgs Sector*, [arXiv:1610.07922].

[34] K.G. Chetyrkin and M.F. Zoller, *Three-loop β-functions for top-Yukawa and the Higgs self-interaction in the standard model*, *JHEP* **2012** (2012) 33.

[35] S. Chigusa, T. Moroi and Y. Shoji, *State-of-the-Art Calculation of the Decay Rate of Electroweak Vacuum in the Standard Model*, *Phys. Rev. Lett.* **119** (2017) 211801.

[36] G. Degrassi, S. Di Vita, J. Elias-Miró et al., *Higgs mass and vacuum stability in the Standard Model at NNLO*, *JHEP* **2012** (2012) 98.

[37] A.V. Bednyakov, B.A. Kniehl, A.F. Pikelner et al., *Stability of the electroweak vacuum: Gauge independence and advanced precision*, *Phys. Rev. Lett.* **115** (2015) 201802.

[38] J. Schechter and J.W.F. Valle, *Neutrino masses in SU(2) $\otimes$ U(1) theories*, *Phys. Rev. D* **22** (1980) 2227–2235.

[39] T. Yanagida, *Horizontal Symmetry and Masses of Neutrinos*, *Progress of Theoretical Physics* **64** (1980) 1103–1105.

[40] R.N. Mohapatra and G. Senjanovic, *Neutrino Mass and Spontaneous Parity Nonconservation*, *Phys. Rev. Lett.* **44** (1980) 912.

[41] F. Borzumati, Y. Grossman, E. Nardi et al., *Neutrino masses and mixing in supersymmetric models without R parity*, *Phys. Lett.* **B384** (1996) 123–130 [arXiv:hep-ph/9606251].

[42] N. Haba, M. Matsuda and M. Tanimoto, *Large neutrino flavor mixings and gauge mediated supersymmetry breaking scenario*, *Phys. Lett.* **B478** (2000) 351–357 [arXiv:hep-ph/9911511].

[43] B.S. DeWitt, *Quantum Theory of Gravity. I. The Canonical Theory*, *Phys. Rev.* **160** (1967) 1113–1148.

[44] B.S. DeWitt, *Quantum Theory of Gravity. II. The Manifestly Covariant Theory*, *Phys. Rev.* **162** (1967) 1195–1239.

[45] B.S. DeWitt, *Quantum Theory of Gravity. III. Applications of the Covariant Theory*, *Phys. Rev.* **162** (1967) 1239–1256.

[46] F. Zwicky, *Die Rotverschiebung von extragalaktischen Nebeln*, *Helvetica Physica Acta* **6** (1933) 110–127.

[47] H.W. Babcock, *The rotation of the Andromeda Nebula*, *Lick Observatory Bulletin* **19** (1939) 41–51.

[48] K.C. Freeman, *On the Disks of Spiral and S0 Galaxies*, **160** (1970) 811.

[49] V.C. Rubin and W.K. Ford, Jr., *Rotation of the Andromeda Nebula from a Spectroscopic Survey of Emission Regions*, **159** (1970) 379.

[50] K.G. Begeman, A.H. Broeils and R.H. Sanders, *Extended rotation curves of spiral galaxies - Dark haloes and modified dynamics*, **249** (1991) 523–537.

[51] A.D. Sakharov, *Violation of CP Invariance, C asymmetry, and baryon asymmetry of the universe*, *Pisma Zh. Eksp. Teor. Fiz.* **5** (1967) 32–35.

[52] Planck collaboration, P.A.R. Ade et al., *Planck 2013 results. XVI. Cosmological parameters*, *Astron. Astrophys.* **571** (2014) A16 [arXiv:1303.5076].

[53] S. Weinberg, *Gauge Hierarchies*, *Phys. Lett.* **82B** (1979) 387–391.

[54] M.D. Schwartz, *Quantum Field Theory and the Standard Model*. Cambridge University Press, 2014.

[55] M.E. Peskin and D.V. Schroeder, *An Introduction to Quantum Field Theory*. Addison-Wesley, Reading, USA, 1995.

[56] G. Isidori, *Lecture notes in Quantum Field Theory II*, Frühjahrsemester 2015, Universität Zürich.

[57] G. Buchalla, *Lecture notes for Introduction to the SM*, Wintersemester 2008, LMU München.

[58] G. Heinrich, *Lecture notes for Colorful Loops: Introduction to Quantum Chromodynamics and Loop Calculations*, Sommersemester 2018, Technische Universität München.

[59] H.B.G. Casimir, *On the Attraction Between Two Perfectly Conducting Plates*, *Indag. Math.* **10** (1948) 261–263.

[60] G. 't Hooft and M. Veltman, *Regularization and renormalization of gauge fields*, *Nuclear Physics B* **44** (1972) 189 – 213.

[61] G. Passarino and M. Veltman, *One-loop corrections for e^+e^- annihilation into $\mu^+\mu^-$ in the Weinberg model*, *Nuclear Physics B* **160** (1979) 151 – 207.

[62] A. Denner and S. Dittmaier, *Reduction schemes for one-loop tensor integrals*, *Nucl. Phys.* **B734** (2006) 62–115 [arXiv:`hep-ph/0509141`].

[63] T. Binoth, J.P. Guillet, G. Heinrich et al., *An algebraic/numerical formalism for one-loop multi-leg amplitudes*, *JHEP* **10** (2005) 015 [arXiv:`hep-ph/0504267`].

[64] J.M. Campbell, E.W.N. Glover and D.J. Miller, *One loop tensor integrals in dimensional regularization*, *Nucl. Phys.* **B498** (1997) 397–442 [arXiv:`hep-ph/9612413`].

[65] J. Fleischer, F. Jegerlehner and O.V. Tarasov, *Algebraic reduction of one loop Feynman graph amplitudes*, *Nucl. Phys.* **B566** (2000) 423–440 [arXiv:`hep-ph/9907327`].

[66] A.I. Davydychev, *A Simple formula for reducing Feynman diagrams to scalar integrals*, *Phys. Lett.* **B263** (1991) 107–111.

[67] Z. Bern, L.J. Dixon and D.A. Kosower, *Dimensionally regulated one loop integrals*, *Phys. Lett.* **B302** (1993) 299–308 [arXiv:`hep-ph/9212308`].

[68] C.G. Callan, *Broken scale invariance in scalar field theory*, *Phys. Rev. D* **2** (1970) 1541–1547.

[69] K. Symanzik, *Small distance behaviour in field theory and power counting*, *Communications in Mathematical Physics* **18** (1970) 227–246.

[70] K. Symanzik, *Small-distance-behaviour analysis and Wilson expansions*, *Communications in Mathematical Physics* **23** (1971) 49–86.

[71] J.C. Ward, *An Identity in Quantum Electrodynamics*, *Phys. Rev.* **78** (1950) 182–182.

[72] Y. Takahashi, *On the generalized Ward identity*, *Il Nuovo Cimento (1955-1965)* **6** (1957) 371–375.

[73] A.D. Martin, W.J. Stirling, R.S. Thorne et al., *Parton distributions for the LHC*, *The European Physical Journal C* **63** (2009) 189–285.

[74] S. Höche, "SLAC Theoretical Physics, Monte-Carlo Simulations." Stanford University. https://theory.slac.stanford.edu/our-research/simulations.

[75] T. Hahn, *Cuba—a library for multidimensional numerical integration*, *Computer Physics Communications* **168** (2005) 78 – 95.

[76] G.P. Lepage, *A new algorithm for adaptive multidimensional integration*, *Journal of Computational Physics* **27** (1978) 192 – 203.

[77] J.H. Friedman and M.H. Wright, *A nested partitioning procedure for numerical multiple integration*, *ACM Trans. Math. Softw.* **7** (1981) 76–92.

[78] W.H. Press and G.R. Farrar, *Recursive Stratified Sampling for Multidimensional Monte Carlo Integration*, *Computers in Physics* **4** (1990) 190–195.

[79] J. Berntsen, T.O. Espelid and A. Genz, *An Adaptive Algorithm for the Approximate Calculation of Multiple Integrals*, *ACM Trans. Math. Softw.* **17** (1991) 437–451.

[80] A. Buckley, J. Ferrando, S. Lloyd et al., *LHAPDF6: parton density access in the LHC precision era*, *The European Physical Journal C* **75** (2015) 132.

[81] J.M. Campbell, R.K. Ellis and W.T. Giele, *A multi-threaded version of MCFM*, *The European Physical Journal C* **75** (2015) 246.

[82] K. Arnold, M. Bähr, G. Bozzi et al., *VBFNLO: A parton level Monte Carlo for processes with electroweak bosons*, *Computer Physics Communications* **180** (2009) 1661 – 1670.

[83] J. Baglio et al., *VBFNLO: A Parton Level Monte Carlo for Processes with Electroweak Bosons - Manual for Version 2.7.0*, [arXiv:1107.4038].

[84] J. Baglio et al., *Release Note - VBFNLO 2.7.0*, [arXiv:1404.3940].

[85] Z. Bern, L.J. Dixon, F. Febres Cordero et al., *The BlackHat Library for One-Loop Amplitudes*, *J. Phys. Conf. Ser.* **523** (2014) 012051 [arXiv:1310.2808].

[86] V. Hirschi, R. Frederix, S. Frixione et al., *Automation of one-loop QCD corrections*, *JHEP* **05** (2011) 044 [arXiv:1103.0621].

[87] V. Hirschi, *New developments in MadLoop*, [arXiv:1111.2708].

[88] R. Pittau, *Status of MadLoop/aMC@NLO*, in *International Workshop on Future Linear Colliders (LCWS11) Granada, Spain, September 26-30, 2011*, 2012, [arXiv:1202.5781].

[89] J. Alwall, R. Frederix, S. Frixione et al., *The automated computation of tree-level and next-to-leading order differential cross sections, and their matching to parton shower simulations*, *JHEP* **2014** (2014) 79.

[90] F. Cascioli, P. Maierhöfer and S. Pozzorini, *Scattering amplitudes with open loops*, *Phys. Rev. Lett.* **108** (2012) 111601.

[91] F. Buccioni, S. Pozzorini and M. Zoller, *On-the-fly reduction of open loops*, *The European Physical Journal C* **78** (2018) 70.

[92] G. Cullen, N. Greiner, G. Heinrich et al., *Automated one-loop calculations with GoSam*, *The European Physical Journal C* **72** (2012) 1889.

[93] G. Cullen, H. van Deurzen, N. Greiner et al., *GoSam-2.0: a tool for automated one-loop calculations within the Standard Model and beyond*, *The European Physical Journal C* **74** (2014) 3001.

[94] S. Actis, A. Denner, L. Hofer et al., *Recursive generation of one-loop amplitudes in the Standard Model*, *JHEP* **04** (2013) 037 [arXiv:`1211.6316`].

[95] S. Actis, A. Denner, L. Hofer et al., *RECOLA: REcursive Computation of One-Loop Amplitudes*, *Comput. Phys. Commun.* **214** (2017) 140–173 [arXiv:`1605.01090`].

[96] G. Bevilacqua, M. Czakon, M.V. Garzelli et al., *HELAC-NLO*, *Comput. Phys. Commun.* **184** (2013) 986–997 [arXiv:`1110.1499`].

[97] S. Badger, B. Biedermann, P. Uwer et al., *Numerical evaluation of virtual corrections to multi-jet production in massless QCD*, *Computer Physics Communications* **184** (2013) 1981 – 1998.

[98] F. Campanario, T.M. Figy, S. Plätzer et al., *Electroweak Higgs Boson Plus Three Jet Production at Next-to-Leading-Order QCD*, *Phys. Rev. Lett.* **111** (2013) 211802.

[99] T. Binoth, F. Boudjema, G. Dissertori et al., *A proposal for a standard interface between Monte Carlo tools and one-loop programs*, *Computer Physics Communications* **181** (2010) 1612 – 1622.

[100] S. Alioli, S. Badger, J. Bellm et al., *Update of the Binoth Les Houches Accord for a standard interface between Monte Carlo tools and one-loop programs*, *Computer Physics Communications* **185** (2014) 560 – 571.

[101] P. Nogueira, *Automatic Feynman Graph Generation*, *Journal of Computational Physics* **105** (1993) 279 – 289.

[102] J.A.M. Vermaseren, *New features of FORM*, [arXiv:`math-ph/0010025`].

[103] T. Peraro, *Ninja: Automated integrand reduction via Laurent expansion for one-loop amplitudes*, *Computer Physics Communications* **185** (2014) 2771 – 2797.

[104] G. Cullen, J.P. Guillet, G. Heinrich et al., *Golem95C: A library for one-loop integrals with complex masses*, *Computer Physics Communications* **182** (2011) 2276 – 2284.

[105] J.P. Guillet, G. Heinrich and J.F. von Soden-Fraunhofen, *Tools for NLO automation: extension of the Golem95C integral library*, *Comput. Phys. Commun.* **185** (2014) 1828–1834 [arXiv:1312.3887].

[106] P. Mastrolia, G. Ossola, T. Reiter et al., *Scattering Amplitudes from Unitarity-based Reduction Algorithm at the Integrand-level*, *JHEP* **08** (2010) 080 [arXiv:1006.0710].

[107] R.K. Ellis and G. Zanderighi, *Scalar one-loop integrals for QCD*, *JHEP* **02** (2008) 002 [arXiv:0712.1851].

[108] A. van Hameren, *Oneloop: For the evaluation of one-loop scalar functions*, *Computer Physics Communications* **182** (2011) 2427 – 2438.

[109] S. Catani and M.H. Seymour, *A General algorithm for calculating jet cross-sections in NLO QCD*, *Nucl. Phys.* **B485** (1997) 291–419 [arXiv:hep-ph/9605323].

[110] S. Frixione, Z. Kunszt and A. Signer, *Three jet cross-sections to next-to-leading order*, *Nucl. Phys.* **B467** (1996) 399–442 [arXiv:hep-ph/9512328].

[111] S. Frixione, *A General approach to jet cross-sections in QCD*, *Nucl. Phys.* **B507** (1997) 295–314 [arXiv:hep-ph/9706545].

[112] G. Salam, *ICTP–SAIFR School on QCD and LHC physics, Sao Paulo, Brazil*, July 2015, CERN Theory Unit.

[113] G. Altarelli and G. Parisi, *Asymptotic Freedom in Parton Language*, *Nucl. Phys.* **B126** (1977) 298–318.

[114] Y.L. Dokshitzer, *Calculation of the Structure Functions for Deep Inelastic Scattering and e^+e^- Annihilation by Perturbation Theory in Quantum Chromodynamics.*, *Sov. Phys. JETP* **46** (1977) 641–653.

[115] V.N. Gribov and L.N. Lipatov, *Deep inelastic ep scattering in perturbation theory*, *Sov. J. Nucl. Phys.* **15** (1972) 438–450.

[116] M. Dasgupta, F.A. Dreyer, K. Hamilton et al., *Logarithmic accuracy of parton showers: a fixed-order study*, *JHEP* **09** (2018) 033 [arXiv:1805.09327].

[117] J. Bellm et al., *Herwig 7.0/Herwig++ 3.0 release note*, *Eur. Phys. J.* **C76** (2016) 196 [arXiv:1512.01178].

[118] S. Frixione and B.R. Webber, *Matching NLO QCD computations and parton shower simulations*, *JHEP* **2002** (2002) 029–029.

[119] S. Frixione, P. Nason and C. Oleari, *Matching NLO QCD computations with parton shower simulations: the POWHEG method*, *JHEP* **2007** (2007) 070–070.

[120] S. Gieseke, P. Stephens and B. Webber, *New formalism for QCD parton showers*, *JHEP* **12** (2003) 045 [arXiv:hep-ph/0310083].

[121] T. Sjöstrand, S. Mrenna and P.Z. Skands, *PYTHIA 6.4 Physics and Manual*, *JHEP* **05** (2006) 026 [arXiv:hep-ph/0603175].

[122] T. Sjöstrand, S. Mrenna and P.Z. Skands, *A Brief Introduction to PYTHIA 8.1*, *Comput. Phys. Commun.* **178** (2008) 852–867 [arXiv:0710.3820].

[123] T. Gleisberg, S. Höche, F. Krauss et al., *Event generation with SHERPA 1.1*, *JHEP* **02** (2009) 007 [arXiv:0811.4622].

[124] B. Andersson, G. Gustafson, G. Ingelman et al., *Parton fragmentation and string dynamics*, *Physics Reports* **97** (1983) 31 – 145.

[125] T. Sjöstrand, S. Ask, J.R. Christiansen et al., *An introduction to PYTHIA 8.2*, *Computer Physics Communications* **191** (2015) 159 – 177.

[126] A. Kupco, *Cluster hadronization in HERWIG 5.9*, in *Monte Carlo generators for HERA physics. Proceedings, Workshop, Hamburg, Germany, 1998-1999*, 292–300, 1998, [arXiv:hep-ph/9906412].

[127] S. Gieseke, F. Loshaj and P. Kirchgaeßer, *Soft and diffractive scattering with the cluster model in Herwig*, *The European Physical Journal C* **77** (2017) 156.

[128] D. Amati and G. Veneziano, *Preconfinement as a property of perturbative QCD*, *Physics Letters B* **83** (1979) 87–92.

[129] O.S. Brüning, P. Collier, P. Lebrun et al., *LHC Design Report*, CERN Yellow Reports: Monographs. CERN, Geneva, 2004.

[130] O. Buning, P. Collier, P. Lebrun et al., *LHC Design Report. 2. The LHC infrastructure and general services.* 2004.

[131] M. Benedikt, P. Collier, V. Mertens et al., *LHC Design Report. 3. The LHC injector chain.* 2004.

[132] "CERN Official Website." CERN. http://public.web.cern.ch/public/en/research/AccelComplex-en.html.

[133] ATLAS collaboration, G. Aad et al., *The ATLAS Experiment at the CERN Large Hadron Collider*, *JINST* **3** (2008) S08003.

[134] ATLAS collaboration, M. Aaboud et al., *Observation of Higgs boson production in association with a top quark pair at the LHC with the ATLAS detector*, *Phys. Lett.* **B784** (2018) 173–191 [arXiv:1806.00425].

[135] ATLAS collaboration, M. Aaboud et al., *Observation of light-by-light scattering in ultraperipheral Pb+Pb collisions with the ATLAS detector*, .

[136] ATLAS collaboration, M. Aaboud et al., *Study of the rare decays of B_s^0 and B^0 mesons into muon pairs using data collected during 2015 and 2016 with the ATLAS detector*, *Submitted to: JHEP* (2018) [arXiv:1812.03017].

[137] M. Aleksa, F. Bergsma, P.A. Giudici et al., *Measurement of the ATLAS solenoid magnetic field*. Dec 2007.

[138] ATLAS collaboration, J. Badiou et al., *ATLAS barrel toroid: Technical design report*, Technical Design Report ATLAS. CERN, Geneva, 1997.

[139] ATLAS collaboration, *ATLAS end-cap toroids: Technical Design Report*, Technical Design Report ATLAS. CERN, Geneva, 1997.

[140] ATLAS collaboration, M.S. Alam et al., *ATLAS inner detector: Technical design report. Vol. 2*. 1997.

[141] ATLAS collaboration, M.S. Alam et al., *ATLAS inner detector: Technical design report. Vol. 1*. 1997.

[142] ATLAS collaboration, M.S. Alam et al., *ATLAS pixel detector: Technical design report*. 1998.

[143] ATLAS collaboration, G. Aad et al., *Operation and performance of the ATLAS semiconductor tracker*, *JINST* **9** (2014) P08009 [arXiv:1404.7473].

[144] ATLAS TRT collaboration, *The ATLAS transition radiation tracker*, in *Astroparticle, particle and space physics, detectors and medical physics applications. Proceedings, 8th Conference, ICATPP 2003, Como, Italy, October 6-10, 2003*, 497–501, 2003, [arXiv:hep-ex/0311058], DOI.

[145] A.S. Boldyrev et al., *The ATLAS transition radiation tracker*, *Instrum. Exp. Tech.* **55** (2012) 323–334.

[146] F. Hügging, *The ATLAS Pixel Insertable B-layer (IBL)*, *Nuclear Instruments and Methods in Physics Research Section A: Accelerators, Spectrometers, Detectors and Associated Equipment* **650** (2011) 45 – 49.

[147] A. La Rosa, *The ATLAS Insertable B-Layer: from construction to operation*, *JINST* **11** (2016) C12036 [arXiv:1610.01994].

[148] H. Pernegger, *The Pixel Detector of the ATLAS Experiment for LHC Run-2*, Tech. Rep. ATL-INDET-PROC-2015-001. 06, CERN, Geneva, Feb 2015.

[149] ATLAS collaboration, *The Upgraded Pixel Detector of the ATLAS Experiment for Run-2 at the LHC*, Tech. Rep. ATL-INDET-PROC-2016-009, CERN, Geneva, Nov 2016.

[150] S. Viel et al., *Performance of silicon pixel detectors at small track incidence angles for the ATLAS Inner Tracker Upgrade*, *Nucl. Instrum. Meth.* **A831** (2016) 254–259.

[151] ATLAS collaboration, M. Aaboud et al., *Performance of the ATLAS Transition Radiation Tracker in Run 1 of the LHC: tracker properties*, *JINST* **12** (2017) P05002 [arXiv:1702.06473].

[152] ATLAS collaboration, *ATLAS liquid-argon calorimeter: Technical Design Report*, Technical Design Report ATLAS. CERN, Geneva, 1996.

[153] P. Strizenec, *Performance of the ATLAS liquid argon calorimeter after three years of LHC operation and plans for a future upgrade*, *Journal of Instrumentation* **9** (2014) C09007–C09007.

[154] ATLAS collaboration, *ATLAS tile calorimeter: Technical Design Report*, Technical Design Report ATLAS. CERN, Geneva, 1996.

[155] A. Hrynevich, *Performance of the ATLAS tile calorimeter*, *Journal of Instrumentation* **12** (2017) C06021–C06021.

[156] ATLAS collaboration, *ATLAS muon spectrometer: Technical Design Report*, Technical Design Report ATLAS. CERN, Geneva, 1997.

[157] D. Boscherini, *Performance and operation of the ATLAS Resistive Plate Chamber system in LHC Run-1*, *JINST* **9** (2014) C12039.

[158] K. Nikolopoulos et al., *Cathode strip chambers in ATLAS : Installation, commissioning and in situ performance*, in *Proceedings, 2008 IEEE Nuclear Science Symposium*, 2819–2824, 2008.

[159] M. Livan, *Monitored drift tubes in ATLAS*, *Nuclear Instruments and Methods in Physics Research Section A: Accelerators, Spectrometers, Detectors and Associated Equipment* **384** (1996) 214 – 218.

[160] K. Nagai, *Thin gap chambers in ATLAS*, *Nuclear Instruments and Methods in Physics Research Section A: Accelerators, Spectrometers, Detectors and Associated Equipment* **384** (1996) 219 – 221.

[161] ATLAS collaboration, M. Aad et al., *Performance of the ATLAS Trigger System in 2010*, *The European Physical Journal C* **72** (2012) 1849.

[162] ATLAS collaboration, A.R. Martínez, *The Run-2 ATLAS Trigger System*, *J. Phys. Conf. Ser.* **762** (2016) 012003.

[163] R. Brun and F. Rademakers, *Root — an object oriented data analysis framework*, *Nuclear Instruments and Methods in Physics Research Section A: Accelerators, Spectrometers, Detectors and Associated Equipment* **389** (1997) 81 – 86.

[164] J. Alwall et al., *A Standard format for Les Houches event files*, *Comput. Phys. Commun.* **176** (2007) 300–304 [arXiv:hep-ph/0609017].

[165] GEANT4 collaboration, S. Agostinelli et al., *GEANT4: A Simulation toolkit*, *Nucl. Instrum. Meth.* **A506** (2003) 250–303.

[166] E. Richter-Was, D. Froidevaux and L. Poggioli, *ATLFAST 2.0 a fast simulation package for ATLAS*, .

[167] ATLAS collaboration, G. Aad et al., *Measurement of the top quark mass with the template method in the $t\bar{t} \to \text{lepton} + \text{jets}$ channel using ATLAS data*, *The European Physical Journal C* **72** (2012) 2046.

[168] ATLAS collaboration, G. Aad et al., *Measurement of the top quark mass in the $t\bar{t} \to$ lepton+jets and $t\bar{t} \to$ dilepton channels using $\sqrt{s} = 7$ TeV ATLAS data*, *The European Physical Journal C* **75** (2015) 330.

[169] ATLAS collaboration, M. Aaboud et al., *Measurement of the $t\bar{t}$ production cross-section using $e\mu$ events with b-tagged jets in pp collisions at $\sqrt{s} = 7$ and 8 TeV with the ATLAS detector*, *The European Physical Journal C* **74** (2014) 3109.

[170] ATLAS collaboration, M. Aaboud et al., *Measurement of the top quark mass in the $t\bar{t}$ dilepton channel from $\sqrt{s} = 8$ TeV ATLAS data*, *Physics Letters B* **761** (2016) 350 – 371.

[171] ATLAS collaboration, M. Aaboud et al., *Measurement of lepton differential distributions and the top quark mass in $t\bar{t}$ production in pp collisions at $\sqrt{s} = 8$ TeV with the ATLAS detector*, *The European Physical Journal C* **77** (2017) 804.

[172] ATLAS collaboration, G. Aad et al., *Determination of the top-quark pole mass using $t\bar{t}$ + 1-jet events collected with the ATLAS experiment in 7 TeV pp collisions*, *JHEP* **10** (2015) 121 [arXiv:`1507.01769`].

[173] ATLAS collaboration, G. Aad et al., *Measurement of the top-quark mass in the fully hadronic decay channel from ATLAS data at $\sqrt{s} = 7$ TeV*, *The European Physical Journal C* **75** (2015) 158.

[174] ATLAS collaboration, M. Aaboud et al., *Top-quark mass measurement in the all-hadronic $t\bar{t}$ decay channel at $\sqrt{s} = 8$ TeV with the ATLAS detector*, *JHEP* **09** (2017) 118 [arXiv:`1702.07546`].

[175] M. Czakon and A. Mitov, *Top++: A Program for the Calculation of the Top-Pair Cross-Section at Hadron Colliders*, *Comput. Phys. Commun.* **185** (2014) 2930 [arXiv:`1112.5675`].

[176] ATLAS collaboration, *Studies on top-quark Monte Carlo modelling for Top2016*, Tech. Rep. ATL-PHYS-PUB-2016-020, CERN, Geneva, Sep 2016.

[177] ATLAS collaboration, *Studies on top-quark Monte Carlo modelling with Sherpa and MG5_aMC@NLO*, Tech. Rep. ATL-PHYS-PUB-2017-007, CERN, Geneva, May 2017.

[178] ATLAS collaboration, *Investigation of systematic uncertainties on the measurement of the top-quark mass using lepton transverse momenta*, Tech. Rep. ATL-PHYS-PUB-2018-001, CERN, Geneva, Feb 2018.

[179] ATLAS collaboration, *Improvements in $t\bar{t}$ modelling using NLO+PS Monte Carlo generators for Run2*, Tech. Rep. ATL-PHYS-PUB-2018-009, CERN, Geneva, Jul 2018.

[180] ATLAS collaboration, M. Aaboud et al., *Measurement of the top quark mass in the $t\bar{t} \to$ dilepton channel from $\sqrt{s} = 8$ TeV ATLAS data*, *Phys. Lett.* **B761** (2016) 350–371 [arXiv:1606.02179].

[181] J.M. Campbell, R.K. Ellis, P. Nason et al., *Top-pair production and decay at NLO matched with parton showers*, *JHEP* **04** (2015) 114 [arXiv:1412.1828].

[182] J. Bellm, S. Gieseke and S. Plätzer, *Merging NLO Multi-jet Calculations with Improved Unitarization*, *Eur. Phys. J.* **C78** (2018) 244 [arXiv:1705.06700].

[183] S. Höche, F. Krauss, P. Maierhöfer et al., *Next-to-leading order QCD predictions for top-quark pair production with up to two jets merged with a parton shower*, *Phys. Lett.* **B748** (2015) 74–78 [arXiv:1402.6293].

[184] S. Höche, P. Maierhöfer, N. Moretti et al., *Next-to-leading order QCD predictions for top-quark pair production with up to three jets*, *Eur. Phys. J.* **C77** (2017) 145 [arXiv:1607.06934].

[185] M. Czakon, D. Heymes and A. Mitov, *High-precision differential predictions for top-quark pairs at the LHC*, *Phys. Rev. Lett.* **116** (2016) 082003 [arXiv:1511.00549].

[186] M. Czakon, D. Heymes and A. Mitov, *Dynamical scales for multi-TeV top-pair production at the LHC*, *JHEP* **04** (2017) 071 [arXiv:1606.03350].

[187] M. Czakon, D. Heymes and A. Mitov, *fastNLO tables for NNLO top-quark pair differential distributions*, [arXiv:1704.08551].

[188] M. Czakon, D. Heymes, A. Mitov et al., *Top-pair production at the LHC through NNLO QCD and NLO EW*, *JHEP* **10** (2017) 186 [arXiv:1705.04105].

[189] W. Hollik and D. Pagani, *The electroweak contribution to the top quark forward-backward asymmetry at the Tevatron*, *Phys. Rev.* **D84** (2011) 093003 [arXiv:1107.2606].

[190] J.H. Kühn, A. Scharf and P. Uwer, *Weak Interactions in Top-Quark Pair Production at Hadron Colliders: An Update*, *Phys. Rev.* **D91** (2015) 014020 [arXiv:1305.5773].

[191] D. Pagani, I. Tsinikos and M. Zaro, *The impact of the photon PDF and electroweak corrections on $t\bar{t}$ distributions*, *Eur. Phys. J.* **C76** (2016) 479 [arXiv:1606.01915].

[192] W. Bernreuther, A. Brandenburg, Z.G. Si et al., *Top quark pair production and decay at hadron colliders*, *Nucl. Phys.* **B690** (2004) 81–137 [arXiv:hep-ph/0403035].

[193] K. Melnikov and M. Schulze, *NLO QCD corrections to top quark pair production and decay at hadron colliders*, *JHEP* **0908** (2009) 049 [arXiv:0907.3090].

[194] J.M. Campbell and R.K. Ellis, *Top-quark processes at NLO in production and decay*, *J. Phys.* **G42** (2015) 015005 [arXiv:1204.1513].

[195] M. Brucherseifer, F. Caola and K. Melnikov, $\mathcal{O}(\alpha_s^2)$ *corrections to fully-differential top quark decays*, *JHEP* **04** (2013) 059 [arXiv:1301.7133].

[196] J. Gao and A.S. Papanastasiou, *Top-quark pair-production and decay at high precision*, *Phys. Rev.* **D96** (2017) 051501 [arXiv:1705.08903].

[197] M. Beneke, P. Falgari, S. Klein et al., *Hadronic top-quark pair production with NNLL threshold resummation*, *Nucl. Phys.* **B855** (2012) 695–741 [arXiv:1109.1536].

[198] M. Cacciari, M. Czakon, M. Mangano et al., *Top-pair production at hadron colliders with next-to-next-to-leading logarithmic soft-gluon resummation*, *Phys. Lett.* **B710** (2012) 612–622 [arXiv:1111.5869].

[199] A. Ferroglia, S. Marzani, B.D. Pecjak et al., *Boosted top production: factorization and resummation for single-particle inclusive distributions*, *JHEP* **01** (2014) 028 [arXiv:1310.3836].

[200] A. Broggio, A.S. Papanastasiou and A. Signer, *Renormalization-group improved fully differential cross sections for top pair production*, *JHEP* **10** (2014) 98 [arXiv:1407.2532].

[201] N. Kidonakis, *High-order threshold corrections for top-pair and single-top production*, in *Proceedings, Meeting of the APS Division of Particles and Fields (DPF 2015): Ann Arbor, Michigan, USA, 4-8 Aug 2015*, 2015, [arXiv:1509.07848].

[202] B.D. Pecjak, D.J. Scott, X. Wang et al., *Resummed differential cross sections for top-quark pairs at the LHC*, *Phys. Rev. Lett.* **116** (2016) 202001 [arXiv:1601.07020].

[203] M.L. Czakon et al., *Top quark pair production at NNLO+NNLL$'$ in QCD combined with electroweak corrections*, in *11th International Workshop on Top Quark Physics (TOP2018) Bad Neuenahr, Germany, September 16-21, 2018*, 2019, [arXiv:1901.08281].

[204] G. Heinrich, A. Maier, R. Nisius et al., *NLO QCD corrections to $W^+W^-b\bar{b}$ production with leptonic decays in the light of top quark mass and asymmetry measurements*, *JHEP* **1406** (2014) 158 [arXiv:1312.6659].

[205] S. Frixione, E. Laenen, P. Motylinski et al., *Single-top hadroproduction in association with a W boson*, *JHEP* **07** (2008) 029 [arXiv:0805.3067].

[206] A. Denner, S. Dittmaier, S. Kallweit et al., *NLO QCD corrections to WWbb production at hadron colliders*, *Phys. Rev. Lett.* **106** (2011) 052001 [arXiv:1012.3975].

[207] A. Denner, S. Dittmaier, S. Kallweit et al., *NLO QCD corrections to off-shell top-antitop production with leptonic decays at hadron colliders*, *JHEP* **10** (2012) 110 [arXiv:1207.5018].

[208] G. Bevilacqua, M. Czakon, A. van Hameren et al., *Complete off-shell effects in top quark pair hadroproduction with leptonic decay at next-to-leading order*, *JHEP* **02** (2011) 083 [arXiv:1012.4230].

[209] R. Frederix, *Top Quark Induced Backgrounds to Higgs Production in the $WW^{(*)} \to ll\nu\nu$ Decay Channel at Next-to-Leading-Order in QCD*, *Phys. Rev. Lett.* **112** (2014) 082002 [arXiv:1311.4893].

[210] F. Cascioli, S. Kallweit, P. Maierhöfer et al., *A unified NLO description of top-pair and associated Wt production*, *Eur. Phys. J.* **C74** (2014) 2783 [arXiv:1312.0546].

[211] A. Denner and M. Pellen, *Off-shell production of top-antitop pairs in the lepton+jets channel at NLO QCD*, *JHEP* **02** (2018) 013 [arXiv:1711.10359].

[212] G. Heinrich, A. Maier, R. Nisius et al., *NLO and off-shell effects in top quark mass determinations*, *JHEP* **07** (2018) 129 [arXiv:1709.08615].

[213] A. Denner, S. Dittmaier, S. Kallweit et al., *NLO QCD corrections to off-shell top-antitop production with leptonic decays at hadron colliders*, *JHEP* **2012** (2012) 110.

[214] S. Höche and J.C. Winter. Private communication.

[215] C. Duhr, S. Höche and F. Maltoni, *Color-dressed recursive relations for multi-parton amplitudes*, *JHEP* **08** (2006) 062 [arXiv:hep-ph/0607057].

[216] T. Gleisberg and S. Höche, *Comix, a new matrix element generator*, *JHEP* **12** (2008) 039 [arXiv:0808.3674].

[217] T. Gleisberg, S. Höche, F. Krauss et al., *How to calculate colourful cross sections efficiently*, [arXiv:0808.3672].

[218] F. Krauss, R. Kuhn and G. Soff, *AMEGIC++ 1.0: A Matrix element generator in C++*, *JHEP* **02** (2002) 044 [arXiv:hep-ph/0109036].

[219] J. Butterworth et al., *PDF4LHC recommendations for LHC Run II*, *J. Phys.* **G43** (2016) 023001 [arXiv:1510.03865].

[220] M. Cacciari, G.P. Salam and G. Soyez, *The Anti-k(t) jet clustering algorithm*, *JHEP* **04** (2008) 063 [arXiv:0802.1189].

[221] M. Cacciari and G.P. Salam, *Dispelling the N^3 myth for the k_t jet-finder*, *Phys. Lett.* **B641** (2006) 57–61 [arXiv:hep-ph/0512210].

[222] M. Cacciari, G.P. Salam and G. Soyez, *FastJet User Manual*, *Eur. Phys. J.* **C72** (2012) 1896 [arXiv:1111.6097].

[223] S. Höche, J. Huang, G. Luisoni et al., *Zero and one jet combined next-to-leading order analysis of the top quark forward-backward asymmetry*, *Phys. Rev.* **D88** (2013) 014040 [arXiv:1306.2703].

[224] A. Buckley, J. Butterworth, L. Lönnblad et al., *Rivet user manual*, *Comput. Phys. Commun.* **184** (2013) 2803–2819 [arXiv:1003.0694].

[225] C.G. Lester and D.J. Summers, *Measuring masses of semiinvisibly decaying particles pair produced at hadron colliders*, *Phys. Lett.* **B463** (1999) 99–103 [arXiv:hep-ph/9906349].

[226] A. Barr, C. Lester and P. Stephens, *m(T2): The Truth behind the glamour*, *J. Phys.* **G29** (2003) 2343–2363 [arXiv:hep-ph/0304226].

[227] C. Buttar, J. D'Hondt, M. Kramer et al., *Standard Model Handles and Candles Working Group: Tools and Jets Summary Report*, March 2008.

[228] I. Fredholm, *Sur une classe d'équations fonctionnelles*, *Acta Math.* **27** (1903) 365–390.

[229] V. Blobel, *An Unfolding method for high-energy physics experiments*, in *Advanced Statistical Techniques in Particle Physics. Proceedings, Conference, Durham, UK, March 18-22, 2002*, 258–267, 2002, [arXiv:hep-ex/0208022], http://www.ippp.dur.ac.uk/Workshops/02/statistics/proceedings//blobel2.pdf.

[230] S. Schmitt, *Data Unfolding Methods in High Energy Physics*, *EPJ Web Conf.* **137** (2017) 11008 [arXiv:1611.01927].

[231] ATLAS collaboration, M. Aaboud et al., *Measurements of top-quark pair spin correlations in the $e\mu$ channel at $\sqrt{s} = 13$ TeV using pp collisions in the ATLAS detector*, *Submitted to: Eur. Phys. J.* (2019) [arXiv:1903.07570].

[232] T. Ježo, J.M. Lindert, P. Nason et al., *An NLO+PS generator for $t\bar{t}$ and Wt production and decay including non-resonant and interference effects*, *Eur. Phys. J.* **C76** (2016) 691 [arXiv:1607.04538].

[233] T. Ježo and P. Nason, *On the Treatment of Resonances in Next-to-Leading Order Calculations Matched to a Parton Shower*, *JHEP* **12** (2015) 065 [arXiv:1509.09071].

[234] ATLAS collaboration, M. Aaboud et al., *Electron reconstruction and identification in the ATLAS experiment using the 2015 and 2016 LHC proton-proton collision data at $\sqrt{s}$ = 13 TeV*, *Submitted to: Eur. Phys. J.* (2019) [arXiv:1902.04655].

[235] ATLAS collaboration, G. Aad et al., *Muon reconstruction performance of the ATLAS detector in proton–proton collision data at $\sqrt{s}$ =13 TeV*, *Eur. Phys. J.* **C76** (2016) 292 [arXiv:1603.05598].

[236] ATLAS collaboration, *ATLAS jet and missing energy reconstruction, calibration and performance in LHC Run-2*, Tech. Rep. ATL-PHYS-PROC-2017-045. 06, CERN, Geneva, May 2017.

[237] ATLAS collaboration, *The ATLAS Tau Trigger in Run 2*, Tech. Rep. ATLAS-CONF-2017-061, CERN, Geneva, Jul 2017.

[238] ATLAS collaboration, G. Aad et al., *Performance of b-Jet Identification in the ATLAS Experiment*, *JINST* **11** (2016) P04008 [arXiv:1512.01094].

[239] ATLAS collaboration, M. Aaboud et al., *Performance of the ATLAS Trigger System in 2015*, *Eur. Phys. J.* **C77** (2017) 317 [arXiv:1611.09661].

[240] ATLAS collaboration, *Electron and photon energy calibration with the ATLAS detector using data collected in 2015 at $\sqrt{s} = 13$ TeV*, Tech. Rep. ATL-PHYS-PUB-2016-015, CERN, Geneva, Aug 2016.

[241] ATLAS collaboration, *Electron efficiency measurements with the ATLAS detector using the 2015 LHC proton-proton collision data*, Tech. Rep. ATLAS-CONF-2016-024, CERN, Geneva, 2016.

[242] ATLAS collaboration, *Electron identification with the ATLAS detector*, Tech. Rep. ATL-PHYS-PROC-2017-173, CERN, Geneva, Sep 2017. 10.22323/1.314.0769.

[243] ATLAS collaboration, G. Aad et al., *Performance of pile-up mitigation techniques for jets in pp collisions at $\sqrt{s} = 8$ TeV using the ATLAS detector*, *Eur. Phys. J.* **C76** (2016) 581 [arXiv:1510.03823].

[244] ATLAS collaboration, M. Aaboud et al., *Jet energy scale measurements and their systematic uncertainties in proton-proton collisions at $\sqrt{s} = 13$ TeV with the ATLAS detector*, *Phys. Rev.* **D96** (2017) 072002 [arXiv:1703.09665].

[245] M. Cacciari and G.P. Salam, *Pileup subtraction using jet areas*, *Phys. Lett.* **B659** (2008) 119–126 [arXiv:0707.1378].

[246] ATLAS collaboration, G. Aad et al., *Jet energy measurement and its systematic uncertainty in proton-proton collisions at $\sqrt{s} = 7$ TeV with the ATLAS detector*, *Eur. Phys. J.* **C75** (2015) 17 [arXiv:1406.0076].

[247] ATLAS collaboration, A. Calandri, *Flavour tagging algorithms and performance at the ATLAS experiment*, no. ATL-PHYS-PROC-2016-105. Geneva, Aug 2016.

[248] M. Lehmacher, *b-Tagging Algorithms and their Performance at ATLAS*, in *Proceedings, 34th International Conference on High Energy Physics (ICHEP 2008): Philadelphia, Pennsylvania, July 30-August 5, 2008*, 2008, [arXiv:0809.4896], http://weblib.cern.ch/abstract?ATL-PHYS-PROC-2008-052.

[249] ATLAS collaboration, M. Aaboud et al., *Secondary vertex finding for jet flavour identification with the ATLAS detector*, no. ATL-PHYS-PUB-2017-011. Geneva, Jun 2017.

[250] G. Piacquadio and C. Weiser, *A new inclusive secondary vertex algorithm for b-jet tagging in ATLAS*, *Journal of Physics: Conference Series* **119** (2008) 032032.

[251] ATLAS collaboration, *Optimisation of the ATLAS b-tagging performance for the 2016 LHC Run*, Tech. Rep. ATL-PHYS-PUB-2016-012, CERN, Geneva, Jun 2016.

[252] A. Knue, R. Nisius, B. Pearson and J. Riménez Peña. Private communication.

[253] NNPDF collaboration, R.D. Ball et al., *Parton distributions for the LHC Run II*, *JHEP* **04** (2015) 040 [arXiv:1410.8849].

[254] *ATLAS Run 1 Pythia8 tunes*, Tech. Rep. ATL-PHYS-PUB-2014-021, CERN, Geneva, Nov 2014.

[255] *Simulation of top quark production for the ATLAS experiment at sqrt(s) = 13 TeV*, Tech. Rep. ATL-PHYS-PUB-2016-004, CERN, Geneva, Jan 2016.

[256] A. Maier, *Precision measurements of the top quark mass in the dileptonic top quark pair decay channel at ATLAS*, February 2016, Ludwig-Maximilians-Universität München. https://publications.mppmu.mpg.de/2016/MPP-2016-76/FullText.pdf.

[257] ATLAS collaboration, G. Aad et al., *Measurement of the top quark mass in the $t\bar{t} \to$ lepton+jets and $t\bar{t} \to$ dilepton channels using $\sqrt{s} = 7$ TeV ATLAS data*, *Eur. Phys. J.* **C75** (2015) 330 [arXiv:1503.05427].

[258] F. James, *MINUIT Function Minimization and Error Analysis: Reference Manual Version 94.1*. 1994.

[259] R. Nisius, *On the combination of correlated estimates of a physics observable*, *Eur. Phys. J.* **C74** (2014) 3004 [arXiv:1402.4016].

[260] R. Barlow, *Application of the Bootstrap resampling technique to Particle Physics experiments*, 1999. http://www.hep.man.ac.uk/preprints/1999.html.

[261] J. Alwall, R. Frederix, S. Frixione et al., *The automated computation of tree-level and next-to-leading order differential cross sections, and their matching to parton shower simulations*, *JHEP* **07** (2014) 079 [arXiv:1405.0301].

[262] ATLAS collaboration, G. Aad et al., *Jet energy resolution in proton-proton collisions at $\sqrt{s} = 7$ TeV recorded in 2010 with the ATLAS detector*, *Eur. Phys. J.* **C73** (2013) 2306 [arXiv:1210.6210].

[263] ATLAS collaboration, M. Aaboud et al., *Measurements of b-jet tagging efficiency with the ATLAS detector using $t\bar{t}$ events at $\sqrt{s} = 13$ TeV*, *JHEP* **08** (2018) 089 [arXiv:1805.01845].

[264] ATLAS collaboration, *Top quark mass in ATLAS*, in *Proceedings, 10th International Workshop on Top Quark Physics (TOP2017): Braga, Portugal, September 17-22, 2017*, 2017, [arXiv:1711.09763].

[265] P. Nason, *The Top Quark Mass at the LHC*, in *Proceedings, Old and New Strong Interactions from LHC to Future Colliders (LFC17): Trento, Italy, September 11-15, 2017*, 65–70, 2017, [arXiv:1801.04826].

[266] ATLAS collaboration, G. Aad et al., *Observation of a new particle in the search for the Standard Model Higgs boson with the ATLAS detector at the LHC*, *Phys. Lett.* **B716** (2012) 1–29 [arXiv:1207.7214].

[267] CMS collaboration, S. Chatrchyan et al., *Observation of a new boson at a mass of 125 GeV with the CMS experiment at the LHC*, *Phys. Lett.* **B716** (2012) 30–61 [arXiv:1207.7235].

[268] E.W.N. Glover and J.J. van der Bij, *Higgs Boson Pair Production via Gluon Fusion*, *Nucl. Phys.* **B309** (1988) 282.

[269] M. Spira, A. Djouadi, D. Graudenz et al., *Higgs boson production at the LHC*, *Nucl. Phys.* **B453** (1995) 17–82 [arXiv:hep-ph/9504378].

[270] R. Bonciani, A. Ferroglia, P. Mastrolia et al., *Two-loop N(F)=1 QED Bhabha scattering differential cross section*, *Nucl. Phys.* **B701** (2004) 121–179 [arXiv:hep-ph/0405275].

[271] C. Anastasiou, S. Beerli, S. Bucherer et al., *Two-loop amplitudes and master integrals for the production of a Higgs boson via a massive quark and a scalar-quark loop*, *JHEP* **01** (2007) 082 [arXiv:hep-ph/0611236].

[272] G. Degrassi, P.P. Giardino and R. Gröber, *On the two-loop virtual QCD corrections to Higgs boson pair production in the Standard Model*, *Eur. Phys. J.* **C76** (2016) 411 [arXiv:1603.00385].

[273] R. Bonciani, V. Del Duca, H. Frellesvig et al., *Next-to-leading order QCD corrections to the decay width H Z*, *JHEP* **08** (2015) 108 [arXiv:1505.00567].

[274] T. Gehrmann, S. Guns and D. Kara, *The rare decay $H \to Z\gamma$ in perturbative QCD*, *JHEP* **09** (2015) 038 [arXiv:1505.00561].

[275] R. Gröber, A. Maier and T. Rauh, *Reconstruction of top-quark mass effects in Higgs pair production and other gluon-fusion processes*, *JHEP* **03** (2018) 020 [arXiv:1709.07799].

[276] R. Bonciani, G. Degrassi, P.P. Giardino et al., *Analytical Method for Next-to-Leading-Order QCD Corrections to Double-Higgs Production*, *Phys. Rev. Lett.* **121** (2018) 162003 [arXiv:1806.11564].

[277] G. Mishima, *High-Energy Expansion of Two-Loop Massive Four-Point Diagrams*, *JHEP* **02** (2019) 080 [arXiv:1812.04373].

[278] J. Davies, G. Mishima, M. Steinhauser et al., *Double Higgs boson production at NLO in the high-energy limit: complete analytic results*, *JHEP* **01** (2019) 176 [arXiv:1811.05489].

[279] S. Borowka, N. Greiner, G. Heinrich et al., *Full top quark mass dependence in Higgs boson pair production at NLO*, *JHEP* **10** (2016) 107 [arXiv:1608.04798].

[280] A. von Manteuffel and C. Studerus, *Reduze 2 - Distributed Feynman Integral Reduction*, [arXiv:1201.4330].

[281] J. Carter and G. Heinrich, *SecDec: A general program for sector decomposition*, *Comput. Phys. Commun.* **182** (2011) 1566–1581 [arXiv:1011.5493].

[282] S. Borowka, J. Carter and G. Heinrich, *Numerical Evaluation of Multi-Loop Integrals for Arbitrary Kinematics with SecDec 2.0*, *Comput. Phys. Commun.* **184** (2013) 396–408 [arXiv:1204.4152].

[283] S. Borowka, G. Heinrich, S.P. Jones et al., *SecDec-3.0: numerical evaluation of multi-scale integrals beyond one loop*, *Comput. Phys. Commun.* **196** (2015) 470–491 [arXiv:1502.06595].

[284] S.P. Jones, *Automation of 2-loop Amplitude Calculations*, *PoS* **LL2016** (2016) 069 [arXiv:1608.03846].

[285] S. Borowka, G. Heinrich, S. Jahn et al., *A GPU compatible quasi-Monte Carlo integrator interfaced to pySecDec*, *Comp. Phys. Comm.* (2018) [arXiv:1811.11720].

[286] J. Baglio, F. Campanario, S. Glaus et al., *Gluon fusion into Higgs pairs at NLO QCD and the top mass scheme*, [arXiv:1811.05692].

[287] G. Buchalla, O. Catá and C. Krause, *Complete Electroweak Chiral Lagrangian with a Light Higgs at NLO*, *Nucl. Phys.* **B880** (2014) 552–573 [arXiv:1307.5017].

[288] G. Buchalla, O. Catá and C. Krause, *On the Power Counting in Effective Field Theories*, *Phys. Lett.* **B731** (2014) 80–86 [arXiv:1312.5624].

[289] G. Buchalla, M. Capozi, A. Celis et al., *Higgs boson pair production in non-linear Effective Field Theory with full m_t-dependence at NLO QCD*, *JHEP* **09** (2018) 057 [arXiv:1806.05162].

[290] C. Degrande, C. Duhr, B. Fuks et al., *UFO - The Universal FeynRules Output*, *Comput. Phys. Commun.* **183** (2012) 1201–1214 [arXiv:1108.2040].

[291] A. Alloul, N.D. Christensen, C. Degrande et al., *FeynRules 2.0 - A complete toolbox for tree-level phenomenology*, *Comput. Phys. Commun.* **185** (2014) 2250–2300 [arXiv:1310.1921].

[292] N.D. Christensen and C. Duhr, *FeynRules - Feynman rules made easy*, *Comput. Phys. Commun.* **180** (2009) 1614–1641 [arXiv:0806.4194].

[293] A. Carvalho, M. Dall'Osso, T. Dorigo et al., *Higgs Pair Production: Choosing Benchmarks With Cluster Analysis*, *JHEP* **04** (2016) 126 [arXiv:1507.02245].

[294] A. Djouadi, M. Spira and P. Zerwas, *Production of Higgs bosons in proton colliders. QCD corrections*, *Physics Letters B* **264** (1991) 440 – 446.

[295] S. Dawson, *Radiative corrections to Higgs boson production*, *Nucl. Phys.* **B359** (1991) 283–300.

[296] R. Gröber, M. Mühlleitner, M. Spira et al., *NLO QCD Corrections to Higgs Pair Production including Dimension-6 Operators*, *JHEP* **09** (2015) 092 [arXiv:1504.06577].

[297] A. Azatov, R. Contino, G. Panico et al., *Effective field theory analysis of double Higgs boson production via gluon fusion*, *Phys. Rev.* **D92** (2015) 035001 [arXiv:1502.00539].

[298] CMS collaboration, A.M. Sirunyan et al., *Measurement and interpretation of differential cross sections for Higgs boson production at $\sqrt{s} = 13$ TeV*, *Phys. Lett.* **B792** (2019) 369 [arXiv:1812.06504].

[299] G. Heinrich, S.P. Jones, M. Kerner et al., *Probing the trilinear Higgs boson coupling in di-Higgs production at NLO QCD including parton shower effects*, [arXiv:1903.08137].

[300] G. Heinrich, S.P. Jones, M. Kerner et al., *NLO predictions for Higgs boson pair production with full top quark mass dependence matched to parton showers*, *JHEP* **08** (2017) 088 [arXiv:1703.09252].

[301] R.W. Clough and J.L. Tocher, *Finite Element Stiffness Matrices for Analysis of Plate Bending. Proceedings, Conference on Matrix Methods in Structural Analysis*, 515–545, Nov. 1966.

[302] E. Jones, T. Oliphant, P. Peterson et al., *SciPy: Open source scientific tools for Python*, 2001. http://www.scipy.org/.

[303] *Les Houches 2017: Physics at TeV Colliders Standard Model Working Group Report*, 2018.

[304] S. Ferrario Ravasio, T. Ježo, P. Nason et al., *A Theoretical Study of Top-Mass Measurements at the LHC Using NLO+PS Generators of Increasing Accuracy*, [arXiv:1801.03944].

A Further template fit plots

A better understanding of the discrepancy between the NLO_{full} prediction and the $\text{NLO}_{\text{NWA}}^{\text{NLOdec}}$, respectively NLO_{PS} calculations is needed. Compared to the NLO_{full} pseudo-data, the $\text{NLO}_{\text{NWA}}^{\text{NLOdec}}$ prediction leads to a rather large offset in the top-quark mass of (0.83 ± 0.07) GeV. On the other hand, the NLO_{PS} prediction gives an offset to the $W^+W^-b\bar{b}$ pseudo-data of only (-0.09 ± 0.07) GeV. New parton-showered predictions $(n_{\text{max}}^{\text{prod}}, n_{\text{max}}^{\text{dec}})$ are produced where the shower is terminated after a certain number of emissions n_{max} in the $t\bar{t}$ production and decay showers. In Fig. A.1, the pseudo-data from these predictions are compared to the full parton-shower and the $\text{NLO}_{\text{NWA}}^{\text{NLOdec}}$ calibration function and pseudo-data. For each of the samples, the offset in m_t is given as a colored bar (in blue for the $\text{NLO}_{\text{NWA}}^{\text{NLOdec}}$ calibration function, respectively in red when using the NLO_{PS} calibration). Then, for only one allowed emission in both production and decay showers, the top-quark mass offset between $\text{NLO}_{\text{PS}}^{(1,1)}$ and $\text{NLO}_{\text{NWA}}^{\text{NLOdec}}$ is reduced to (-0.11 ± 0.06) GeV. Thus, the additional radiation accounts for the observed discrepancy in the offsets.

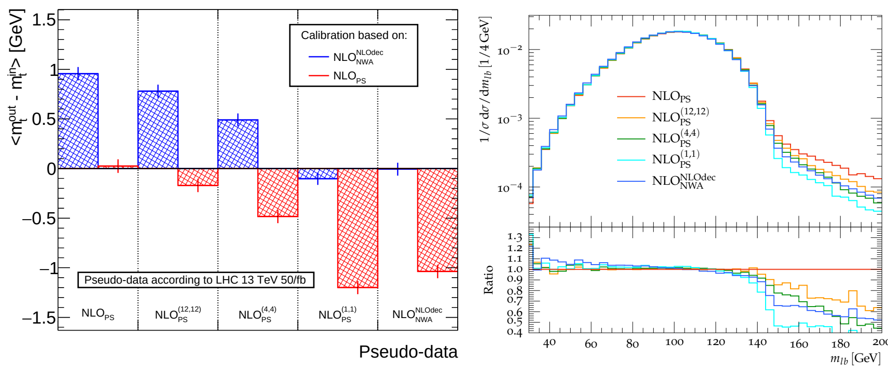

(a) (b)

Figure A.1: (a) The offsets fitted from the $m_{\ell b}$ distribution are shown for $\text{NLO}_{\text{PS}}^{(n_{\text{max}}^{\text{prod}}, n_{\text{max}}^{\text{dec}})}$ restricted-shower pseudo-data samples. (b) The normalized $m_{\ell b}$ distribution is plotted for the mentioned predictions at $m_t = 172.5$ GeV.

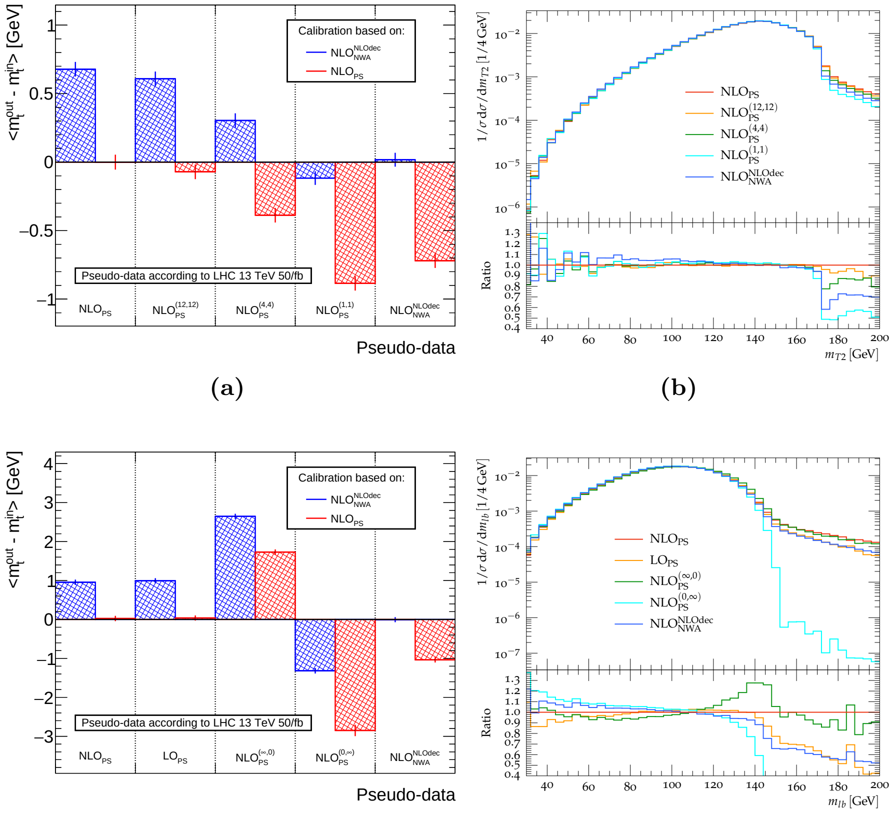

(a) (b) (c) (d)

Figure A.2: (a-b) Same as A.1 for m_{T2}. (c-d) Same as Fig. A.1, but for the NLO$_{\mathrm{PS}}$ and LO$_{\mathrm{PS}}$ cases, as well as for pseudo-data sets generated by predictions where the decay shower, respectively the production shower are entirely deactivated.

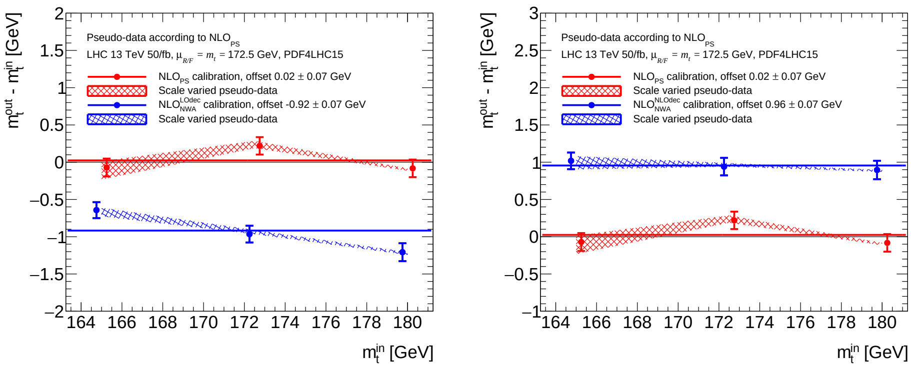

(a) (b)

Figure A.3: Further band plots from $m_{\ell b}$ fitted pseudo-data sets.

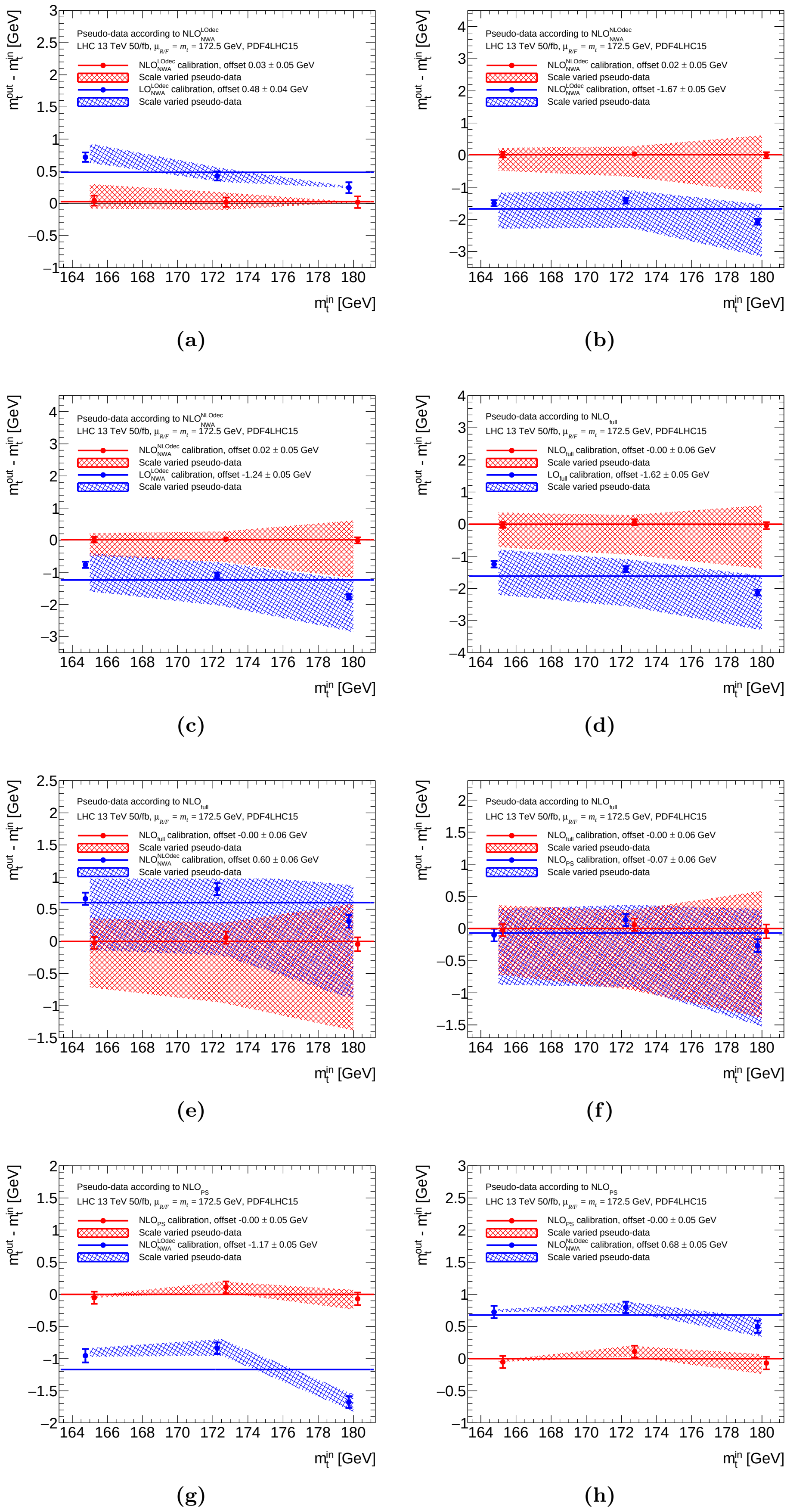

Figure A.4: Further band plots from m_{T2} fitted pseudo-data sets.

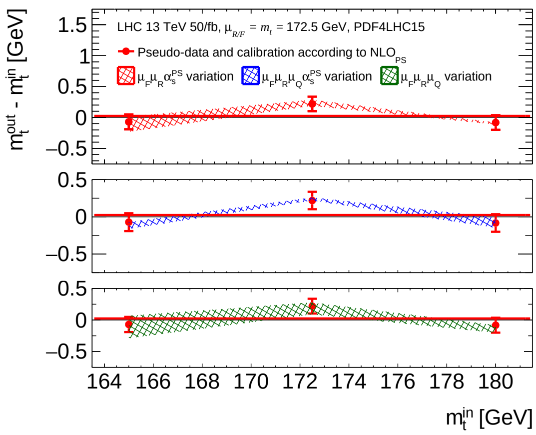

(a) $m_{\ell b}$

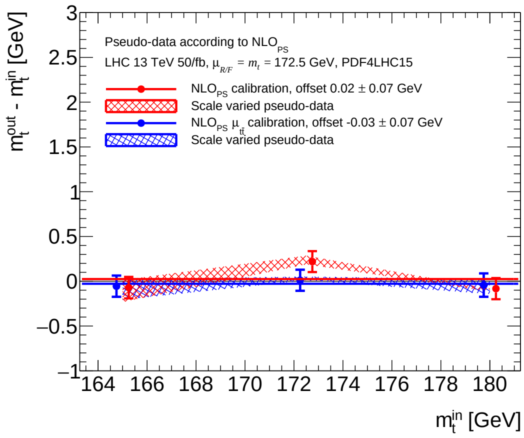

(b) $m_{\ell b}$

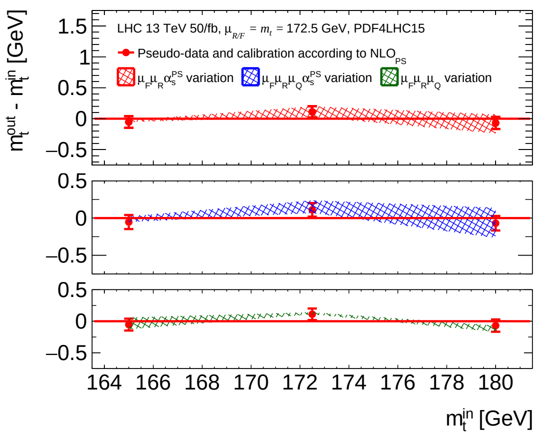

(c) m_{T2}

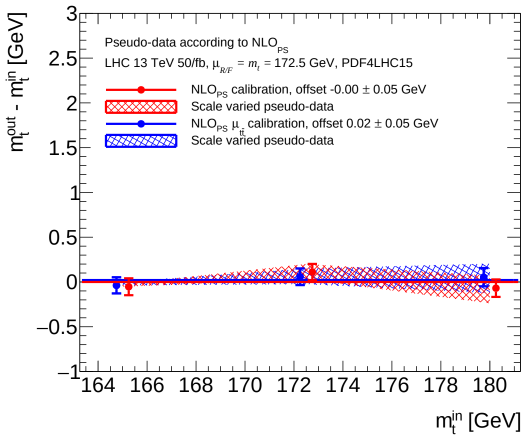

(d) m_{T2}

Figure A.5: Offsets from NLO_{PS} predictions comparing (a) different prescriptions for evaluating the shower scale uncertainties and (b) the two different central scale choices described in the text.

B MC samples at detector level

Sample DSID	Generator (ME + PS/Had)	m_t [GeV]	Simulation tags
NLO $t\bar{t}$ (NWA)			
411053	Powheg+Pythia8	171	e6696_a875_r9364_p3629
411054	Powheg+Pythia8	172	e6696_a875_r9364_p3629
410472	Powheg+Pythia8	172.5	e6348_a875_r9364_p3629
411057	Powheg+Pythia8	173	e6696_a875_r9364_p3629
411058	Powheg+Pythia8	174	e6696_a875_r9364_p3629
NLO $W^+W^-b\bar{b}$			
999991	bb4l+Pythia8	171	–
999992	bb4l+Pythia8	172	–
999995	bb4l+Pythia8	172.5	–
999993	bb4l+Pythia8	173	–
999994	bb4l+Pythia8	174	–
NLO single-top W^-t (DR)			
411109	Powheg+Pythia8	171	e6852_a875_r9364_p3629
411111	Powheg+Pythia8	172	e6852_a875_r9364_p3629
410646	Powheg+Pythia8	172.5	e6552_a875_r9364_p3629
411117	Powheg+Pythia8	173	e6852_a875_r9364_p3629
411119	Powheg+Pythia8	174	e6852_a875_r9364_p3629
NLO single-top $W^+\bar{t}$ (DR)			
411110	Powheg+Pythia8	171	e6852_a875_r9364_p3629
411112	Powheg+Pythia8	172	e6852_a875_r9364_p3629
410647	Powheg+Pythia8	172.5	e6552_a875_r9364_p3629
411118	Powheg+Pythia8	173	e6852_a875_r9364_p3629
411120	Powheg+Pythia8	174	e6852_a875_r9364_p3629
$t\bar{t}$ variation samples			
410482	Powheg+Pythia8 $h_{\mathrm{damp}}^{\mathrm{up}}$	172.5	e6454_a875_r9364_p3629
410558	Powheg+Herwig7.0.4	172.5	e6366_a875_r9364_p3629
410465	aMC@NLO+Pythia8	172.5	e6762_a875_r9364_p3629

Table B.1: Summary of the MC derivations used as input to the top-quark mass analysis presented in Chapters 8-9.

C Template fit parameters at detector level

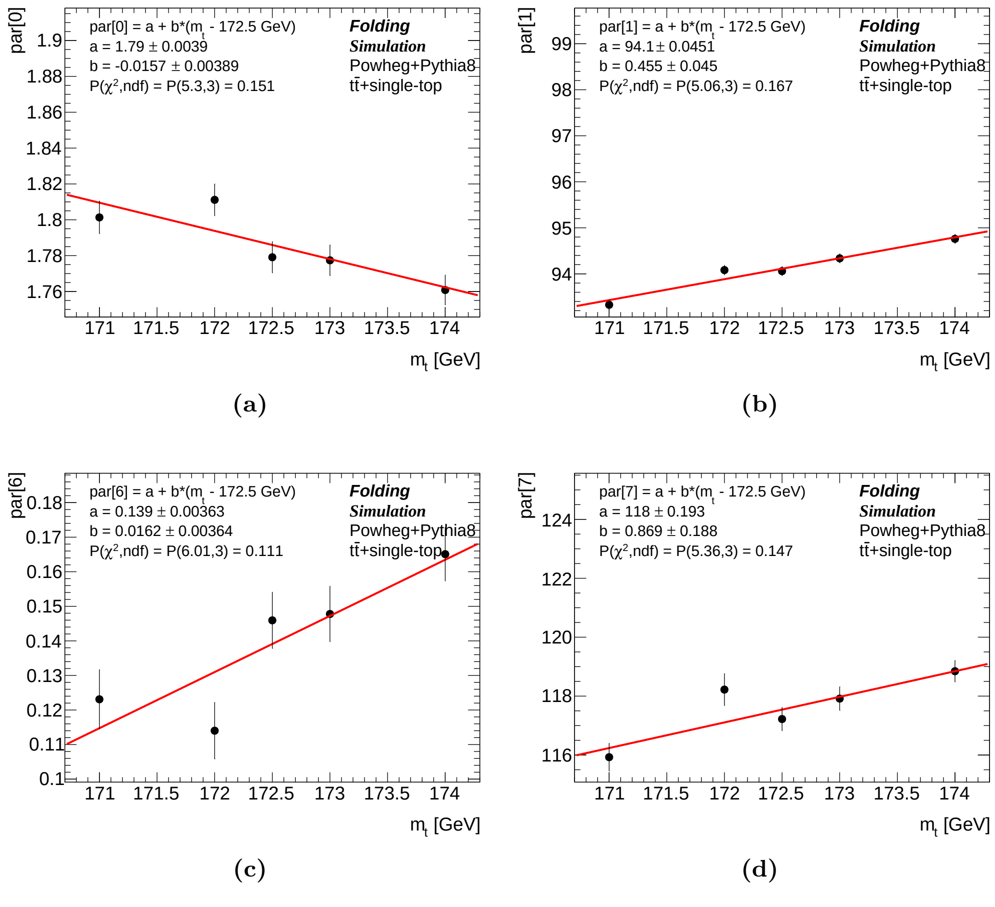

Figure C.1: The linear dependence of the four free functional fit parameters on the MC input top-quark mass, for the $t\bar{t}$+single-top samples at detector level. From the nine original parameters from the three Gaussian functions, four are left floating and five are fixed.

D Control plots with ATLAS 2015/2016 data

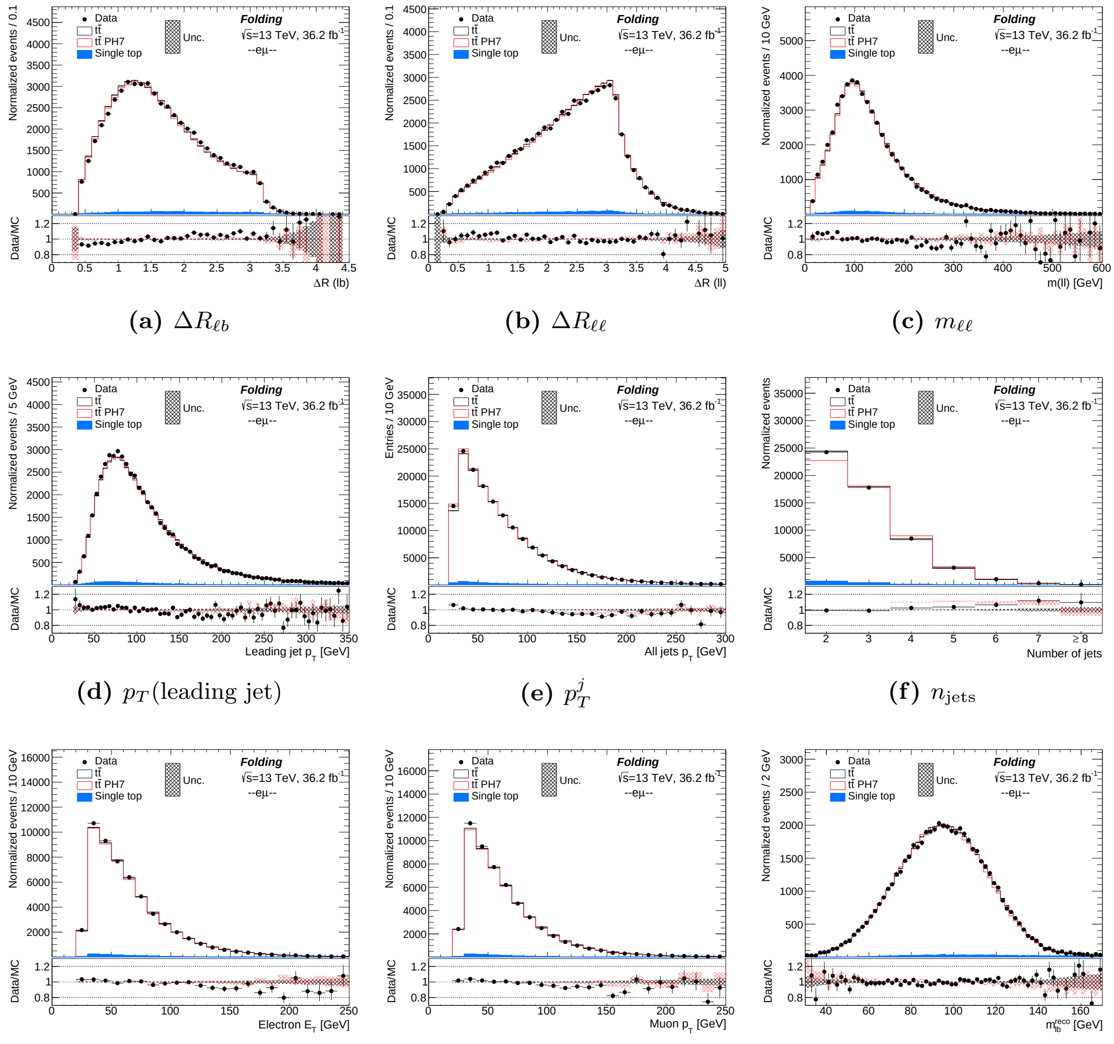

(a) $\Delta R_{\ell b}$ **(b)** $\Delta R_{\ell\ell}$ **(c)** $m_{\ell\ell}$

(d) p_T(leading jet) **(e)** p_T^j **(f)** n_{jets}

(g) p_T^e **(h)** p_T^μ **(i)** $m_{\ell b}$

Figure D.1: Some control plots are shown for $t\bar{t}$+single-top. The nominal prediction stems from Powheg+Pythia8, which is compared to Powheg+Herwig7 and to ATLAS data in the $e\mu$ dilepton channel recorded in 2015 and 2016, for a total integrated luminosity of 36.2 fb^{-1}.

E BSM benchmark points in hh production

The coefficients $A_i,\ i = 1, \dots 23$ (15) defined for the general expression of the NLO (LO) cross-section as a function of the anomalous Higgs couplings in Eq. (10.16) are shown in Table E.1, at 13 TeV at LHC. To compute these, the cross-section was calculated for different values of the couplings that were replaced in Eq. (10.16), thus giving a system of equations that one can project out to extract the values of the coefficients A_i.

The LO and NLO coefficients for $\sqrt{s} = 13, 14$ and 27 TeV are available on the arXiv e-print of Ref. [289], as well as a Mathematica file explaining how to use them. These can also be derived differentially for a fixed bin width. The differential coefficients can be downloaded for the m_{hh} distribution, with the binning shown in the histograms.

A_i	A_i^{LO}	ΔA_i^{LO}	A_i^{NLO}	ΔA_i^{NLO}
A_1	2.0806	0.0016	2.2339	0.0101
A_2	10.2011	0.0081	12.4598	0.0424
A_3	0.2781	0.0019	0.3422	0.0154
A_4	0.3140	0.0003	0.3468	0.0033
A_5	12.2731	0.0101	13.0087	0.0962
A_6	−8.4931	0.0089	−9.6455	0.0504
A_7	−1.3587	0.0015	−1.5755	0.0136
A_8	2.8025	0.0131	3.4385	0.0772
A_9	2.4802	0.0128	2.8669	0.0772
A_{10}	14.6908	0.0311	16.6912	0.1785
A_{11}	−1.1592	0.0031	−1.2529	0.0291
A_{12}	−5.5118	0.0131	−5.8122	0.1340
A_{13}	0.5605	0.0034	0.6497	0.0287
A_{14}	2.4798	0.0190	2.8593	0.1930
A_{15}	2.8943	0.0158	3.1448	0.1487
A_{16}			−0.008162	0.000225
A_{17}			0.020865	0.000399
A_{18}			0.016816	0.000783
A_{19}			0.029858	0.000829
A_{20}			−0.027025	0.000702
A_{21}			0.072692	0.001288
A_{22}			0.014523	0.000704
A_{23}			0.123291	0.006506

Table E.1: The coefficients defined in Eqs. (10.15), (10.16) are determined by computing cross-sections for a subset of parameters, and projecting out equations for the A_i's. Statistical uncertainties are propagated from the cross-section level to the coefficient result, without correlations.

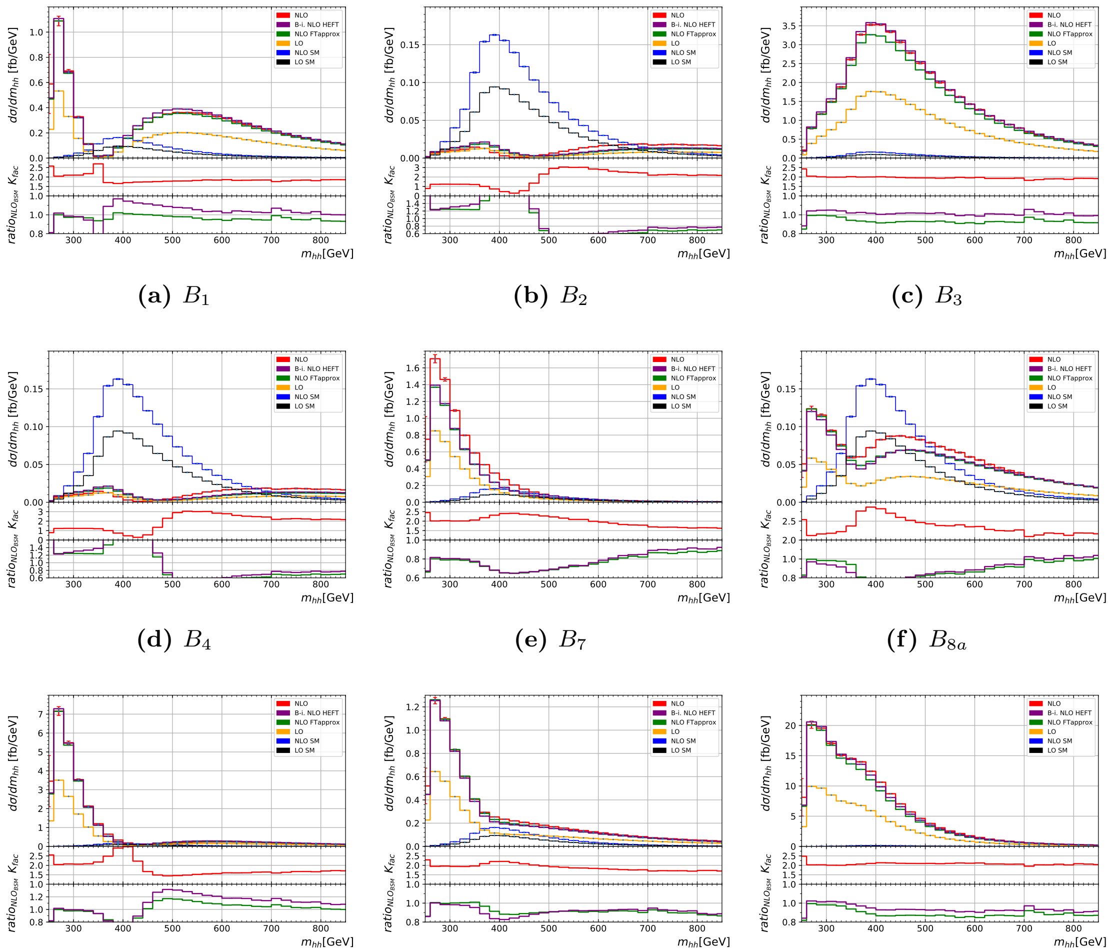

(a) B_1 **(b)** B_2 **(c)** B_3

(d) B_4 **(e)** B_7 **(f)** B_{8a}

(g) B_{10} **(h)** B_{11} **(i)** B_{12}

Figure E.1: The invariant mass of the Higgs boson pair m_{hh} is shown for the different benchmark points $B_i,\ i = 1, \ldots, 12$ defined in Table 10.1 and not already shown in Chapter 10.

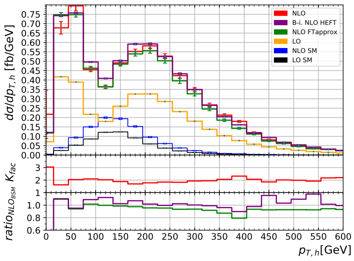

(a) B_1

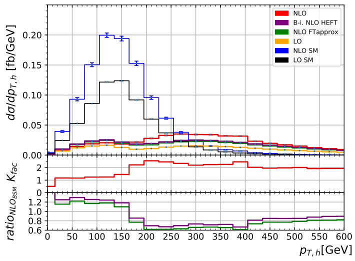

(b) B_2

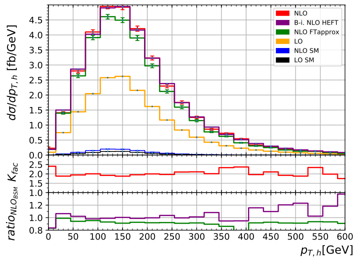

(c) B_3

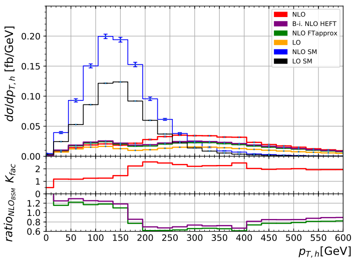

(d) B_4

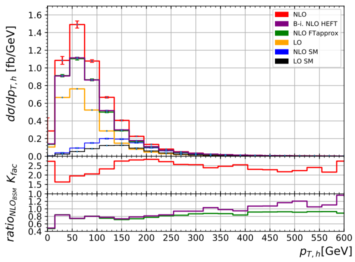

(e) B_7

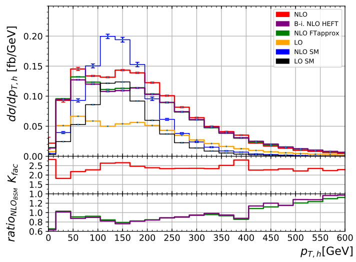

(f) B_{8a}

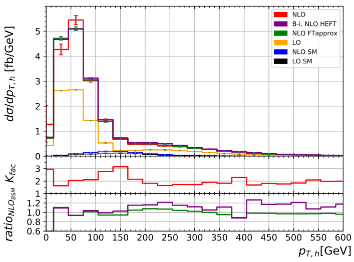

(g) B_{10}

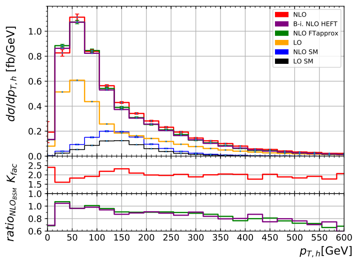

(h) B_{11}

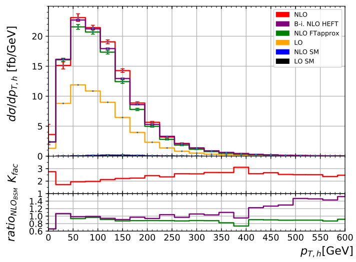

(i) B_{12}

Figure E.2: The transverse momentum $p_{T,h}$ of one (any) Higgs boson is shown for the different benchmark points $B_i,\ i = 1, \ldots, 12$ defined in Table 10.1 and not already shown in Chapter 10.

F Hardness definitions in parton-shower matching

The technical parameters for matching the PYTHIA8 parton-shower to LHE files produced by POWHEG are defined in a file called `main31.cmnd`, which bases on the LHE showering example from PYTHIA. There, several definitions for the additional radiation have to be set in order for the parton-shower to avoid double-counting regions of phase-space already covered by POWHEG. The following definitions are set:

- The number of final-state particles in the Born process $gg \to hh$.

```
POWHEG:nFinal = 2
```

- The parton-shower vetoes emissions that have a transverse momentum higher than the hardest POWHEG emission, and checks the first three. A veto is applied if `pTemt` > `pThard` (see below).

```
POWHEG:veto = 1
POWHEG:vetoCount = 3
```

- The `pTemt` and `pThard` scale definition is set: `pTemt` is set to the transverse momentum of the radiated particle with respect to the emitting parton, and `pThard` is set to the `SCALUP` value read in the LHE event, and set by POWHEG. The definition of the emitted parton is chosen by PYTHIA for the final-state radiation.

```
POWHEG:pTemt = 0
POWHEG:pThard = 0
POWHEG:emitted = 0
POWHEG:pTdef = 1
```

The hardness `pTdef` is defined by the transverse momentum p_T for initial-state radiation, and with the distance between radiator and emitted partons d_{ij} for final-state radiation corresponding to the POWHEG definition given by:

$$d_{ij} = \frac{m_{ij}^2 E_i E_j}{(E_i + E_j)^2} \ . \tag{F.1}$$

Acknowledgments

First and foremost, I am infinitely grateful to both my supervisors, Stefan Kluth on the ATLAS computing side, and Gudrun Heinrich in the phenomenology group, for actively following my progress and keeping me on the right track with always astute advice. I could not have done it without their considerate help and encouragement.

I am much obliged to all my publication collaborators, past and present, for their hard work, spontaneity and for maintaining an ever enjoyable working atmosphere: G. Buchalla, A. Celis, M. Capozi, G. Heinrich, S. Jones, M. Kerner, G. Luisoni, R. Mahbubani, A. Maier, R. Nisius, H. Rzehak, J. Schlenk, M. Schulze and J. Winter. I would also like to thank A. Knue and B. Pearson for their incredible understanding of all the tiny details of the ATLAS analysis. They are responsible for making the interface comprehensible, which probably saved me a lot of nightmarish headaches.

Of course, there is no office without officemates: my appreciation goes to A. Knue, A. Verbytskyi, D. Britzger, F. Klimpel and S. Schulte from the ATLAS computing group, for the lively discussions and the enormous pleasure I had working with you.

Much valued was the time spent with the people from Gudrun's phenomenology group: it is not always easy to move to a new city or meet entirely new people, and for the casual climate and the few Oktoberfest visits together, I am most grateful. Thanks to H. Bahl, M. Capozi, L. Chen, S. Hessenberger, S. Jahn, V. Papara, C. Pietsch, J. Schlenk, T. Zirke for making especially my first few months in Munich brighter.

I am eternally indebted to all the excellent friends that made the time at the Institute seem relativistically short, in particular those living permanently in, or sporadically passing by Connollystrasse: E. Bertoldo, M. Capozi, N. Ferreiro, M. Mancuso and F. Putzolu, E. Vitagliano, F. Guescini.

I cannot stress enough how much friends were important to my mental sanity: after the long hours and weekends of work, it was always good to know whom to count on for some entertainment. This also applies to all the people whose visits from Switzerland rekindled the spark during a weekend of partying. Lots and lots of thanks in particular to A. Arbet-Engels, C. Crusem, B. Despond, I. El Mais, M. Predikaka and K. Novoselc, A. Du Cos, A. Lichtlé, G. Mathys, C. Traveletti and all my friends from Zurich.

To my girlfriend at the time, Marthe, I want to say how grateful I am for the moments we enjoyed together. I am glad to have walked part of the path with you.

Finally, I offer my last resounding thanks to my whole family, in particular to my parents and my siblings. Without my parents, I would never have a life nearly as exciting and vibrant as this one. Thank you for what I know sometimes amounted to difficult sacrifices and for your unfaltering support. To my brother and sister, thanks for the frequent calls, the fun times in Gruyère, Munich or wherever halfway was, and generally for keeping me anchored in the normal world.